



**UNIVERSITY OF
BIRMINGHAM**

**Vacuum-ultraviolet photoexcitation of
some non-metal halides.**

By

RAYMOND YIN LOONG CHIM

**A thesis submitted to the
University of Birmingham for the degree of
DOCTOR OF PHILOSOPHY**

**School of Chemistry
The University of Birmingham
May 2003**

UNIVERSITY OF
BIRMINGHAM

University of Birmingham Research Archive

e-theses repository

This unpublished thesis/dissertation is copyright of the author and/or third parties. The intellectual property rights of the author or third parties in respect of this work are as defined by The Copyright Designs and Patents Act 1988 or as modified by any successor legislation.

Any use made of information contained in this thesis/dissertation must be in accordance with that legislation and must be properly acknowledged. Further distribution or reproduction in any format is prohibited without the permission of the copyright holder.

ABSTRACT

The vacuum-ultraviolet (VUV) fluorescence spectroscopy of CX_2Y_2 ($X, Y = H, Cl$ or Br) has been studied following gaseous photoexcitation in the range 9-22 eV using synchrotron radiation. Fluorescence excitation, dispersed emission and action spectra have been recorded to probe the molecule in this way. Photoexcitation of these molecules has resulted in the population of Rydberg states of the neutral molecule and outer valence states of the parent ion. The study has shown that the emitters in the range 190-690 nm are due to either, neutral fragments formed by dissociation of Rydberg states of the neutral molecule or excited states of the parent ion. The identity of some of the dominant dissociation channels have also been identified *via*. appearance potentials extracted from action spectra.

The threshold photoelectron photoion coincidence (TPEPICO) spectroscopy of $CX_2Y_2^+$ ($X, Y = H, Cl$ or Br), SeF_6^+ , TeF_6^+ , $SF_5CF_3^+$ and SF_5Cl^+ has been studied following gaseous photoexcitation in the range *ca.* 12-27 eV using synchrotron radiation. The identity of some of the dominant dissociation channels have been identified in a similar way in which the information is extracted from action spectra in fluorescence spectroscopy. Appearance potentials extracted from ion yield plots have allowed comparison with known calculated thermochemistry. Measurement of fixed-energy TPEPICO spectra have been used to determine the decay dynamics of some two-bodied ionic dissociations. Finally, using a variation of TPEPICO spectroscopy, the kinetic energy released into certain fragments over a range of energies has been determined. Using an impulsive model, the data has been extrapolated to zero kinetic energy to obtain a value for the first dissociative ionisation energy of these molecules. From this value, more thermochemical data has been inferred.

Acknowledgments

I would like to thank my supervisor, Dr. Richard Tuckett for his patience, help and encouragement, through good times and bad. I would also like to thank Dan Collins, Chris Howle, Clair Atterbury, Weidong Zhou, Gary Jarvis and Hans-Werner Jochims for their help with experiments at various times. A special thanks goes to Dominic Seccombe whose help, courage and friendship has been inspirational.

I would also like to thank my family and Amy for their support throughout.

Finally I to dedicate this thesis to my Father and Grandfather whose lives I cherish everyday...

Table of Contents

CHAPTER 1 :	INTRODUCTION	1
1.1	The primary excitation process.....	1
1.2	Secondary processes.....	2
1.2.1	Fluorescence and phosphorescence.....	3
1.2.2	Internal conversion and intersystem crossing.....	3
1.2.3	Dissociation.....	3
1.3	Excitation sources.....	4
1.3.1	Photon sources.....	4
1.3.1.1	Discharge line and continuum lamp sources.....	4
1.3.1.2	Synchrotron radiation.....	6
1.3.1.3	Monochromators.....	7
1.3.1.4	Lasers.....	8
1.3.2	Non-photon sources.....	8
1.3.2.1	Electrons.....	8
1.3.2.2	Metastables.....	9
1.4	Detectors.....	9
1.4.1	Light detectors.....	9
1.4.2	Electrons and ions.....	10
1.5	Experimental techniques.....	10
1.5.1	Photoabsorption.....	10
1.5.2	Electron energy loss spectroscopy (EELS).....	12
1.5.3	Fluorescence spectroscopy.....	13
1.5.4	Photoelectron and threshold photoelectron spectroscopy.....	15
1.5.5	Ionisation mass spectrometry.....	16
1.5.6	Threshold photoelectron-photoion coincidence spectroscopy.....	17
1.5.7	Pulsed field ionisation.....	18
1.6	Objectives of this Thesis.....	19
1.7	References.....	20
CHAPTER 2 :	EXPERIMENTAL	22
2.1	Synchrotron light sources and monochromators.....	22
2.1.1	Daresbury laboratory synchrotron radiation source.....	22
2.1.2	Berliner electronspeicherring-gesellschaft fur synchrotronstrahlung.....	23
2.2	Photoabsorption.....	24
2.3	Fluorescence.....	27
2.4	Photoionisation.....	30
2.5	References.....	38
CHAPTER 3 :	THE VUV FLUORESCENCE SPECTROSCOPY OF CX₂Y₂ (X, Y = H, Cl OR Br)	39
3.1	Introduction.....	39
3.2	Experimental.....	39
3.3	Energetics of the key dissociation channels.....	40
3.4	Results.....	42
3.4.1	CH ₂ Br ₂	42

3.4.1.1	The fluorescence excitation and absorption spectroscopy of CH ₂ Br ₂	42
3.4.1.2	The dispersed fluorescence spectroscopy of CH ₂ Br ₂	46
3.4.1.3	The action spectroscopy of CH ₂ Br ₂	48
3.4.1.4	Lifetime measurements of CH ₂ Br ₂	51
3.4.2	CH ₂ Cl ₂	54
3.4.2.1	The fluorescence excitation and absorption spectroscopy of CH ₂ Cl ₂	54
3.4.2.2	The dispersed fluorescence spectroscopy of CH ₂ Cl ₂	56
3.4.2.3	The action spectroscopy of CH ₂ Cl ₂	57
3.4.2.4	Lifetime measurements of CH ₂ Cl ₂	60
3.4.3	CBr ₂ Cl ₂	62
3.4.3.1	The fluorescence excitation and absorption spectroscopy of CBr ₂ Cl ₂	62
3.4.3.2	The dispersed fluorescence spectroscopy of CBr ₂ Cl ₂	63
3.4.3.3	The action spectroscopy of CBr ₂ Cl ₂	65
3.4.3.4	Lifetime measurements of CBr ₂ Cl ₂	67
3.5	Discussion : elucidation of the dominant dissociation channels.....	71
3.5.1	CCl ₂ $\tilde{A}^1B_1 - \tilde{X}^1A_1$	71
3.5.2	CCl A $^2\Delta - X^2\Pi$	71
3.5.3	CBr A $^2\Delta - X^2\Pi$	71
3.5.4	Cl ₂ D' $2^3\Pi_g - A' 2^3\Pi_u$ from CBr ₂ Cl ₂ and CH ₂ Cl ₂	72
3.5.5	Br ₂ D' $2^3\Pi_g$ from CBr ₂ Cl ₂ and CH ₂ Br ₂	73
3.5.6	CH C $^2\Sigma^+ - X^2\Pi$, B $^2\Sigma^- - X^2\Pi$ and A $^2\Delta - X^2\Pi$ from CH ₂ Cl ₂ and CH ₂ Br ₂	73
3.5.7	Parent ion emission in CH ₂ Cl ₂ and CH ₂ Br ₂	74
3.6	Conclusions.....	76
3.7	References.....	78

**CHAPTER 4 : FRAGMENTATION OF THE OUTER VALENCE STATES OF
CX₂Y₂⁺ (X, Y = H, Cl OR Br) PROBED BY THRESHOLD
PHOTOELECTRON PHOTOION COINCIDENCE
SPECTROSCOPY.....80**

4.1	Introduction.....	80
4.2	Experimental.....	81
4.3	Energetics Of The Key Dissociation Channels.....	81
4.4	Results.....	83
4.4.1	CH ₂ Br ₂	83
4.4.1.1	Threshold photoelectron spectrum	83
4.4.1.2	Scanning TPEPICO experiments.....	84
4.4.1.3	Fixed Energy TPEPICO Experiments.....	87
4.4.2	CH ₂ Cl ₂	89
4.4.2.1	Threshold photoelectron spectrum	89
4.4.2.2	Scanning TPEPICO experiments.....	91
4.4.2.3	Fixed Energy TPEPICO Experiments.....	95
4.4.3	CBr ₂ Cl ₂	97
4.4.3.1	Threshold photoelectron spectrum	97
4.4.3.2	Scanning TPEPICO experiments.....	98
4.4.3.3	Fixed Energy TPEPICO Experiments.....	100
4.5	Discussion.....	101
4.5.1	Elucidation of dominant fragmentation channels.....	101
4.5.2	Determination of the dissociation dynamics.....	103
4.6	Conclusions.....	104
4.7	References.....	106

CHAPTER 5 : FRAGMENTATION OF ENERGY-SELECTED SF₅CF₃⁺ PROBED BY THRESHOLD PHOTOELECTRON PHOTOION COINCIDENCE (TPEPICO) SPECTROSCOPY : THE BOND DISSOCIATION ENERGY OF SF₅-CF₃, AND ITS ATMOSPHERIC IMPLICATIONS108

5.1	Introduction.....	108
5.2	The first dissociative ionisation energy (DIE) of CF ₄ , SF ₆ and SF ₅ CF ₃	109
5.3	Experimental.....	112
5.4	Determination of the total mean translational kinetic energy release, <KE> _t	112
5.5	Results.....	114
5.5.1	Measurement of the first dissociative ionisation energy of CF ₄ and SF ₆	114
5.5.2	Measurement of the first dissociative ionisation energy of SF ₅ CF ₃	120
5.5.3	Threshold photoelectron spectrum of SF ₅ CF ₃	122
5.5.4	Scanning-energy TPEPICO spectrum of SF ₅ CF ₃	124
5.5.5	Fixed-energy TPEPICO spectra of SF ₅ CF ₃	126
5.5.6	Thermochemistry.....	128
5.6	Discussion.....	130
5.7	Conclusions.....	131
5.8	References.....	134

CHAPTER 6 : THE VACUUM-UV ABSORPTION SPECTRUM OF SF₅CF₃ ; IMPLICATIONS FOR ITS LIFETIME IN THE EARTH'S ATMOSPHERE.....136

6.1	Introduction.....	136
6.2	Experimental.....	137
6.3	The lifetime of SF ₅ CF ₃ in the Earth's atmosphere.....	139
6.4	Conclusions.....	143
6.5	References.....	144

CHAPTER 7 : FRAGMENTATION OF THE VALENCE ELECTRONIC STATES OF SF₅Cl⁺ PROBED BY THRESHOLD PHOTOELECTRON- PHOTOION COINCIDENCE SPECTROSCOPY.....146

7.1	Introduction.....	146
7.2	Experimental.....	146
7.3	Energetics of the key dissociation channels.....	147
7.4	Results.....	148
7.4.1	Threshold photoelectron spectrum of SF ₅ Cl.....	148
7.4.2	Scanning-energy TPEPICO spectrum of SF ₅ Cl.....	149
7.4.3	Fixed-energy TPEPICO experiments.....	151
7.4.4	Measurement of the first dissociative ionisation energy of SF ₅ Cl.....	152
7.5	Discussion.....	155
7.5.1	Elucidation of dominant fragmentation channels.....	155
7.5.2	Determination of the dissociation dynamics.....	155
7.6	Conclusions.....	156
7.7	References.....	157

CHAPTER 8 :	FRAGMENTATION OF THE VALENCE ELECTRONIC STATES OF	
	SeF₆⁺ AND TeF₆⁺ PROBED BY THRESHOLD PHOTOELECTRON-	
	PHOTOION COINCIDENCE SPECTROSCOPY	158
8.1	Introduction.....	158
8.2	Experimental.....	158
8.3	Results.....	159
	8.3.1 Threshold photoelectron spectrum.....	159
	8.3.2 Scanning TPEPICO experiments.....	162
	8.3.3 Kinetic energy release measurements.....	166
8.4	Conclusions.....	171
8.5	References.....	173

List of figures

Chapter 1

Figure 1.1	Schematic of the excited electronic states of AB*.....	2
Figure 1.2	Illustration of predissociation into ion pairs.....	4
Figure 1.3	Comparison of spectral brilliance for different photon sources.....	7
Figure 1.4	A schematic of a general absorption experiment.....	11
Figure 1.5	A schematic of electron scattering in electron energy loss spectroscopy.....	12
Figure 1.6	Examples of resonant and non-resonant features.....	14
Figure 1.7	A schematic of the energy level scheme in pulsed-field ionisation.....	19

Chapter 2

Figure 2.1	A schematic of the Daresbury synchrotron radiation source.....	23
Figure 2.2	A schematic of the absorption apparatus used at BESSY1.....	25
Figure 2.3	Graph showing $\ln(I_0/I)$ plotted as a function of pressure for GeCl ₄ photoexcited at 130 nm or 9.55 eV.....	27
Figure 2.4	A schematic of the dispersed fluorescence apparatus used at BESSY1.....	28
Figure 2.5	A VUV fluorescence excitation spectrum of N ₂ ⁺	29
Figure 2.6	A schematic of the threshold photoelectron photoion coincidence apparatus employed at Daresbury laboratories.....	31
Figure 2.7	3-D threshold photoelectron photoion spectrum of PSCl ₃ (unpublished data).....	33
Figure 2.8	3-D contour graph of the 3-D threshold photoelectron photoion coincidence spectrum of CH ₂ Br ₂	33
Figure 2.9	The threshold photoelectron and total ion spectra of Ar.....	34
Figure 2.10	A fixed-energy threshold photoelectron photoion coincidence TOF spectrum of Ar measured with a photon energy of 15.8 eV.....	36
Figure 2.11	The fit of computed TOF peaks to the experimental TPEPICO-TOF spectrum of CF ₃ ⁺ from SF ₅ CF ₃ , photoionised at 14.25 eV.....	37

CHAPTER 3

Figure 3.1	The fluorescence excitation and absorption spectra of CH ₂ Br ₂	44
Figure 3.2	The absorption spectrum of CH ₂ Br ₂ with a spectral resolution of 0.08 nm.....	45
Figure 3.3	Dispersed fluorescence spectra of CH ₂ Br ₂	47
Figure 3.4	Dispersed fluorescence spectra of CH ₂ Br ₂	48
Figure 3.5	Action spectra of CH ₂ Br ₂	50
Figure 3.6	Action spectra of CH ₂ Br ₂	51
Figure 3.7	Time-resolved fluorescence spectra of CH ₂ Br ₂	53
Figure 3.8	The fluorescence excitation and absorption spectra of CH ₂ Cl ₂	55
Figure 3.9	The absorption spectrum of CH ₂ Cl ₂ with a spectral resolution of 0.08 nm.....	56
Figure 3.10	Dispersed fluorescence spectra of CH ₂ Cl ₂	57
Figure 3.11	Action spectra of CH ₂ Cl ₂	58
Figure 3.12	Action spectra of CH ₂ Cl ₂	59
Figure 3.13	Time-resolved fluorescence spectra of CH ₂ Cl ₂	61
Figure 3.14	The fluorescence excitation and absorption spectra of CBr ₂ Cl ₂	63
Figure 3.15	Dispersed fluorescence spectra of CBr ₂ Cl ₂	64
Figure 3.16	Action spectra of CBr ₂ Cl ₂	66
Figure 3.17	Action spectra of CBr ₂ Cl ₂	67
Figure 3.18	Time-resolved fluorescence spectra of CBr ₂ Cl ₂	69

Figure 3.19	Time-resolved fluorescence spectra of CBr_2Cl_2	70
Figure 3.20	Fluorescence excitation spectrum of CH_2Br_2 measured at Daresbury Laboratory.....	75
Figure 3.21	Fluorescence excitation spectrum of CH_2Cl_2 measured at Daresbury Laboratory.....	76

CHAPTER 4

Figure 4.1	The TPES of CH_2Br_2	84
Figure 4.2	Ion yield plots of CH_2Br_2^+ , CH_xBr^+ and CH_2^+	85
Figure 4.3	TPEPICO-TOF spectra at various excitation wavelengths in the CH_xBr^+ region (where $x = 0, 1$ or 2).....	86
Figure 4.4	Comparison of the sum of three gaussian fits of the three isotopomers of CH_2Br_2^+ to TPEPICO-TOF spectra of CH_2Br_2^+	88
Figure 4.5	The TPES of CH_2Cl_2	90
Figure 4.6	The high resolution TPES of CH_2Cl_2 with an optical resolution of 1 \AA	91
Figure 4.7	Ion yield plots of CH_2Cl_2^+ , CH_2Cl^+ (where $x = 1$ or 2), CHCl^+ and CH_2^+	93
Figure 4.8	TPEPICO-TOF spectra at various excitation wavelengths in the CH_xCl_2^+ region (where $x = 0, 1$ or 2).....	94
Figure 4.9	TPEPICO-TOF spectra at various excitation wavelengths in the CH_xCl^+ region (where $x = 0, 1$ or 2).....	95
Figure 4.10	Comparison of the sum of three gaussian fits of the three isotopomers of CH_2Cl_2^+ to TPEPICO-TOF spectra of CH_2Cl_2^+	96
Figure 4.11	TPES of CBr_2Cl_2	98
Figure 4.12	Ion yield plots of CBrCl_2^+ , CBr_2Cl^+ , CBrCl^+ , CCl_2^+ , CBr^+ and CCl^+	99

CHAPTER 5

Figure 5.1	The energetics of dissociation of the ground state of SF_5CF_3 and SF_5CF_3^+	110
Figure 5.2	Mean total kinetic energy released in the reaction $\text{CF}_4 + h\nu \rightarrow \text{CF}_3^+ + \text{F} + \text{e}^-$ for photon energies in the range 15.5 to 18.8 eV	115
Figure 5.3	TPEPICO-TOF spectra (open circles) for (a) $\text{CF}_3^+ / \text{CF}_4$, (b) $\text{SF}_5^+ / \text{SF}_6$ and (c) $\text{CF}_3^+ / \text{SF}_5\text{CF}_3$ recorded at photon energies of 16.05 , 15.72 and 14.09 eV , respectively.....	117
Figure 5.4	Mean total kinetic energy released in the reaction $\text{SF}_6 + h\nu \rightarrow \text{SF}_5^+ + \text{F} + \text{e}^-$ for photon energies in the range 15.1 to 19.1 eV	119
Figure 5.5	Mean total kinetic energy released in the reaction $\text{SF}_5\text{CF}_3 + h\nu \rightarrow \text{CF}_3^+ + \text{SF}_5 + \text{e}^-$ for photon energies in the range 13.3 to 15.5 eV	121
Figure 5.6	(a) Threshold photoelectron spectrum of SF_5CF_3 . (b) Coincidence ion yields of CF_3^+ and SF_3^+	123
Figure 5.7	Time-of-flight spectrum of the fragment ions from SF_5CF_3 , summed over the range of photoexcitation energies 12.7 to 26.4 eV	125
Figure 5.8	(a) Coincidence TOF spectrum of CF_3^+ from SF_5CF_3 photoionised at 14.25 eV into the ground, \tilde{X} state of the parent cation.....	127

CHAPTER 6

Figure 6.1	Vacuum-UV absorption spectrum of CF_4 recorded at a resolution of 0.08 nm	138
Figure 6.2	Vacuum-UV absorption spectrum of SF_5CF_3 recorded at a resolution of 0.12 nm	139

CHAPTER 7

Figure 7.1	Threshold photoelectron spectrum of SF ₅ Cl at a resolution of 0.3 nm.....	148
Figure 7.2	Ion yield plots of SF ₅ ⁺ , SF ₄ Cl ⁺ , SF ₄ ⁺ and SF ₃ ⁺	150
Figure 7.3	Time of flight spectra of SF ₅ ⁺ from SF ₅ Cl at various energies.....	152
Figure 7.4	Mean total kinetic energy released in the reaction SF ₅ Cl + hv → SF ₅ ⁺ + F + e ⁻ for photon energies in the range 12.0-14.3 eV.....	154

CHAPTER 8

Figure 8.1	Threshold photoelectron spectrum of SeF ₆	160
Figure 8.2	Threshold photoelectron spectrum of TeF ₆	161
Figure 8.3	TPEPICO coincidence ion yields of SeF ₅ ⁺ , SeF ₄ ⁺ , SeF ₃ ⁺ and SeF ₂ ⁺	163
Figure 8.4	TPEPICO coincidence ion yields of TeF ₅ ⁺ , TeF ₄ ⁺ , TeF ₃ ⁺ and TeF ₂ ⁺	165
Figure 8.5	Measured total kinetic energy released in the process SeF ₆ + hv → SeF ₅ ⁺ + F + e ⁻ for photon energies in the range 15.7 to 17.7 eV.....	167
Figure 8.6	Measured total kinetic energy released in the process TeF ₆ + hv → TeF ₅ ⁺ + F + e ⁻ for photon energies in the range 15.7 to 17.7 eV.....	168
Figure 8.7	TPEPICO-TOF spectra (symbols) for (a) SeF ₅ ⁺ /SeF ₆ and (b) TeF ₅ ⁺ /TeF ₆ recorded at a photon energy of 16.8 eV and 16.9 eV respectively.....	170

List of tables

Chapter 1

Table 1.1	Examples of some commonly used windows.....	5
Table 1.2	Examples of some commonly used gaseous discharge lamps.....	5
Table 1.3	A summary of commonly used rare gas metastables.....	9

Chapter 3

Table 3.1	Energetics of the key dissociation channels of CH ₂ Cl ₂ , CH ₂ Br ₂ , and CBr ₂ Cl ₂	40
Table 3.2	The Rydberg assignments of the photoabsorption bands in CH ₂ Br ₂	45
Table 3.3	Summary of the emission bands observed following photoexcitation of CH ₂ Br ₂	49
Table 3.4	Lifetimes of fragments produced following the (pre-)dissociation of CH ₂ Br ₂	52
Table 3.5	The Rydberg assignments of the photoabsorption bands in CH ₂ Cl ₂	54
Table 3.6	Summary of the emission bands observed following photoexcitation of CH ₂ Cl ₂	60
Table 3.7	Lifetimes of fragments produced following the (pre-) dissociation of CH ₂ Cl ₂	62
Table 3.8	Summary of the emission bands observed following photoexcitation of CBr ₂ Cl ₂	65
Table 3.9	Lifetimes of fragments produced following the (pre-) dissociation of CBr ₂ Cl ₂	68

Chapter 4

Table 4.1	Energetics of the key dissociation channels of CH ₂ Br ₂ , CH ₂ Cl ₂ and CBr ₂ Cl ₂	81
Table 4.2	Appearance energies of the fragment ions formed following photoexcitation of CH ₂ Br ₂	86
Table 4.3	Mean translational KE releases (<KE> _t) of the two-body fragmentation processes of the valence states of CH ₂ Br ₂ ⁺	89
Table 4.4	Peak positions and assignments associated with the \tilde{X} state of CH ₂ Cl ₂ ⁺	91
Table 4.5	Appearance energies of the fragment ions formed following photoexcitation of CH ₂ Cl ₂	95
Table 4.6	Mean translational KE releases (<KE> _t) of the two-body fragmentation processes of the valence states of CH ₂ Cl ₂ ⁺	96
Table 4.7	Appearance energies of the fragment ions formed following photoexcitation of CBr ₂ Cl ₂	99
Table 4.8	Mean translational KE releases (<KE> _t) of the two-body fragmentation processes of the valence states of CBr ₂ Cl ₂ ⁺	100

Chapter 5

Table 5.1	Total mean translational kinetic energy release, <KE> _t , of the two-body fragmentation of the valence states of SF ₅ CF ₃ ⁺	126
Table 5.2	Energetics of important dissociation channels and ionisation energies of SF ₅ CF ₃	129

Chapter 6

Table 6.1	Thermal electron attachment rate constants, absorption cross-sections at 121.6 nm, and atmospheric lifetimes for CF ₄ , SF ₆ and SF ₅ CF ₃	140
Table 6.2	Energetics of reactions of SF ₅ CF ₃ at 0 K with zero-energy electrons and photons.....	142

Chapter 7

Table 7.1	Energetics of the key dissociation channels of SF ₅ Cl.....	147
Table 7.2	Appearance energies of the fragment ions following photoexcitation of SF ₅ Cl.....	149
Table 7.3	Mean translational KE releases (<KE> _i) of the two-body fragmentation processes of the valence states of SF ₅ Cl ⁺	151

Chapter 8

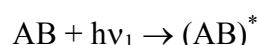
Table 8.1	Thermochemistry of fragment ions produced from photoionisation of SF ₆ , SeF ₆ and TeF ₆	164
------------------	---	-----

CHAPTER 1 : INTRODUCTION

The aim of the work presented in this thesis is to probe the nature of the excited electronic states of some non-metal halides and their cations. Later chapters describe the experiments performed and the results obtained. This chapter provides an overview of the research field, but only appropriate to the vacuum-ultraviolet where the primary photon has wavelength, $\lambda < 150$ nm (or 8 eV). Firstly, the primary excitation process and the secondary processes that may occur when a molecule is excited in the vacuum-UV are described. Secondly, the various components of an experiment are discussed.

1.1 The primary excitation process

When an electron or photon of energy $h\nu_1$ interacts with a molecule, a number of processes can occur. Absorption of part or all of the energy may be absorbed and the molecule may experience translational, rotational, vibrational and/or electronic excitation:¹



This reaction is termed a resonant process. This is because the quantisation of energy ensures that only discrete amounts of energy can be transferred. Excited electronic states of molecules ($(AB)^*$) generally lie more than 10000 cm^{-1} (1.24 eV) above the ground state. Whether bound or dissociative, excited states can be conveniently classified as valence or Rydberg. A schematic is shown in Fig. 1.1. Valence states result from excitation of electrons to higher valence orbitals. In the case of closed-shell molecules, this generally means populating antibonding orbitals. Rydberg states result from excitation of electrons into Rydberg orbitals. In general, the electrons in such orbitals spend most of their time a large distance away from the core which is perceived as a point charge. Rydberg orbitals therefore have an atomic-like nature. Electronic transitions to Rydberg states from the ground state of a molecule tend to occur in the $50000\text{-}100000\text{ cm}^{-1}$ region, and their positions are given by the well known Rydberg formula:¹

$$E = IP - R_H / (n-\delta)^2 \quad (1.1)$$

In this formula R_H is the Rydberg Constant, IP is the ionisation potential to which the Rydberg states converge, n is the principle quantum number of the Rydberg orbital and δ is its associated quantum defect. The physical interpretation of δ is a matter of some complexity. For the purpose of the present discussion it can be described as the deviation of the core from an impenetrable point charge. The intensity of a Rydberg transition is proportional to n^{-3} . Apart from the ease of fitting Rydberg transitions in a series governed by the Rydberg formula, they show other qualitative differences from valence

transitions. Since valence transitions mostly originate from bonding or non-bonding orbitals a substantial geometry change may result. This causes the oscillator strength of the transition to be spread over a broad Franck-Condon (FC) region. By contrast, Rydberg transitions tend to show more narrow FC envelopes, and often have less extensive vibrational structure.

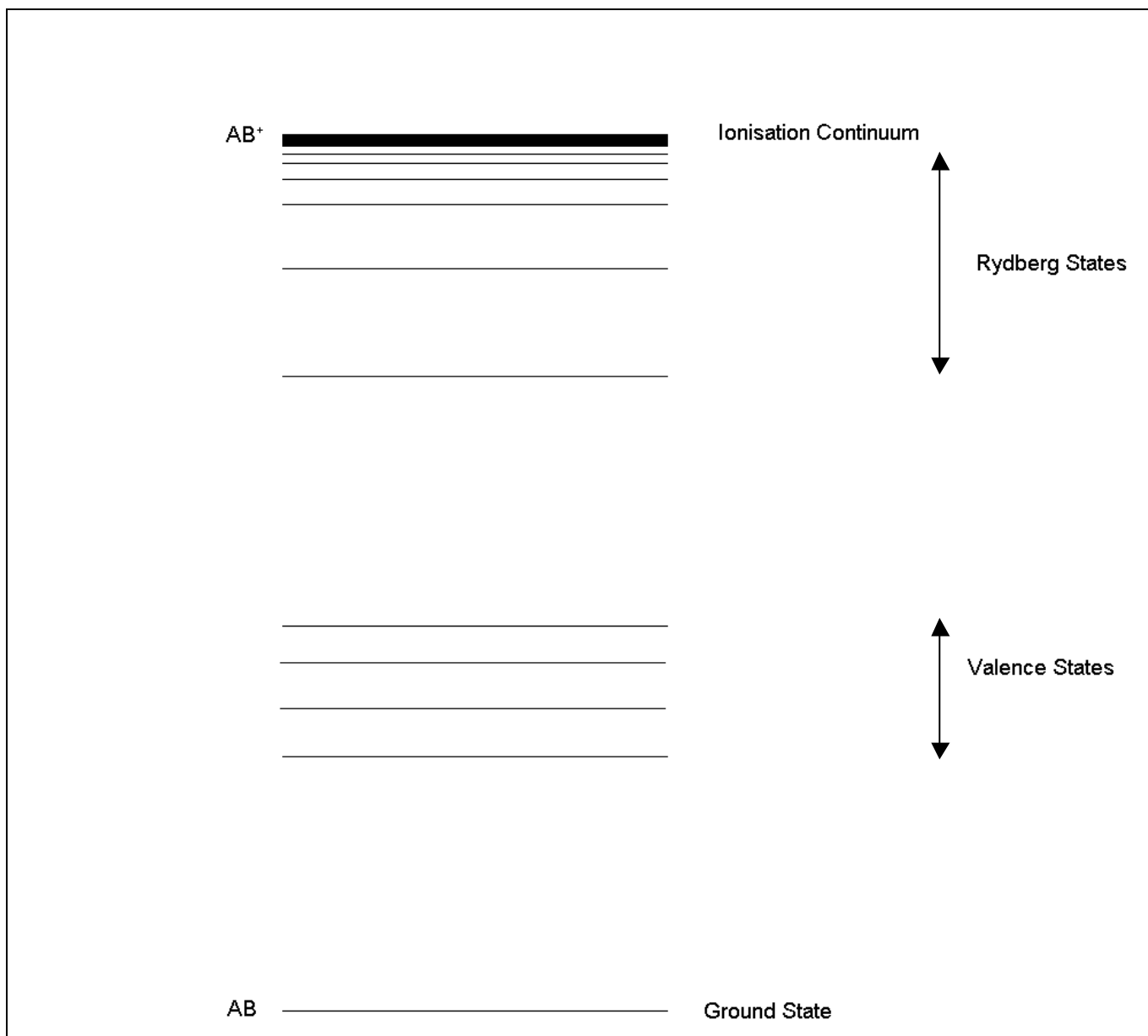


Figure 1.1 Schematic of the excited electronic states of AB*.

1.2 Secondary Processes.

The secondary process is defined by the fate of the initially-excited molecule (AB)*. Possible processes include phosphorescence, fluorescence, internal conversion, intersystem crossing, isomerisation, dissociation, ion-pair formation and autoionisation, and these processes all follow the excitation of a molecule into a neutral or ionic state.

1.2.1 Fluorescence and phosphorescence.

These two radiative processes involve the spontaneous emission of electromagnetic radiation :



If the emission results from electronic states which have the same spin multiplicity, then the process is called fluorescence ($\Delta S = 0$). Phosphorescence results from electronic transitions from states whose multiplicities are different. Phosphorescent transitions are forbidden, hence they occur on a much longer time-scale to fluorescence. The time scale ranges from $10^{-9} - 10^{-6}$ s for fluorescence and $10^{-6} - 10^0$ s for phosphorescence. Processes that do not result in the emission of radiation are termed non-radiative. The two most common are internal conversion and intersystem crossing.

1.2.2 Internal conversion and intersystem crossing.

The intramolecular conversion of electronic energy to vibrational energy or electronic relaxation occurs with no change in the total internal energy.² The $\Delta S = 0$ selection rule also applies here to this non-radiative process, similar to that of the radiative processes of fluorescence and phosphorescence. If electronic relaxation occurs between states of the same multiplicity, then the process is called internal conversion. Intersystem crossing results from electronic relaxation occurring between two states whose spin multiplicity is different. Like phosphorescence, intersystem crossing is formally forbidden. However, the overlap of vibrational wavefunctions of individual electronic states is critical to the rate of the process, and adhesion to the $\Delta S = 0$ selection rule is not strict. In general a small difference in geometry and a small energy difference result in good overlap and hence fast electronic relaxation. The probability of a favourable energy level scheme is therefore more probable with larger molecules as the density of states is relatively high compared to small molecules.

1.2.3 Dissociation

Direct dissociation can occur into neutrals or ions:



The simplest way in which dissociation may occur is through excitation into a repulsive state. This process is extremely rapid *ca.* $10^{-15} - 10^{-12}$ s. However, this type of fragmentation of excited states is not the only way dissociation can occur. Dissociation can also occur as a result of the potential energy surface of the initially-excited state lying below the dissociation limit. However, it is crossed by another state

lying above a different, but lower, dissociation threshold. This process is called predissociation. Finally, dissociation can result from a large geometry change between the ground state and the excited state. Excitation into the excited state can populate high vibrational levels which may be above the dissociation limit.

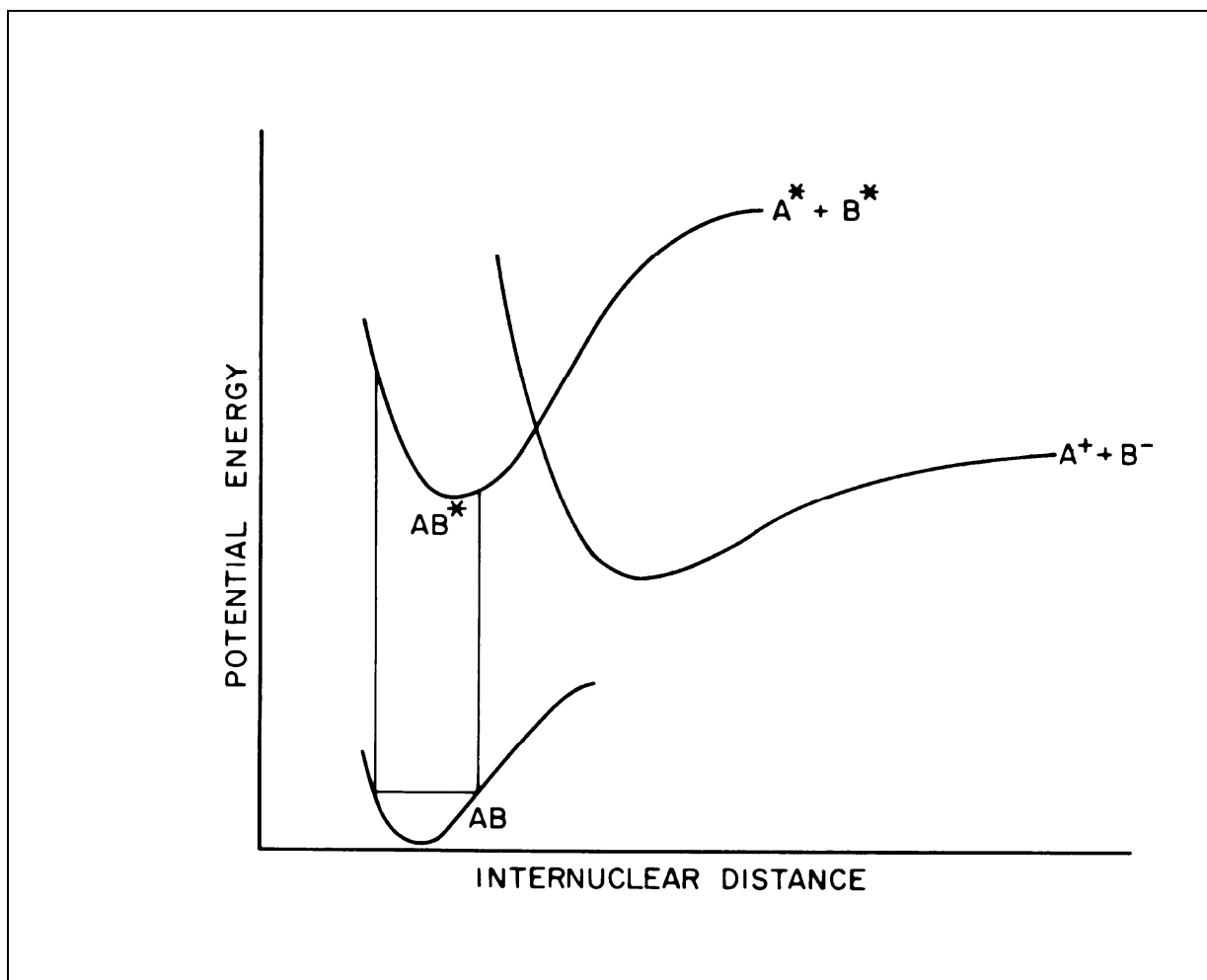


Figure 1.2 Illustration of predissociation into ion pairs. Adapted from reference 1.

1.3 EXCITATION SOURCES

1.3.1 Photon sources

1.3.1.1 Discharge line and continuum lamp sources

There are many gaseous discharge lamps that provide line and continuum photon sources in the vacuum ultraviolet (VUV). Line or fixed energy sources are produced from a transition between two stable states within an excited atom or molecule.⁴ An electrical discharge in a low pressure (<1 Torr) system provides the environment which produces the transition. The resulting reemitted radiation constitutes the source of photons. Perhaps the most commonly used single line source in the VUV is the He lamp which produces the He I emission line at 21.22 eV. This corresponds to the transition between the excited state He (1s 2p, ¹P) and the ground state He (1s², ¹S). At lower pressure (<0.1 Torr), He⁺ ions become

dominant and the He II emission line at 40.78 eV is produced. It should be noted that these sources need a constrained separation between the source of radiation and the experiment due to differing operating pressures. Ideally a window capable of transmitting the radiation is placed at the interface between the two regions. Some examples of commonly used windows are shown in Table 1.1,⁵ and more examples of gaseous discharge lamps are given in Table 1.2.^{4,6,7} It can be seen from these tables that emissions below 105 nm cannot use a window as there are no known materials that will transmit this range of radiation. In this case a windowless system of orifices and differential pumping may be used to isolate the two regions. Although the two regions not separated completely, pressure differentials of several orders of magnitude can be achieved.

Table 1.1 Examples of some commonly used windows.

Window Material	Transmission Range / nm
LiF	105 – 7000
MgF ₂	122 – 9700
CaF ₂	125 – 12000
SiO ₂	165 - 4000
NaCl	210 - 25000

Table 1.2 Examples of some commonly used gaseous discharge lamps.

Source	Transition	Wavelength / nm	Photon Energy / eV
H Lyman α	$2p^1 - 1s^1$	121.57	10.20
Ar I	$3p^5 4s^1 - 3p^6$	106.66, 104.82	11.62, 11.83
Xe I	$5p^5 6s^1 - 5p^6$	146.96, 129.56	8.44, 9.57
He I	$1s^1 2p^1 - 1s^2$	58.43	21.22
He II	$2p^1 - 1s^1$	30.38	40.81
Ne I	$1s^1 2p^1 - 1s^2$	74.37, 73.59	16.67, 16.85

Continuum sources are produced by a transition from a bound excited state of a molecule to a repulsive lower state. In general, continuum sources are less intense than line sources. These types of sources are particularly useful when a range of energies is needed. A continuum discharge lamp operates at higher pressures to line sources (up to 200 Torr). Perhaps the most commonly used continuum source in the VUV is the Hopfield continuum of helium.⁸ This broad band continuum extends from 11.8 to 20.6 eV. Due to the high pressures required considerable differential pumping is needed.

1.3.1.2 Synchrotron radiation (SR)

Perhaps the most useful continuum source is synchrotron radiation due to its range across the whole electromagnetic spectrum, much wider than any laboratory photon source. This photon source is the

radiative emission generated by radially accelerating charged particles to relativistic speeds. Electrons are usually the preferred choice of particle due to their high charge-to-mass ratio, although positrons can also be used. The total power of a single particle is given by:^{9,10}

$$\text{Power} = \chi[(z^2 E^4)/(m^4 R^2)] \quad (1.2)$$

where χ is equal to $\frac{1}{2}(3c^7)$, m is the mass, c is the charge, E is the energy of the particle and R is the radius of the circular orbit. Such sources are generally comprised of three components. Electrons are accelerated in a linear accelerator and further accelerated in a booster ring. The electrons are then injected into a storage ring where a series of bending magnets bend the particles into a circular orbit. Synchrotron radiation is then emitted tangentially to the motion of the electrons. Electron scattering and collisions are the main removal of particles and the lifetime of sources are such that typically injections are needed every 4 – 24 hours. Originally synchrotron radiation was a by-product of particle acceleration and accounted for substantial energy loss. The energy lost by the synchrotron radiation is replenished by radio frequency cavities which also bunch the electrons together. In multi-bunch mode, most experiments are not sensitive to the high frequencies so the source is regarded as pseudo-continuous. In single-bunch mode, only one bunch of electrons are stored in the storage ring at one time compared to *ca.* 100 bunches in multi-bunch mode ; time-resolved experiments are then possible.

There are numerous excitation sources available in the VUV range. Fig 1.3 shows a general comparison of the spectral brilliance of different sources over a range of wavelengths. The unit of brilliance is the most comprehensive unit providing a required quantitative description of a source due to the fact that it takes into account the divergence of the beam. Fig 1.3 shows that SR is a very useful source in the VUV due to its tunability over a wide spectral range and its high brilliance. In the range of wavelengths which are used in this thesis (500 – 1500 Å), this figure shows clearly that synchrotron radiation is one of the preferred sources.

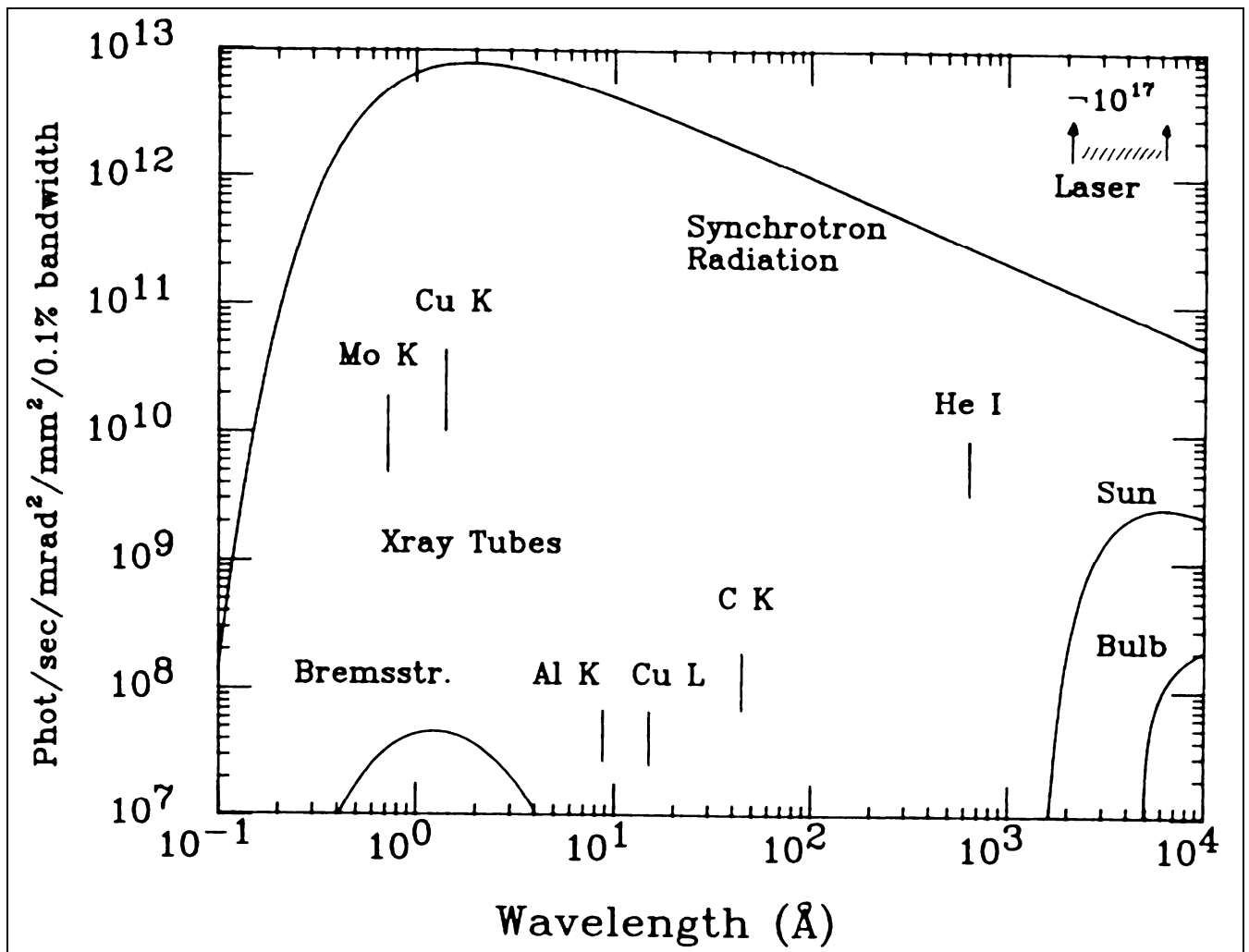


Figure 1.3 Comparison of spectral brilliance for different photon sources.¹¹

1.3.1.3 Monochromators

Some sources described in the previous sections, namely gaseous discharge continua and synchrotron radiation, require energy selection. Prisms and interferometers cannot be used as most materials are opaque in the VUV region and are not discussed here. Monochromators for the VUV region exclusively use diffraction gratings as a dispersing device. A diffraction grating is generally made of glass or ceramic coated with a reflective material into which uniform lines are cut. The diffracted wavelengths are given by the Bragg law:¹²

$$n\lambda = d[\sin(\theta) + \sin(\phi)] \quad (1.3)$$

where n is an integer and represents the order of light, λ is the wavelength, d is the distance between the lines, θ is the angle of incidence and ϕ is the angle of dispersion. A high flux of first order radiation ($n=1$) is required from the from the monochromator grating. The resolution of light emitted from a monochromator is given by:¹⁵

$$\Delta\lambda = [(x_n^2 + x_x^2)^{1/2}d\cos\theta]/fn \quad (1.4)$$

where $\Delta\lambda$ is the resolution, x_n and x_x are the monochromator entrance and exit slit widths, f is the focal length and n is the order of light. The wavelength of light is selected by varying the position of the grating.

1.3.1.4 Lasers

Lasers are coherent, bright (brilliant) due to low divergence and highly monochromatic.³ The radiation is produced in a cavity by light amplification by stimulated emission. Typically lasers produce radiation in the IR to the ultraviolet regions. However, the photon energy of lasers still lie below the ionisation potential of most molecules. Whilst doubling and mixing crystals enable higher energies, lasers still offer only limited tunability and do not stretch very far into the ultra-violet region. However, due to their high brightness, lasers are able to produce species at higher energies *via* multi-photon processes.¹³ Multi-photon ionisation involves populating an excited state using two or more photons *via* a virtual state. Excitation *via* real states is known as resonance enhanced multi-photon ionisation. The intermediate states act as a stepping-stone to higher excited states. Thus lasers may probe phenomenon relating to electronic transitions in the VUV region, but the lack of a truly tunable source is a severe hindrance in these types of experiment.

1.3.2 Non-photon sources

1.3.2.1 Electrons

Electrons can be used to excite or ionise molecules and some techniques using electrons as an excitation source are described later in sections 1.5.2 and 1.5.5 ; these sections describe electron energy loss spectroscopy and electron ionisation mass spectrometry. Electron beams can be created in many ways but perhaps the most common and simplest method is *via* thermionic emission. An electron-rich filament is heated, producing electrons spread over a distribution of energies. The electrons are energy selected by an electron monochromator to produce a monoenergetic electron beam.¹⁴ The electron monochromator consists of electrodes whose voltages are accurately defined to select a narrow distribution of electrons, typically in the range 20 – 50 meV. This resolution depends upon the energy of the electron beam and, in general, will improve as the energy of the beam increases due to the ease of focussing higher-energy electrons.

1.3.2.2 Metastables

Molecules can be excited by collisions with electronically excited atoms. Some excited state states in atoms and molecules are metastable with respect to emission because the transitions to lower electronic

states are formally forbidden. Table 1.3 shows some examples of metastables and their energies. Metastables can exist long enough to transfer their excess energy *via* a collisional process. These metastable states are created by flowing a gas (*ca.* 10 Torr) through a microwave discharge cavity. Too high a pressure and the species will undergo rapid collisional deactivation.

Table 1.3 A summary of commonly used rare gas metastables.¹⁵

Atom	Metastable state	Energy / eV
He	¹ S	20.61
	³ S	19.82
Ne	³ P ₀	16.72
	³ P ₂	16.62
Ar	³ P ₀	11.72
	³ P ₂	11.55

1.4 Detectors

1.4.1 Light detectors

When conducting experiments that require the photon energy to be scanned, it is necessary to know the relative intensity of light as a function of photon energy. Without this information, flux normalisation is not possible. The most common types of detectors used to monitor VUV radiation are the photodiode and the photomultiplier tube. Photodiodes are simply a cathode and an anode. When the cathode is exposed to radiation it emits electrons that travel towards the anode. The resulting current is then amplified to a detectable current. Photodiodes are not suitable for low light level detection due to the high noise level caused by the amplification. However, photodiodes have the advantage that they can be used in the VUV as they are windowless.

Photomultiplier tubes consist of a photocathode and a series of dynodes with secondary emission coefficients greater than unity. Radiation is admitted into the photomultiplier tube through a window. When the photocathode is exposed to radiation, a bunch of electrons are ejected and travel towards the first dynode which has a positive potential. The electrons hit the dynode and each electron produces several more electrons that travel towards the next dynode, which has a higher potential than the first. The electrons then hit a third dynode and the process continues all the way to the end of the tube where a current detector is situated. The gain of a 12-stage photomultiplier tube at 2000 V is typically 10^7 .¹⁶ Since amplification takes place inside the evacuated tube, there is essentially no noise. In addition to this, cooling can further reduce dark counts. Due to the photomultiplier tube not being a windowless system, the detectable wavelengths of light are limited to the cut-off threshold of the window material. This

makes the *direct* detection of VUV radiation impossible. However, by using a window coated on the inside with a material that emits visible fluorescence when exposed to VUV radiation, and by detecting this visible radiation with a photomultiplier tube, the intensity of the VUV light may be detected *indirectly*. Sodium salicylate is commonly used for this purpose as the fluorescent quantum efficiency is known to be constant over a wide range of the VUV, and emission from sodium salicylate spans 350 – 550 nm.⁴

1.4.2 Electrons and Ions

Perhaps one of the most common electron detectors is the single electron multiplier, otherwise known as the channeltron. Such a device is more sensitive than the electrometer, which simply measures current. Like photomultipliers, the channeltron uses gain to create this sensitivity. This type of detector is basically a rounded glass funnel with a highly resistive surface. This surface constitutes a continuous dynode when a potential is applied at both ends, and like the photomultiplier, when an electron strikes the surface, several secondary electrons are produced. Although ions can also be detected in this way, a more common device used to detect ions is the microchannel plate. This device is a glass plate which has several channels through which ion can travel. Each channel wall is coated with a material that is highly resistive, and like the channeltron, when a potential is applied across the plate, a continuous dynode is created. The principle is the same as in channeltrons; a cascade of secondary electrons are created when the channel walls are struck by an ion. Both channeltrons and microchannel plates only operate in good vacuum.

1.5 Experimental techniques

1.5.1 Photoabsorption

The amount of radiation absorbed by a species is governed by the Beer-Lambert law¹ and depends on the concentration of the species, the photoabsorption cross-section and the pathlength through which the radiation passes:

$$I = I_0 \exp(-\sigma c L) \quad (1.5)$$

In this equation, I_0 and I are the intensity of the incident and transmitted radiation respectively, σ is the absorption cross-section, c is the number density and L is the path length. A schematic of a typical absorption experiment is given in Fig. 1.4. The aim of a photoabsorption experiment is to determine the absorption cross-section for a range of wavelengths. This can be achieved by filling a closed cell of defined path length with a sample gas. One way to define the path length of the absorption cell is to use a window at either side that does not attenuate the light. The material used depends on the wavelength of light for which the experiment has been designed. For example, lithium fluoride windows may be used

for $\lambda > 105$ nm. The cell must have a uniform distribution of sample. The cell is irradiated, and a detector mounted behind the absorption cell detects the transmitted light. In experiments described later in this thesis, the incident wavelength is scanned, and I measured as a function of wavelength. The cell is then evacuated, and the experiment repeated to determine I_0 for every value of λ . Thus σ can be determined as a function of λ .

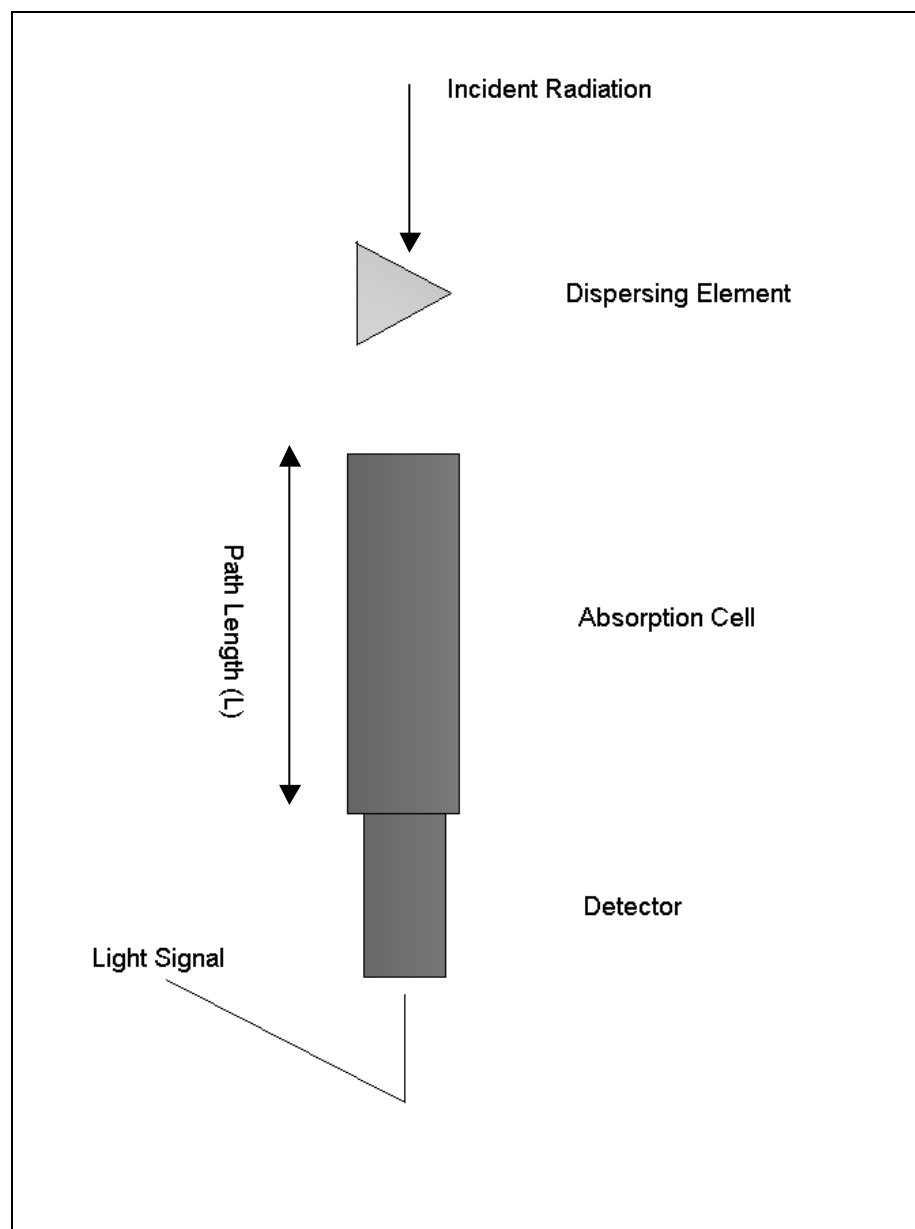


Figure 1.4 A schematic of a general absorption experiment.

1.5.2 Electron energy loss spectroscopy (EELS)

Electron energy loss spectroscopy is a pseudo-absorption experiment that uses energetic electrons as the excitation source. A monochromatic beam of electrons is passed through a sample. The electrons impart kinetic energy to the molecule, and the electrons are inelastically scattered in the direction of the primary

beam. The residual kinetic energy of the electron is subsequently analysed by an electron energy analyser. The difference between the initial and final kinetic energy of the electron is equal to the energy gained by the sample, and therefore the difference corresponds to the energy between the ground and excited state of the sample gas. A pseudo-absorption spectrum of cross section vs. electron energy loss (or corresponding photon wavelength) can then be obtained, although there may be problems in putting the cross section on to an absolute scale.¹⁷ The maximum energy of transitions that can be observed is limited to the energy of the impacting electron, typically hundreds of eV. The selection rules in EELS are not as strict as for optical spectroscopy, since the excitation source is non-resonant. Therefore, formally-forbidden transitions in optical spectroscopy may be observed as well as allowed ones.¹⁸ This technique is very general, but in comparison with optical techniques suffers from inferior resolution, typically 0.5-1.0 eV.

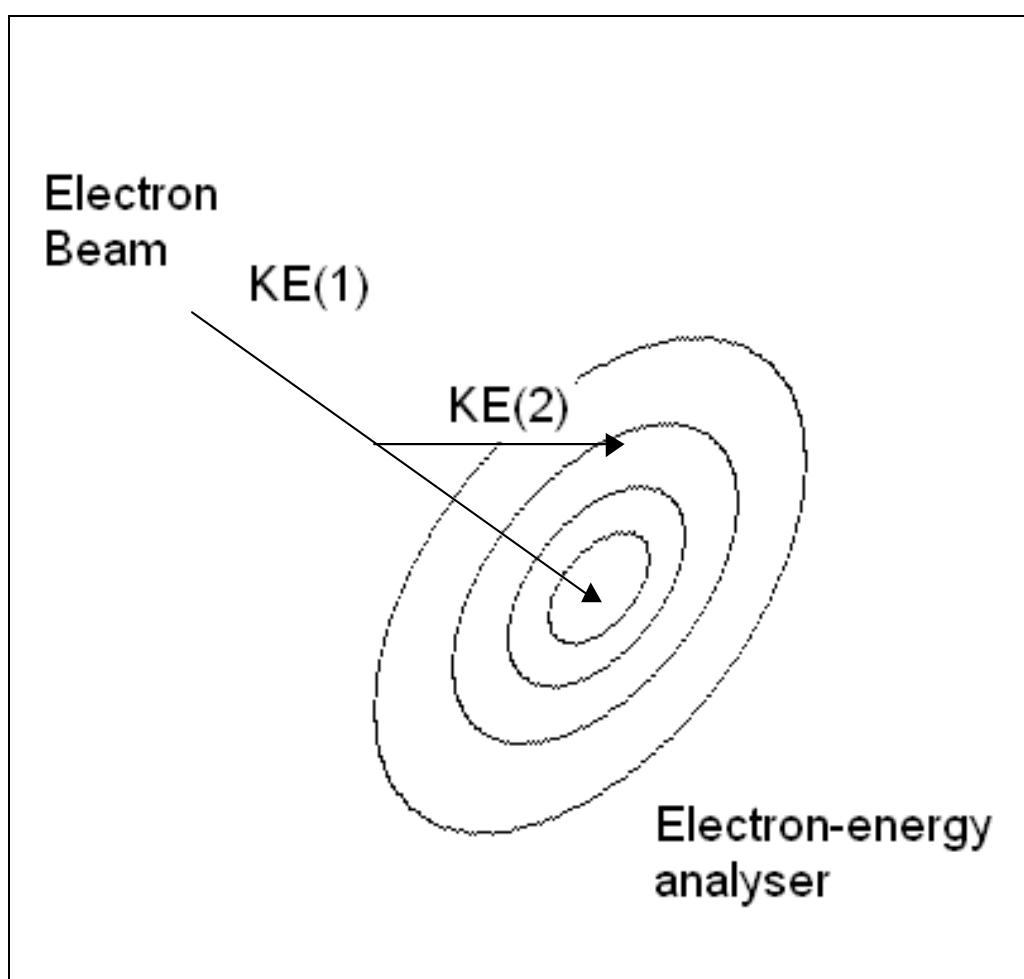


Figure 1.5 A schematic of electron scattering in electron energy loss spectroscopy.

1.5.3 Fluorescence spectroscopy

The development of synchrotron radiation has transformed the field of fluorescence spectroscopy. This is mostly due to its unrivalled tunability and relatively high resolution. The simplest technique, the

measurement of the total fluorescence signal as a function of excitation energy, is known as fluorescence excitation spectroscopy. The fluorescence detector is usually positioned to detect fluorescence perpendicular to the path of the light source to prevent the observation of a high background signal. This type of experiment provides information about $(AB)^*$. Thus, this experiment is ultimately an absorption experiment, that is only sensitive to excited states of AB that fluoresce or decay non-radiatively to fluorescing states of A or B. If the absorption and fluorescence cross-sections are known then the fluorescence quantum yield can be determined. Variations in the quantum yield can give information into the dynamics of the photodissociation process.

By defining the wavelengths of the fluorescence emitted, another technique is possible. This experiment is known as *action* spectroscopy, where the wavelength-dependent fluorescence signal is measured as a function of excitation energy and usually incorporates an interference filter, a secondary monochromator or a multi-channel analyser. In this way, an excitation spectrum can be measured for production of an individual emission. Emission thresholds determined by action spectroscopy can enable the identification of the emitters by comparison with calculated thermodynamic thresholds (Chapter 3). The employment of a secondary monochromator also allows the possibility of probing the emission bands of AB, A or B directly by scanning the secondary monochromator for a fixed photon energy. This technique is known as dispersed fluorescence spectroscopy, and allows the identification of the emitting photofragment as well as its electronic state.

The measurement of radiative lifetimes of $(AB)^*$ or of photofragment A^* or B^* is done using a pulsed excitation source (e.g. single-bunch mode at BESSY1). These measurements can aid the identification of fluorescing species by comparison with other studies. Using a pulsed light source allows the decay of the fluorescence signal to be observed in real time in the period between pulses. This assumes that the intensity of the fluorescence signal is proportional to the concentration of the fluorescing species:

$$[A^*] \propto \exp(-t/\tau) \quad (1.6)$$

where t is the time and τ is the radiative lifetime of the state. Low pressures sometimes have to be used as collisional effects may affect the measurement if τ is very short.

Fluorescence experiments yield substantial information about the excited states of the molecule being probed. Fluorescence excitation spectra map the excited states of the parent molecule (or ion) whose production leads to fluorescence. The shape of the spectral feature can indicate whether the process is either resonant or non-resonant. Resonant features generally indicate the production of a neutral state ($AB + hv \rightarrow (AB)^*$ or $AB + hv \rightarrow A^* + B$ or $A + B^*$). Non-resonant features generally indicate the production

of an ionic state of the parent molecule ($AB + h\nu \rightarrow (AB)^{*+}$). A resonant process can only take place in the Franck-Condon region, whereas a non-resonant process may occur at energies well in excess of its threshold.

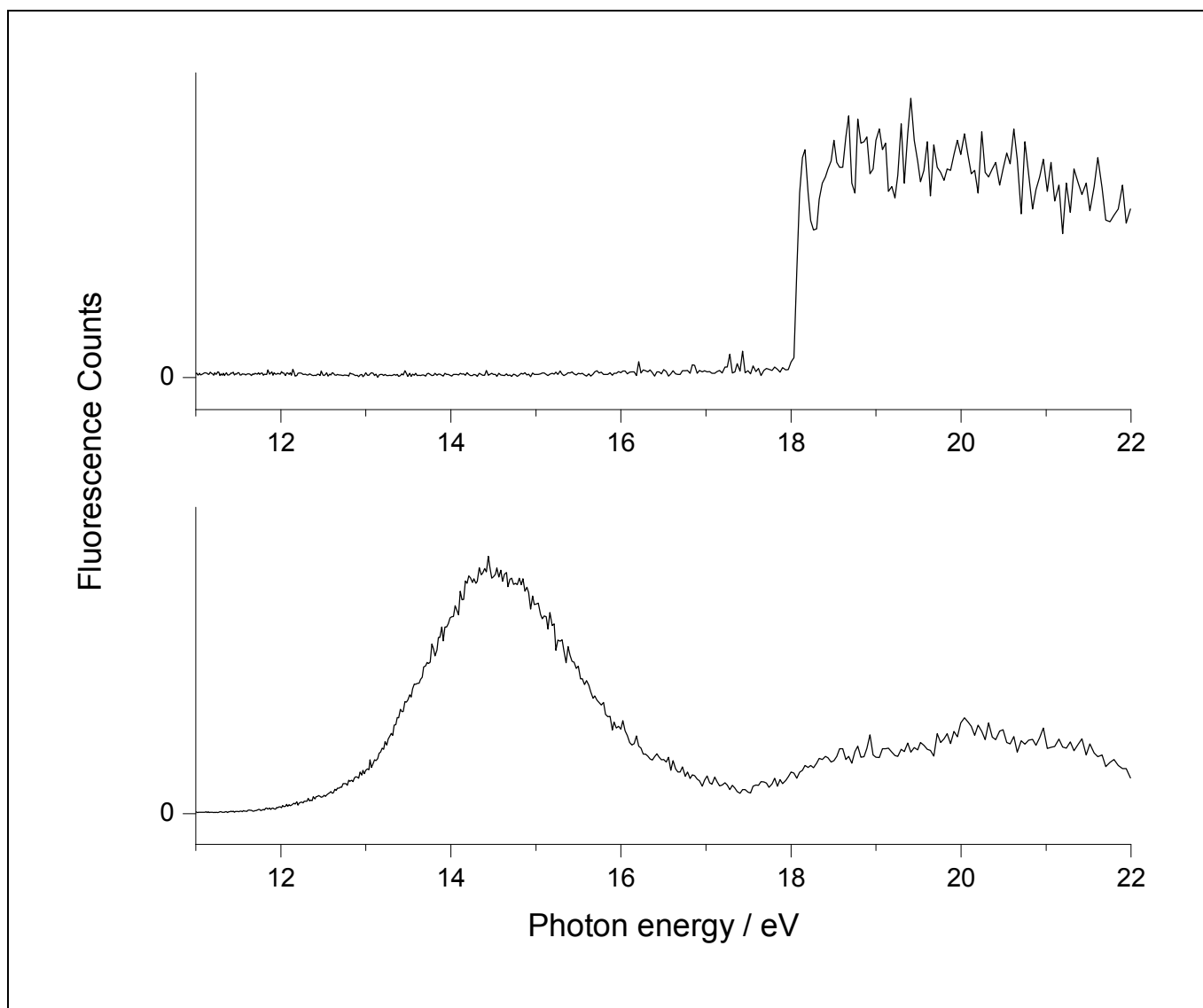


Figure 1.6 The top panel shows an example of a non-resonant feature in a fluorescence excitation spectrum. It shows the fluorescence action spectrum of $\text{CO}_2^+ \tilde{B}^2\Sigma_u^+ - \tilde{X}^2\Pi_g$ from CO_2 . The bottom panel shows an example of a resonant feature. It shows the action spectrum of $\text{CH } A^2\Delta - X^2\Pi$ from CH_3Cl (unpublished data).

1.5.4 Photoelectron and threshold photoelectron spectroscopy.

There are two basic ways in which photoelectron spectroscopy can be performed. Firstly, using a non-resonant light source of fixed energy (e.g. He I at 21.22 eV), a sample is irradiated and electrons are ejected from occupied molecular orbitals. The photoelectrons produced are energy analysed using an electron spectrometer. If it is assumed that a negligible amount of the ionisation energy is transferred to

the parent ion, then the kinetic energy of the photoelectron relates directly to the ionisation potential (IP) of the molecular orbital from which it was ejected:

$$KE = h\nu - IP \quad (1.7)$$

where $h\nu$ is the photon energy of the source and KE is the kinetic energy of the photoelectron. It is also noted that for molecular species, the ejection of a photoelectron may produce an ion that is rovibronically excited:

$$KE = h\nu - (IP + E(v,j)) \quad (1.8)$$

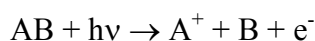
where $E(v,j)$ is the energy of the excited ion. Therefore, the peaks in these spectra occur at electron energies that correspond to the difference between the energy of the ground state and energy of the excited state. This technique therefore enables the qualitative mapping of the electronic structure of the neutral molecule. Alternatively, a resonant photon source may be employed (e.g. a continuum source in conjunction with a monochromator). In this case, electrons of a defined energy are detected. When the photoelectrons are of zero kinetic energy, the technique is called threshold photoelectron spectroscopy. By applying a small electric field across the interaction region, a large percentage of electrons can be collected. The collection of energetic electrons is significantly less efficient than that of zero-energy electrons, since the collection efficiency is governed by the angular acceptance of the particular spectrometer that is used to monitor the kinetic energy of the electron.

The appearance of photoelectron spectra can highlight additional features regarding the nature of the orbitals from which the extracted electrons originate. Extended vibrational progressions indicate that the ionisation has a large associated geometry change caused by the removal of an electron from a strongly bonding or anti-bonding orbital. Conversely, narrow vibrational progressions arise when electrons are removed from non-bonding orbitals. Vibrational frequencies of ionic states can be derived from analysis of the vibrational progressions. If the values are already known for the neutral molecule then a comparison can distinguish bonding and antibonding orbitals. Effects unique to the ion, such as spin-orbit and Jahn-Teller splittings, can also be observed. The two main differences between photoelectron spectra and threshold photoelectron spectra may be the relative intensities of the spectral features. First, the relative intensities of the peaks may vary due to differences in the ionisation cross-section under threshold and non-threshold conditions. Second, additional features may appear in the threshold photoelectron spectrum due to autoionisation, a process that is not usually observed with a non-resonant source.

1.5.5 Ionisation mass spectrometry

The other product from the ionisation process is the cation. A mass-selected cation can also be detected as a function of excitation energy.¹⁹ Since electrons are not collected, this technique is sensitive to ion-pair formation.²⁰ As with threshold photoelectron spectroscopy, a tunable excitation source is required, and this is a resonant technique. Prior to the development of photoelectron spectroscopy, electron impact mass spectrometry was the only method for measuring ionisation energies. Initially it was the case that electrons were used as the excitation source (electron impact mass spectrometry), but over the last two decades, photons have become the preferred choice (photoionisation mass spectrometry). Operating pressures are kept relatively low (10^{-5} Torr), especially when detecting negative ions, as the secondary process of electron attachment must be minimised.

Thermochemical data may be determined *via* the appearance potential (AP) of either the parent or the fragment ions:



The standard heats of formation are related to each other by:^{1,21}

$$AP(A^+) \geq \Delta_f H^0(A^+) + \Delta_f H^0(B) - \Delta_f H^0(AB) \quad (1.9)$$

Generally $\Delta_f H^0(B)$ is the value of interest. An upper limit for it can be evaluated provided $\Delta_f H^0(A^+)$ and $\Delta_f H^0(AB)$ are known independently. This value of $\Delta_f H^0(B)$ will be relevant to the temperature at which $AP(A^+)$ is measured. If the measurements are made at a temperature T , usually 298 K, then a procedure exists for allowing for internal energy effects, and a small correction needs to be applied to the value of $AP(A^+)$ used in equation (1.9).²¹ Alternatively, the AP at 0 K can be determined by adding the average internal energy of AB to the measured $AP(A^+)$ at temperature T :

$$AP_0(A^+) = AP_T(A^+) + \frac{r}{2} k_B T + \sum_i \frac{h\nu_i}{\exp(h\nu_i / k_B T) - 1} \quad (1.10)$$

The number of rotational modes of AB is represented by r (three for a non-linear, two for a linear molecule), and the vibrational frequency of the i th vibrational mode is represented by ν_i . Under these circumstances, an upper limit for $\Delta_f H^0(B)$ at 0 K can be determined.

1.5.6 Threshold Photoelectron Photoion Coincidence (TPEPICO) Spectroscopy

Coincidence techniques enable the correlation of two or more events. In threshold photoelectron photoion spectroscopy the techniques of threshold photoelectron spectroscopy and photoionisation mass spectrometry are combined.²² The use of a threshold electron analyser, a time-of-flight mass spectrometer to differentiate the different fragment ions, and a resonant excitation source enables state-selected ions to be defined by the photon energy. TPEPICO spectroscopy provides insight into the identity and dynamics of the dissociation channels of the ground and excited states of the parent ion. As with non-coincidence spectrometric methods, appearance potentials of fragment ions can be measured, although the accuracy is usually reduced. However, ambiguity about the identity of dissociation channels is sometimes avoided as negative ions are not detected.

TPEPICO spectroscopy also allows the fragmentation channels of the electronic states of the parent ion to be investigated. This is done by comparing the appearance potential of an ion to calculated thermochemistry. The technique can also allow the determination of the decay dynamics of excited states of molecular cations *via* the determination of the kinetic energy of the fragment cation. Two limits are possible which are applied to the decay of large and small molecular ions, namely the statistical and impulsive mechanisms, respectively.²³ These mechanisms are now briefly described.

An impulsive decay is characterised by a short lived precursor. In this case, dissociation occurs on a faster timescale than intramolecular vibrational energy redistribution and electronic relaxation. Therefore, molecules that decay impulsively are characterised by having a large fraction of the excess energy being partitioned into translation. Initially momenta and energy are localised on the atoms of the breaking bond. The repulsion between the atoms cause intramolecular collisions between themselves and the remainder of their recoiling fragments after dissociation. The result of this is excitation to rovibronic modes of the fragments. Under these circumstances $\langle KE \rangle_t$ is defined as:^{24,25}

$$\langle KE \rangle_t = \frac{\mu_b}{\mu_f} E_{\text{avail}} \quad (1.11)$$

where μ_b is the reduced mass of the two atoms whose bond is broken and μ_f is the reduced mass of the two products of the dissociation. Dissociation in this case is assumed to proceed along a pseudodiatomic exit channel of the excited state potential energy surface.

A statistical decay is characterised by a long-lived precursor. In this case, dissociation occurs slowly enough for prior intramolecular vibrational energy redistribution and electronic relaxation to occur. Dissociation proceeds along the ground electronic state potential energy surface, and such dissociations assume that this state of the parent ion is bound, at least in some regions of its multi-dimensional potential

energy surface. Molecules that decay statistically are characterised by having a smaller fraction of the excess energy being partitioned into translation. Klots²⁶ has shown that, for dissociation of a parent ion to a daughter ion plus neutral atom, $\langle KE \rangle_t$ and E_{avail} are related by :

$$E_{avail} = \frac{r-1}{2} \langle KE \rangle_t + \langle KE \rangle_t + \sum_i \frac{h\nu_i}{\exp(h\nu_i / \langle KE \rangle_t) - 1} \quad (1.12)$$

where r and ν_i are the number of rotational degrees of freedom and the vibrational frequency of the i th vibrational mode of the daughter ion. It is also possible to estimate a lower limit of $\langle KE \rangle_t$ by :¹⁴

$$\frac{\langle KE \rangle_t}{E_{avail}} = \frac{1}{x+1} \quad (1.13)$$

where x is the number of vibrational degrees of freedom in the transition state.

1.5.7 Pulsed field ionisation: ZEKE and MATI Zero Energy Kinetic Electron and Mass Analysed Threshold Ionisation Spectroscopy

Pulsed field ionisation was developed by Muller-Dethlefs *et. al.*²⁷⁻²⁹ A molecule is excited to Rydberg state just below a chosen ionisation potential. A small field extracts the electrons produced by autoionisation and stabilises the populated Rydberg state by inducing l and m_l mixing. After a short time, a larger field is applied causing the Rydberg state to be pulse field ionised. Detection of the resulting electrons constitutes the ZEKE technique, whereas detection of the mass-selected ions is the basis of MATI spectroscopy. These techniques are capable of very high resolution and are limited only to the bandwidth of the photon energy and the applied voltage. ZEKE and MATI techniques have mostly been performed using lasers as excitation sources, but the improved synchrotron radiation sites such as the Advanced Light Source (Berkeley, USA) have allowed these facilities to be used.³⁰⁻³²

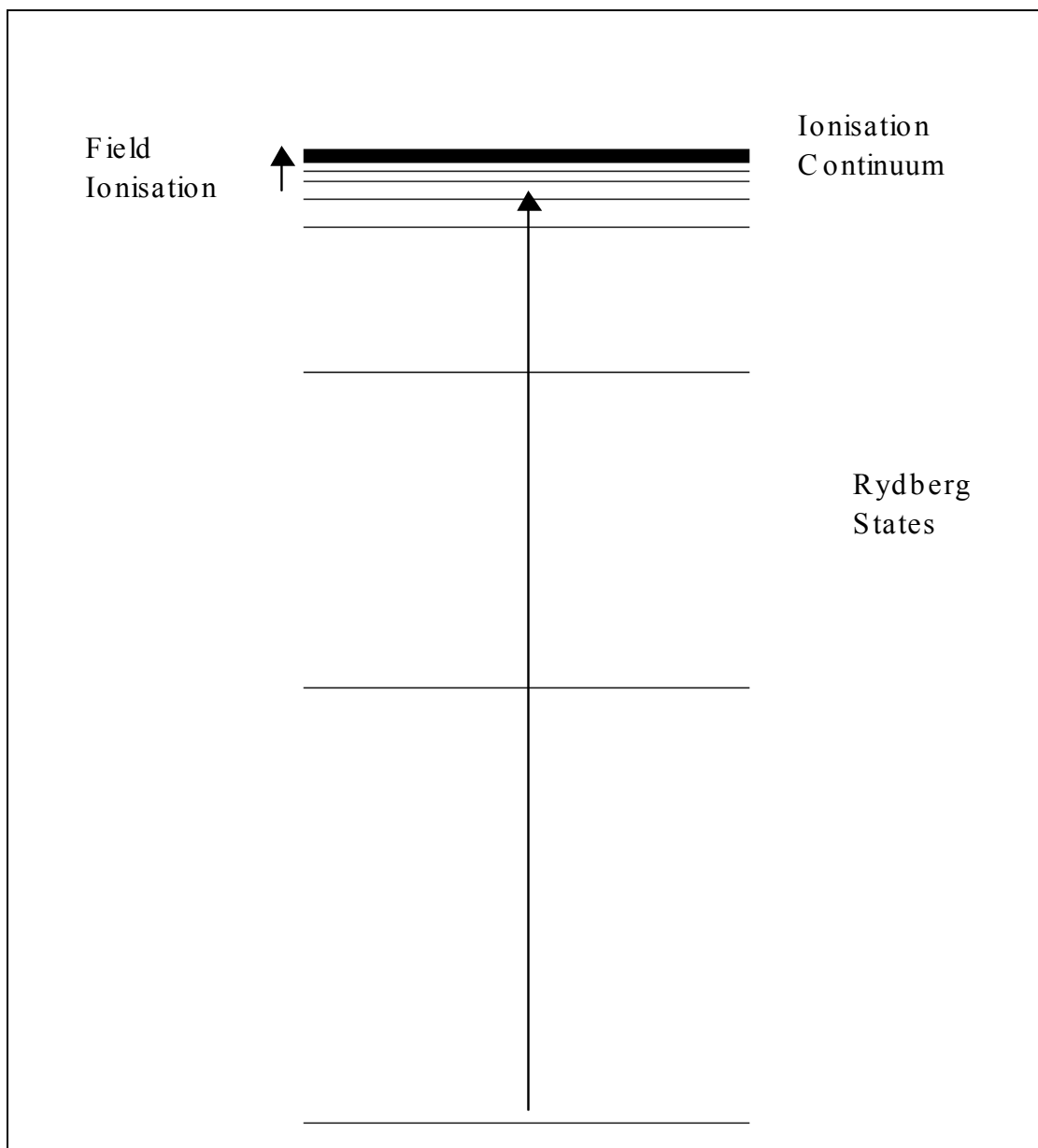


Figure 1.7 A schematic of the energy level scheme in pulsed-field ionisation.

1.6 Objectives of this Thesis

Before we proceed to the results chapters, the aims and objectives of this thesis are discussed briefly to put the work into context. All experimental techniques employ a synchrotron radiation light source. Three types of experiment have been performed and can be categorised ; photoabsorption, fluorescence and photoionisation.

The principal aim of the fluorescence experiments is to study the photodissociation dynamics of both the Rydberg states of polyatomic molecules and the valence states of their parent molecular ion. Specifically these experiments are sensitive to those Rydberg states that photodissociate to an excited state of a fragment that fluoresces and to valence states of the parent molecular ion that fluoresce.

Photoabsorption measurements have been made for two separate objectives. Firstly, absorption measurements made in conjunction with fluorescence excitation measurements allow comparison to elucidate the importance of a particular decay pathway but only on a qualitative level. Secondly, the photoabsorption studies in Chapter 6 have been made to measure the absorption cross-section of SF₅CF₃ at 121.6 nm. This data is needed to determine a more accurate lifetime of SF₅CF₃ in the atmosphere.

Threshold photoelectron photoion coincidence spectroscopy (photoionisation) is a well-established technique by which information on the decay dynamics of individual vibronic states of positively charged molecular ions can be obtained. Specifically, this technique enables ion yield plots and the kinetic energy released into fragment channels to be determined. The measurements are important guides to determine whether the decay of the parent ion occurs statistically or impulsively. Specifically, important thermochemical data has been determined for SF₅CF₃. This has been made possible by using a novel method to manipulate the data.

1.7 References

1. J. Berkowitz, *Photoabsorption, Photoionisation and Photoelectron Spectroscopy*, Academic Press, 1979.
2. R. P. Wayne, *Principles and Applications of Photochemistry*, Oxford University Press, 1988.
3. J. M. Hollas, *Modern Spectroscopy*, 2nd edition, Wiley, 1992.
4. J. A. R. Samson, *Techniques of Vacuum Ultraviolet Spectroscopy*, Wiley, 1967.
5. J. H. Moore, C. C. Davis and M. A. Coplan, *Building Scientific Apparatus*, Second Edition, Addison-Wesley, 1989.
6. T. Baer, *Annu. Rev. Phys. Chem.*, 1989, **40**, 637.
7. J. H. D. Eland, *Photoelectron Spectroscopy*, Butterwoths, London, 1974.
8. J. J. Hopfield, *Phys. Rev.*, 1930, **35**, 1133.
9. J. Schwinger, *Phys. Rev.*, 1946, **70**, 798.
10. J. Schwinger, *Phys. Rev.*, 1949, **75**, 1912.
11. S. Ebashi, M. Koch and E. Rubenstein, *Handbooh on Synchrotron Radiation 4*, First Edition, North-Holland, 1990.
12. P. W. Atkins, *Molecular Quantum Mechanics*, second edition, Oxford University Press, 1983.
13. I. Powis, T. Baer and C. Y. Ng, *High Resolution Laser Photoionisation and Photoelectron Studies*, First Edition, Wiley, 1995.
14. E. Illenberger and J. Momigny, *Gaseous Molecular Ions*, First Edition, Steinkoff, 1992.
15. D. H. Stedman and D. W. Setser, *Prog. React. Kin.*, 1971, **6**, 193.

16. *Mullard technical handbook, Book 2: Valves and tubes, Part 3: Photomultiplier tubes, Phototubes, Channel electron multipliers.*, 1985.
17. P. A. Kendall, N. J. Mason, *J. Elec. Spec. Rel. Phen.*, 2001, **120**, 27.
18. J. H. D. Eland, *Photoelectron Spectroscopy*, Butterworths, London, 1974.
19. C. Y. Ng, *Adv. Chem. Phys.*, 1983, **52**, 263.
20. D. P. Seccombe, R. Y. L. Chim, G. K. Jarvis and R. P. Tuckett, *Phys. Chem. Chem. Phys.*, 2000, **2**, 769.
21. J. C. Traeger, R. G. McLoughlin, *J. Am. Chem. Soc.*, 1981, **103**, 3647.
22. B. Brehm and E. von Puttakamer, *Z. Naturforsch.*, 1967, **22a**, 8.
23. P. A. Hatherly, D. M. Smith and R. P. Tuckett, *Z. Physikl. Chemie*, 1996, **195**, 97.
24. G. E. Busch and K. R. Wilson, *J. Chem. Phys.*, 1972, **56**, 3626.
25. I. Powis, *Mol. Phys.*, 1980, **39**, 311.
26. C. E. Klots, *J. Chem. Phys.*, 1973, **58**, 5364.
27. K. Muller-Dethlefs, M. Sander and E. W. Schlag, *Z. Naturforsch.*, 1984, **39a**, 1089.
28. K. Muller-Dethlefs, M. Sander and E. W. Schlag, *Chem. Phys. Lett.* 1984, **112**, 291.
29. K. Muller-Dethlefs and E. W. Schlag, *Annu. Rev. Phys. Chem.*, 1991, **42**, 109.
30. K. M. Weitzel and F. Guthe, *Chem. Phys. Lett.*, 1996, **251**, 295.
31. G. K. Jarvis, Y. Song and C. Y. Ng, *Rev. Sci. Instr.*, 1999, **70**, 2615.
32. G. K. Jarvis, K. M. Weitzel, M. Malow, T. Baer, Y. Song and C. Y. Ng, *Rev. Sci. Instr.*, 1999, **70**, 3892.

CHAPTER 2 : EXPERIMENTAL

2.1 Synchrotron light sources and monochromators

The experiments conducted in this thesis are divided into three categories; photoabsorption, fluorescence and photoionisation. In all cases, the light source employed is synchrotron radiation, either from Berliner Electronspeicherring-Gesellschaft für Synchrotronstrahlung (BESSY1) in Berlin, Germany, or the Daresbury Laboratory Synchrotron Radiation Source (SRS) in Cheshire, UK. Synchrotron radiation is a highly tunable continuous source and spans the electromagnetic spectrum from the infrared to the X-ray region and is one of the most useful sources for spectroscopy. This section describes the light sources, the beamlines and the monochromators in detail.

2.1.1 Daresbury Laboratory Synchrotron Radiation Source (SRS).

The SRS was the first research facility in the UK that was dedicated to the production and the use of synchrotron radiation. The SRS achieves a maximum average energy for electrons of 2 GeV. Experiments utilising radiation from the near-infrared to the hard X-ray regions are supported. It can be seen from Fig. 2.1 that the source is made up of three major components; a linear accelerator, a booster ring and a storage ring. Electrons are emitted from the linear accelerator at an energy of 120 MeV into the 800 MeV booster ring. Here they are accelerated to near-relativistic speeds before being injected into the storage ring where they can be stored for up to *ca.* 20 hours. Multi-bunch mode provides the greatest intensity of radiation. Typical injection currents are *ca.* 260 mA. Electrons travel around the storage ring (circumference = 96 m) within a vacuum, producing synchrotron radiation at each of the bending magnets and insertion devices. In the multi-bunch mode 160 bunches of electrons (width = 0.2 ns, separation = 2 ns) circulate the ring. The revolution times of the pulses is 320 ns and the light output is pulsed at 500 MHz. Most experiments are not sensitive to such high frequencies hence the source is regarded as pseudo-continuous. Only multi-bunch mode is utilised at the SRS for the experiments in this thesis, hence single-bunch mode is not described.

The most important constituent of an experimental station is the monochromator. Photoionisation measurements were made using station 3.1. This station utilises a 1 m Seya-Namioka monochromator to wavelength select radiation in the range 30 – 500 nm at resolutions down to 0.05 nm. This wavelength range is covered by three interchangeable diffraction gratings, two of which can be installed at any one time (only one grating can be exposed to radiation at a time). The monochromator is made up of four optical elements. After the bending magnet on line 3.1, there is a fixed horizontally-dispersing plane mirror and a fixed vertically-dispersing mirror which focuses the radiation onto the entrance slit. After the entrance slit is the diffraction grating, then after the exit slit is an adjustable focussing mirror. Only two of the gratings were used to conduct the experiments in this thesis. The “high” energy grating (40-100 nm)

and “medium” energy grating (60-150 nm) are blazed at 55 and 80 nm respectively, with a quoted peak output of 1×10^{10} and 3×10^9 photon s^{-1} per 0.1 % bandwidth per 100 mA beam current.

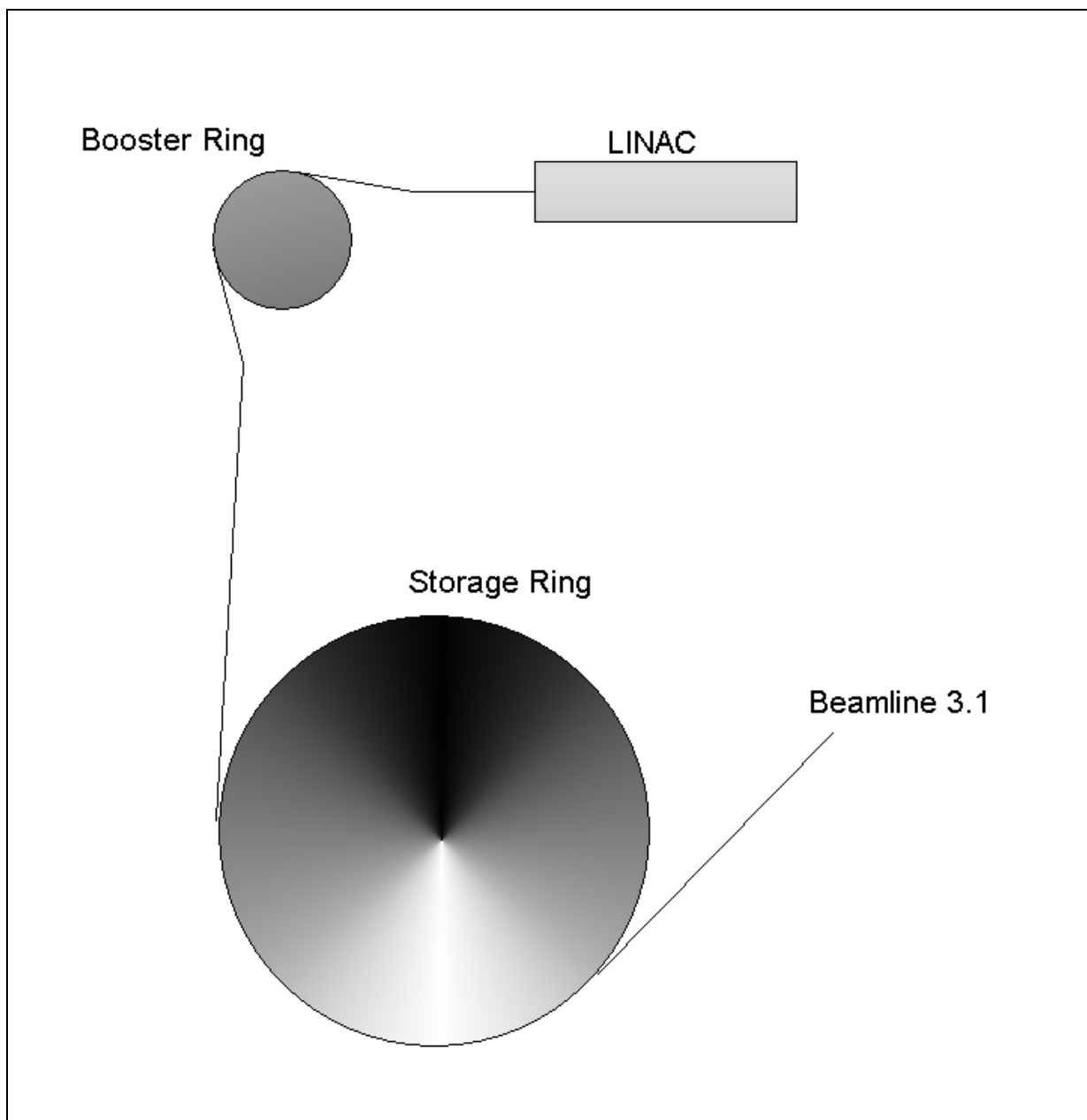


Figure 2.1 A schematic of the Daresbury synchrotron radiation source.

2.1.2 Berliner Electronspeicherring-Gesellschaft für Synchrotronstrahlung (BESSY1)

BESSY1 is no longer in operation and was dismantled in December 1999. BESSY1 achieved a maximum energy for the electrons of 800 MeV. Experiments utilising radiation from the VUV to the soft X-ray regions were supported. Electrons were fired from a 20 MeV microtron into a booster synchrotron with a circumference of 38.4 m. Here the electrons were accelerated to their final energy of 800 MeV by strong electric fields in a high frequency cavity. The magnetic field of the ring increased synchronously

with the electron energy so that a fixed trajectory was maintained. The electrons were then fed into the storage ring (circumference = 62.4 m) producing synchrotron radiation at each of the bending magnets and insertion devices. BESSY1 operated in two modes, multi-bunch and single-bunch. In multi-bunch mode, 104 bunches of electrons (width = 20 ps, separation = 2 ns) were created. The revolution time of the pulses was 208 ns. Like the Daresbury SRS, the light output was pulsed at 500 MHz. Typical injection currents were 750 mA. In single-bunch mode, only one bunch of electrons were injected, also with a period of 208 ns. Hence the revolution frequency in single-bunch mode was 4.8 MHz, and typical injection currents were then 80 mA. The VUV station was employed to perform dispersed fluorescence and photoabsorption experiments presented in this thesis. The beamline consisted of a 1.5 m normal-incidence McPherson monochromator and a data acquisition system. The grating used to obtain the data in Chapter 3 was ruled with 1200 lines mm^{-1} , and had an energy range of 6-21 eV. The best resolution of the monochromator was 0.03 nm.

The VUV absorption spectrum of SF_5CF_3 described in Chapter 6 was obtained by courtesy of Drs J M Lemaire, F Dulieu and H W Jochims at the SuperAco synchrotron source in Paris, and they sent the data to Birmingham for analysis. The SA63 beamline at SuperAco possessed a 1 m normal incidence monochromator with a 1200 lines mm^{-1} grating. The best resolution of this monochromator was *ca.* 0.05 nm.

2.2 Photoabsorption

The VUV absorption apparatus (Fig. 2.2) was attached to the Bessy1 storage ring *via* the 1.5 m normal incidence monochromator described above. Photons in the range 6-21 eV at a resolution of 0.08 nm were used. The apparatus comprises of a partitioned aluminium cube (which acts as the differential pumping region, see Section 2.3) to which an absorption cell is attached. LiF or MgF_2 windows cannot be used at these high energies, and the two components are therefore linked by a 1 x 5 mm slit and a collimated mesh. The mesh is constructed from 1 mm thick stainless steel, but has 200000-300000 holes each *ca.* 25 μm in diameter allowing transmission of VUV radiation. The mesh can thus provide differential pumping, yet still allows the pathlength of the cell to be defined. The absorption cell itself is 300 mm long and has a diameter of 35 mm. The radiation transmitted through the absorption cell is detected by a photomultiplier tube *via* the visible fluorescence from a sodium salicylate window, mounted at the end of the cell. Gas is effused into the absorption cell *via* a high precision Nupro needle valve. The operating pressures used depend on the absorbance of the sample. Typical pressures range from 5-60 μbar . The scanning of the monochromator and data acquisition was controlled by a dedicated personal computer attached to the station.

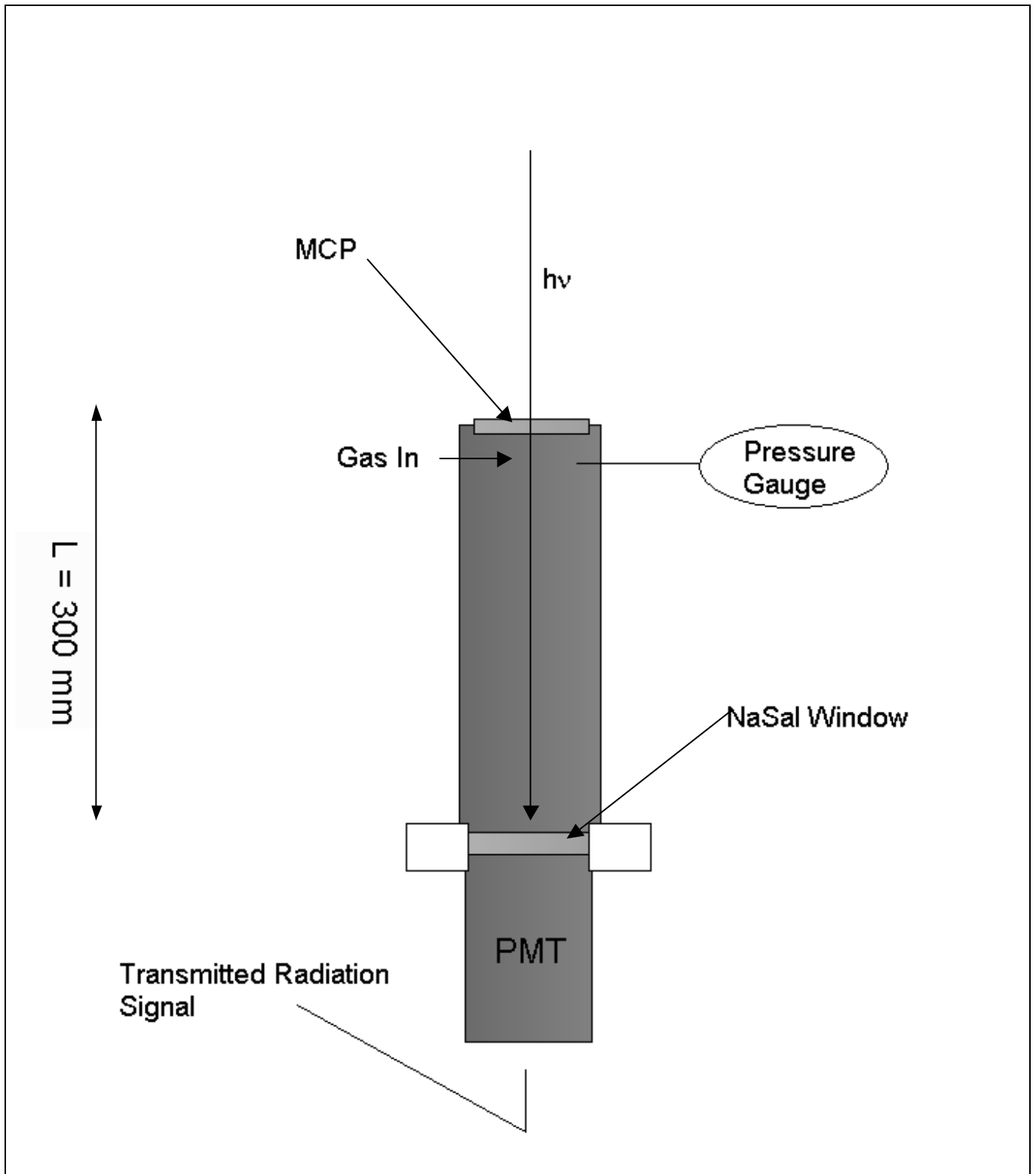


Figure 2.2 A schematic of the absorption apparatus used at BESSY1.

The measurement of an absorption spectrum yields the absorption cross-section as a function of photon energy. The absorption cross-section is given by the Beer-Lambert law:

$$\sigma = (\ln(I_0/I)) / cL \quad (2.1)$$

where σ is the absolute absorption cross-section (in units of $\text{cm}^2 \text{ molecule}^{-1}$), I_0 is the intensity of light prior to interaction with the sample and I is the light intensity after interaction with the sample, c is the concentration of sample (in molecules cm^{-3}) and L is the path length of the light through the sample (in cm). I is measured by slowly flowing sample gas through the absorption cell and measuring the transmitted light as a function of photon energy. I_0 is measured by evacuating the absorption cell and again measuring the transmitted light as a function of photon energy. Since the concentration can be calculated *via* the pressure of gas and the temperature, and the optical path length is also known, absorption cross-sections can be calculated. It should also be noted that the measured signals of I_0 and I are corrected for the decay of the beam current that occurs during a scan, and the concentration is corrected for any changes in pressure.

Two further points are made. First, to ensure linearity of the absorbance with concentration and hence an absence of saturation effects, at certain energies $\ln(I_0/I)$ was plotted as a function of pressure (see Fig. 2.3). A straight line through the origin confirmed the absence of saturation, and hence determined the range of pressures over which it was appropriate to measure the cross section. Second, a determination of σ *via* the Beer-Lambert law assumes that the linewidth of the radiation is much smaller than the linewidth of the absorption line. In our VUV experiments, the linewidth of 0.08 nm (or 120 cm^{-1} at 15 eV) means that this is unlikely to be the case, although the absorption lines will often have unresolved rovibrational features. No account has been taken of this effect. Overall, it is estimated that VUV cross-sections measured in this way are accurate to *ca.* 10-15 %.

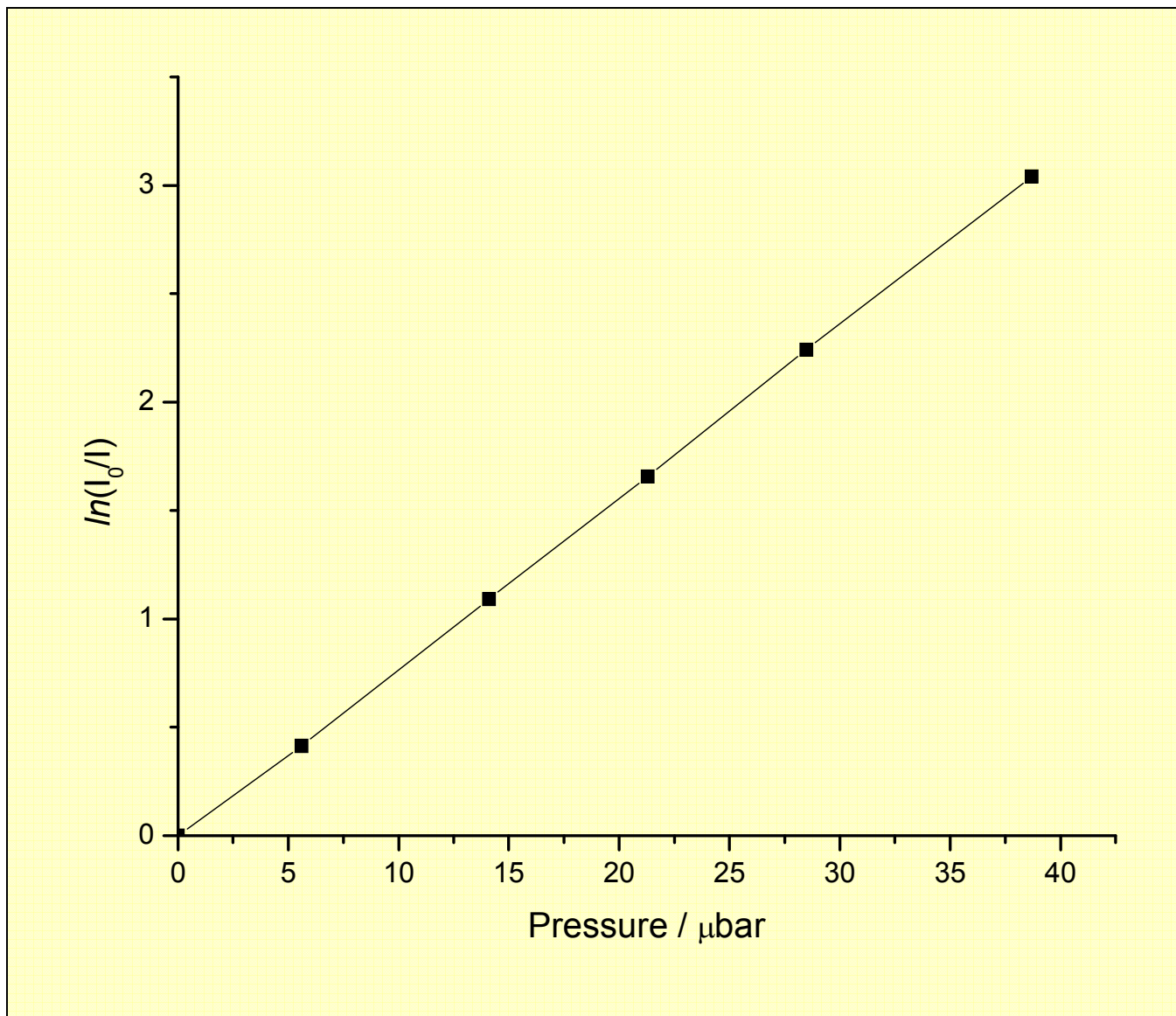


Figure 2.3 Graph showing $\ln(I_0/I)$ plotted as a function of pressure for GeCl_4 photoexcited at 130 nm or 9.55 eV. The absorption cross section at this energy is $2.3 \times 10^{-16} \text{ cm}^2$ (unpublished data). Linearity shows that no saturation effects are present, and therefore pressures up to at least 40 μbar are appropriate for such measurements.

2.3 Fluorescence

The dispersed fluorescence apparatus (Fig. 2.4) facilitates the measurement of fluorescence excitation, dispersed fluorescence and action spectra with the multi-bunch mode of BESSY1. Furthermore, individual emission bands may be isolated and single-bunch mode can be used for lifetime experiments. The apparatus was attached to the storage ring *via* the 1.5 normal incidence monochromator which was generally set to a resolution of 0.3 nm. The monochromatised light then passes through a partitioned aluminium cube (side = 12 cm) and into a brass cube (side = 5 cm). The aluminium cube is a two stage differential pumping region. The two differential pumping regions are linked by a 3 x 10 mm vertical orifice and are respectively pumped by rotary-backed turbo pumps. A lithium fluoride window can be

positioned before the exit slit of the monochromator. The main use of this optic is to eliminate second-order radiation in experiments performed at excitation wavelengths > 105 nm. The sample gas is effused into the brass cube and it is here that the sample and synchrotron radiation interact. The brass cube and the aluminium cube are connected by a 1×5 mm horizontal slit. The pressure in the first pumping region is measured using a Penning gauge. The pressure in the interaction region is higher but this pressure could not be measured directly. The induced fluorescence that results from the interaction region is dispersed by a Jobin Yvon H20VIS monochromator of focal length 20 cm. The grating is blazed at 450 nm and has a linear reciprocal dispersion of 4 nm mm^{-1} . With a 2 mm exit slit, this secondary monochromator has an effective resolution of *ca.* 8 nm and is sensitive to wavelengths of 190-650 nm. The fluorescence is detected by a fast, red-sensitive Hamamatsu R6060 photomultiplier tube which is water cooled to 280 K.

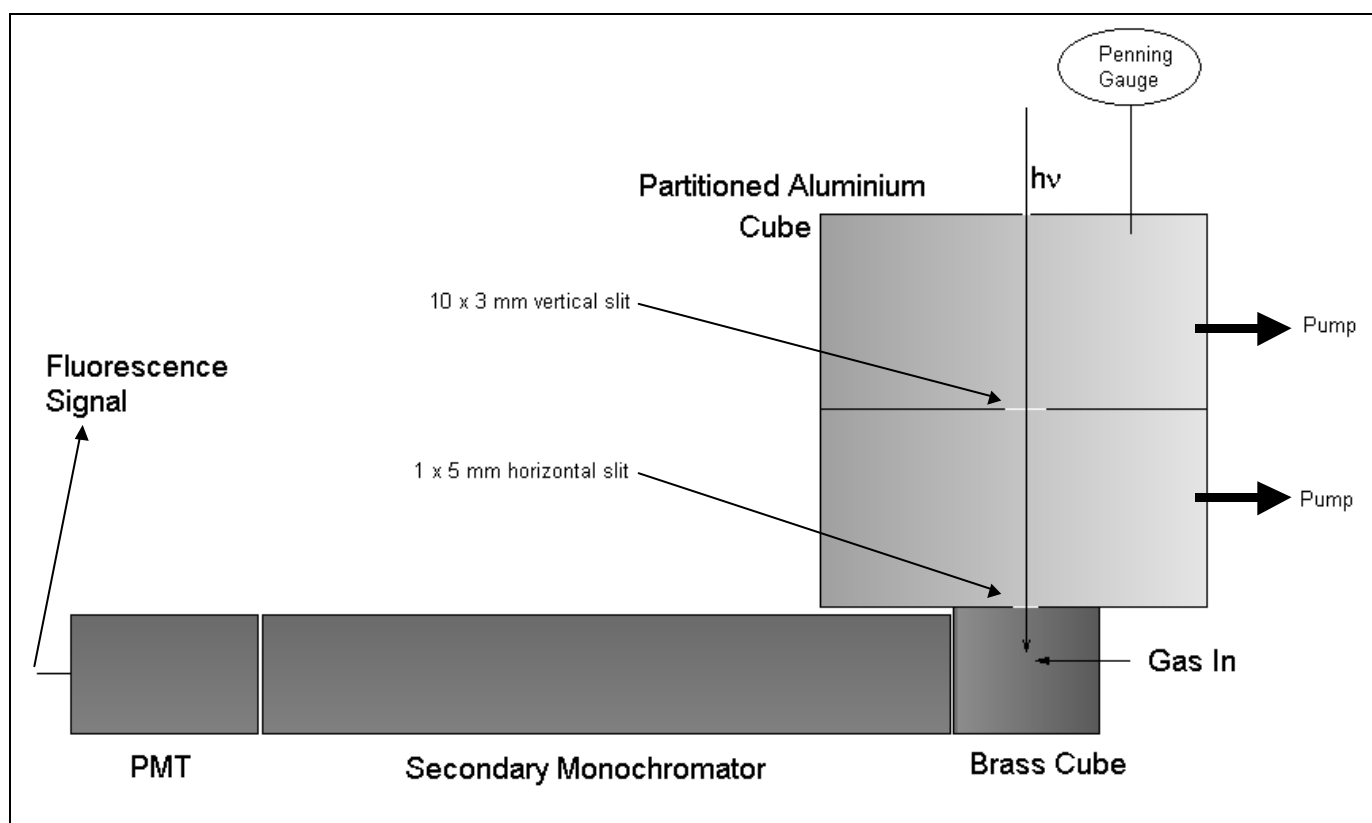


Figure 2.4 A schematic of the dispersed fluorescence apparatus used at BESSY1.

In multi-bunch mode, fluorescence excitation, dispersed fluorescence, and action spectra are recorded. Fluorescence excitation spectra are performed by setting the secondary monochromator to zero order and scanning the excitation energy. The dispersed fluorescence spectra are performed by dispersing the induced fluorescence through the secondary monochromator for a fixed VUV excitation energy. Lastly, action spectra are performed in a similar way to fluorescence excitation spectra; the secondary monochromator is set to a specific wavelength and the VUV excitation energy is scanned. The two

monochromators are calibrated using the $\text{N}_2^+ \text{B}^2\Sigma_u^+ - \text{X}^2\Sigma_g^+ (0,0)$ emission band at 391 nm,¹ the threshold of which is 18.76 eV (Fig. 2.5).² Data acquisition and the scanning of the two monochromators were controlled by a personal computer and dedicated electronics. The dispersed fluorescence signal was passed through an amplifier-discriminator before entering the electronic circuitry. No attempt was made to correct the dispersed fluorescence spectra to the variation of sensitivity of the secondary monochromator with wavelength. It was not possible to normalise the fluorescence excitation or the action spectra *in situ* to the primary photon flux. However, a separate experiment, where a sodium salicylate window and photomultiplier tube was attached directly to the primary monochromator, was performed; this is the absorption apparatus (Section 2.2) with no gas. The fluorescence excitation and action spectra could then be normalised to the photon flux.

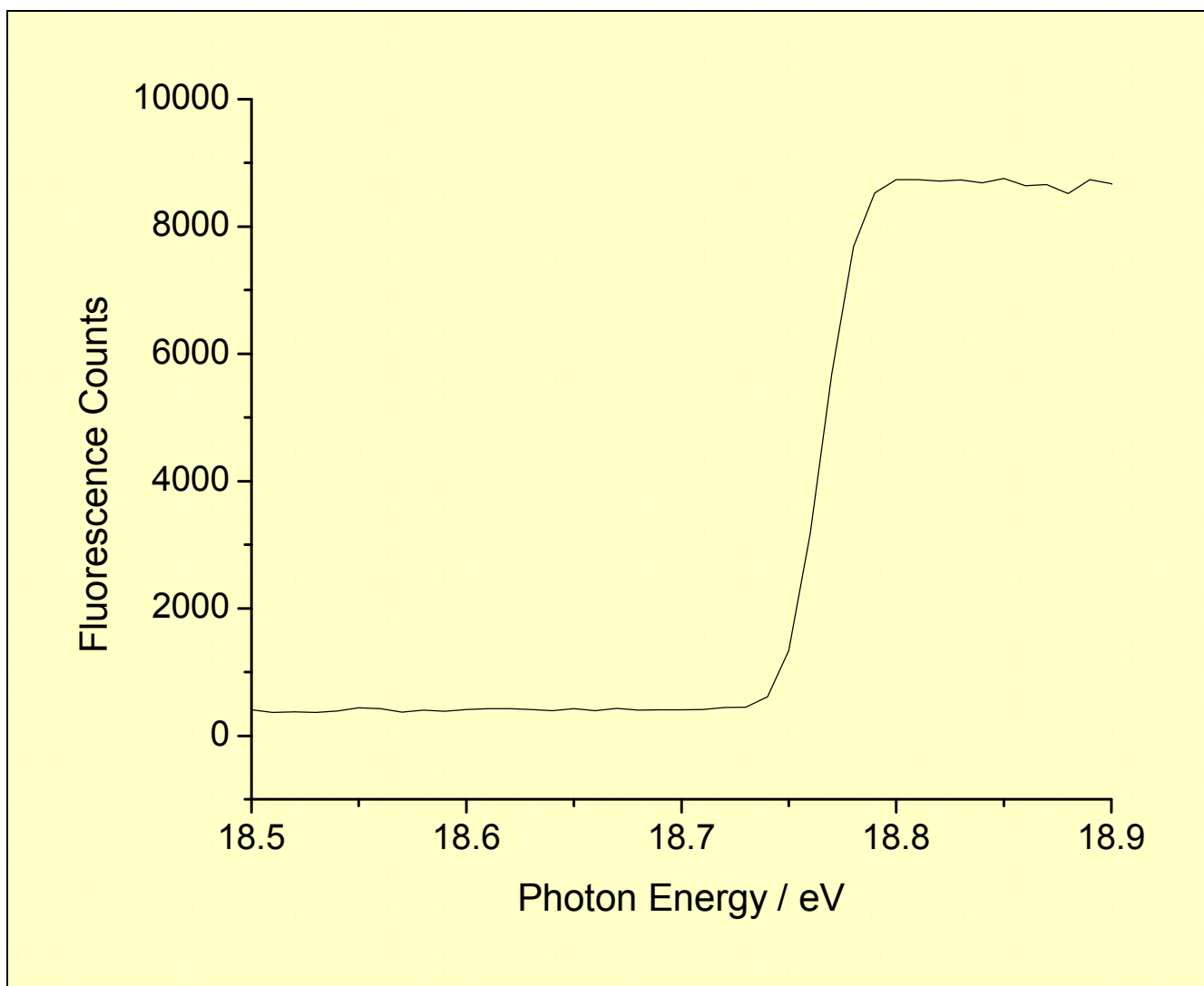


Figure 2.5 A VUV fluorescence excitation spectrum of N_2^+ , with the fluorescence being detected at 390 ± 10 nm with an interference filter. This wavelength range corresponds to the $\text{B}^2\Sigma_u^+ - \text{X}^2\Sigma_g^+$ transition in N_2^+ .

Using the single-bunch mode at BESSY1, lifetimes of emitting states can be determined, using the same apparatus shown in Fig. 2.4. To isolate the emission, the photon energy and the fluorescence wavelength were defined. The fluorescence signal from the Hamamatsu R6060 photomultiplier tube (rise time *ca.* 1.5ns) is used as the start signal for a time-amplitude converter (Ortec 567 TAC). Stop pulses are provided by the synchrotron bunch maker. The data is collected on a multichannel analyser card mounted in a personal computer. The measured signal is a convolution of three components; the fluorescence decay, the “prompt” or instrument component, and a background signal. The “prompt” is a convolution of the timing profile of the single-bunch in the storage ring and the response time of the photomultiplier and the associated detection electronics. A reasonable approximation of the “prompt” component is the measurement of the timing profile of scattered light. This profile was measured before each measurement of experimental lifetime decay. This is done by setting both monochromators to zero order to maximise the scattered light. The real signal was then deconvoluted from the prompt and fitted to a single or double exponential function. A non-linear square fitting routine, FLUORX_ERR,³ was used for this analysis. In practice, the range of lifetimes that can be measured is 3-100 ns. These measurements are limited by the response time of the photomultiplier tube and associated electronics, and by the period of the single-bunch mode.

2.4 Photoionisation

The photoionisation and coincidence experiments were performed with an apparatus (Fig. 2.6) at the Daresbury Laboratory using the 1 m Seya-Namioka monochromator. The major components of this apparatus are a threshold electron analyser and a time-of-flight mass spectrometer.⁴ Monochromatised radiation is admitted into the coincidence apparatus through a 2 mm internal diameter, 100 mm long glass capillary. This component provides the required differential pumping and therefore the constrained separation between the apparatus and the monochromator. The photon flux is monitored by a photomultiplier tube (EMI 9924 B) *via* the visible fluorescence of a sodium salicylate window, mounted behind the interaction region. Sample gas is effused into the interaction region *via* a high precision needle valve. Typical operating pressures range from 3-7 x 10⁻⁵ Torr.

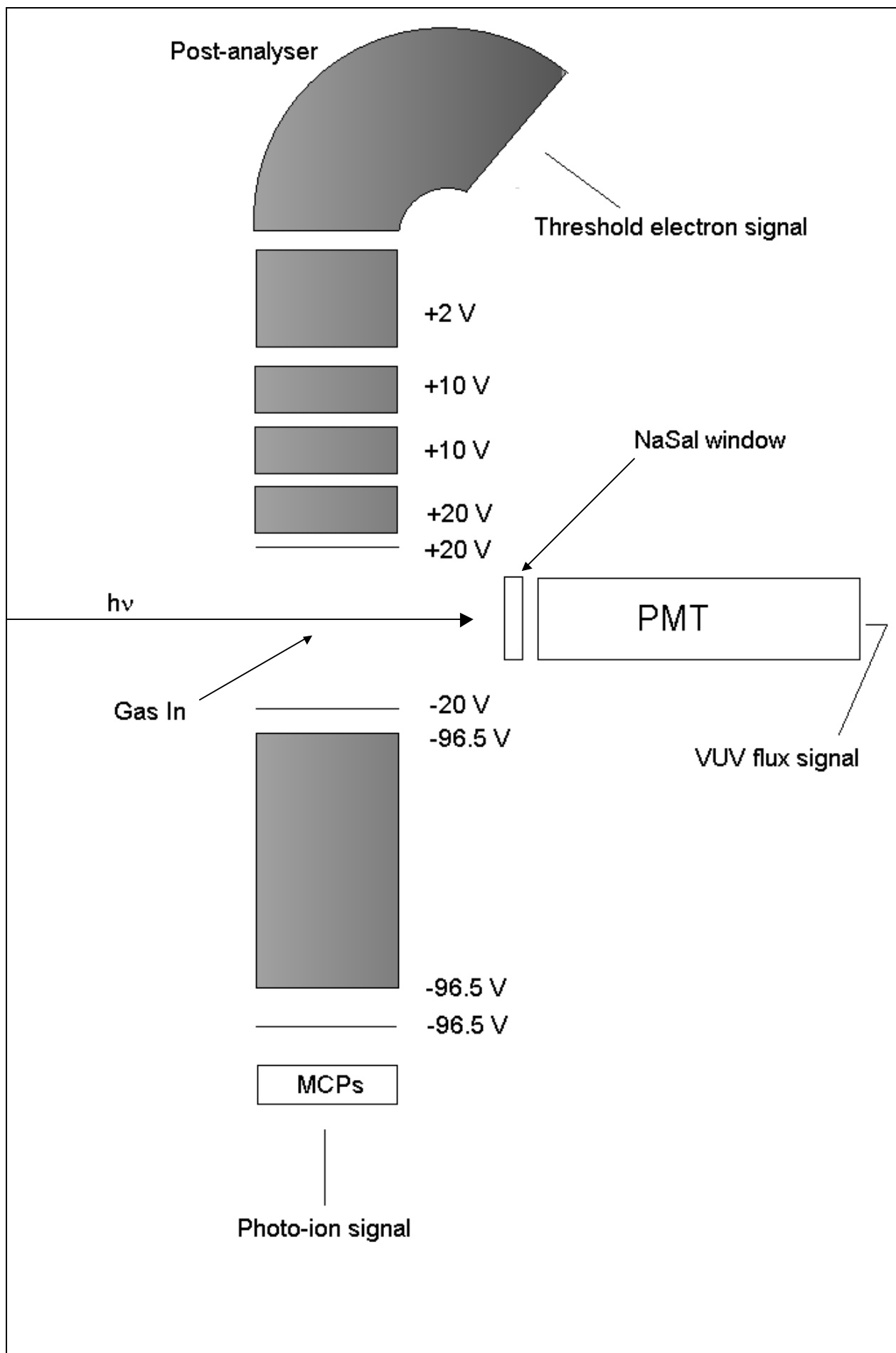


Figure 2.6 A schematic of the threshold photoelectron photoion coincidence apparatus employed at Daresbury laboratories.

The threshold electron analyser consists of a cylindrical electrostatic lens stack and a 127° post analyser to stop energetic electrons that enter on-axis. The first electron lens provides an extraction field of 20 V cm^{-1} , and is designed with large chromatic aberrations; it performs a similar job to a steradiancy-type analyser. The electrons are then focussed onto the 2 mm aperture of a 127° post analyser, where further electron selection occurs. The electron signal is detected by a channeltron electron-multiplier (Phillips X818BL). The instrument was designed to detect threshold electrons and its resolution is *ca.* 10 meV. This resolution is about five times superior to that of the optical resolution of the monochromator (usually 0.3 nm or 54 meV at 15 eV). Therefore, the resolution of the experiment is not determined by the threshold electron analyser, but by the optical resolution of the monochromator. Cations are extracted from the interaction region by the same 20 V cm^{-1} field and are drawn towards the ion detector down a drift tube. The drift tube consists of a second accelerating region (76.5 V cm^{-1}) and a field free region (length = 186 mm). This two-stage accelerating region is configured in such a way that the spacial focussing condition is satisfied.⁵ This ensures that ions of the same mass, charge and velocity arrive at the accelerating region at the same time, irrespective of their point of production. The ion signals are detected by a pair of microchannel plates (Hamamatsu F4296-10) arranged in the Chevron orientation. This configuration of the ion optics allows a sufficient time-of-flight resolution to enable the measurement of kinetic energy releases from dissociative ionisation processes, whilst still maintaining moderately high collection efficiencies. Raw pulses from the channeltron electron-multiplier and the multichannel plates are passed through a discriminator (HVL100) and pulse shaping circuitry to create fast and clean NIM pulses. These NIM pulses pass to a purpose-built time-to-digital converter and a counter card mounted inside a dedicated personal computer. With the time-to-digital converter set in “multihit” mode, the threshold electron signal provides the “start” pulse and the ion signal provides the “stop” pulse. Thus electrons and ions created from the same ionisation event are detected in delayed coincidence. In addition, the counter card records the total ion, threshold electron and flux signals. Therefore, threshold photoelectron, total ion and threshold photoelectron photoion coincidence spectra can be measured concurrently as the two cards operate simultaneously.

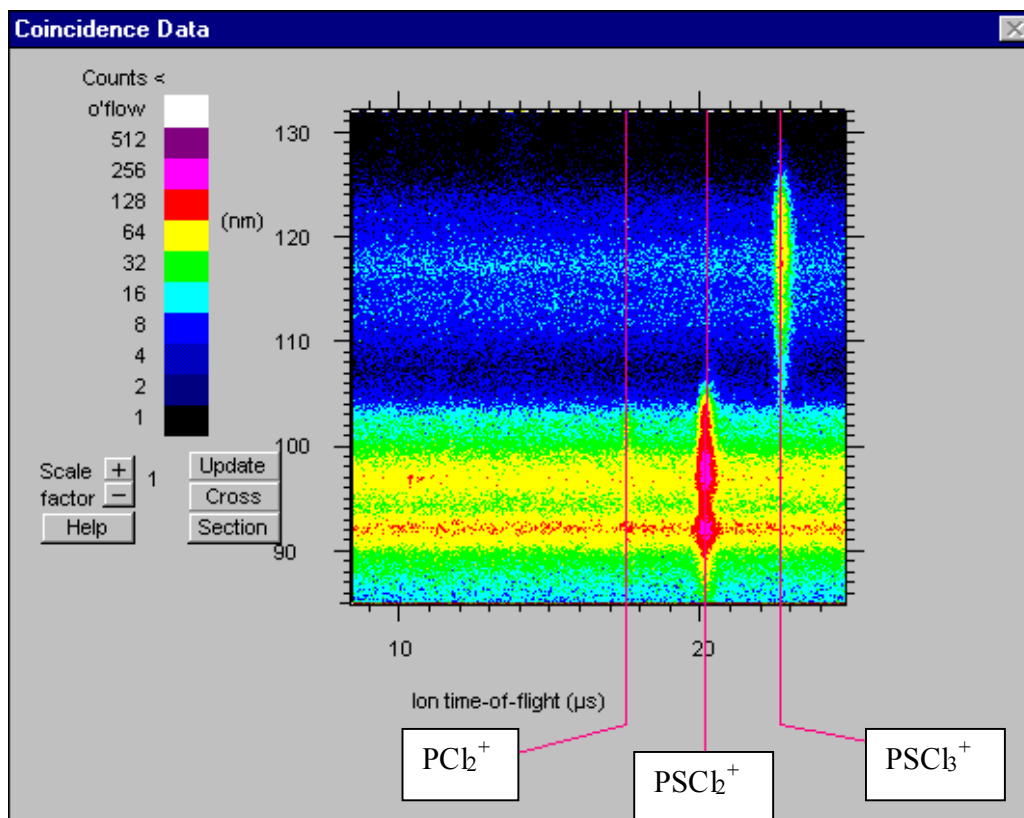


Figure 2.7 3-D threshold photoelectron photoion spectrum of $PSCl_3$ (unpublished data). The figure is a screen capture from the data acquisition interface. The spectrum represents excitation wavelength on the y-axis, ion time-of-flight on the x-axis, and coincidence counts represented by a logarithmic scale on the z-axis.

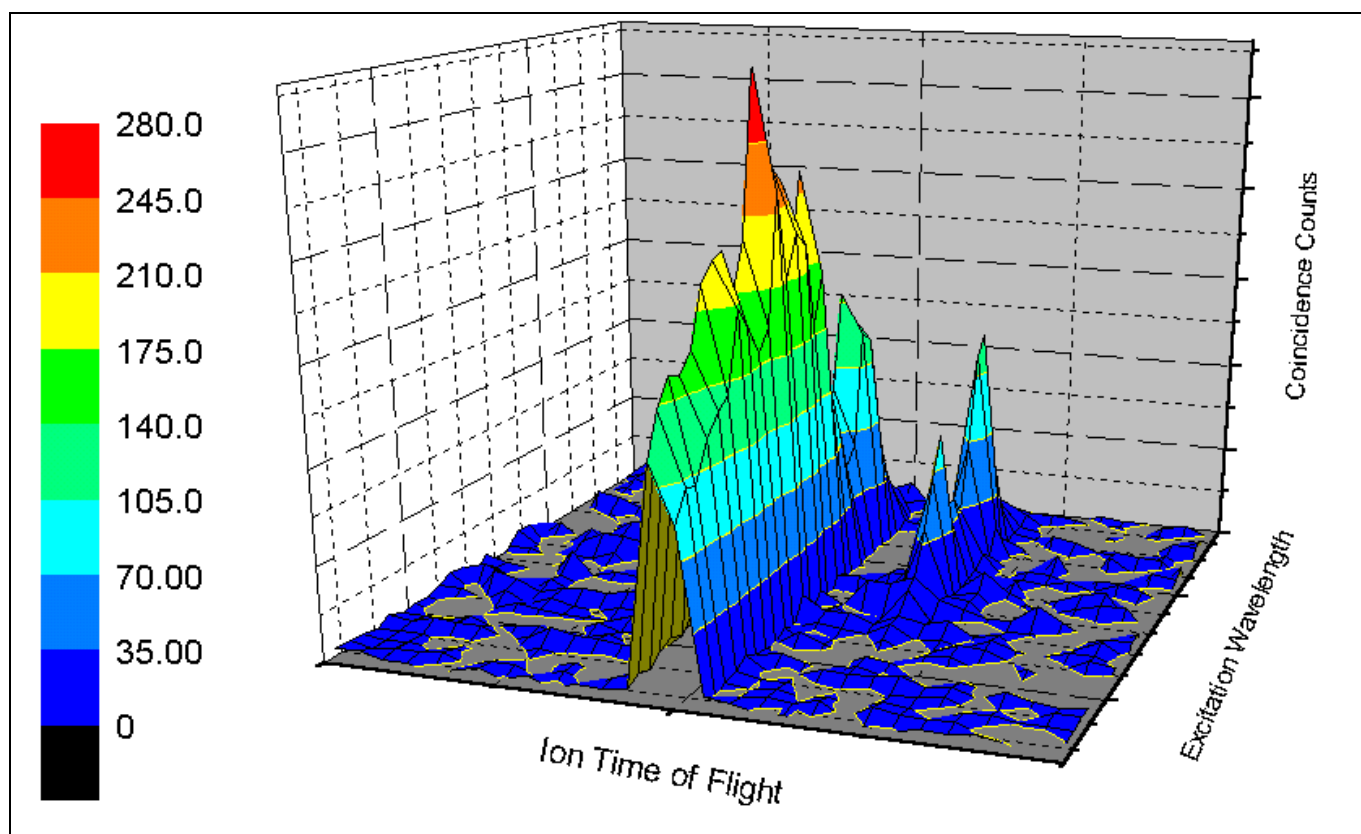


Figure 2.8 3-D contour graph of the 3-D threshold photoelectron photoion coincidence spectrum of CH_2Br_2 .

Experiments can be performed at a fixed photon energy or whilst scanning the photon energy. Experiments performed in the scanning-energy mode allow the investigation of the fragmentation of the valence states of parent ions. The time-of-flight resolution is generally degraded in these experiments to allow detection of all possible ions produced during photoionisation. Threshold photoelectron photoion coincidence (TPEPICO) spectra are obtained. These are 3D histograms where the coincidence count is plotted against both the photon energy and the cation time of flight. Fig. 2.7 shows a screen capture of the data acquisition program and displays a raw TPEPICO spectrum. Fig. 2.8 shows another representation of a TPEPICO spectrum after a background subtraction. Cross-sections taken at fixed ion time of flights yield ion yield plots. Since the ion time of flight is dependent only on the mass of the ion and the drift tube parameters, its identity is generally unambiguous. Horizontal cross-sectional cuts yield the ions formed at a certain energy. In addition to scanning-energy TPEPICO spectra, threshold photoelectron and total ion spectra can be measured. Calibration of the monochromator is achieved by recording the threshold photoelectron spectrum of the $^2P_{3/2}$ and $^2P_{1/2}$ spin-orbit states of Ar^+ (Fig. 2.9). These two ionic states are known to occur at 15.759 and 15.937 eV respectively.

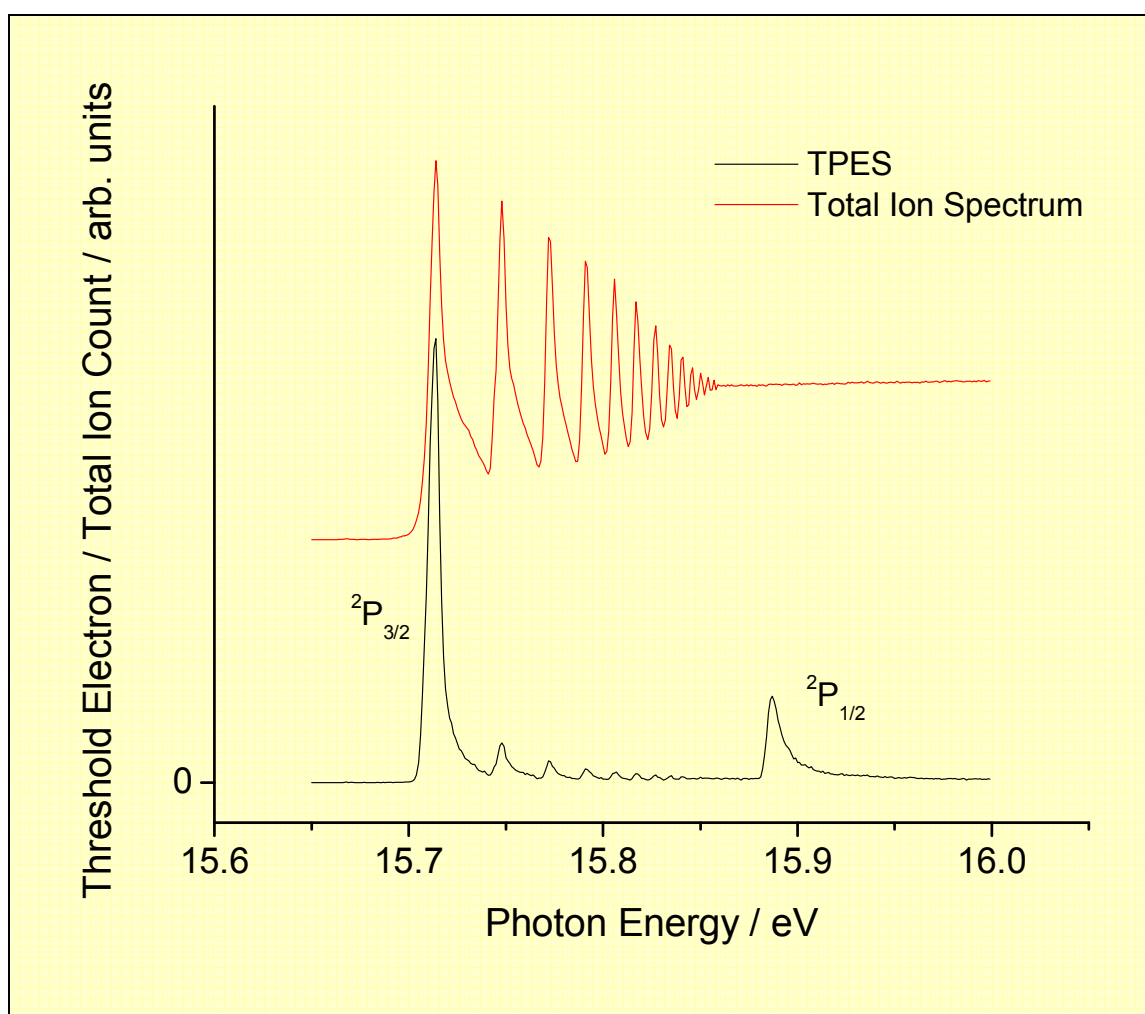


Figure 2.9 The threshold photoelectron and total ion spectra of Ar recorded on station 3.2 of the Daresbury SRS with a resolution of 0.3 Å.

In the fixed-energy mode, TPEPICO time-of-flight spectra are recorded with improved time of flight resolution (an example is shown in Fig. 2.10). The spectra are then 2D graphs that plot the coincidence count as a function of the ion time of flight. This experiment is sometimes performed to identify a particular ion if the scanning TPEPICO spectrum is unable to identify a cation due to poor resolution. More commonly, however, the fixed-energy experiment is performed to yield a mean kinetic energy release, $\langle KE \rangle_t$.

The ion time of flight is dependent on its mass, charge, and the geometry of the mass spectrometer. To a first approximation the time of flight is proportional to mass^{1/2}. Since the experiments are performed at 298 K, the parent ions that are formed by photoionisation will have a range of thermally distributed velocities. Franklin *et al.*⁶ have calculated the expected full width at half maximum (FWHM) in seconds of parent ion peaks:

$$\text{FWHM} = [1.665(2mk_B T)^{1/2}] / qE \quad (2.2)$$

where m is the mass of the ion (in units of kg), k_B is the Boltzmann constant, T is the temperature (in K), q is the charge of the ion (in C), and E is the extraction field (in $V m^{-1}$). This equation was later parameterised by Eland:⁷

$$\text{FWHM} / \text{ns} = [22.294(MT)^{1/2}] / E \quad (2.3)$$

where M is the mass in u , T is the temperature in K, and E is the extraction field in $V cm^{-1}$. However, the time-of-flight distributions of daughter ions formed by the dissociation of the parent ion is somewhat more complicated. Fragment ions often obtain enough translational energy during dissociation for significant broadening of the time of flight peaks to be observed. This broadening is attributed to the kinetic energy released during fragmentation.

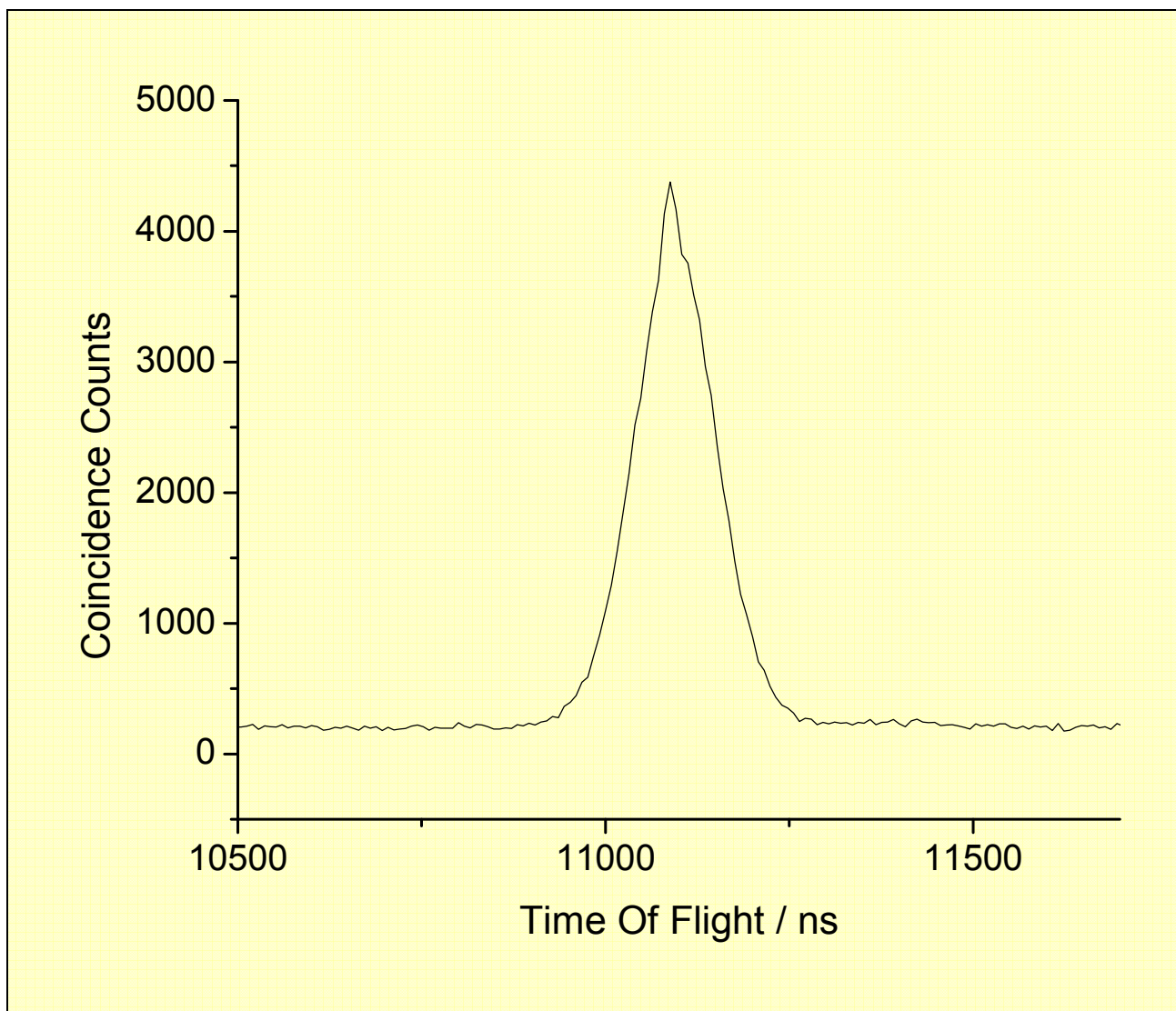


Figure 2.10 A fixed-energy threshold photoelectron photoion coincidence TOF spectrum of Ar measured with a photon energy of 15.8 eV. The full width at half maximum of this peak is 121 ns. This is the expected fwhm for a parent ion of mass 40 u at a T of 298 K in an extraction field of 20 V cm⁻¹.⁷

Analysis of the experimental peak shapes of the TPEPICO-TOF spectra allows the kinetic energy release to be obtained. The time-of-flight spectra are analysed using a method developed by Powis *et al.*⁸ This was later modified by Jarvis *et al.*⁹ to include the possible effects of isotopes in the daughter ion. A basis set of TOF peaks, each with a discrete energy release ϵ_i , is computed, and assigned a reduced probability. The discrete energies are defined by $\epsilon_i(n) = [(2n-1)^2] \cdot \Delta E$, where $n = 1, 2, 3, 4, \dots$ and ΔE is the kinetic energy release of the first peak. The values of n_{\max} and ΔE that are employed depend on the statistical quality of the data. Each computed TOF peak is a convolution of a rectangular ‘fission-energy’ component and a gaussian ‘thermal-energy’ component. The FWHM of the former is proportional to $[m\epsilon_i(n)]^{1/2} / E$, where m is the mass of the daughter ion and E is the extraction field. Each computed TOF peak is taken to be a reasonable representation of the kinetic energy spanning the range $4(n-1)^2 \cdot \Delta E$ to $4n^2 \cdot \Delta E$, centred at $[\epsilon_i(n) + \Delta E]$. The reduced probability of each discrete energy, defined as the

probability of the energy release divided by the span of energies, is varied by linear regression until a best fit to the experimental data is obtained. This analysis yields the kinetic energy release distribution (KERD) and the mean kinetic energy release of the fragment ion, $\langle KE \rangle_{\text{ion}}$ (see Fig. 2.11). In practise, the KERD is relatively insensitive to the fitting parameters and is therefore not interpreted. The value of $\langle KE \rangle_{\text{ion}}$, however, is normally quite robust. If the dissociation is two-bodied, the total mean kinetic energy release, $\langle KE \rangle_t$, can readily be inferred:

$$\langle KE \rangle_t = \left(1 + \frac{M_{\text{ion}}}{M_{\text{neutral}}} \right) \langle KE \rangle_{\text{ion}} \quad (2.4)$$

where M_{ion} and M_{neutral} are the masses of the two fragments. This fitting procedure has the great advantage that it makes no assumptions about the shape of the experimental TOF peak.

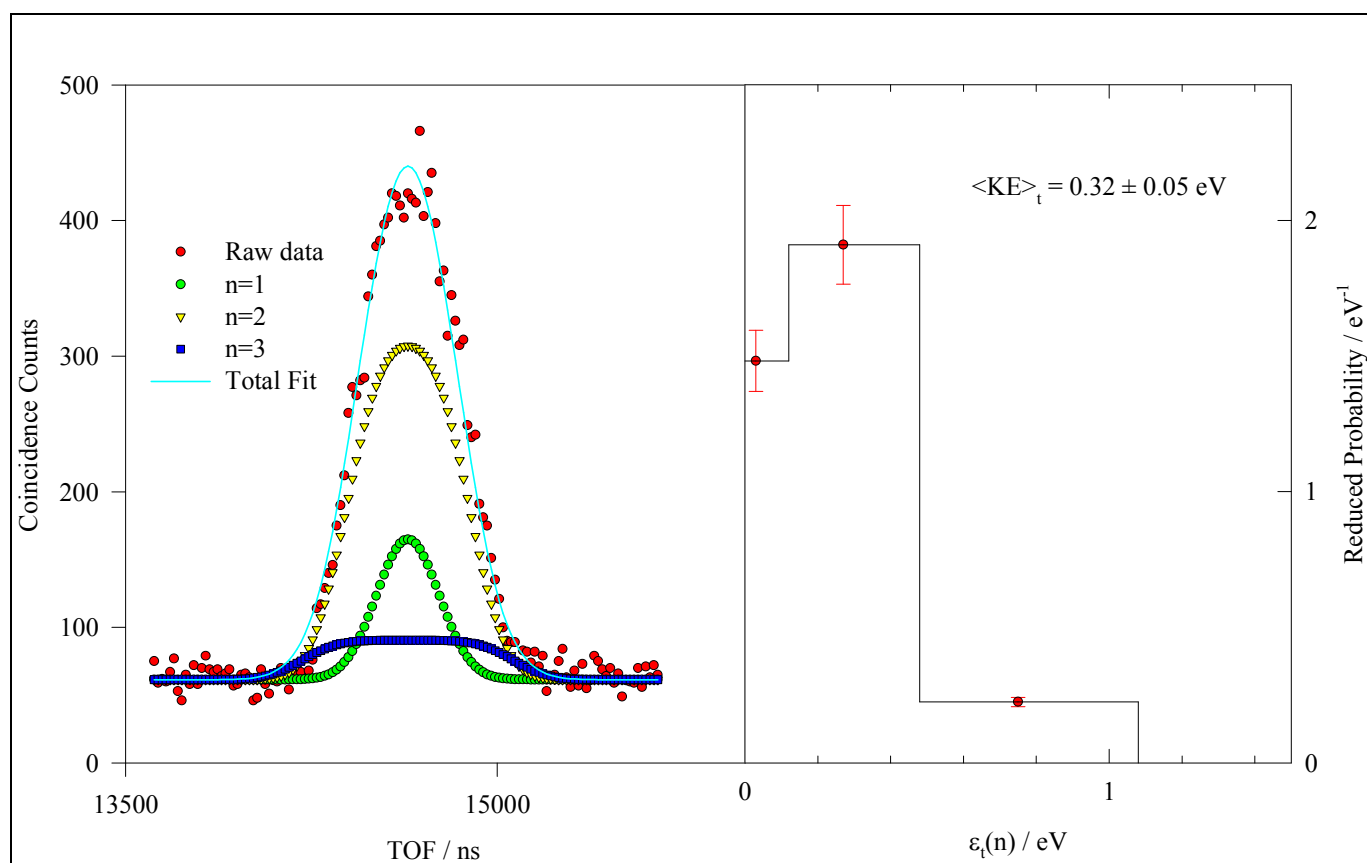


Figure 2.11 The fit of computed TOF peaks to the experimental TPEPICO-TOF spectrum of CF_3^+ from SF_5CF_3 , photoionised at 14.25 eV (left). The best fit is obtained with three components in the basis set ($n = 3$) and a value for ΔE of 0.03 eV (see text). The fit yields a total mean translational kinetic energy into $\text{CF}_3^+ + \text{SF}_5$ of 0.32 ± 0.05 eV. The kinetic energy release distribution from the fit is shown in the right-hand panel.

2.5 References

1. G. Herzberg, *Ann. Physik*, 1928, **86**, 189.
2. G. R. Cook and P. H. Metzger, *J. Chem. Phys.*, 1964, **41**, 321.
3. C. M. Gregory, M. A. Hayes, G. R. Jones and E. Pantos, *Technical Memorandum, Daresbury Laboratory*, 1994, reference DL/SCI/TM98E.
4. P. A. Hatherly, M. Stankiewicz, K. Codling, J. C. Creasy, H. M. Jones and R. P. Tuckett, *Meas. Sci. Tech.*, 1992, **3**, 891.
5. W. C. Wiley and I. H. Maclaren, *Rev. Sci. Instrum.*, 1955, **26**, 1150.
6. J. L. Franklin, P. M. Hierl and D. A. Whan, *J. Chem. Phys.*, 1967, **47**, 3148.
7. J. H. D. Eland, *Int. J. Mass. Spectrom. Ion Phys.*, 1972, **8**, 143.
8. I. Powis, P. I. Mansell and C. J. Danby, *Int. J. Mass Spectrom. Ion Phys.*, 1979, **32**, 15.
9. G. K. Jarvis, D. P. Seccombe and R. P. Tuckett, *Chem. Phys. Lett.*, 1999, **315**, 287.

CHAPTER 3 : THE VUV FLUORESCENCE SPECTROSCOPY OF CX₂Y₂ (X, Y = H, Cl OR Br).

3.1 Introduction

The results in this chapter extend the investigations of the Tuckett Group into the fluorescence spectroscopy of the halides of groups III, IV and V of the periodic table. In the past few years, using vacuum-ultra violet radiation, supplied by Berliner Elekronspeicherring-Gesellschaft für Synchrotronstrahlung (BESSY1) in the range 8-30 eV, several molecules have been probed. These include BX₃ (X = F, Cl and Br),¹⁻⁵ PX₃ (X = F, Cl, Br),^{6,7} MCl₄ (M = C, Si, Ge)⁸ and MF₄ (M = Si, Ge),^{9,10} CF₃X (X = F, Cl, H and Br),¹¹ and CCl₃X (X = F, H and Br).¹² The work of other groups in this field has been reviewed by Whitehead.¹³

The experimental set-up allows complete control over both the excitation energy, E₁ and the emission wavelength, λ₂. Therefore by measuring the fluorescence excitation, dispersed fluorescence and the action spectra of CX₂Y₂, a comprehensive study of the fluorescence spectroscopy has been performed.

3.2 Experimental

Fluorescence excitation, dispersed fluorescence, action and time-resolved fluorescence spectra were measured at BESSY1. Fluorescence excitation, dispersed fluorescence and action spectra were measured using the multi-bunch mode. The fluorescence chamber was attached to the storage ring *via* a 1.5 meter McPherson monochromator employing an optical resolution of 0.3 nm. The dispersed fluorescence was detected using a visible-UV monochromator in the range 190-690nm. An optical resolution of 8 nm was employed with this secondary monochromator. Using frequently recorded flux curves, the fluorescence excitation and action spectra were normalised due to the significant variation in the radiation throughput as the photon energy is varied between 6 and 21 eV. Using the same fluorescence chamber time-resolved spectra were measured in single-bunch mode of the synchrotron. Here, lifetimes of a particular emitting species are measured. Since excitation occurs only every 208 ns, decay of the fluorescence can be observed in real time. The photon energy and the fluorescence wavelength are defined to isolate the emission. The measured decay was fitted with the FLOUR¹⁴ program. Absorption experiments were also performed to compare with fluorescence excitation measurements. A detailed description is given in Chapter 6 of the experimental set up. In brief, the apparatus comprises a partitioned aluminium cube for differential pumping and an absorption cell. The absorption cell is 300 mm long and has a diameter of 35 mm. The cell is directly attached to the aluminium cube between which there is a 1 x 5 mm slit and a collimated mesh. The mesh provides differential pumping but still allows the pathlength to be defined.

The transmitted light through the absorption cell is detected *via* the fluorescence of a sodium salicylate window by a photomultiplier tube. Typical operating pressures range from 20-60 μ bar.

A more detailed description of the all experimental techniques and apparatus in this chapter are included in Chapter 2. All the samples used were liquids and manufactured by Aldrich. All samples were subjected to several freeze-thaw cycles before effusion into the interaction region.

3.3 Energetics of the key dissociation channels

Since all observed emissions are either excited states of parent ion or neutral fragments of CX_2Y_2 (where X, Y = H, Cl or Br), thermochemical evaluation of the dissociation channels and values of the ionisation potentials are of considerable importance. Thus the thermochemistry of such processes allows elucidation of the various pathways open at a particular excitation energy. The energetics of key dissociation channels and the ionisation energies of the ground ionic and excited ionic states are given in Table 3.1. The ground state energies were generally calculated from 0 K heats of formation. These were taken from the JANAF tables.¹⁵ Where values were not available, 298 K heats of formation were taken from Lias *et al.*¹⁶ However, Table 3.1 is hindered as many possible emitters from CBR_2Cl_2 are unknown. Hence dissociation energies including these fragments are not included. The energies of the excited states of most of the emitting fragments were taken from standard sources.^{17,18} The energies of the D' $^3\Pi_g$ ion-pair states of Br_2 and Cl_2 were taken from Tellinghuisen.¹⁹ The ionisation potentials (IP) of the valence states of $CH_2Cl_2^+$, $CH_2Br_2^+$ and $CBR_2Cl_2^+$ included in Table 3.1 were taken from T.Pradeep *et al.*²⁰, A. W. Potts *et al.*²¹ and J. C. Bunzli *et al.*²², respectively.

Table 3.1 Energetics of the key dissociation channels of CH_2Cl_2 , CH_2Br_2 , and CBR_2Cl_2 .

Molecule	Ion	Dissociation Channel	Adiabatic (vertical) IP / eV	Dissociation Energy / eV
	$CH_2Br_2^+ \tilde{G} \ ^2A_1$	$Br_2 D' \ ^2^3\Pi_g + C + 2H$	(19.70 ²¹)	17.92
	$CH_2Br_2^+ \tilde{F} \ ^2B_1$	$CBr A \ ^2\Delta + Br + 2H$	(16.25 ²¹)	15.08
	$CH_2Br_2^+ \tilde{E} \ ^2A_1$	$CH C \ ^2\Sigma^+ + H + 2Br$	(14.75 ²¹)	14.74
	$CH_2Br_2^+ \tilde{D} \ ^2B_2$	$Br_2 D' \ ^2^3\Pi_g + CH + H$	13.8 ²¹ (14.12 ²¹)	14.43
		$CH B \ ^2\Sigma^- + H + 2Br$		14.03

CH ₂ Br ₂	CH ₂ Br ₂ ⁺ \tilde{B} ² B ₁ and \tilde{C} ² A ₁	CH A ² Δ + H + 2Br	(11.28 ²¹)	13.67	
		Br ₂ D' 2 ³ Π _g + C + H ₂		13.44	
		CH C ² Σ ⁺ + H + Br ₂		12.30	
		CH B ² Σ ⁻ + H + Br ₂		11.59	
		CBr A ² Δ + HBr + H		11.32	
	CH ₂ Br ₂ ⁺ \tilde{A} ² A ₂ CH ₂ Br ₂ ⁺ \tilde{X} ² B ₂	CH A ² Δ + H + Br ₂	(10.82 ²¹) (10.61 ²¹)	11.23	
		CH C ² Σ ⁺ + HBr + Br		10.98	
	CH ₂ Br ₂		CBr A ² Δ + Br + H ₂		10.60
			CH B ² Σ ⁻ + HBr + Br		10.27
			Br ₂ D' 2 ³ Π _g + CH ₂		10.07
CH A ² Δ + HBr + Br			9.91		
CH ₂ b ¹ B ₁ + 2Br			7.71		
CH ₂ b ¹ B ₁ + Br ₂			5.27		
			0		
CH ₂ Cl ₂	CH ₂ Cl ₂ ⁺ \tilde{G} ² A ₁ CH ₂ Cl ₂ ⁺ \tilde{F} ² B ₁	Cl ₂ D' 2 ³ Π _g + C + 2H	(20.30 ²¹) (16.77 ²¹)	19.87	
					CH ₂ Cl ₂ ⁺ \tilde{E} ² A ₁ CH ₂ Cl ₂ ⁺ \tilde{D} ² B ₂
	CCl A ² Δ + 2H + Cl	16.25			
	CH C ² Σ ⁺ + H + 2Cl	15.70			
	CH ₂ Cl ₂ ⁺ \tilde{B} ² B ₁ and \tilde{C} ² A ₁	Cl ₂ D' 2 ³ Π _g + C + H ₂	(15.94 ²¹) 14.9 ²¹ (15.30 ²¹)	15.39	
		CH B ² Σ ⁻ + H + 2Cl		14.99	
		CH A ² Δ + H + 2Cl		14.63	
		CH C ² Σ ⁺ + Cl ₂ + H		13.27	
		CH B ² Σ ⁻ + Cl ₂ + H		12.51	
	CH ₂ Cl ₂ ⁺ \tilde{X} ² B ₂ and \tilde{A} ² A ₂	CH A ² Δ + Cl ₂ + H Cl ₂ D' 2 ³ Π _g + CH ₂ CCl A ² Δ + HCl + H CCl A ² Δ + Cl + H ₂	(12.22 ²¹) 11.320 ²⁰ (11.40 ²¹)	12.15	
				12.02	
				11.82	
				11.77	
	CH ₂ Cl ₂		CH C ² Σ ⁺ + HCl + Cl		11.27
CH B ² Σ ⁻ + HCl + Cl			10.56		
CH A ² Δ + HCl + Cl			10.20		
CCl ₂ A ¹ B ₁ + 2H			10.00		
CHCl A ¹ A'' + H + Cl			9.38		
CH ₂ b ¹ B ₁ + 2Cl			8.67		
CH ₂ b ¹ B ₁ + Cl ₂			6.19		
CCl ₂ A ¹ B ₁ + H ₂			5.52		

CH ₂ Cl ₂		CHCl A ¹ A'' + HCl		4.95 0
	CBr ₂ Cl ₂ ⁺ \tilde{I} ² A ₁	Cl ₂ D' 2 ³ Π _g + C + 2Br	(15.94 ²²)	16.82
		Br ₂ D' 2 ³ Π _g + C + 2Cl		15.83
		Cl ₂ D' 2 ³ Π _g + C + Br ₂		14.38
		Br ₂ D' 2 ³ Π _g + C + Cl ₂		13.35
	CBr ₂ Cl ₂ ⁺ \tilde{H} ² A ₁		(12.88 ²²)	
	CBr ₂ Cl ₂ ⁺ \tilde{G} ² A ₂		(12.76 ²²)	
		CCl A ² Δ + 2Br + Cl		13.20
		CBr A ² Δ + 2Cl + Br		12.99
	CBr ₂ Cl ₂ ⁺ \tilde{F} ² A ₁		(12.14 ²²)	
	CBr ₂ Cl ₂ ⁺ \tilde{E} ² B ₁		(11.90 ²²)	
	CBr ₂ Cl ₂ ⁺ \tilde{D} ² B ₂		(11.65 ²²)	
	CBr ₂ Cl ₂ ⁺ \tilde{C} ² A ₁		(11.60 ²²)	
		Br ₂ D' 2 ³ Π _g + CCl + Cl		12.38
	CBr ₂ Cl ₂ ⁺ \tilde{B} ² A ₂		(11.18 ²²)	
		CCl A ² Δ + BrCl + Br		10.97
	CBr ₂ Cl ₂ ⁺ \tilde{A} ² B ₂		(10.94 ²²)	
		CCl A ² Δ + Br ₂ + Cl		10.76
		CBr A ² Δ + ClBr + Cl		10.76
	CBr ₂ Cl ₂ ⁺ \tilde{X} ² B ₁		(10.67 ²²)	
		CBr A ² Δ + Cl ₂ + Br		10.51
		Br ₂ D' 2 ³ Π _g + CCl ₂		8.44
		CCl ₂ A ¹ B ₁ + 2Br		6.95
CBr ₂ Cl ₂		CCl ₂ A ¹ B ₁ + Br ₂		4.51 0

3.4 Results

3.4.1 CH₂Br₂

3.4.1.1 The Fluorescence Excitation and Absorption Spectroscopy of CH₂Br₂.

The fluorescence excitation spectrum of CH₂Br₂ was recorded with an optical resolution of 0.3 nm in the energy range *ca.* 9-22 eV and is shown in Fig. 3.1. The fluorescence excitation spectrum is presented here on an arbitrary scale (y-axis) and does not represent the absolute fluorescence cross-section. It therefore follows that any apparent quantitative relationship between the intensities of the fluorescence and absorption peaks in the figure is not significant. In other words, the absolute fluorescence quantum yield cannot be inferred. All peaks have shapes characteristic of a resonant primary excitation process,

indicating that the fluorescence from excited states of the parent ion is very weak. It is likely that, since there exist many non-radiative decay channels for Rydberg states of polyatomic molecules, most of the observed fluorescence is not due to transitions in the parent molecule, but to fragments produced by predissociation. The fluorescence excitation spectrum therefore yields the energies of the Rydberg states which predissociate to fluorescing fragments. Comparison of the fluorescence excitation spectrum with the VUV absorption spectrum will make known the importance of this decay pathway, but only at a qualitative level.

The absorption spectrum of CH₂Br₂ was recorded with an optical resolution of 0.08 nm. The electronic configuration of the outer-valence molecular orbitals of the parent molecule is ... $(1b_1)^2(1a_1)^2(2a_1)^2(2b_1)^2(3a_1)^2(1b_2)^2(4a_1)^2(3b_1)^2(1a_2)^2(2b_2)^2$, where the numbering scheme does not include core orbitals. Thus the HOMO is labelled 2b₂ and removal of an electron from this orbital yields the ground \tilde{X}^2B_2 state of CH₂Br₂⁺. The (HOMO -1) is labelled 1a₂, and electron removal from this orbital yields the first excited state \tilde{A}^2A_2 of CH₂Br₂⁺. Figure 3.2 shows an expansion of the absorption spectrum in the energy range 7.0-11.5 eV. A number of peaks are observed. The Rydberg assignments of the absorption spectrum are shown in Table 3.2. Quantum defects have also been determined using the well known Rydberg formula (see Chapter 2):

$$E = IP - \frac{R_H}{(n - \delta)^2} \quad (3.1)$$

where E is the energy of the transition, IP is the ionisation potential to which the Rydberg state converges, R_H is the Rydberg constant, and n and δ are the principle quantum number and the quantum defect of the Rydberg orbital respectively. It is necessary to decide whether vertical or adiabatic ionisation potentials should be used. The geometry of the Rydberg state should be similar to that of the parent ion state to which it converges. Since vibrational structure is only resolved occasionally, the peaks of a Rydberg series should converge to the vertical ionisation potential. Thus vertical ionisation potentials have been used and the values are shown in Table 3.2. The quantum defects determined for the Rydberg states (Table 3.2) are generally in reasonable agreement with those determined for an isolated Br atom (ns = 2.96, np = 2.51, nd = 1.10).²³ This suggests that the 1a₁, 3b₁ and 1a₂ molecular orbitals of CH₂Br₂ are essentially Br 4pπ non-bonding orbitals.

However, several peaks in the absorption spectrum remain unassigned as no successful model could be found based on the Rydberg formula and sensible predictions for values of δ. Finally, it is noted that, at all energies, there is no obvious similarity between the absorption and fluorescence excitation spectra. This suggests that decay of excited states of CH₂Br₂ to fluorescing fragments probably is a minor channel.

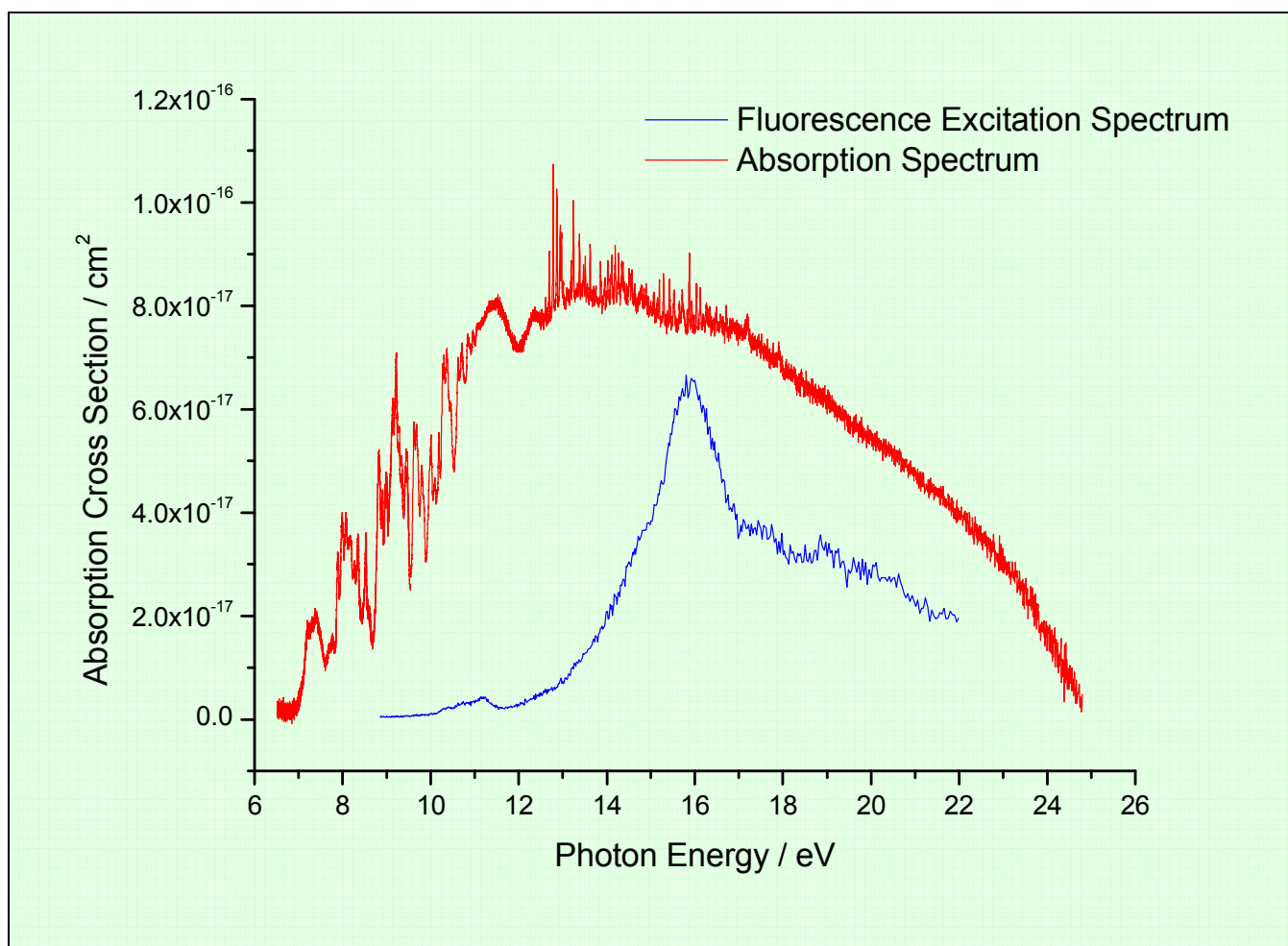


Figure 3.1 The fluorescence excitation and absorption spectra of CH₂Br₂. Spectral resolutions of 0.3 and 0.08 nm were employed for the fluorescence excitation and absorption spectra, respectively. The absorption cross-sections shown are absolute, whereas the fluorescence signal is arbitrary and has been scaled for optimum comparison with the absorption spectrum.

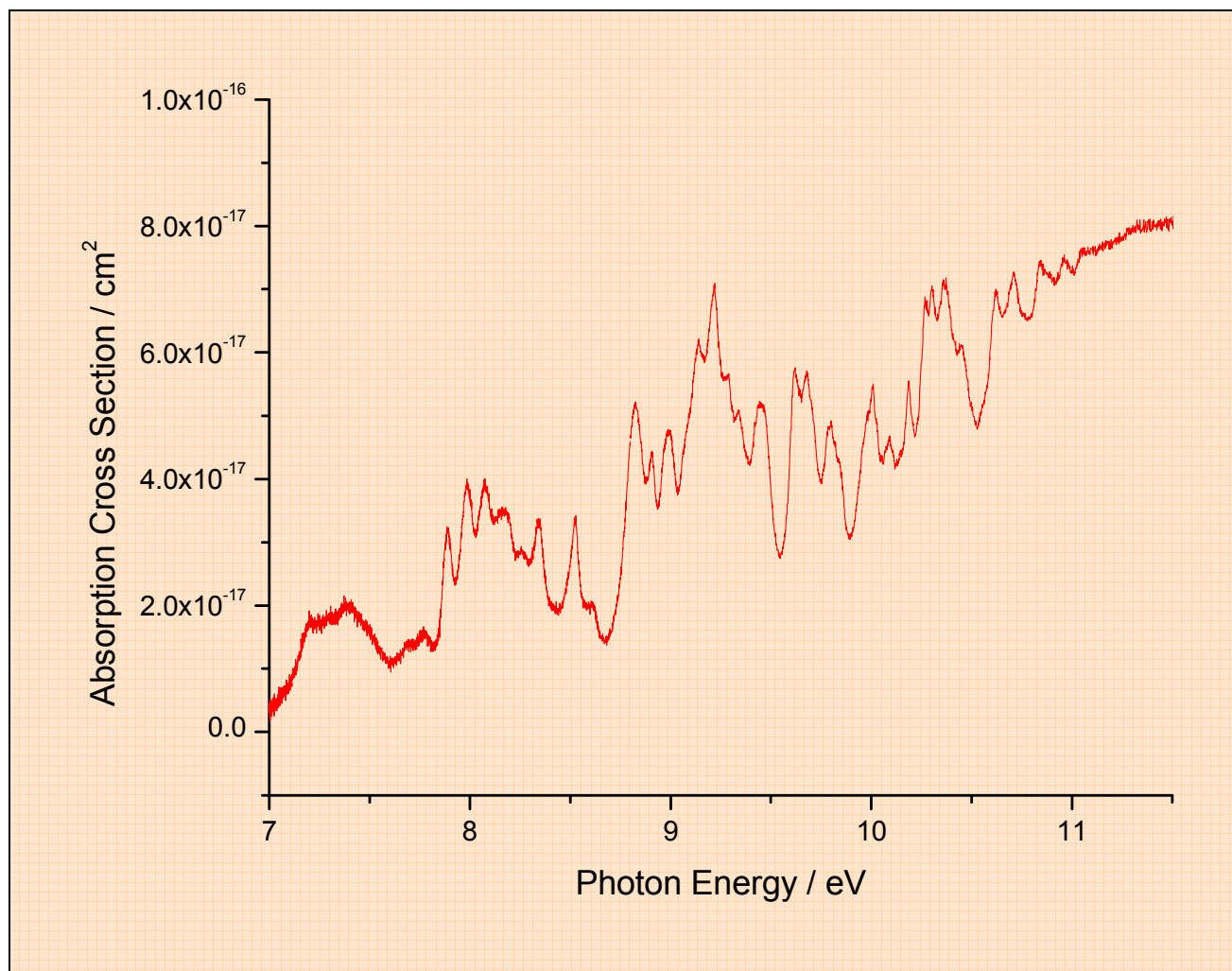


Figure 3.2 The absorption spectrum of CH_2Br_2 with a spectral resolution of 0.08 nm.

Table 3.2 The Rydberg assignments of the photoabsorption bands in CH_2Br_2 .

Peak position / eV	Assignment	IP used / eV	Quantum Defect
7.40	$5s \leftarrow 1a_2$ or $3d \leftarrow 3b_1$	10.82 or 11.28	3.01 or 1.13
8.53	$5p \leftarrow 1a_2$	10.82	2.56
9.22	$7s \leftarrow 3b_1$	11.28	4.43
9.28	$6s \leftarrow 1a_2$	10.82	3.03
9.62	$4d \leftarrow 3b_1$	11.28	1.14
9.68	$6p \leftarrow 1a_2$	10.82	2.55

10.01	7s ← 1a ₂	10.82	2.90
10.19	8s ← 3b ₁	11.28	4.47
10.37	8p ← 1a ₂ or 5d ← 3b ₁	10.82 or 11.28	2.51 or 1.13
10.62	9s ← 3b ₁	11.28	4.46
10.71	6d ← 3b ₁	11.28	1.11
10.84	10s ← 3b ₁	11.28	4.43
10.96	11s ← 3b ₁	11.28	4.44

3.4.1.2 The Dispersed Fluorescence Spectroscopy of CH₂Br₂.

The dispersed fluorescence spectra shown in Figs 3.3 and 3.4 were recorded at excitation energies of 11.2, 14.7, 15.7, 17.4 and 19.6 eV over the range 190-690 nm. For $E_1 = 11.2$ eV several emitters are observed. The spectrum is dominated by the CH A $^2\Delta - X$ $^2\Pi$ emission at 426 nm. CH B $^2\Sigma^- - X$ $^2\Pi$ is also observed at 388 nm. Bromine derivatives Br₂ D' $2^3\Pi_g - A'$ $2^3\Pi_u$ and CBr A $^2\Delta - X$ $^2\Pi$ are also observed at 288 and 309 nm, respectively, although CBr A $^2\Delta - X$ $^2\Pi$ emission is very weak. A broad band centered at *ca.* 600 nm is tentatively assigned to CBr₂ $\tilde{A}^1B_1 - \tilde{X}^1A_1$. For $E_1 = 14.7$ eV, the same emitters are present, plus peaks at 330 nm and 355 nm. The former cannot be assigned, but the latter is attributed to emission from the D' $2^3\Pi_g$ state of Br₂.¹⁹ For $E_1 = 15.7$ eV an additional emitter is observed at 485 nm. This emission is assigned to parent ion, CH₂Br₂⁺ $\tilde{D}^2B_2 - \tilde{C}^2A_1$. For $E_1 > 17$ eV, only four emitters remain at 288, 309, 388 and 426 nm corresponding to Br₂ D' $2^3\Pi_g - A'$ $2^3\Pi_u$, CBr A $^2\Delta - X$ $^2\Pi$, CH B $^2\Sigma^- - X$ $^2\Pi$ and CH A $^2\Delta - X$ $^2\Pi$.

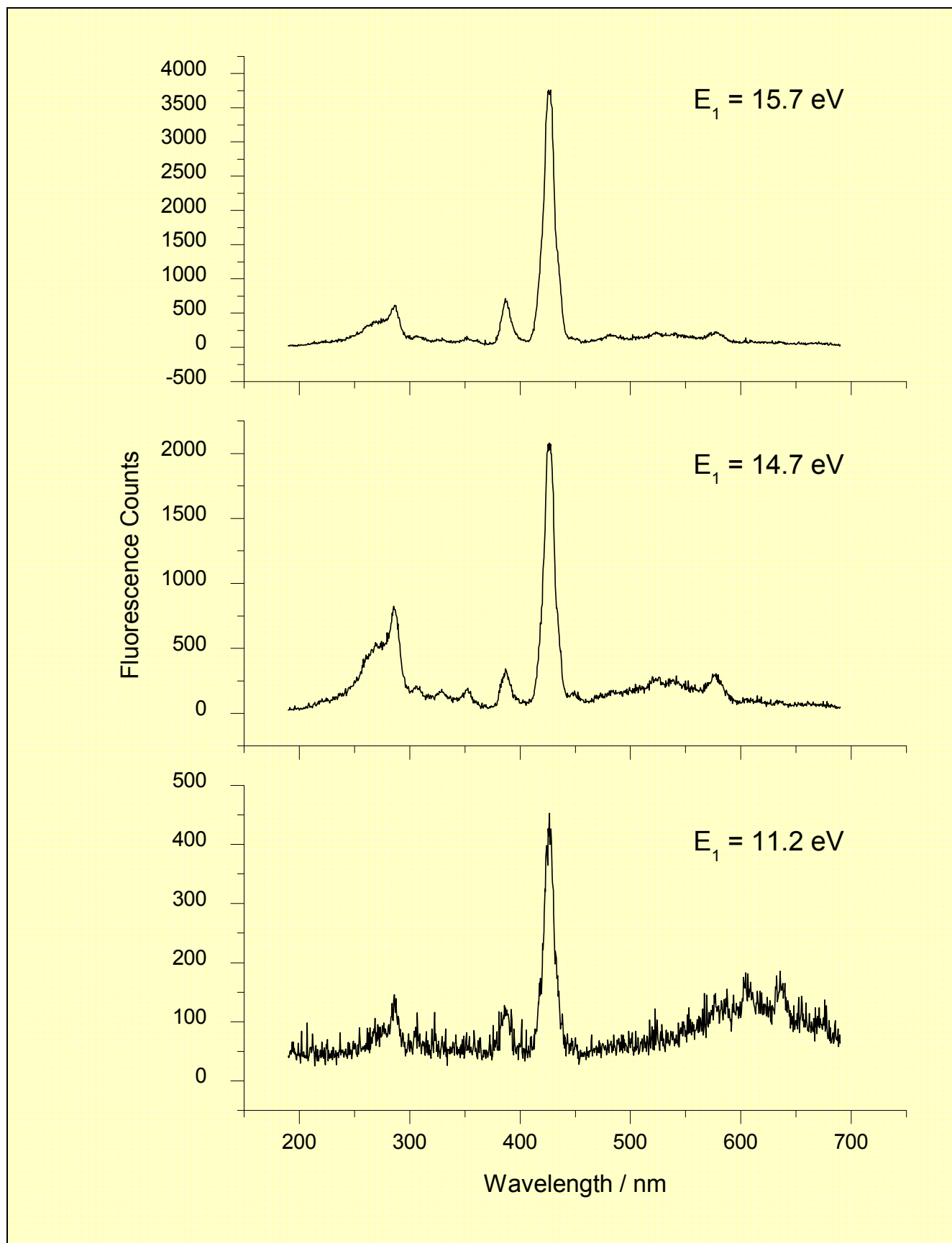


Figure 3.3 Dispersed fluorescence spectra of CH_2Br_2 . The spectral resolution employed for the dispersing spectrometer was 8 nm.

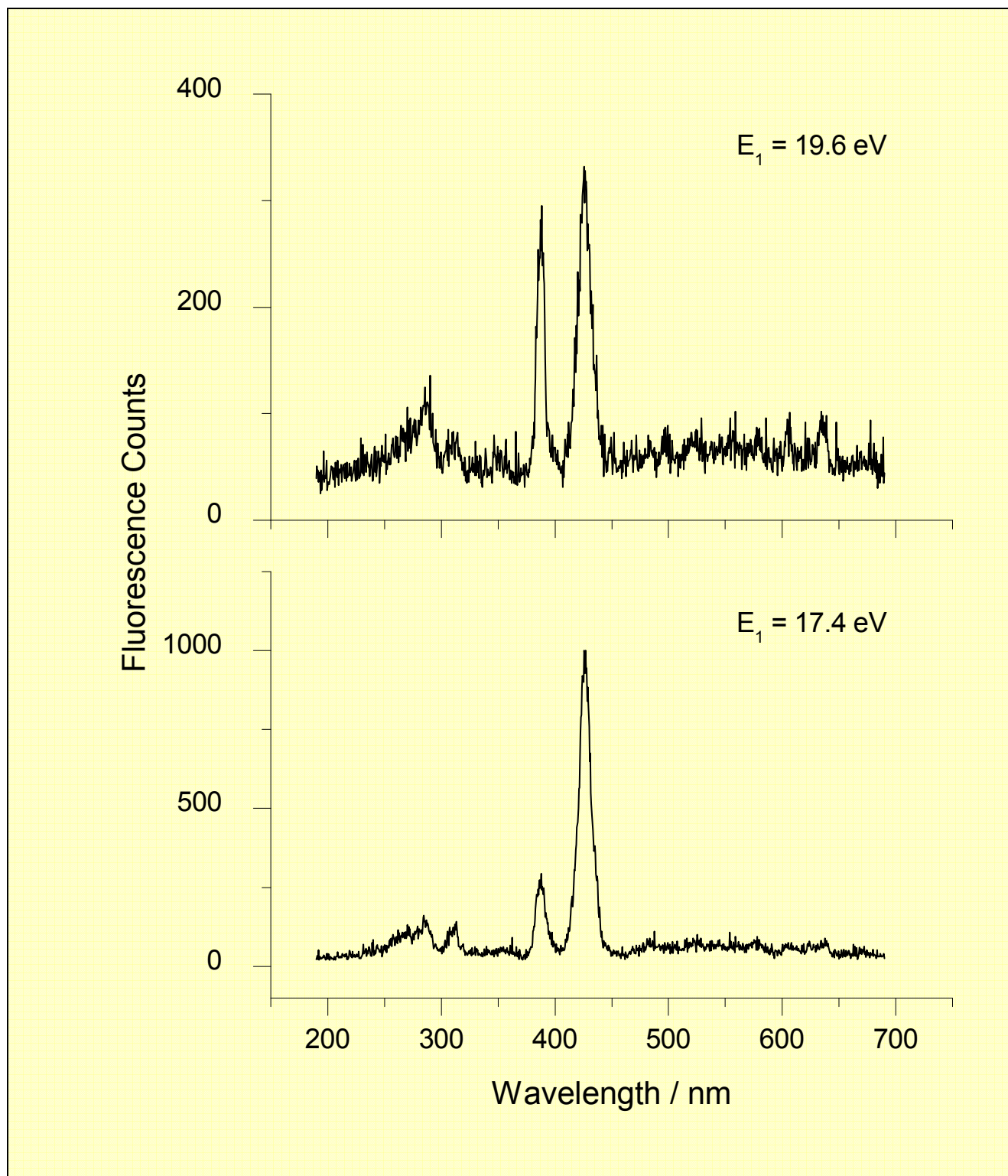


Figure 3.4 Dispersed fluorescence spectra of CH₂Br₂. The spectral resolution employed for the dispersing spectrometer was 8 nm.

3.4.1.3 The Action Spectroscopy of CH₂Br₂.

Action spectra were recorded from 9 – 22 eV for λ_2 values of 288, 309, 426, 485 and 600 nm. This corresponds to the isolation of the Br₂ D' $2^3\Pi_g - A' 2^3\Pi_u$, CBr A $^2\Delta - X^2\Pi$, CH A $^2\Delta - X^2\Pi$, CH₂Br₂⁺ $\tilde{D}^2B_2 - \tilde{C}^2A_1$ and CBr₂ $\tilde{A}^1B_1 - \tilde{X}^1A_1$ bands, respectively. These spectra are shown in Figures 3.5

and 3.6. Such spectra can also yield appearance potentials for the formation of excited fragments. It is therefore possible to compare the appearance potentials to the thermochemistry in Table 3.1 to identify the dissociation pathway. A summary of the range of excitation energies, emission wavelengths and appearance potentials for the fluorescence observed following VUV photoexcitation of CH₂Br₂ is presented in Table 3.3. The results show an inconsistency between the dispersed fluorescence spectrum measured at E₁ = 11.2 eV and the action spectra of the emitters observed. Inspection of Table 3.3 highlights the fact that only CBr A ²Δ – X ²Π and CBr₂ \tilde{A} ¹B₁ – \tilde{X} ¹A₁ have onsets below 11.2 eV, yet emission is also observed from excited states of CH and Br₂. It is therefore probable that the signal due to CH A ²Δ – X ²Π and CH B ²Σ⁻ – X ²Π is a result of second-order radiation from the excitation source.

Table 3.3 Summary of the emission bands observed following photoexcitation of CH₂Br₂.

Emitter	Appearance Potential / eV	E ₁ range / eV	λ ₂ range / nm	Assignment
Br ₂ D' 2 ³ Π _g	11.5 ± 0.5	> 11.5	240-290	Br ₂ D' 2 ³ Π _g – A' 2 ³ Π _u
CBr A ² Δ	11.0 ± 0.5	> 11.0	300-320	CBr A ² Δ – X ² Π
CH A ² Δ	13.4 ± 0.3	> 13.4	410-440	CH A ² Δ – X ² Π
CH ₂ Br ₂ ⁺ \tilde{D} ² B ₂	13.6 ± 0.3	> 13.6	475-495	CH ₂ Br ₂ ⁺ \tilde{D} ² B ₂ – \tilde{C} ² A ₁
CBr ₂ \tilde{A} ¹ B ₁	10.0 ± 0.2	> 10.0	520-690	CBr ₂ \tilde{A} ¹ B ₁ – \tilde{X} ¹ A ₁

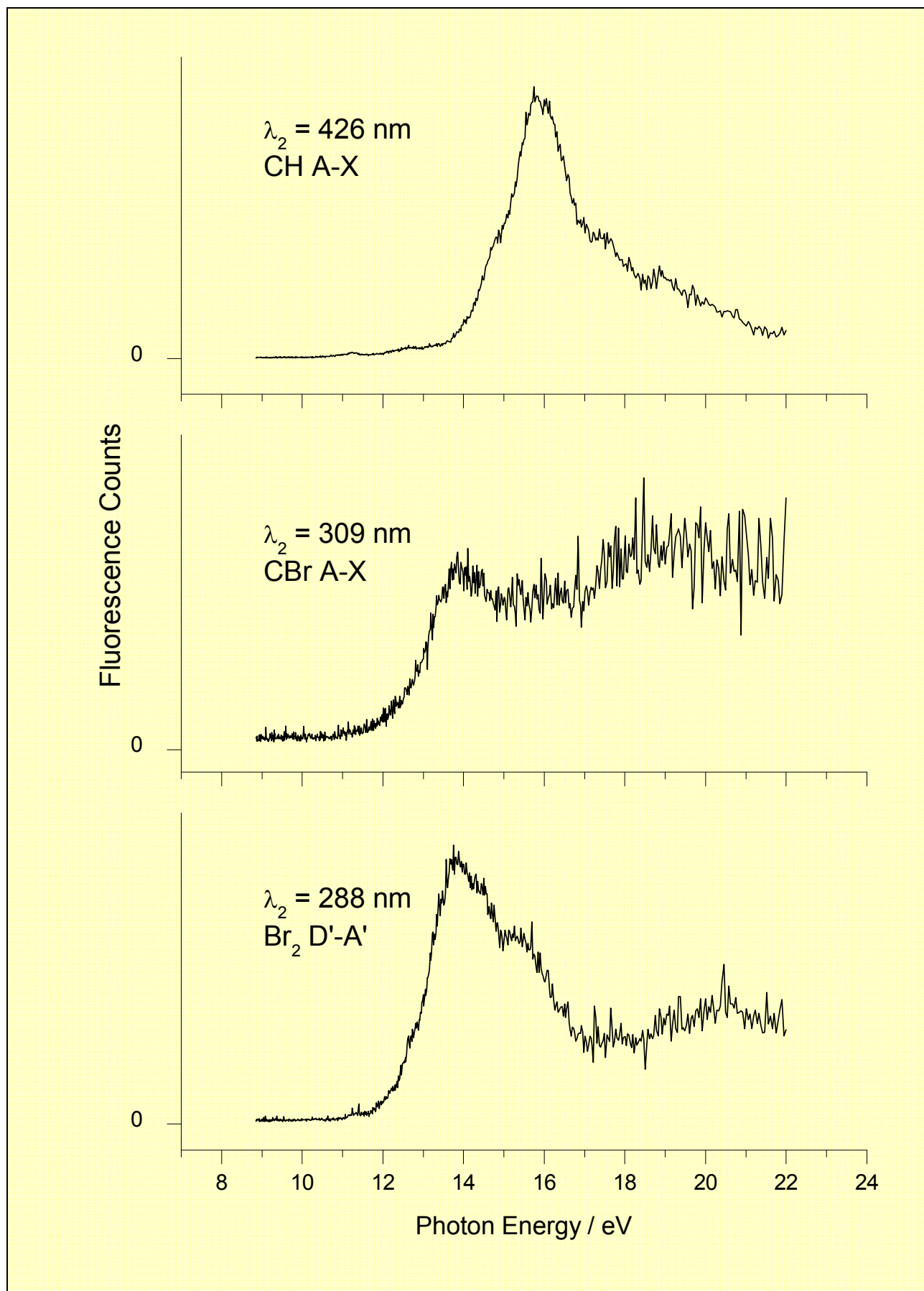


Figure 3.5 Action spectra of CH_2Br_2 . The spectral resolution employed for the excitation vacuum-UV photon source, E_1 , was 0.3 nm.

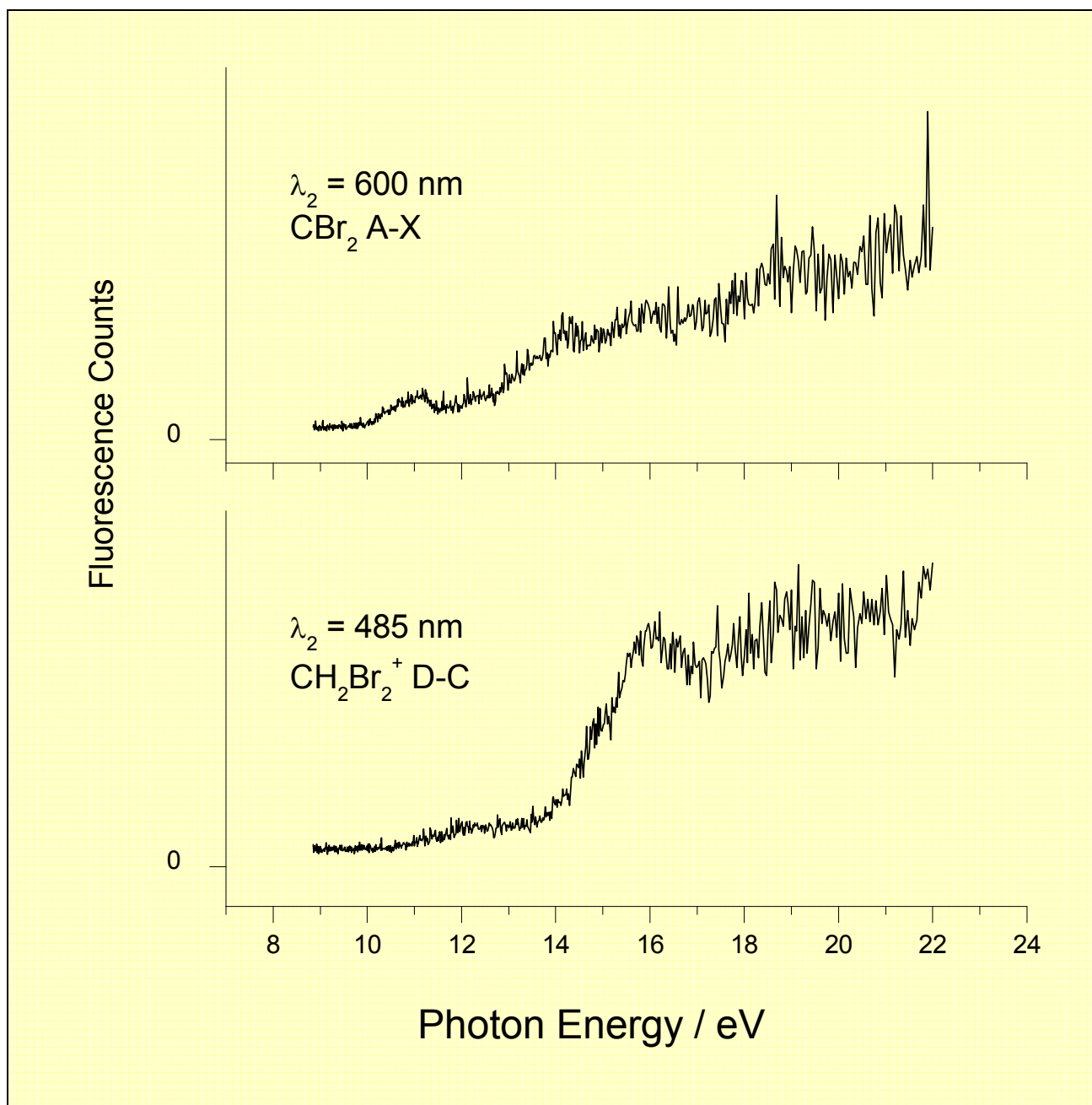


Figure 3.6 Action spectra of CH_2Br_2 . The spectral resolution employed for the excitation vacuum-UV photon source, E_1 , was 0.3 nm.

3.4.1.4 Lifetime measurements of CH_2Br_2 .

Using single bunch mode, the fluorescence lifetimes of two of the emitting states following VUV photoexcitation of CH_2Br_2 have been measured (Fig. 3.7). The results are given in Table 3.4. The uncertainties in the lifetime measurements throughout this chapter are due to the statistical quality of the data and errors are no more than $\pm 2\text{ns}$. It is also noted that the elevated baselines of the spectra are due to

scattered light. It was not possible to make realistic measurements of the lifetimes of the $B^2\Sigma^-$ and $A^2\Delta$ states of CH from the CH B-X and A-X emissions, since their values, 380 and 534 ns respectively,¹⁷ exceed the upper limit which can readily be measured, *ca.* 100 ns. By comparison with the lifetime of the \tilde{A}^1B_1 state of CCl_2 which is 3.6 μ s,¹⁸ the lifetime of the \tilde{A}^1B_1 state of CBr_2 was not measured for the same reason. The value for the $D' 2^3\Pi_g$ state of Br_2 , from the emission centred at $\lambda_2 = 288$ nm, is 11.8 ns. This value compares reasonably with that of 22.6 ns, made from selective photoexcitation of CF_2Br_2 .²⁴ The $A^2\Delta$ state of CBr , determined from CBr A-X emission centred at 310 nm, gives a value of 14.4 ns. This is in good agreement with the value obtained from CCl_3Br , 15.5 ns.¹² The agreement of these measured lifetimes with previously determined values give confidence to the assignments made in this section. In retrospect, it is unfortunate that we were not able to measure the lifetime of the \tilde{D}^2B_2 state of the parent ion of CH_2Br_2 , because an equivalent measurement for $CH_2Cl_2^+$ yielded a value, 6.2 ns, which could easily be measured with high accuracy (see Section 3.4.2.4)

Table 3.4 Lifetimes of fragments produced following the (pre-)dissociation of CH_2Br_2 .

E_1 / eV	λ_2 / nm	Emitter	Lifetime / ns
13.8	288	$Br_2 D' 2^3\Pi_g$	11.8
13.8	310	$CBr A^2\Delta$	14.4

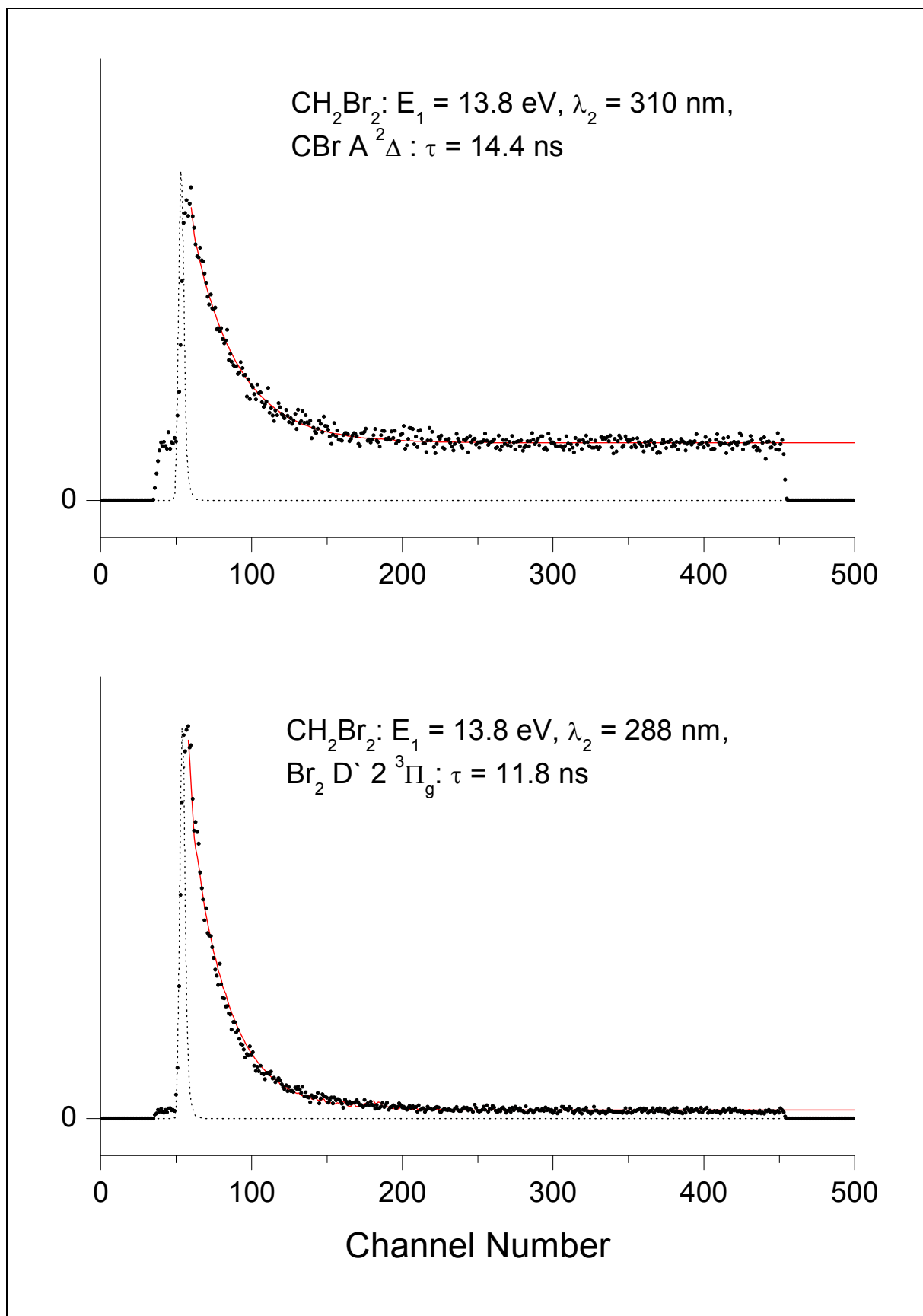


Figure 3.7 Time-resolved fluorescence spectra of CH₂Br₂. Each spectrum shows the experimental data points (black dots), the prompt signal (black dashed line), and the fit to the data (red solid line). The time resolution is 0.481 ns per channel. The proposed emitters and the fitted lifetimes are shown.

3.4.2 CH₂Cl₂

3.4.2.1 The Fluorescence Excitation and Absorption Spectroscopy of CH₂Cl₂.

The fluorescence excitation spectrum of CH₂Cl₂ was recorded with an optical resolution of 0.3 nm in the energy range *ca.* 9-22 eV and is shown in Fig. 3.8. In contrast to the fluorescence excitation spectrum of CH₂Br₂, a non-resonant feature is observed at *ca.* 14.9 eV. This feature probably arises from the fluorescence of an excited state of the parent ion. All other features have peak shapes characteristic of a resonant primary excitation process.

The absorption spectrum of CH₂Cl₂ was recorded with an optical resolution of 0.08 nm. As with CH₂Br₂, the electronic configuration of the outer valence molecular orbitals of the parent molecule is ... $(1b_1)^2(1a_1)^2(2a_1)^2(2b_1)^2(3a_1)^2(1b_2)^2(4a_1)^2(3b_1)^2(1a_2)^2(2b_2)^2$, where the numbering scheme does not include core orbitals. Figure 3.9 shows an expansion of the absorption spectrum in the energy range 7.0-12.2 eV. A number of peaks are observed, and some of them have been assigned using the well-known Rydberg formula. Quantum defects have been determined and are presented in Table 3.5. They are generally in good agreement with those determined for an isolated chlorine atom ($ns = 2.01$, $np = 1.57$).²³ As with CH₂Br₂, this implies that the $1a_2$ molecular orbital of CH₂Cl₂ is essentially that of a Cl $3p\pi$ non-bonding orbital.

Several peaks remain unassigned as no successful model was found based on the Rydberg formula. As with CH₂Br₂, there is obvious no similarity between the absorption and fluorescence excitation spectra of CH₂Cl₂.

Table 3.5 The Rydberg assignments of the photoabsorption bands in CH₂Cl₂.

Peak position / eV	Assignment	IP used / eV	Quantum Defect
8.25	4s ← 1a ₂	11.40	2.15
9.10	4p ← 1a ₂	11.40	1.57
10.57	5s ← 1a ₂	11.40	2.15
11.31	6s ← 1a ₂	11.40	2.13
11.65	7s ← 1a ₂	11.40	2.13
11.83	8s ← 1a ₂	11.40	2.08
11.94	9s ← 1a ₂	11.40	2.01
12.01	10s ← 1a ₂	11.40	1.97
12.04	11s ← 1a ₂	11.40	2.12

12.08	$12s \leftarrow 1a_2$	11.40	2.11
12.12	$13s \leftarrow 1a_2$	11.40	1.55

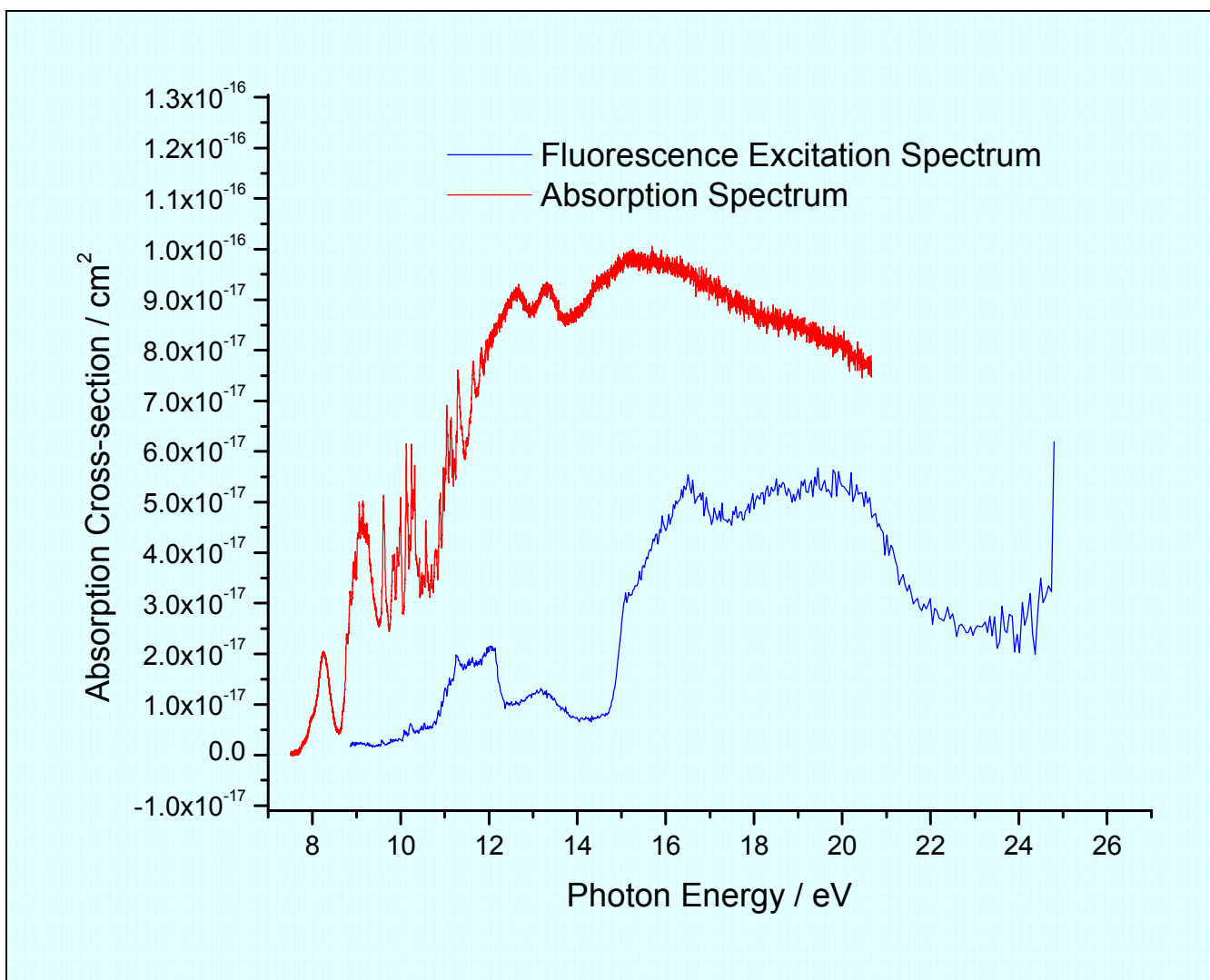


Figure 3.8 The fluorescence excitation and absorption spectra of CH_2Cl_2 . Spectral resolutions of 0.3 and 0.08 nm were employed for the fluorescence excitation and absorption spectra respectively. The absorption cross-sections shown are absolute, whereas the fluorescence signal is arbitrary and has been scaled for optimum comparison with the absorption spectrum.

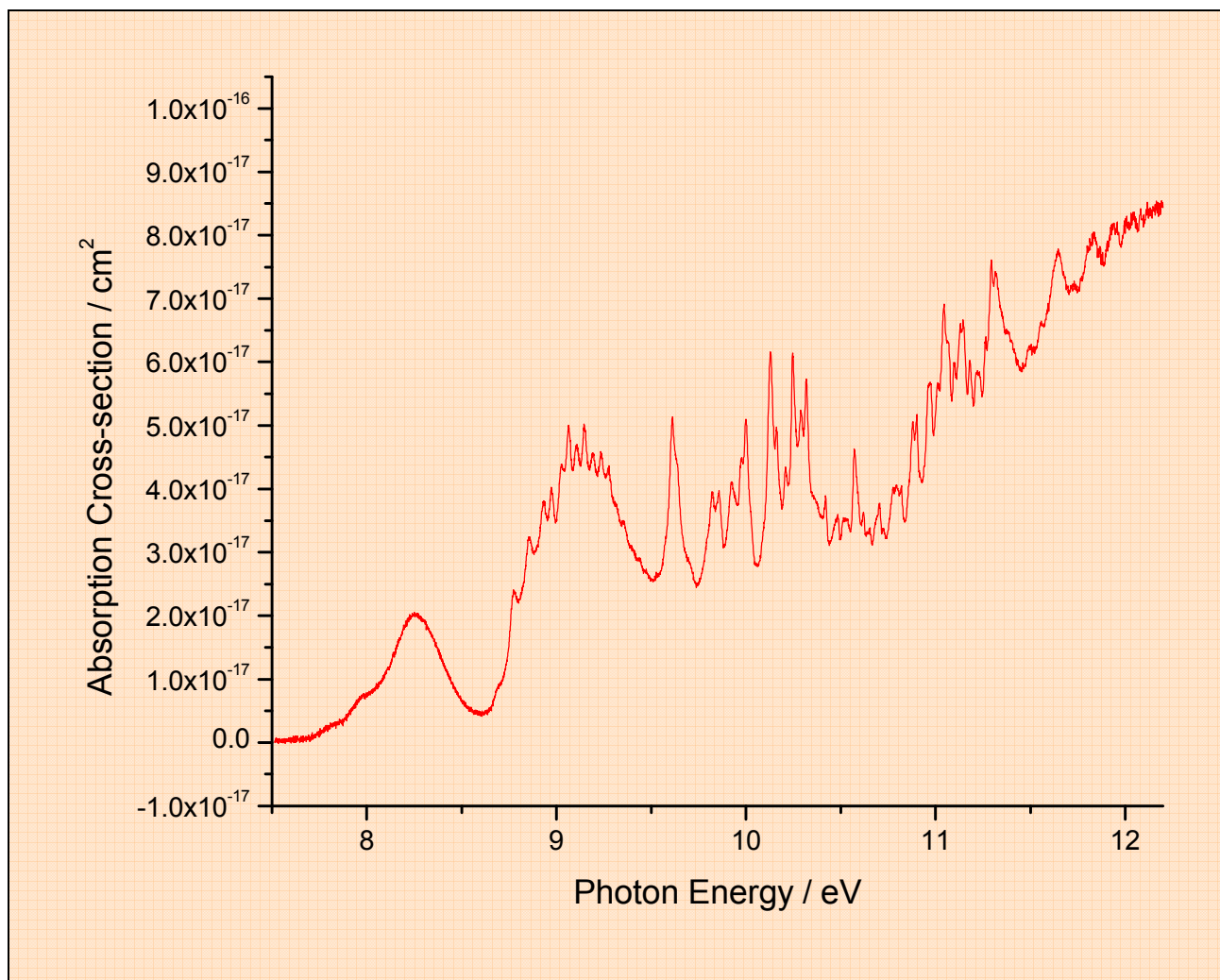


Figure 3.9 The absorption spectrum of CH_2Cl_2 with a spectral resolution of 0.08 nm.

3.4.2.2 The Dispersed Fluorescence Spectroscopy of CH_2Cl_2 .

The dispersed fluorescence spectra shown in Fig 3.10 were recorded at excitation energies of 11.3, 12.0, 13.2, 16.4 and 19.6 eV over the range 190-690 nm. For $E_1 = 11.3$ eV, three emitters are observed. The spectrum is dominated by the $\text{CH } A^2\Delta - X^2\Pi$ emission at 426 nm. $\text{CH } B^2\Sigma^- - X^2\Pi$ is also observed at 388 nm. The broad band peaking at *ca.* 570 nm is assigned as either $\text{CHCl } \tilde{A}^1A'' - \tilde{X}^1A'$ or $\text{CCl}_2 \tilde{A}^1B_1 - \tilde{X}^1A_1$. For an excitation energy of 12.0 eV, an extra band is observed with a peak at 278 nm. This emission results from $\text{CCl } A^2\Delta - X^2\Pi$. The relative intensity of the CHCl or CCl_2 band at this photon energy is greatly reduced. For an excitation energy of 13.2 eV, this emission band disappears completely. For $E_1 = 16.4$ eV, five bands are observed with peaks at 255, 278, 388, 426 and 483 nm. The emissions at 255 and 483 nm result from $\text{Cl}_2 D' 2^3\Pi_g - A' 2^3\Pi_u$ and $\text{CH}_2\text{Cl}_2^+ \tilde{D}^2B_2 - \tilde{C}^2A_1$, respectively. For $E_1 = 19.6$ eV, the emission assigned to $\text{CCl } A^2\Delta - X^2\Pi$ disappears and a new band appears centred at 315 nm. This has been assigned to the $\text{CH } C^2\Sigma^+ - X^2\Pi$ transition.

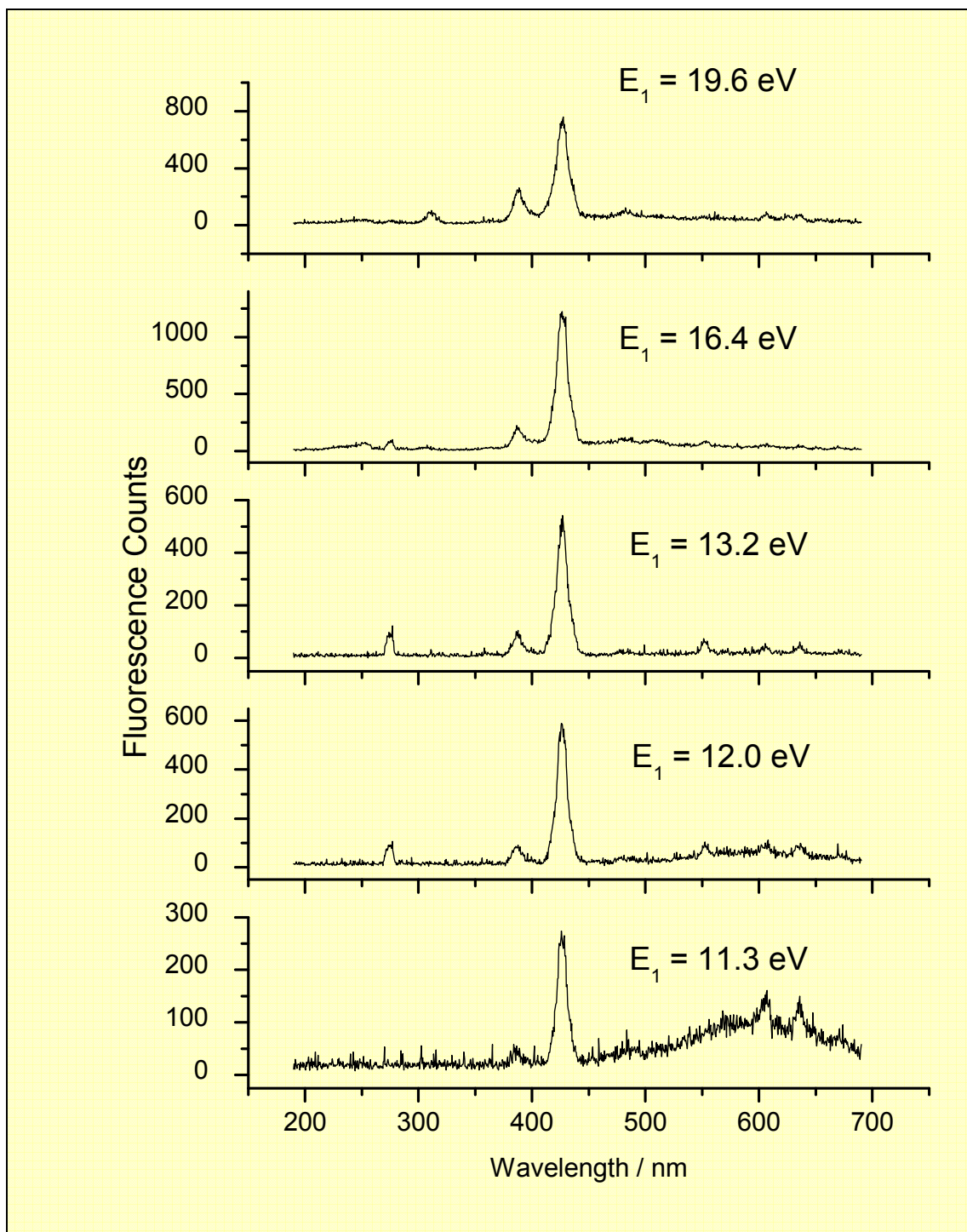


Figure 3.10 Dispersed fluorescence spectra of CH_2Cl_2 . The spectral resolution employed for the dispersing spectrometer was 8 nm.

3.4.2.3 The Action Spectroscopy of CH_2Cl_2 .

Action spectra were recorded from 9 – 22 eV for λ_2 values of 255, 278, 315, 389, 429, 483 and 583 nm. This corresponds to the isolation of the $\text{Cl}_2 \text{D}' 2^3\Pi_g - \text{A}' 2^3\Pi_u$, $\text{CCl A } 2^2\Delta - \text{X } 2^2\Pi$, $\text{CH C } 2^2\Sigma^+ - \text{X } 2^2\Pi$, $\text{CH B } 2^2\Sigma^- - \text{X } 2^2\Pi$, $\text{CH A } 2^2\Delta - \text{X } 2^2\Pi$, $\text{CH}_2\text{Cl}_2^+ \tilde{\text{D}} 2^2\text{B}_2 - \tilde{\text{C}} 2^2\text{A}_1$, and $\text{CHCl } \tilde{\text{A}} 1^1\text{A}'' - \tilde{\text{X}} 1^1\text{A}'$ or $\text{CCl}_2 \tilde{\text{A}} 1^1\text{B}_1 - \tilde{\text{X}} 1^1\text{A}_1$ bands, respectively. These spectra are shown in Figs. 3.11 and 3.12. All action spectra appear to be consistent with the dispersed emission spectra. Furthermore, all action spectra seem to have

successfully isolated specific emissions. However, one exception to the last statement is the action spectrum for $\lambda_2 = 583$ nm. This spectrum includes both emissions from $\text{CHCl } \tilde{A}^1A'' - \tilde{X}^1A'$ or $\text{CCl}_2 \tilde{A}^1B_1 - \tilde{X}^1A_1$ and from the parent ion, $\text{CH}_2\text{Cl}_2^+ \tilde{D}^2B_2 - \tilde{C}^2A_1$. Fortunately, there appears to be little or no convolution of the peaks, and the early onset of $\text{CHCl } \tilde{A}^1A'' - \tilde{X}^1A'$ or $\text{CCl}_2 \tilde{A}^1B_1 - \tilde{X}^1A_1$ allows an easy extraction of the appearance potential.

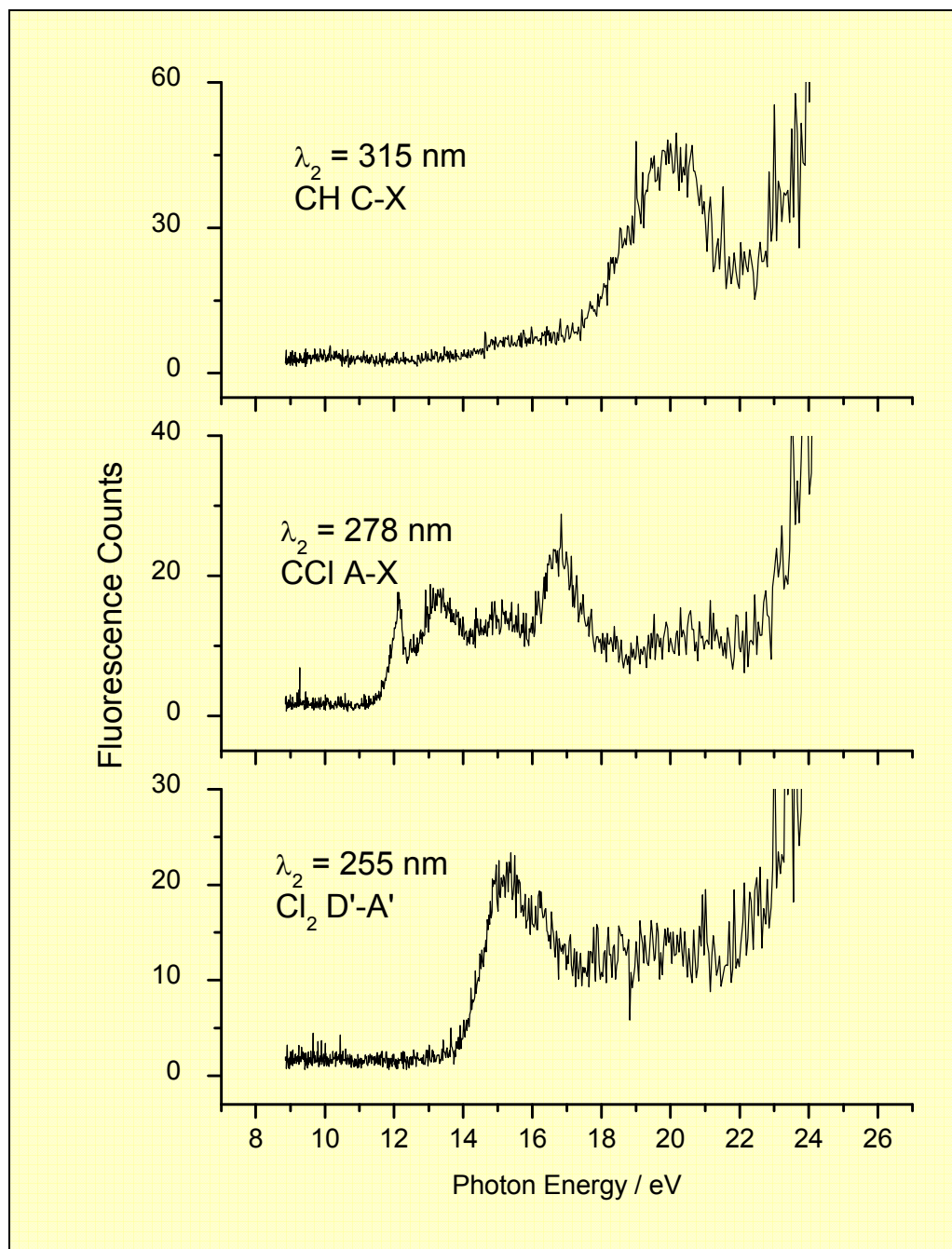


Figure 3.11 Action spectra of CH_2Cl_2 . The spectral resolution employed for the excitation vacuum-UV photon source, E_1 , was 0.3 nm.

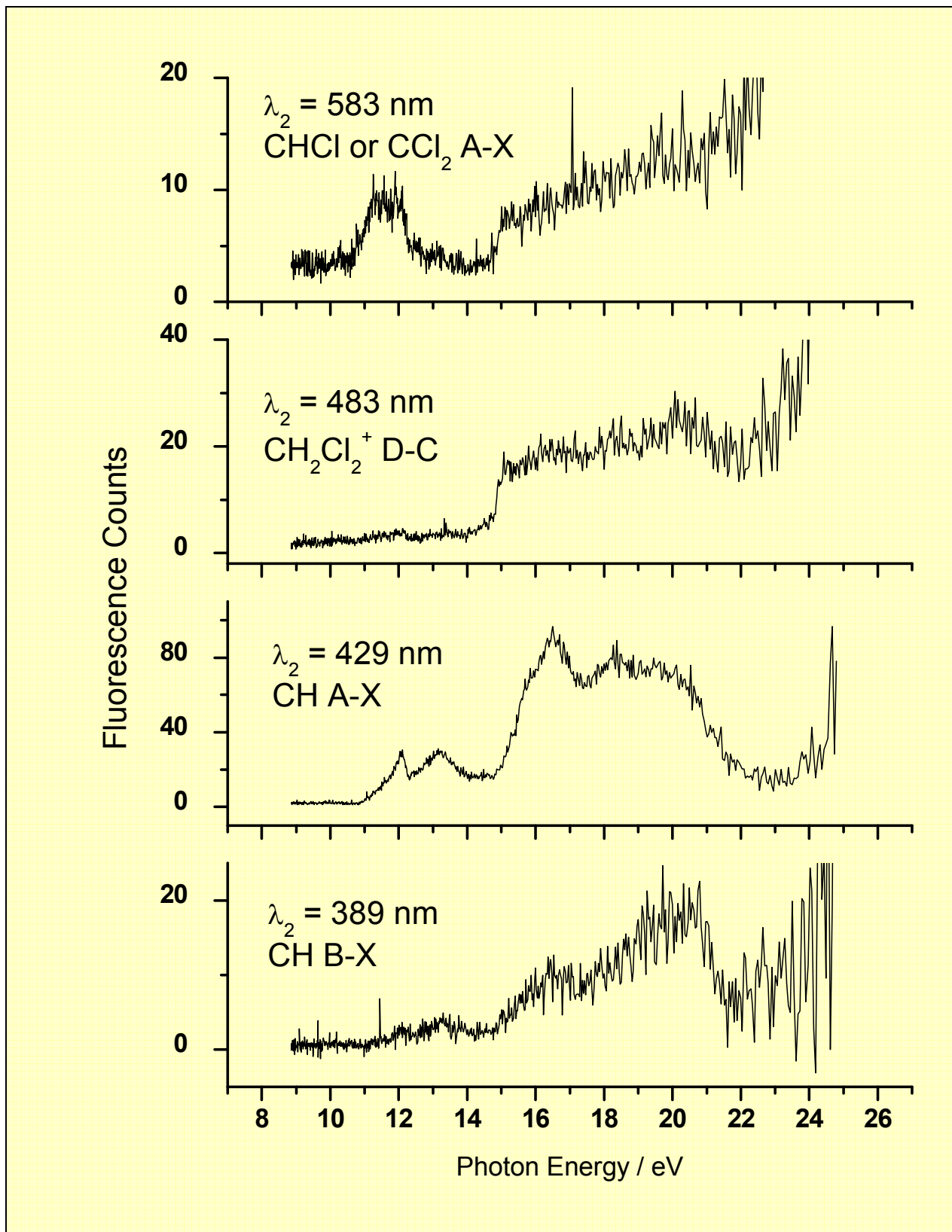


Figure 3.12 Action spectra of CH_2Cl_2 . The spectral resolution employed for the excitation vacuum-UV photon source, E_1 , was 0.3 nm.

Table 3.6 Summary of the emission bands observed following photoexcitation of CH_2Cl_2 .

Emitter	Appearance Potential / eV	E ₁ range / eV	λ ₂ range / nm	Assignment
Cl ₂ D' 2 ³ Π _g	13.5 ± 0.2	>13.5	245-260	Cl ₂ D' 2 ³ Π _g – A' 2 ³ Π _u
CCl A ² Δ	11.2 ± 0.2	>11.2	268-280	CCl A ² Δ – X ² Π
CH C ² Σ ⁺	17.2 ± 0.4	>17.2	300-325	CH C ² Σ ⁺ – X ² Π
CH B ² Σ ⁻	11.1 ± 0.2	>11.1	375-400	CH B ² Σ ⁻ – X ² Π
CH A ² Δ	10.9 ± 0.1	>10.9	410-440	CH A ² Δ – X ² Π
CH ₂ Cl ₂ ⁺ \tilde{D} ² B ₂	14.4 ± 0.2	>14.4	469-495	CH ₂ Cl ₂ ⁺ \tilde{D} ² B ₂ – \tilde{C} ² A ₁
CHCl \tilde{A} ¹ A'' or CCl ₂ \tilde{A} ¹ B ₁	10.4 ± 0.1	>10.4	500-690	CHCl \tilde{A} ¹ A'' – \tilde{X} ¹ A' or CCl ₂ \tilde{A} ¹ B ₁ – \tilde{X} ¹ A ₁

3.4.2.4 Lifetime measurements of CH₂Cl₂.

Using single bunch mode, the fluorescence lifetimes of some of the emitting states following VUV photoexcitation of CH₂Cl₂ have been measured. The results are given in Table 3.7. Several emitters have been measured here. The value measured for the A²Δ state of CCl from its A–X emission spectrum, 56 ns, compares reasonably well to the values obtained from selective photoexcitation of CCl₃F, CCl₃H and CCl₃Br (39, 55 and 42 ns, respectively).¹² Note that all these values are substantially lower than the accepted value for the v'=0 level of 105 ns.²⁵ Larsson *et al.*,²⁶ however, have shown that the lifetimes of the v'=1 and v'=2 levels are substantially lower (17 and 86 ns) due to predissociation of the A²Δ state. We conclude that photodissociation of CH₂Cl₂ at 13.2 eV must produce a different distribution of CCl A²Δ (v') vibrational levels from that of VUV photoexcitation of CCl₃X. The value for the Cl₂ D' 2³Π_g state, 9.2 ns, is in good agreement with that determined from CCl₃H and CCl₃Br (11.2 and 11.6 ns).¹² A fluorescence lifetime of 9.7 ns was measured for the C²Σ⁺ state of CH from its C–X emission band. This is in reasonable agreement with the accepted range of 10 – 24 ns for v'=0.¹⁷ The literature value for v'=1 is even smaller, so it seems probable that there is a distribution of vibrational levels produced in our experiment. This is the first observation of parent ion emission in CH₂Cl₂ and the determination of the lifetime of the \tilde{D} ²B₂ state of CH₂Cl₂⁺, 6.2 ns. This value is comparable with that determined by earlier experiments of the Tuckett group for the lifetime of the fluorescing \tilde{D} ²A₁ and \tilde{C} ²T₂ states of CF₄⁺.²⁷

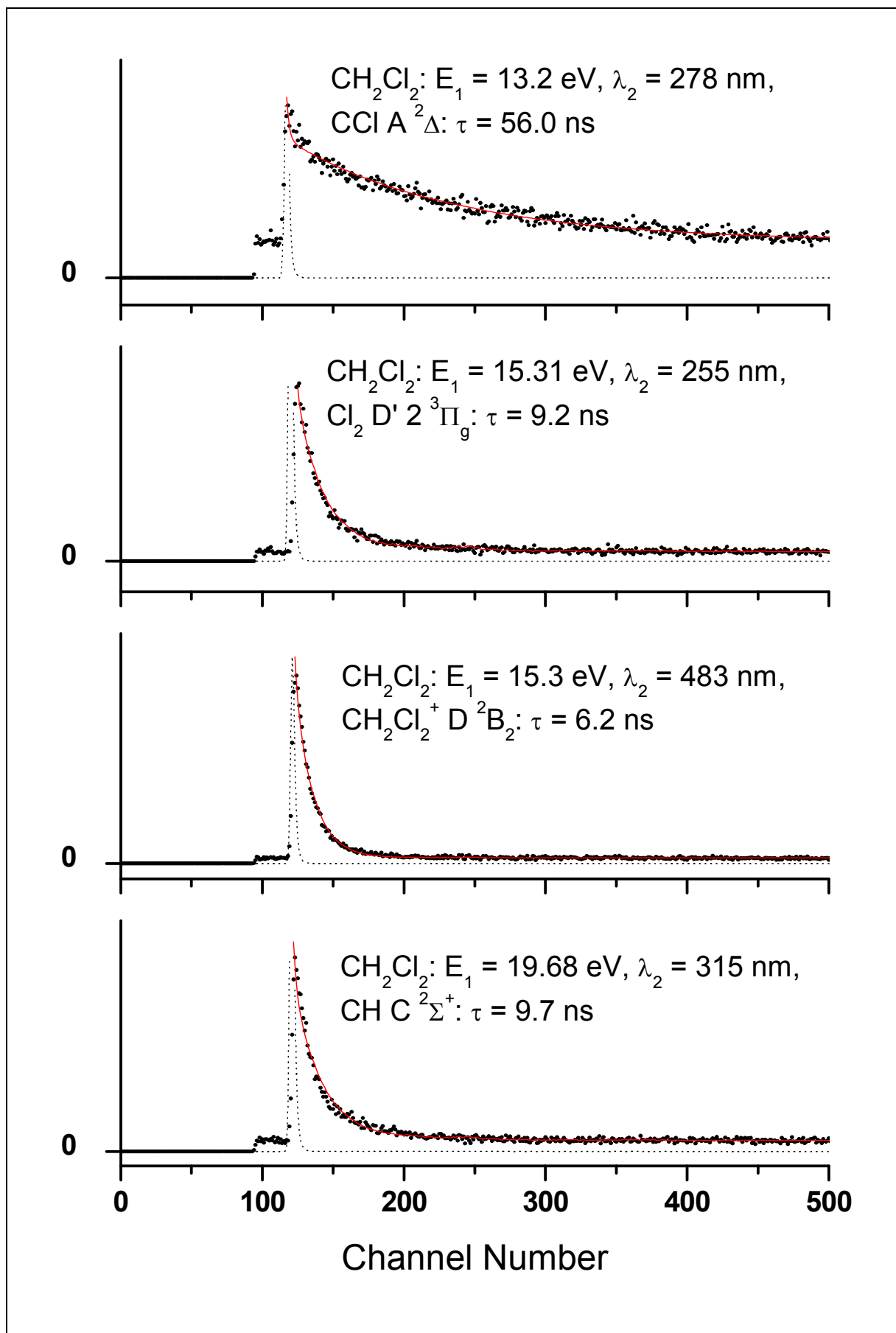


Figure 3.13 Time-resolved fluorescence spectra of CH₂Cl₂. Each spectrum shows the experimental data points (black dots), the prompt signal (black dashed line), and the fit to the data (red solid line). The time resolution is 0.480 ns per channel. The proposed emitters and the fitted lifetimes are shown.

Table 3.7 Lifetimes of fragments produced following the (pre-) dissociation of CH_2Cl_2 .

E_1 / eV	λ_2 / nm	Emitter	Lifetime / ns
13.2	278	$\text{CCl A } ^2\Delta$	56.0
15.3	255	$\text{Cl}_2 \text{ D}' 2 ^3\Pi_g$	9.2
15.3	483	$\text{CH}_2\text{Cl}_2^+ \tilde{\text{D}} ^2\text{B}_2$	6.2
19.7	315	$\text{CH C } ^2\Sigma^+$	9.7

3.4.3 CBr_2Cl_2

3.4.3.1 The Fluorescence Excitation and Absorption Spectroscopy of CBr_2Cl_2 .

The fluorescence excitation spectrum of CBr_2Cl_2 was recorded with an optical resolution of 0.3 nm in the energy range *ca.* 9-22 eV and is shown in Fig. 3.14. All peaks have shapes characteristic of a resonant primary excitation process, indicating that the fluorescence from excited states of the parent ion is very weak or non-existent.

The absorption spectrum of CBr_2Cl_2 was recorded with an optical resolution of 0.08 nm and is also shown in Fig. 3.14. It was not possible to assign any of the peaks of this spectrum due to the high density of ionic states of CBr_2Cl_2 in the range 10.6-12.9 eV (Table 3.1). Therefore, identification of the ionisation potentials to which the Rydberg states converge is difficult. By contrast with the other two molecules in this Chapter, comparison of the fluorescence excitation and absorption spectra of CBr_2Cl_2 does produce some similarities. The first bands in both spectra appear similar although the band in the fluorescence excitation spectrum is shifted to higher energy. Also, the band centered at *ca.* 15 eV appears to be the same band centred at 13 eV in the absorption spectrum.

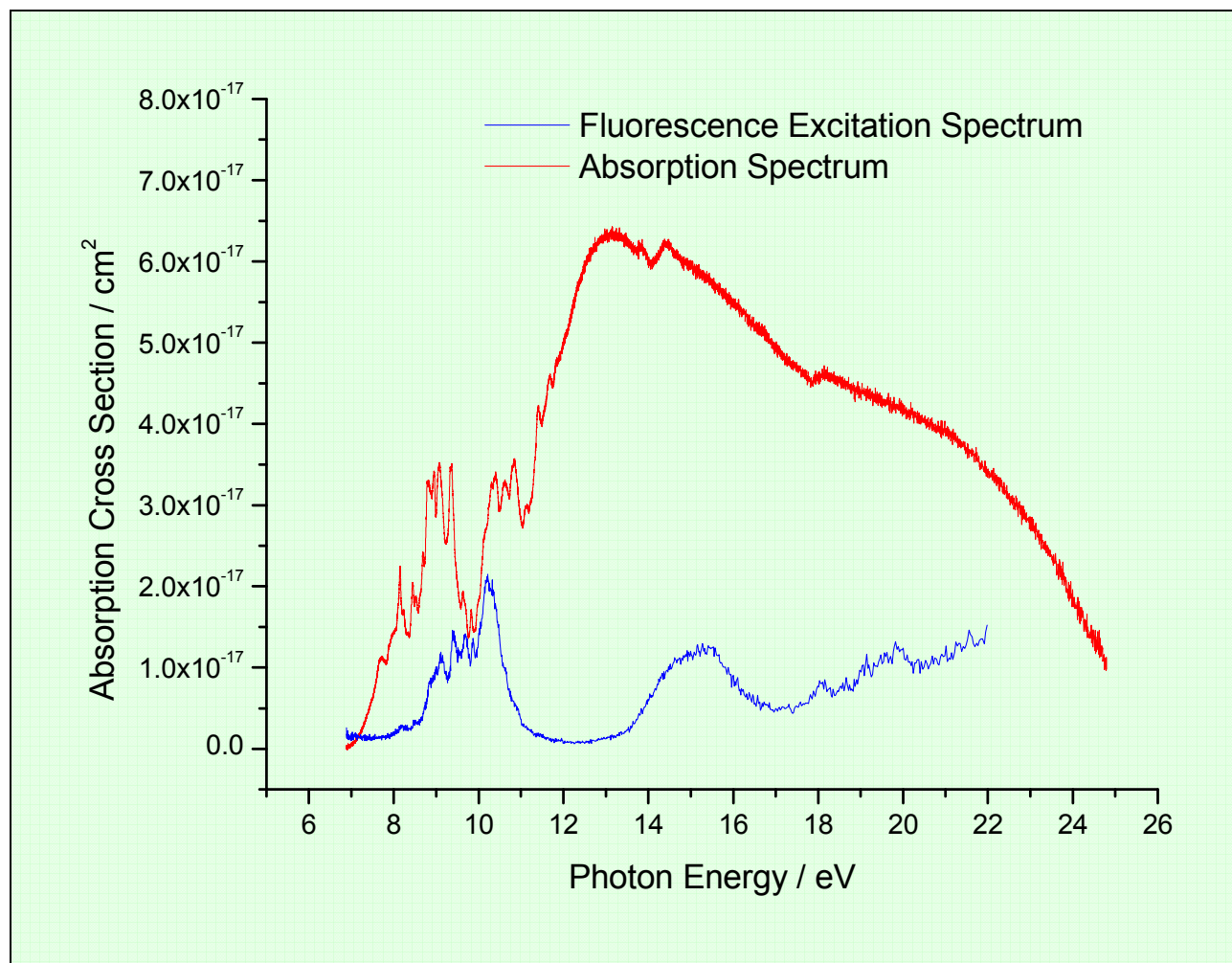


Figure 3.14 The fluorescence excitation and absorption spectra of CBr_2Cl_2 . Spectral resolutions of 0.3 and 0.08 nm were employed for the fluorescence excitation and absorption spectra respectively. The absorption cross-sections shown are absolute, whereas the fluorescence signal is arbitrary and has been scaled for optimum comparison with the absorption spectrum.

3.4.3.2 The Dispersed Fluorescence Spectroscopy of CBr_2Cl_2 .

The dispersed fluorescence spectra shown in Fig. 3.15 were recorded at excitation energies of 9.1, 10.2, 15.0 and 19.8 eV over the range 190-690 nm. For $E_1 = 9.1$ and 10.2 eV only one emitter is observed. This broad band peaking at 470 nm is assigned to $\text{CCl}_2 \tilde{A}^1\text{B}_1 - \tilde{X}^1\text{A}_1$ emission. For $E_1 = 15.0$ eV several emitters are observed. The strong peak at 278 nm is assigned to the $\text{CCl A}^2\Delta - \text{X}^2\Pi$ transition. The peak at *ca.* 560 nm is probably the $\text{CCl A}^2\Delta - \text{X}^2\Pi$ transition in second order. Three further emissions are observed at 290, 310 and 355 nm. The peak at 310 nm is attributed to $\text{CBr A}^2\Delta - \text{X}^2\Pi$ emission whilst the peaks observed at 290 and 355 nm are assigned to transitions in Br_2 . The 290 nm peak is almost certainly due to $\text{D}' 2^3\Pi_g - \text{A}' 2^3\Pi_u$. For an excitation energy of 19.8 eV the same emitters are present, with the exception of the $\text{CCl A}^2\Delta - \text{X}^2\Pi$ transition.

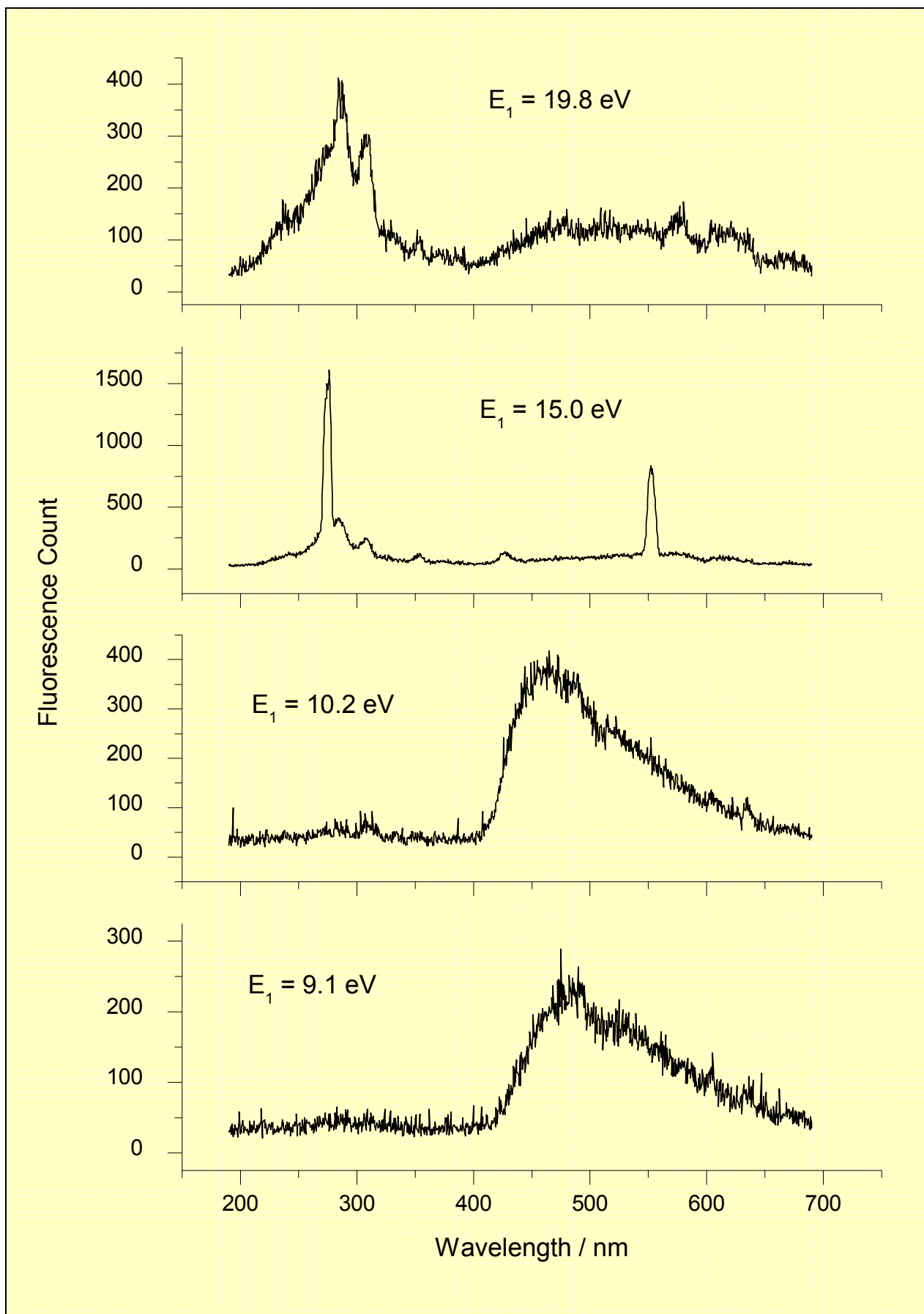


Figure 3.15 Dispersed fluorescence spectra of CBr_2Cl_2 at defined values of the excitation energy, E_1 . The spectral resolution employed for the dispersing spectrometer was 8 nm.

3.4.3.3 The Action Spectroscopy of CBr₂Cl₂.

Action spectra were recorded from 9 – 22 eV for λ_2 values of 278, 291, 310, 356 and 491 nm and are shown in Figs. 3.16 and 3.17. This corresponds to the isolation of the CCl A ² Δ – X ² Π , Br₂ D' 2 ³ Π_g – A' 2 ³ Π_u , CBr A ² Δ – X ² Π , Br₂ D' 2 ³ Π_g – ? and CCl₂ \tilde{A} ¹B₁ – \tilde{X} ¹A₁ bands, respectively. These spectra are shown in figs. 3.14 and 3.15. The spectra recorded for $\lambda_2 = 291, 310$ and 356 nm appear very similar. This is because the emission wavelengths of CBr and Br₂ are very close and cannot be isolated with the secondary monochromator, which has a resolution of 8 nm. The spectra are dominated by Br₂^{*} emission (see section 3.5). A summary of the range of excitation energies, emission wavelengths and appearance potentials for the fluorescence observed following VUV photoexcitation of CBr₂Cl₂ is presented in Table 3.8.

Table 3.8 Summary of the emission bands observed following photoexcitation of CBr₂Cl₂.

Emitter	Appearance Potential / eV	E ₁ range / eV	λ_2 range / nm	Assignment
Br ₂ D' 2 ³ Π_g	13.0 ± 0.2	>13.0	240-290	Br ₂ D' 2 ³ Π_g – A' 2 ³ Π_u
CCl A ² Δ	12.7 ± 0.2	12.7-17.0	268-280	CCl A ² Δ – X ² Π
CBr A ² Δ	>13.0 ± 0.2	>13.0	300-320	CBr A ² Δ – X ² Π
Br ₂ D' 2 ³ Π_g	13.0 ± 0.2	>13.0	340-360	Br ₂ D' 2 ³ Π_g – ?
CCl ₂ \tilde{A} ¹ B ₁	8.6 ± 0.2	8.6-11.0	410-650	CCl ₂ \tilde{A} ¹ B ₁ – \tilde{X} ¹ A ₁

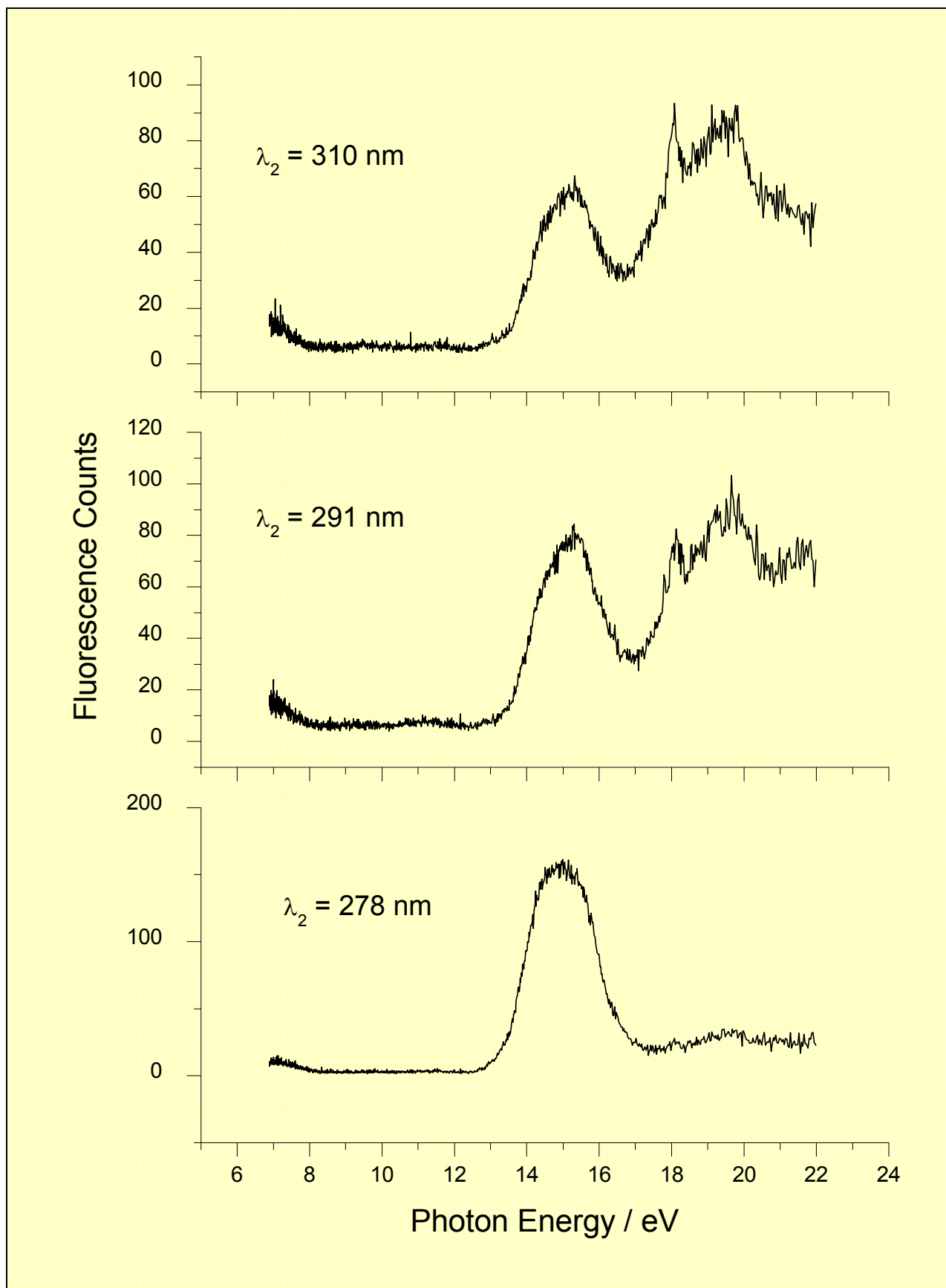


Figure 3.16 Action spectra of CBr_2Cl_2 . The spectral resolution employed for the excitation vacuum-UV photon source, E_1 , was 0.3 nm.

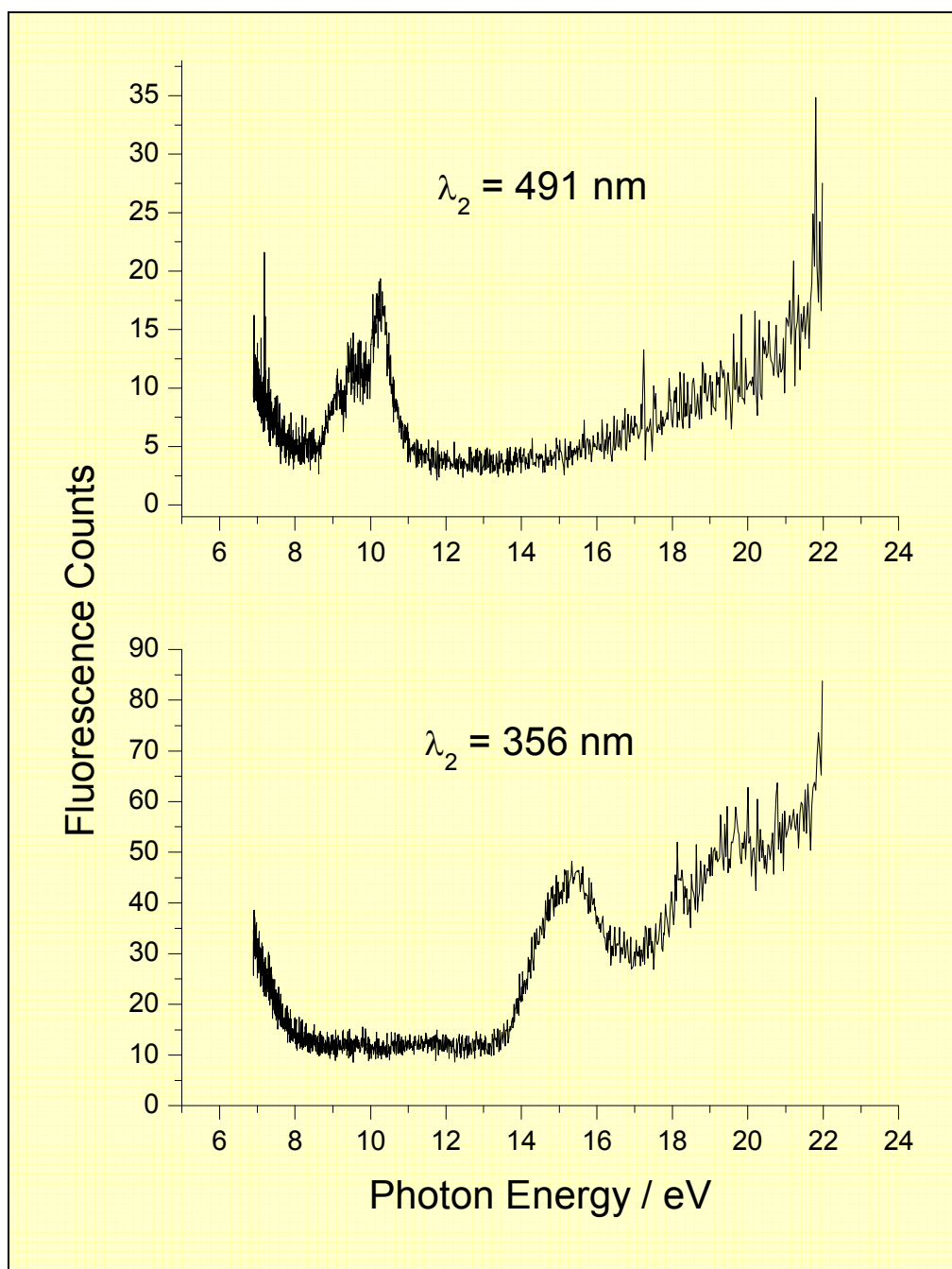


Figure 3.17 Action spectra of CBr_2Cl_2 . The spectral resolution employed for the excitation vacuum-UV photon source, E_1 , was 0.3 nm.

3.4.3.4 Lifetime measurements of CBr_2Cl_2 .

Using single bunch mode, the fluorescence lifetimes of some of the emitting states following VUV photoexcitation of CBr_2Cl_2 have been measured. The results are given in Table 3.9. Several emitters have been measured here. The values for CBr (14.9 ns for $E_1 = 15.0$ eV and 14.6 ns for $E_1 = 19.8$ eV) agree very well with the same measurement made for CH_2Br_2 (14.4 ns). It also agrees well with the value of 15.5 eV measured from CCl_3Br .¹² Two values have been measured for the Br_2 D' $2^3\Pi_g$ state. With an

excitation energy of 15.0 eV and a dispersed wavelength of 353 nm, the lifetime of Br_2^* has been found to be 25.3 ns. This agrees extremely well with the previous measurement by Seccombe et al.²⁴ in which CF_2Br_2 was the precursor to create the emitter (22.6 ns). This measured lifetime does not however, agree so well with the value measured for Br_2^* from CH_2Br_2 in section 3.4.1.4 when dispersing at $\lambda_2 = 289$ nm (11.8 ns). Furthermore, the lifetime measured for Br_2^* from CBr_2Cl_2 , $\lambda_2 = 286$ nm is 13.2 ns. This does compare well with the value measured in section 3.4.1.4. This would suggest that the emissions at $\lambda_2 = 353$ nm and 286 nm come from different upper states. This phenomenon remains unexplained.

Table 3.9 Lifetimes of fragments produced following the (pre-) dissociation of CBr_2Cl_2 .

E_1 / eV	λ_2 / nm	Emitter	Lifetime / ns
15.0	278	$\text{CCl A } ^2\Delta$	9.2 and 63.5
15.0	308	$\text{CBr A } ^2\Delta$	14.9
15.0	353	$\text{Br}_2 \text{ D}' 2 \ ^3\Pi_g$	25.3
19.8	286	$\text{Br}_2 \text{ D}' 2 \ ^3\Pi_g$	13.2
19.8	308	$\text{CBr A } ^2\Delta$	14.6

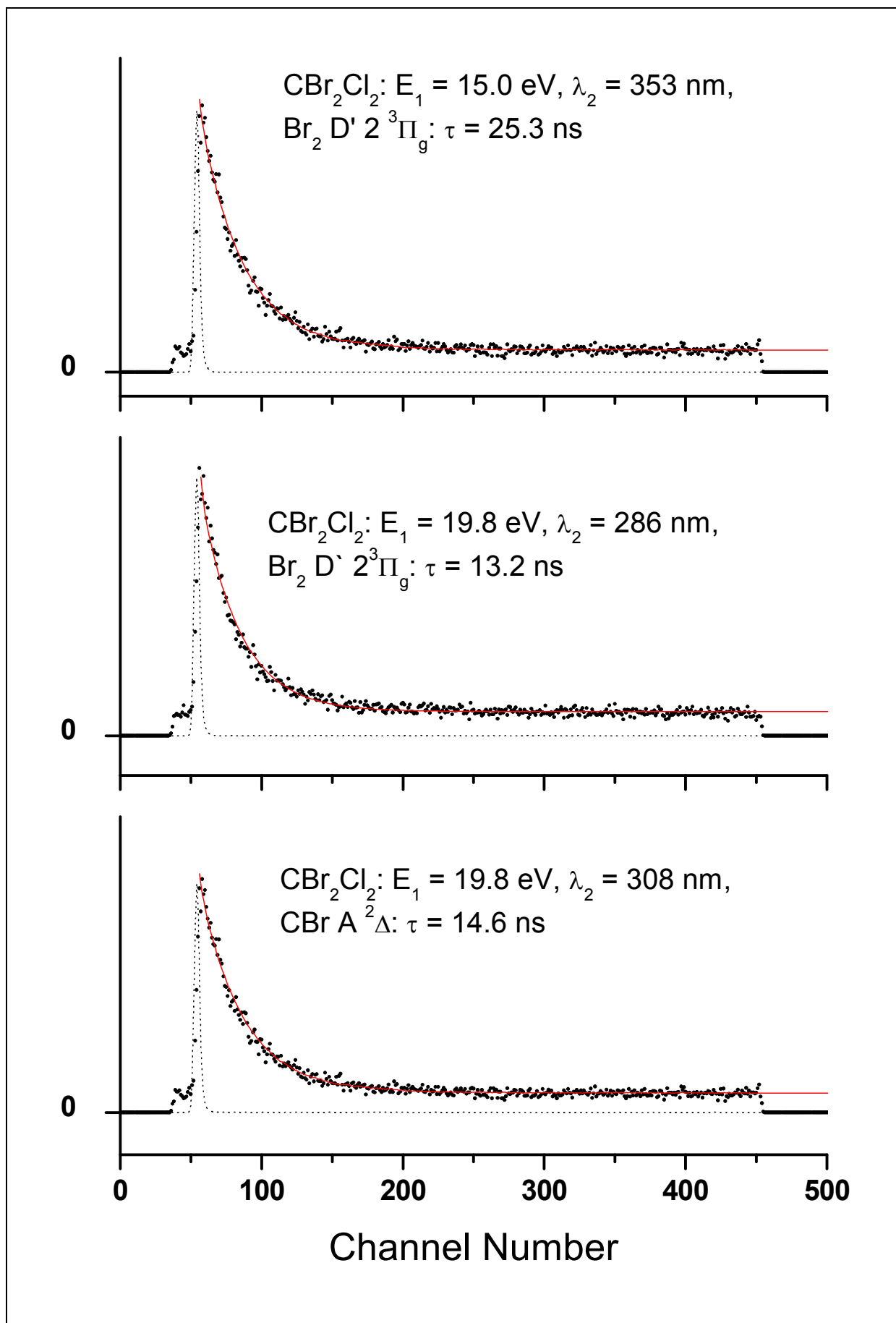


Figure 3.18 Time-resolved fluorescence spectra of CBr_2Cl_2 . Each spectrum shows the experimental data points (black dots), the prompt signal (black dashed line), and the fit to the data (red solid line). The time resolution is 0.481 ns per channel. The proposed emitters and the fitted lifetimes are shown.

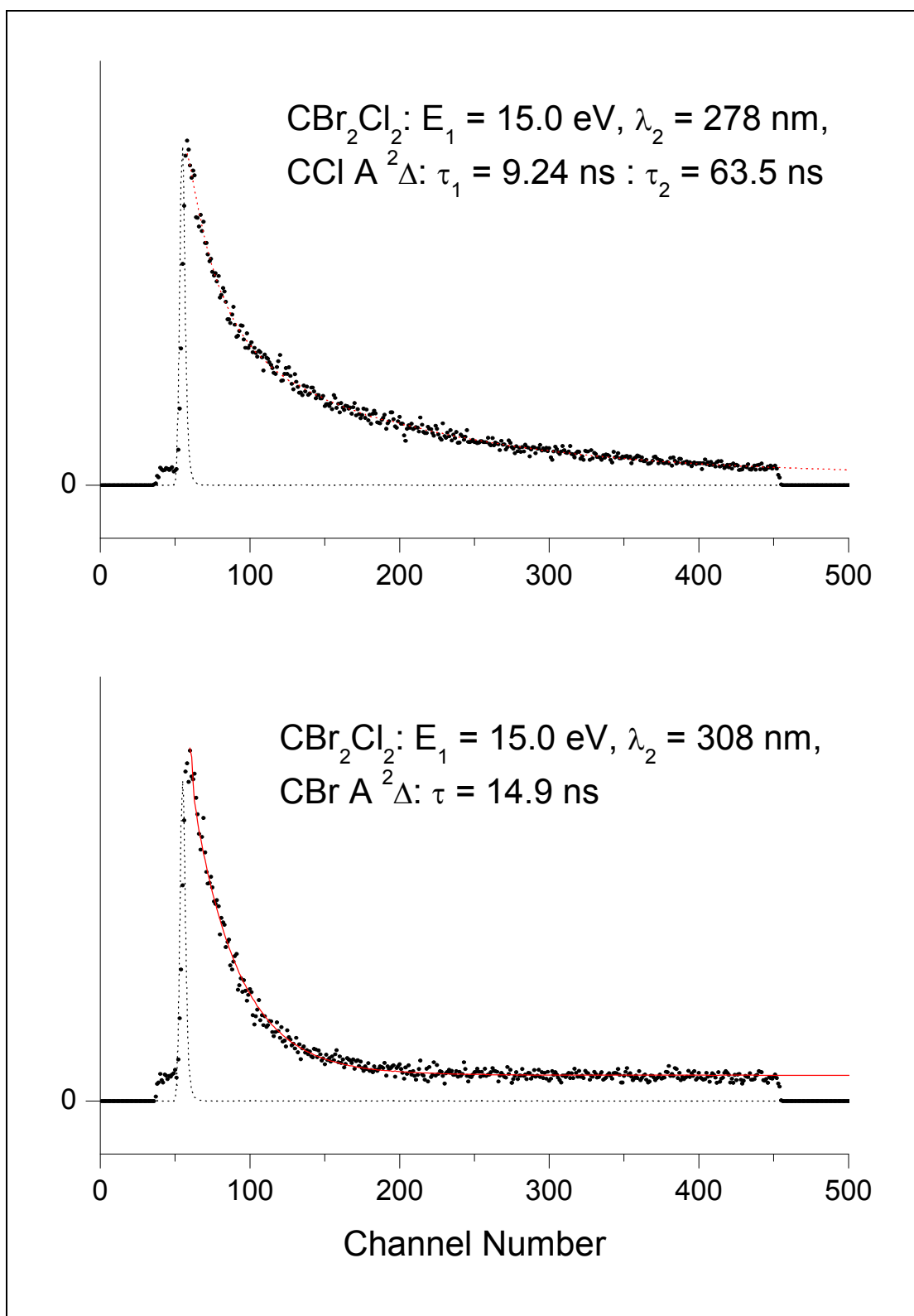


Figure 3.19 Time-resolved fluorescence spectra of CBr_2Cl_2 . Each spectrum shows the experimental data points (black dots), the prompt signal (black dashed line), and the fit to the data (red solid line). The time resolution is 0.481 ns per channel. The proposed emitters and the fitted lifetimes are shown.

3.5 Discussion : elucidation of the dominant dissociation channels.

The enthalpies of different dissociation channels which result in the formation of fluorescing fragments are given in Table 3.1. When more than one bond is broken to form the excited species, there always exists at least two possible pathways for the dissociation. The appearance potential can be extracted from the action spectrum recorded for a particular isolated emission. By comparing the appearance energy and the thermochemistry given in Table 3.1, it can sometimes be possible to determine the dominant dissociation channel.

3.5.1 $\text{CCl}_2 \tilde{A}^1\text{B}_1 - \tilde{X}^1\text{A}_1$

The appearance potential of the $\tilde{A}^1\text{B}_1$ state of CCl_2 from CBr_2Cl_2 is 8.6 eV. This value lies above two dissociation pathways that form with two bromine atoms and molecular bromine. Therefore assignment cannot be made unambiguously. For CH_2Cl_2 , the identification of the broad band emission in the dispersed fluorescence spectrum measured at an excitation energy of 11.3 eV is unclear ; it could be due to either $\text{CCl}_2 \tilde{A}^1\text{B}_1 - \tilde{X}^1\text{A}_1$ or $\text{CHCl} \tilde{A}^1\text{A}'' - \tilde{X}^1\text{A}'$. The appearance potential of this fragment is 10.4 eV. If this emission is $\text{CCl}_2 \tilde{A}^1\text{B}_1 - \tilde{X}^1\text{A}_1$, then this appearance potential would suggest that CCl_2^* forms with two hydrogen atoms although formation of molecular hydrogen cannot be ruled out as this thermochemical threshold is surpassed also (see Table 3.1). This seems likely as energetically this appearance potential is very close to the thermochemical threshold (10.0 eV).

3.5.2 $\text{CCl} \text{A}^2\Delta - \text{X}^2\Pi$

The appearance potentials for the formation of the $\text{A}^2\Delta$ state of CCl are 11.2 and 12.7 eV from CH_2Cl_2 and CBr_2Cl_2 , respectively. Considering first CH_2Cl_2 , the appearance potential is close to that of the dissociation channels forming $\text{H}_2 + \text{Cl}$ (11.77 eV) and $\text{HCl} + \text{H}$ (11.82 eV), but significantly lower than that of $2\text{H} + \text{Cl}$ (16.25 eV). It seems likely, therefore, that CCl^* forms with a diatomic molecule and atom as neutral products. Considering CBr_2Cl_2 , in principle three dissociation channels are possible. However, the appearance energy is below the highest-energy pathway to form CCl with atomic products, and therefore this channel is closed. The appearance energy is higher than the two lower energy pathways. However, it is not possible to elucidate the dominant channel as the two channels are very similar in energy (10.76 and 10.97 eV).

3.5.3 $\text{CBr} \text{A}^2\Delta - \text{X}^2\Pi$

$\text{CBr} \text{A}^2\Delta - \text{X}^2\Pi$ emission is produced with both CH_2Br_2 and CBr_2Cl_2 . The appearance potential of the $\text{A}^2\Delta$ state of CBr from CH_2Br_2 is 11.0 eV (Table 3.3). The dissociation can be assigned unambiguously to formation with $\text{H}_2 + \text{Br}$, which is the lowest-energy pathway. The appearance potential lies above this pathway, but below the dissociation channel to form $\text{HBr} + \text{H}$. Dissociation to $\text{Br} + 2\text{H}$ lies even higher,

and is therefore also energetically closed. For CBr_2Cl_2 , an appearance potential could not be extracted due to the secondary monochromator not being able to isolate CBr^* from Br_2^* signal (see section 3.5.5); CBr^* signal is obscured by strong Br_2^* emission with an appearance potential of 13.0 ± 0.2 eV. However, there is no evidence of CBr signal before this onset and therefore an appearance potential of > 13.0 eV can be assumed. This value is higher than the highest-energy pathway and therefore allows the possibility of fragmentation *via* all three pathways. However, by analogy with previous work on the CCl_3X and CF_2X_2 series of molecules,^{12,23} it is most likely that the diatomic fluorescing fragment, in this case $\text{CBr}^* \text{A}^2\Delta$, forms with three atoms *via* the highest-energy channel.

The behaviour of these two fragmentations appears to show some similar characteristics to the behaviour of $\text{CF}_2 \tilde{\text{A}}^1\text{B}_1$ formation from photodissociation of CF_2X_2 ($\text{X} = \text{H}, \text{Cl}$ and Br).²³ The appearance potentials of the two sterically-hindered molecules, CF_2Cl_2 and CF_2Br_2 , were in close agreement to the thermodynamic energies of the higher-energy dissociation channels in which atoms were formed. It was deduced that the anomalous behaviour of CF_2H_2 , in which the lowest-energy process ($\text{CF}_2^* + \text{H}_2$) was the only possible channel, related to the structure of the transition state. In order for X_2 to be produced, the dissociation must proceed *via* a tightly-constrained transition state so that the X-X bond is formed whilst the C-X bonds break. Such a structure would be sensitive to steric constraints. Hence the process is observed for CF_2H_2 where the relatively light H_2 molecule is produced but not for CF_2Cl_2 and CF_2Br_2 where the bulky Cl_2 and Br_2 molecules have to be produced. It seems that this type of phenomenon is being observed for CH_2Br_2 and CBr_2Cl_2 .

3.5.4 $\text{Cl}_2 \text{D}' 2^3\Pi_g - \text{A}' 2^3\Pi_u$ from CBr_2Cl_2 and CH_2Cl_2

The absence of $\text{Cl}_2 \text{D}'-\text{A}'$ emission centred at 255 nm in the dispersed fluorescence spectra of CBr_2Cl_2 is noted. However, it is not clear if its absence in the spectra is due to an absence of emission. It is possible that the feature may be obscured by $\text{Br}_2 \text{D}'-\text{A}'$ and $\text{CCl} \text{A}-\text{X}$ fluorescence at 290 and 278 nm. $\text{Cl}_2 \text{D}'-\text{A}'$ emission is observed from CH_2Cl_2 with an appearance potential of 13.5 eV. Four different dissociation channels are possible with various combinations of atomic and molecular products. It is clear from the thermochemistry shown in Table 3.1 that $\text{Cl}_2 \text{D}' 2^3\Pi_g$ must form with CH_2 . The thermochemical threshold of this channel is 12.02, *ca.* 1.5 eV below the appearance potential. The next highest threshold is at 15.39 eV, forming with C and H_2 , which lies above the appearance potential. This channel is therefore closed. The other two channels lie at even higher energy.

3.5.5 $\text{Br}_2 \text{D}' 2^3\Pi_g$ from CBr_2Cl_2 and CH_2Br_2

Br_2 emission is observed in both bromine-containing molecules. For CBr_2Cl_2 , problems arise due to the resolving power of the secondary monochromator. The three action spectra at 278, 291 and 310 nm are close enough in wavelength that there is not complete isolation of the fluorescing species. Closer

inspection of the spectrum at 278 nm yields a different onset from the spectra at 291 and 310 nm, as well as the first peak differing in shape. Therefore the spectrum at 278 nm is due to a different emitter from those observed in the action spectra of 291 and 310 nm, and is assigned to CCl A – X. The action spectra for $\lambda_2 = 291$ and 310 nm are very similar in appearance, and at first glance it is not clear whether the signal is due to Br₂, CBr or both species. However, the action spectrum for $\lambda_2 = 356$ nm (assigned as emission from the D' 2³Π_g state of Br₂) also looks very similar. With the secondary monochromator set to 356 nm, resolution issues do not arise and isolation of the emission is complete. Therefore it seems probable that both spectra for $\lambda_2 = 291$ and 310 nm are due to Br₂ D' 2³Π_g emission. CBr signal is probably too weak to be observed on top of the Br₂ emission. All three spectra ($\lambda_2 = 291, 310$ and 356 nm) have an onset of 13.0 ± 0.2 eV. The lowest thermochemical threshold forms Br₂^{*} + CCl₂ (8.44 eV). The next highest dissociation energy is at 12.38 eV with the products CCl + Cl. The emission is tentatively assigned to this channel, as the appearance potential lies below the next highest-energy threshold at 13.35 eV (with C + Cl₂).

No resolution problems with the secondary monochromator occur with CH₂Br₂ as the parent molecule. Br₂^{*} emission has an appearance potential of 11.5 eV. This value is higher than the lowest-energy thermochemical threshold to form CH₂ as the other product (10.07 eV), but lower than the next highest threshold (13.44 eV) to form C + H₂. Therefore the dissociation pathway for production of this emitter is identified as the lowest-energy channel. The arguments used in the previous section, that atomic neutrals are most likely to form with sterically-constrained CBr₂Cl₂ and molecular neutrals are more likely to form from the less sterically-constrained CH₂Br₂, are also valid here.

3.5.6 CH C²Σ⁺ – X²Π, B²Σ⁻ – X²Π and A²Δ – X²Π from CH₂Cl₂ and CH₂Br₂

CH C–X emission is only observed from CH₂Cl₂ with an appearance energy of 17.2 eV. All three possible dissociation channels (H + 2Cl, HCl + Cl, Cl₂ + H) are open. It seems likely that dissociation occurs *via* the highest-energy pathway with atomic products. CH B–X emission is observed in both CH₂Cl₂ and CH₂Br₂, although for the latter molecule an action spectrum was not possible to record due to a nitrogen impurity ; CH B–X and N₂⁺ B–X emissions both occur at very similar wavelengths, *ca.* 390 nm. For CH₂Cl₂, an appearance potential of 11.1 eV was measured. On comparison with the thermochemistry in Table 3.1, this can only correspond to the dissociation pathway that forms HCl + Cl (10.51 eV). CH A²Δ – X²Π in CH₂Cl₂ can also only form through the lowest-energy pathway ; with an appearance potential of 10.9 eV, the fluorescing emitter is produced with HCl + Cl. The next highest-energy pathway to Cl₂ + H at 12.15 eV is closed.

One might expect that CH A – X emission from CH₂Br₂ to behave similarly, but this is not the case. The appearance potential of CH A – X in CH₂Br₂ is 13.4 eV, which is just below the highest-energy pathway

to form atomic products. The nearest alternative channel is formed with $\text{H} + \text{Br}_2$ which has a thermochemical threshold of 11.23 eV. Although the appearance potential is below the highest-energy pathway, within experimental error this threshold is surpassed. Also, the appearance potential of the emitter is energetically a lot higher than the lower threshold (*ca.* 2.2 eV). The pathway is therefore probably assigned to be the highest-energy dissociation channel.

3.5.7 Parent ion emission in CH_2Cl_2 and CH_2Br_2

Parent ion emission is observed from both CH_2Cl_2 and CH_2Br_2 . Figs 3.20 and 3.21 show fluorescence excitation spectra recorded at the Daresbury Laboratory by Dominic Seccombe, a previous member of the Tuckett research group. This work has not yet been published elsewhere. Both spectra utilise an Oriel 500 filter that limits λ_2 detection wavelengths to $\lambda_2 > 500$ nm. These spectra (especially that of CH_2Cl_2) illustrate the non-resonant appearance of the emission spectra very well, and hence allows the definitive assignment of the emission as being due to the parent ion. Both emissions are assigned to the $\tilde{D} \ ^2\text{B}_2 - \tilde{C} \ ^2\text{A}_1$ transition in CH_2X_2^+ . Similar spectra were recorded at the BESSY1 synchrotron radiation source in Berlin, but the parent ion emission is not observed nearly so clearly. First, CH_2Br_2^+ emission was dispersed at 485 nm (Fig. 3.6). It is noted that the difference in vertical ionisation potentials of the \tilde{D} and \tilde{C} states for this molecule is 2.84 eV (437 nm), which is somewhat low in wavelength compared to 485 nm where the secondary monochromator was set to disperse. This difference may be attributed to Franck – Condon effects. The fluorescence excitation spectrum from Daresbury shows an appearance potential of 13.9 eV. Comparison with the ionisation potentials in Table 3.1 shows that this is in excellent agreement with the adiabatic ionisation energy of the $\tilde{D} \ ^2\text{B}_2$ state of CH_2Br_2^+ (13.8 eV). Second, for CH_2Cl_2 a similar behaviour is observed (Fig. 3.12). Again the difference in ionisation potentials of the \tilde{D} and \tilde{C} states is 3.08 eV (403 nm), which is somewhat low in wavelength compared to 483 nm where the emitter was dispersed. Again this may be attributed to Franck – Condon effects. The appearance potential of $\text{CH}_2\text{Cl}_2^+ \ \tilde{D} \ ^2\text{B}_2$ from the Daresbury fluorescence excitation spectrum (14.8 eV) is in excellent agreement with the adiabatic ionisation potential of $\text{CH}_2\text{Cl}_2^+ \ \tilde{D} \ ^2\text{B}_2$ (14.9 eV).

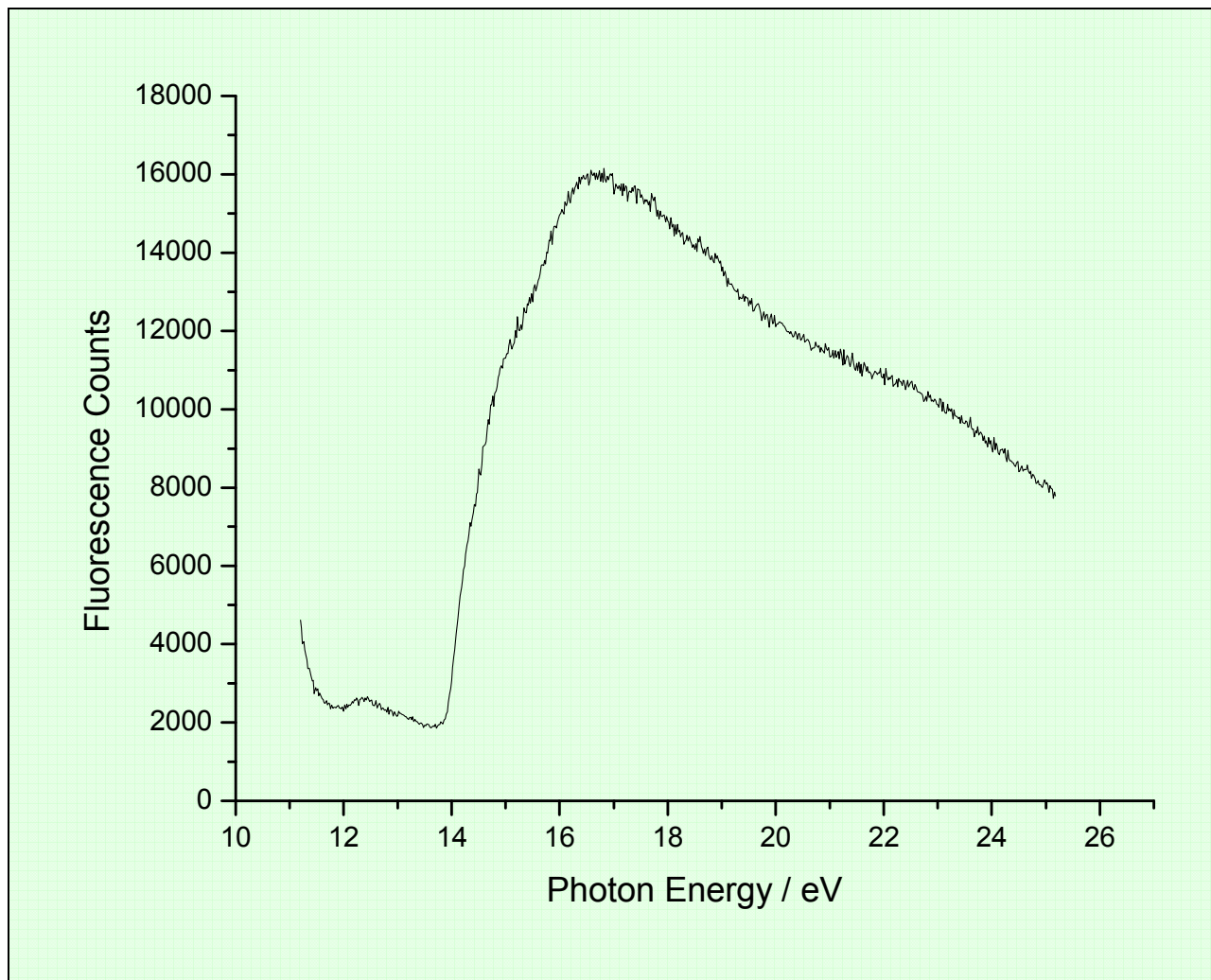


Figure 3.20 Fluorescence excitation spectrum of CH_2Br_2 measured at Daresbury Laboratory. The resolution employed was 0.1 nm. An Oriel 500 filter was used to confine the range of wavelengths to $\lambda_2 > 500$ nm.

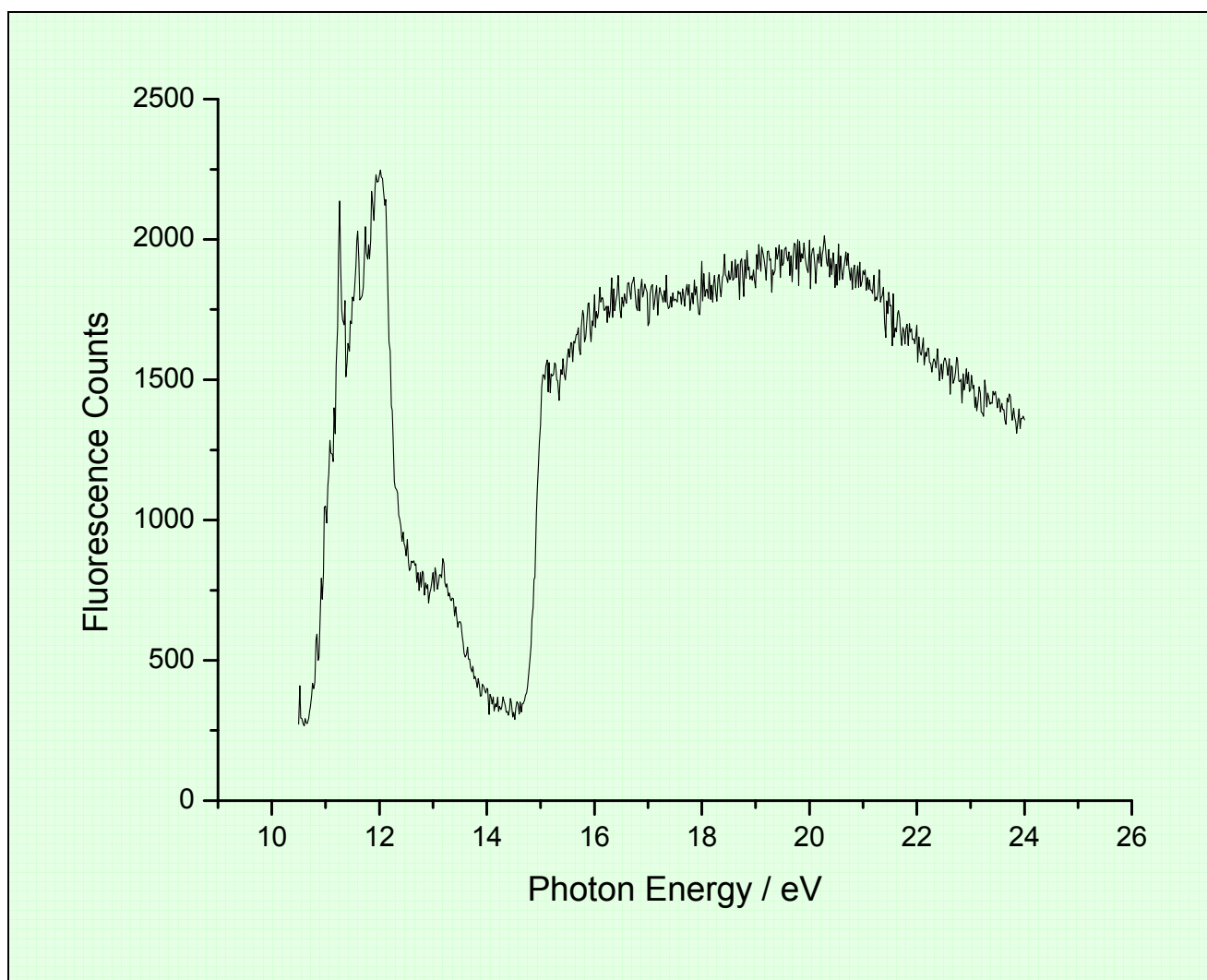


Figure 3.21 Fluorescence excitation spectrum of CH₂Cl₂ measured at Daresbury Laboratory. The resolution employed was 0.1 nm. An Oriel 500 filter was used to confine the range of wavelengths to $\lambda_2 > 500$ nm.

3.6 Conclusions

A comprehensive study of the VUV fluorescence spectroscopy of CX₂Y₂ (where X, Y = H, Cl or Br) has been presented. Like the CCl₃X (X = F, H and Br) and CF₂X₂ (X = H, Cl and Br) series,^{12,24} most emitters are assigned to transitions in neutral fragments formed by (pre-)dissociation of the Rydberg states of the parent molecule. Definitive emission from the parent ion of CH₂Br₂ and CH₂Cl₂ is observed for the first time. In fragmentations which require the fission of at least two bonds, CBr₂Cl₂ sometimes dissociates *via* the highest-energy, fission-only pathways which probably have very low or zero barriers. CH₂Br₂ and CH₂Cl₂, however, generally dissociate to some degree *via* lower pathways involving the production of molecular products *via* tightly-constrained transition states. This phenomenon is presumably a steric effect. There has also been some success in assigning the Rydberg states involved in the primary excitation process *via* the measurement of high-resolution absorption spectra. However, the spectrum of

CBr₂Cl₂ remains unassigned as no successful scheme was found based on the Rydberg formula. This is caused by the difficulty of identifying the ionisation potential to which the Rydberg states converge. The research described in this chapter is currently being prepared for publication.²⁸

3.7 References

1. J. C. Creasey, P. A. Hatherly, H. M. Jones, I. R. Lambert and R. P. Tuckett, *Mol. Phys.*, 1993, **78**, 837.
2. J. C. Creasey, P. A. Hatherly, I. R. Lambert and R. P. Tuckett, *Mol. Phys.*, 1993, **79**, 413.
3. H. Biehl, J. C. Creasey, D. M. Smith, R. P. Tuckett, K. R. Yoxall, H. Baumgärtel, H-W Jochims and U. Rockland, *J. Chem. Soc., Faraday Trans.*, 1995, **91**, 3073.
4. H. Biehl, D. M. Smith, R. P. Tuckett, K. R. Yoxall, H. Baumgärtel, H. W. Jochims and U. Rokland, *Mol. Phys.*, 1996, **87**, 119.
5. K. J. Boyle, D. P. Seccombe, R. P. Tuckett, H. Baumgärtel and H. W. Jochims, *J. Phys. B*, 1999, **32**, 2569.
6. H. Biehl, K. J. Boyle, D. P. Seccombe, R. P. Tuckett, H. Baumgärtel and H. W. Jochims, *J. Chem. Phys.*, 1998, **108**, 857.
7. K. J. Boyle, G. K. Jarvis, R. P. Tuckett, H. Baumgärtel and H. W. Jochims, *J. Chem. Soc., Faraday Trans.*, 1998, **94**, 2073.
8. H. Biehl, K. J. Boyle, D. P. Seccombe, D. M. Smith, R. P. Tuckett, H. Baumgärtel and H. W. Jochims, *J. Elec. Spec Rel. Phen.*, 1998, **97**, 89.
9. H. Biehl, K. J. Boyle, D. P. Seccombe, D. M. Smith, R. P. Tuckett, K. R. Yoxall, H. Baumgärtel and H. W. Jochims, *J. Chem. Phys.*, 1997, **107**, 720.
10. K. J. Boyle, D. P. Seccombe, R. P. Tuckett, H. Baumgärtel and H. W. Jochims, *Chem. Phys. Lett.*, 1998, **294** 507.
11. H. Biehl, K. J. Boyle, R. P. Tuckett, H. Baumgärtel and H. W. Jochims, *Chem. Phys.*, 1997, **214**, 367.
12. D. P. Seccombe, R. P. Tuckett, H. Baumgärtel and H. W. Jochims, *Phys. Chem. Chem. Phys.*, 1999, **1**, 773.
13. J. C. Whitehead, *Ann. Rep. Roy. Soc. Chem.*, 1998, **94c**, 293.
14. C. M. Gregory, M. A. Hayes, G. R. Jones and E. Pantos, *Technical Memorandum, Daresbury Laboratory*, 1994, reference DL/SCI/TM98E.
15. M. W. Chase, C. A. Davies, J. R. Downey, D. J. Frurip, R. A. McDonald and A. N. Syverud, *J. Phys. Chem. Ref. Data*, 1985, **14**, supplement 1.
16. S. G. Lias, J. E. Bartmess, J. F. Liebman, J. L. Holmes, R. D. Lerin and W. G. Mallard, *J. Phys. Chem. Ref. Data*, 1988, **17**, supplement 1.

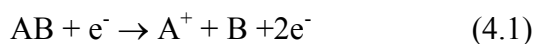
17. K. P. Huber and G. Herzberg, *Molecular Spectra and Molecular Structure* (Van Nostrand, New York, 1979), vol IV.
18. M. E. Jacox, *Vibrational and Electronic energy levels of polyatomic transient molecules*, *J. Phys. Chem. Ref. Data*, 1994, monograph No. 3.
19. J. Tellinghuisen and D. K. Chakraborty, *Chem. Phys. Letts.*, 1987, **134**, 565.
20. T. Pradeep and D. A. Shirley, *J. Electron Spectrosc. Relat. Phenom.*, 1993, **66**, 125.
21. A. W. Potts, H. J. Lempka, D. G. Streets and W. C. Price, *Phil. Trans. Roy. Soc. Lond. A.*, 1970, **268**, 59.
22. R. N. Dixon, J. N. Murrell and B. Narayan, *Mol. Phys.*, 1971, **20**, 611.
23. C. E. Theodosiou, M. Inokuti and S. T. Manson, *Atomic Data and Nuclear Tables.*, 1986, **35**, 473.
24. D. P. Secombe, R. P. Tuckett, H. Baumgärtel and H. W. Jochims, *J. Chem. Phys.*, 2001, **114**, 4058.
25. R. A. Gottsho, R. H. Burton and G. P. Davis, *J. Chem. Phys.*, 1982, **77**, 5298.
26. M. Larsson, M. R. A. Blomberg and P. E. M. Siegbahn, *Mol. Phys.*, 1982, **46**, 365.
27. I. R. Lambert, S. M. Mason, R. P. Tuckett and A. Hopkirk, *J. Chem. Phys.*, 1988, **89**, 2683.
28. R. Y. L. Chim, D. P. Secombe, R. P. Tuckett, H. Baumgärtel and H. W. Jochims, *Phys. Chem. Chem. Phys.*, in preparation.

CHAPTER 4 : FRAGMENTATION OF THE OUTER VALENCE STATES OF $CX_2Y_2^+$ (X, Y = H, Cl OR Br) PROBED BY THRESHOLD PHOTOELECTRON PHOTOION COINCIDENCE SPECTROSCOPY.

4.1 Introduction

This work continues the study of non-metal halides of groups (III) – (VI) by the Tuckett group. Examples of the ions whose fragmentation has been investigated includes SF_6^+ ,¹ CF_3X^+ (X = F, Cl and Br),^{1,2} MCl_4^+ (M = C, Si and Ge),^{3,4} PX_3^+ (X = Cl and Br),⁵ CCl_3X^+ (X = F, H and Br)⁶ and $CF_2X_2^+$ (X = H, Cl and Br).⁷

The spectroscopic and dynamic interest in these systems derives from the fact that such molecules lie between the “large” and “small” molecule limits and therefore whether dissociation is thermodynamically controlled or state specific. A number of groups have studied the VUV fragmentation of $CH_2Cl_2^+$ and $CH_2Br_2^+$ extensively using mass spectrometric methods.⁸⁻¹⁹ Most of these studies report the measurement by electron impact methods of appearance potentials of fragment ions to obtain further information concerning the heats of formation of these ions. The principles of the method for obtaining radical heats of formation are as follows, for the process:



The standard heats of formation are related to each other by:

$$AP(A^+) = \Delta_f H^0(A^+) + \Delta_f H^0(B) - \Delta_f H^0(AB) + E \quad (4.2)$$

where AP is the appearance potential and E is any excess energy which may be associated with either the charged or uncharged fragments. Generally $\Delta_f H^0(B)$ is the value of interest. It can be evaluated provided E can be measured or can be assumed to be zero, and provided $\Delta_f H^0(A^+)$ and $\Delta_f H^0(AB)$ are known independently.

He I and in some cases He II photoelectron spectra have been measured for all molecules in this chapter.²²⁻²⁸ However, no threshold photoelectron spectra have been reported in the literature. The first fragmentation study of $CBr_2Cl_2^+$ is presented. The aim of this work is to determine the dominant fragmentation channels and the mechanisms for dissociation of each molecule.

4.2 Experimental

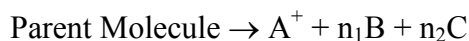
The photoionisation experiments required the use of the electron analyser and the time of flight drift tube described earlier in Chapter 2. Synchrotron radiation dispersed with the 1m Seya-Namioka monochromator on beamline 3.1 at SRS (Daresbury, UK) was used as the photon source. The two gratings used were calibrated using argon. Spectra were flux normalised via the visible fluorescence of a NaSal window. All samples were liquids purchased from Aldrich and were further purified by several freeze-pump-thaw cycles prior to use.

4.3 Energetics of the key dissociation channels

Many of the valence states of CH_2Br_2^+ , CH_2Cl_2^+ and $\text{CBr}_2\text{Cl}_2^+$ fragment into smaller ions. Thus the thermochemistry of such processes allows elucidation of the various pathways open at a particular excitation energy. The energetics of key dissociation channels and the vertical ionisation potentials (IP) of the ground ionic and excited ionic states are given in Table 4.1. The calculated dissociation energies are the enthalpies of reaction:

$$\Delta_r H^0 = \sum \Delta_f H^0_{(\text{products})} - \sum \Delta_f H^0_{(\text{reactants})} \quad (4.3)$$

associated with the process:



where $n_{1,2} = 0, 1, 2$ or 3 and A^+ , B and C are the dissociation products.

Table 4.1 Energetics of the key dissociation channels of CH_2Br_2 , CH_2Cl_2 and CBr_2Cl_2 .

Neutral/Parent Ion	Dissociation Channel	Adiabatic (vertical) IP/eV	Dissociation Energy/eV
$\text{CH}_2\text{Br}_2^+ \tilde{G} \ ^2\text{A}_1$	$\text{CH}^+ + 2\text{Br} + \text{H}$	(19.70 ²³)	22.52
	$\text{CBr}^+ + 2\text{H} + \text{Br}$		21.42
	$\text{CH}^+ + \text{H} + \text{Br}_2$		18.76
	$\text{CH}^+ + \text{Br} + \text{HBr}$		17.74
	$\text{CBr}^+ + \text{H} + \text{HBr}$		17.66
	$\text{CBr}^+ + \text{H}_2 + \text{Br}$		16.94
$\text{CH}_2\text{Br}_2^+ \tilde{F} \ ^2\text{B}_1$ $\text{CH}_2\text{Br}_2^+ \tilde{E} \ ^2\text{A}_1$ $\text{CH}_2\text{Br}_2^+ \tilde{D} \ ^2\text{B}_2$	$\text{CH}_2^+ + 2\text{Br}$	(16.25 ²³)	16.64
	$\text{CH}_2^+ + \text{Br}_2$ $\text{CHBr}_2^+ + \text{H}$	(14.7 ²³)	14.20
			11.94
$\text{CH}_2\text{Br}_2^+ \tilde{B} \ ^2\text{B}_1$ and $\tilde{C} \ ^2\text{A}_1$	$\text{CH}_2\text{Br}^+ + \text{Br}$	(14.12 ²³)	10.93
		(11.28 ²³)	
$\text{CH}_2\text{Br}_2^+ \tilde{A} \ ^2\text{A}_2$		(10.82 ²³)	

CH ₂ Br ₂ ⁺ \tilde{X} ² B ₂ CH ₂ Br ₂		(10.61 ²³)	0
CH ₂ Cl ₂ ⁺ \tilde{G} ² A ₁	CH ⁺ +2Cl+H CH ⁺ +Cl ₂ +H CCl ⁺ +2H+Cl CH ⁺ +HCl+H CH ₂ ⁺ +2Cl CCl ₂ ⁺ +2H CClH ⁺ +Cl+H	(20.30 ²³)	22.45 19.97 19.52 19.02 17.76 17.45 17.32
CH ₂ Cl ₂ ⁺ \tilde{F} ² B ₁		(16.77 ²³)	
CH ₂ Cl ₂ ⁺ \tilde{E} ² A ₁		(15.94 ²³)	
CH ₂ Cl ₂ ⁺ \tilde{D} ² B ₂	CH ₂ ⁺ +Cl ₂ CCl ⁺ +HCl+H CCl ⁺ +H ₂ +Cl CCl ₂ ⁺ +H ₂ CClH ⁺ +HCl CHCl ₂ ⁺ +H	(15.30 ²³)	15.25 15.09 15.04 12.97 12.89 12.40
CH ₂ Cl ₂ ⁺ \tilde{B} ² B ₁ and \tilde{C} ² A ₁	CClH ₂ ⁺ +Cl	(12.22 ²³)	12.10
CH ₂ Cl ₂ ⁺ \tilde{X} ² B ₂ and \tilde{A} ² A ₂ CH ₂ Cl ₂		11.320 ²² (11.40 ²³)	0
CBr ₂ Cl ₂ ⁺ \tilde{I} ² A ₁	CBr ⁺ + 2Cl + Br CBr ⁺ + BrCl + Cl CBr ⁺ + Cl ₂ + Br CCl ⁺ + 2Br + Cl CCl ₂ ⁺ + Br + Br CCl ⁺ + BrCl + Br CCl ⁺ + Br ₂ + Cl	(15.94 ²⁸)	19.33 17.10 16.85 16.47 14.40 14.24 14.03
CBr ₂ Cl ₂ ⁺ \tilde{H} ² A ₁		(12.88 ²⁸)	
CBr ₂ Cl ₂ ⁺ \tilde{G} ² A ₂		(12.76 ²⁸)	
CBr ₂ Cl ₂ ⁺ \tilde{F} ² A ₁	CCl ₂ ⁺ + Br ₂	(12.14 ²⁸)	11.96
CBr ₂ Cl ₂ ⁺ \tilde{E} ² B ₁		(11.90 ²⁸)	
CBr ₂ Cl ₂ ⁺ \tilde{D} ² B ₂		(11.65 ²⁸)	
CBr ₂ Cl ₂ ⁺ \tilde{C} ² A ₁		(11.60 ²⁸)	
CBr ₂ Cl ₂ ⁺ \tilde{B} ² A ₂		(11.18 ²⁸)	
CBr ₂ Cl ₂ ⁺ \tilde{A} ² B ₂		(10.94 ²⁸)	
CBr ₂ Cl ₂ ⁺ \tilde{X} ² B ₁		(10.67 ²⁸)	

CBr ₂ Cl ₂	CBr ₂ Cl ⁺ + Cl		?
	CBrCl ₂ ⁺ + Br		?
			0

Where possible, only 0 K values of the enthalpy of formation were used to avoid the affects of internal energy. All neutral fragment enthalpies of formation were taken from the JANAF tables.²⁹ However, ionic enthalpies of formation are not included in this source. Ion values at 298 K were taken from Lias *et al.*³⁰

No thermochemical data is available for BrCl⁺, CHBr, CHBr⁺, CBr₂⁺, CBrCl, CBrCl⁺, CBrCl₂, CBrCl₂⁺, CBr₂Cl and CBr₂Cl⁺, which is the case for many bromine containing molecules. The thermochemistry of the channels involving these fragments is unknown.

The vertical ionisation potentials of the valence states of CH₂Cl₂⁺, CH₂Br₂⁺ and CBr₂Cl₂⁺ are included in Table 4.1. The values of which were taken from T.Pradeep *et al.*²², A. W. Potts *et al.*²³ and J. C. Bunzli *et al.*²⁸, respectively.

4.4 Results

4.4.1 CH₂Br₂.

4.4.1.1 Threshold photoelectron spectrum

The TPES of CH₂Br₂ was measured between 9.9-24.8 eV at an optical resolution of 3Å and is shown in Fig. 4.1. Two gratings were needed to cover the spectral range. The onset of ionisation is determined to be 10.21 ± 0.1 eV. The vertical ionisation potentials for the \tilde{X} , \tilde{A} , \tilde{B}/\tilde{C} , \tilde{D} , \tilde{E} , \tilde{F} , \tilde{G} and \tilde{H} states are determined to be 10.64, 10.84, 11.27, 12.52, 14.13, 14.72, 16.02 and 20.87 eV respectively. Dixon *et al.*²⁴ recorded the photoelectron spectrum of CH₂Br₂ in the range 11-13 eV. This He I data agrees very well with the data presented here with one exception, the peak at 12.52 eV recorded with threshold conditions does not appear. This is also the case with measurements made by Potts *et al.*²³ It is possible that this difference in spectra is due to auto-ionisation. Using a resonant source allows this process to be probed and would rationalise this difference. In addition, Potts *et al.*²³ observes the \tilde{G} and \tilde{H} states at 16.25 and 19.7 eV respectively. Although these bands are relatively broad the disagreement could be due to differences in the relative ionisation cross-sections between He I and threshold conditions.

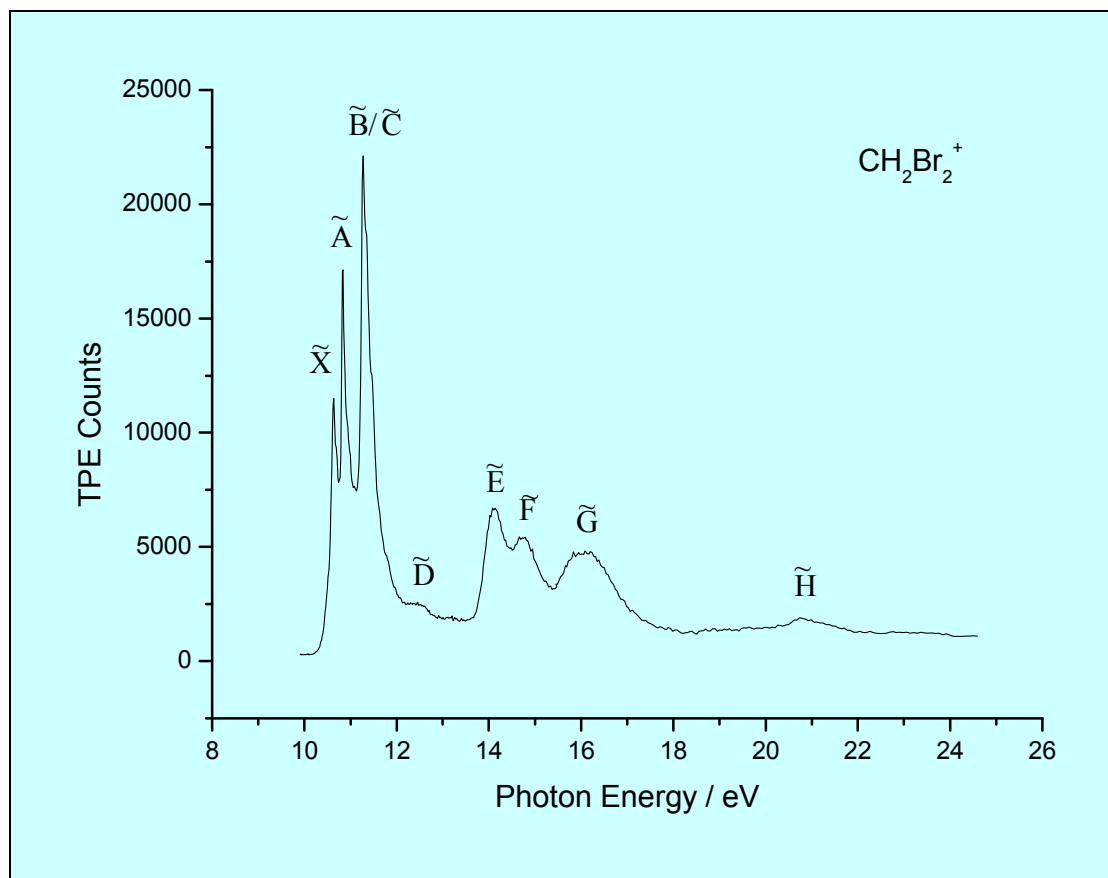


Figure 4.1 The TPES of CH_2Br_2 with an optical resolution of 3\AA .

4.4.1.2 Scanning TPEPICO experiments.

The scanning TPEPICO spectrum of CH_2Br_2 was measured between 9.9–24.8 eV at an optical resolution of 3\AA and an ion time-of-flight resolution of 128 ns. The presence of two hydrogens in the parent molecule causes difficulty in identifying fragment ions. However, two unambiguous and one composite ion yield plot are shown in Fig. 4.2. Parent ion as well as fragment ions CH_xBr^+ ($x = 0, 1$ or 2) and CH_2^+ were detected. The ambiguity in the assignments arises as a result of poor time-of-flight resolution. A series of fixed energy TPEPICO spectra with improved time-of-flight resolution (8 ns, see Chapter 2) at a series of photon energies reveals the identity of these fragment ions. The high-resolution TPEPICO spectra reveal that parent ion, CH_2Br^+ , CHBr^+ , CBr^+ and CH_2^+ are formed. However, ion yield plots and therefore appearance potentials were not possible to extract for all ions. Fig. 4.3 shows several fixed energy TPEPICO spectra recorded at different photon energies. It can be clearly seen that there is a shift in the time of flights of these spectra and that the figure represents three different fragments. The time-of-flight spectrum recorded at 108 nm is a doublet due to the two isotopes of bromine. This phenomenon is not observed with fragment cations at higher photon energies as the isotope effect is convoluted with kinetic energy broadening. A comparison of appearance energies for each fragment ion with previous work is shown in Table 4.2.

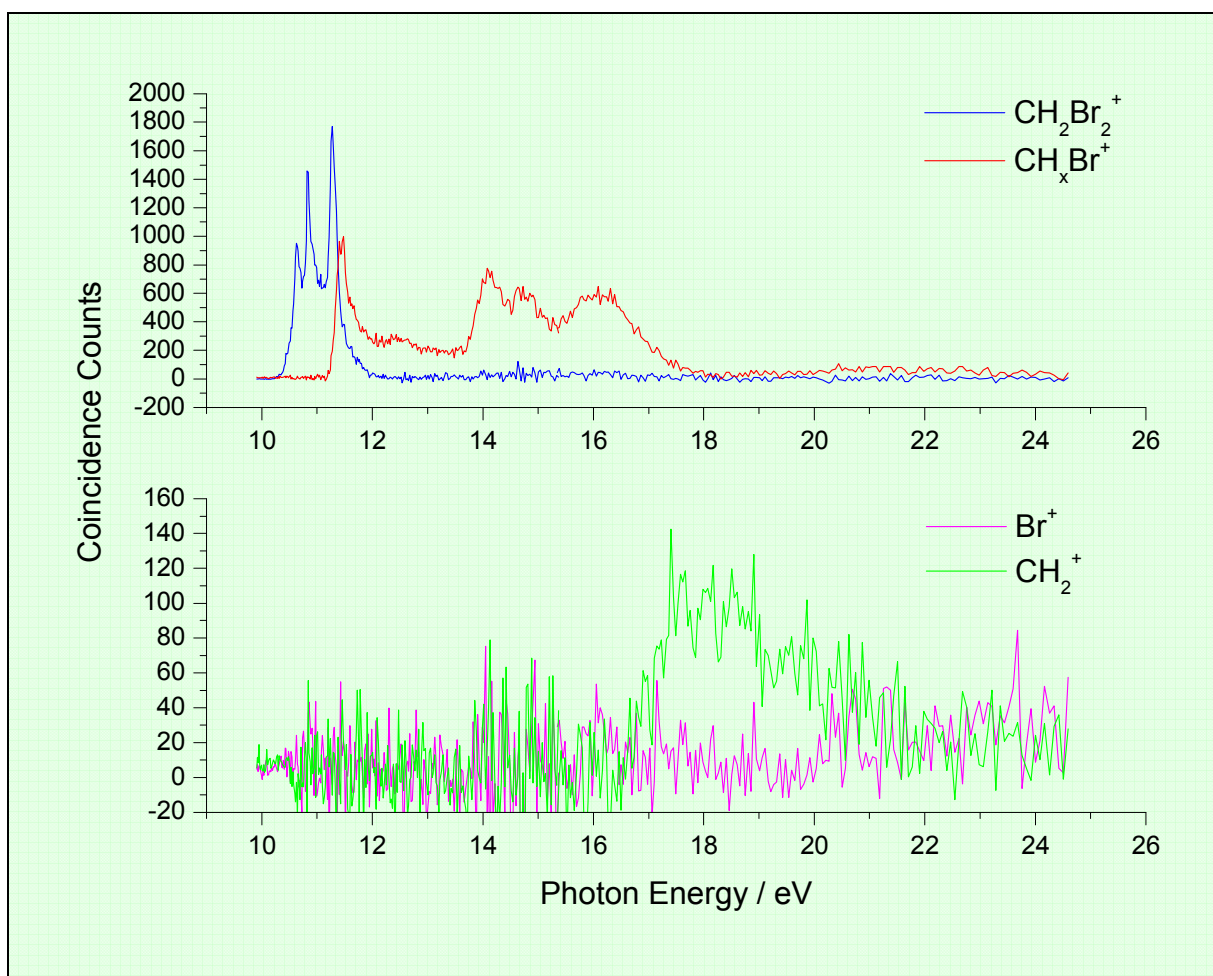


Figure 4.2 Ion yield plots of CH_2Br_2^+ , CH_xBr^+ and CH_2^+ measured with an optical resolution of 3\AA and a TOF resolution of 128 ns.

As expected the \tilde{X} and \tilde{A} states have a bound well and form solely parent ion as the ground and first excited state ionisation energies lie below the first thermodynamic dissociation channel $\text{CH}_2\text{Br}_2 \rightarrow \text{CH}_2\text{Br}^+ + \text{Br} + \text{e}^-$ (10.93 eV). The \tilde{B}/\tilde{C} state also forms predominantly parent ion but falls away with the onset of CH_2Br^+ which is present in the \tilde{D} state and solely in the \tilde{E} state. It is noted that CH_2Br^+ forms at 11.18 eV, 0.25 eV above its theoretical onset. This state selective behaviour is consistent with the removal of a non-bonding bromine lone pair electron followed by rapid non-statistical C-Br bond fission.

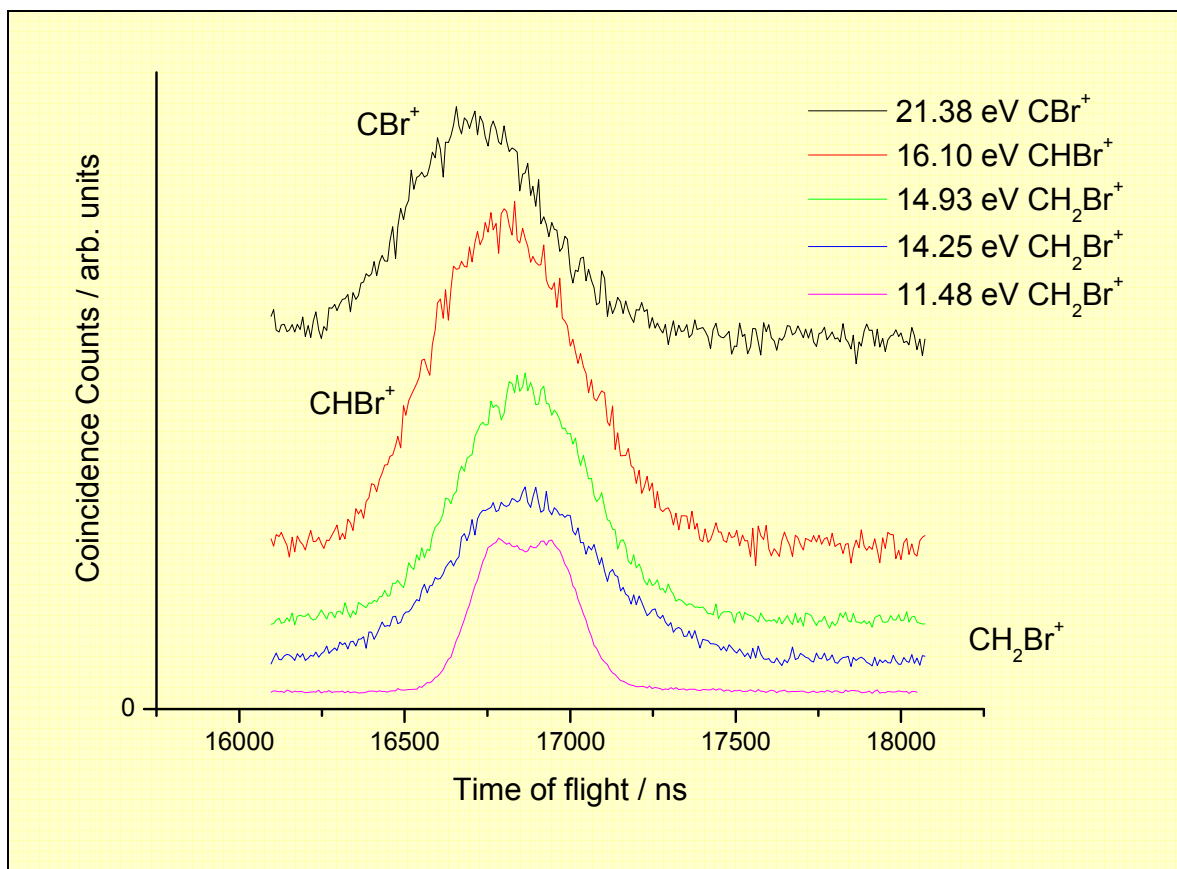


Figure 4.3 TPEPICO-TOF spectra at various excitation wavelengths in the CH_xBr^+ region (where $x = 0, 1$ or 2). Measured with a TOF resolution of 8 ns.

Table 4.2 Appearance energies / eV of the fragment ions formed following photoexcitation of CH_2Br_2 .

Daughter ion	Reed and Snedden ⁸	Franklin and Haney ⁹	DeCorpo <i>et al.</i> ¹⁰	Tsai <i>et al.</i> ¹¹	Kaposi <i>et al.</i> ¹²	Holmes <i>et al.</i> ¹³	Ma <i>et al.</i> ¹⁴	This Study
CH_2Br^+	10.93±0.04			11.35±0.02	11.1±0.2	11.29	11.27	11.18±0.2
CHBr^+					16.0±0.5			14.9-16.1
CBr_2^+					15.6±0.5			
CH_2^+					17.1±0.3			16.6±0.5
CH^+	21.55±0.05				22.0±0.5			
CBr^+					19.6±0.3			16.1-21.4
HBr^+					18.2±0.2			
Br_2^+					20.7±0.5			
C^+	24.52±0.05				22.7±0.5			
Br^+		16.0	15.5±0.1					^a

^a Br^+ is observed but due to poor signal an appearance potential could not be extracted.

It can be seen from Table 4.2, that there is little consistency in the literature regarding the principal fragmentation products and appearance potentials of this molecule. Only Tsai *et al.*¹¹ have used the TPEPICO technique.

Although appearance potentials of CHBr^+ and CBr^+ could not be extracted, from the high resolution fixed energy TPEPICO experiments, it can be stated that the appearance potential of CHBr^+ lies between 14.9 and 16.1 eV and likewise CBr^+ lies between 16.1 and 21.38 eV. Unfortunately the enthalpy of formation for CHBr^+ is unknown and therefore the dissociation energies for reactions forming this ion are unknown. Furthermore, a determination of the neutral products formed with CBr^+ is not possible due to the imprecise value of our appearance potential. The appearance potential of CH_2Br^+ agrees well with all previous work, except for that determined by Reed and Snedden.⁸ The appearance potential measured for CH_2^+ (16.6 ± 0.5 eV) is in reasonable agreement with the work of Kaposi *et al.*¹² but several fragments observed by the authors have not been reproduced in this study. This could be due to one or a combination of two reasons. Firstly, the TPEPICO apparatus may not be as sensitive as the electron impact spectrometer of Kaposi *et al.*¹² Secondly, formation of these cations may be due to ion pair formation.

4.4.1.3 Fixed Energy TPEPICO Experiments.

Several TPEPICO-TOF spectra of the parent ion were recorded at 11.27, 10.88 and 10.69 eV with a TOF resolution of 8 ns. The observed spectra represent the superposition of the three isotopomers of CH_2Br_2 . Three gaussians, each representing an isotopomer of CH_2Br_2 have been compared to the spectral feature. The heights are determined by the relative abundance, the time of flight by mass and the full width at half maximums calculated from the Franklin equation.³³ The sum of these fits give a total fit that should simulate the raw TPEPICO-TOF spectra. It can be seen from Fig. 4.4 that the total fit is reasonably good. This indicates that the temperature in the interaction region is *ca.* 298 K and that the spacial focussing is configured correctly.

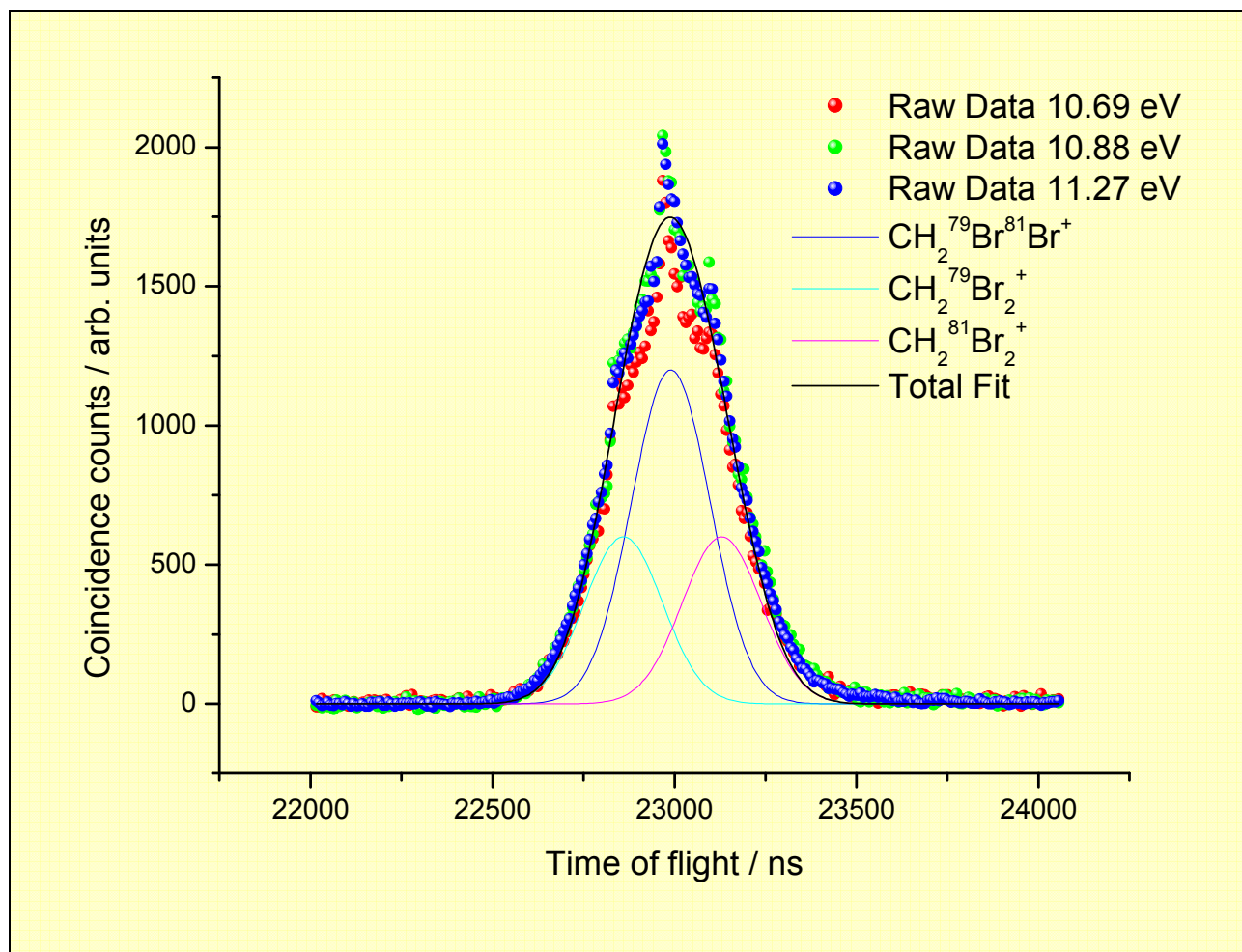


Figure 4.4 Comparison of the sum of three gaussian fits of the three isotopomers of CH_2Br_2^+ to TPEPICO-TOF spectra of CH_2Br_2^+ .

TPEPICO-TOF spectra were measured for $(\text{CH}_2\text{Br}_2^+)^* \rightarrow \text{CH}_2\text{Br}^+ + \text{Br}$ at photon energies of 11.48, 14.25 and 14.85 eV with a TOF resolution of 8 ns. The excitation energies correspond to the initial formation of the \tilde{B}/\tilde{C} , \tilde{E} and \tilde{F} states of the parent ion. Experimental values of $\langle \text{KE} \rangle_t$ and the fractional ratios as well as the theoretical statistical and impulsive limits are given in Table 4.3. A more detailed description of the calculation of the statistical and impulsive decay limits is given in section 5.4. The two isotopes of bromine (50% Br^{79} , 50% Br^{81}) have been allowed for in the experimental values quoted in Table 4.3.

Table 4.3 Mean translational KE releases ($\langle KE \rangle_t$) of the two-body fragmentation processes of the valence states of CH_2Br_2^+ .

	Fragment	Photon energy / eV	E_{avail}^a / eV	$\langle KE \rangle_t$ / eV	Fractional Ratio ^b		
					Experimental	Statistical	Impulsive
$\text{CH}_2\text{Br}_2^+ \tilde{B}/\tilde{C}$	CH_2Br^+	11.48	0.63	^c	^c	0.10	0.24
$\text{CH}_2\text{Br}_2^+ \tilde{D}$	CH_2Br^+	14.25	3.40	0.62 ± 0.08	0.18	0.10	0.24
$\text{CH}_2\text{Br}_2^+ \tilde{E}$	CH_2Br^+	14.85	4.00	0.36 ± 0.08	0.09	0.10	0.24

^a E_{avail} = Photon Energy – thermochemical threshold for forming the daughter ion + thermal energy of parent molecule at 298 K

^bFractional ratio = $\langle KE \rangle_t / E_{\text{avail}}$

^cIt was not possible to fit this TOF spectrum

The measurement corresponding to the \tilde{E} state of parent ion excited at 14.85 eV suggests mostly impulsive behaviour. The measurement corresponding to the \tilde{F} state of the parent ion at 14.85 eV fits well to the statistical dissociation limit. Unfortunately it was not possible to fit the measurement made at the \tilde{B}/\tilde{C} state. This is probably due to the fact that the spectrum was recorded very close to the onset of the fragment ion. There seems to be, however, an overall transition from impulsive to statistical behaviour as the photon energy increases. It should be noted that throughout this thesis, the value of the $\langle KE \rangle_t$ is fairly insensitive to the fitting parameters used (see section 2.4). Therefore, a set of robust fits and values are yielded. The uncertainty in $\langle KE \rangle_t$ does not affect the interpretation of the data presented here due to its small magnitude.

4.4.2 CH_2Cl_2

4.4.2.1 Threshold photoelectron spectrum

The TPES of CH_2Cl_2 was measured between 10.3-24.8 eV at a spectral resolution of 3 Å and is shown in Fig. 4.5. The onset of ionisation is determined to be 11.16 ± 0.1 eV. The vertical ionisation energies for the \tilde{X}/\tilde{A} , \tilde{B}/\tilde{C} , \tilde{D} , \tilde{E} , \tilde{F} and \tilde{G} states are determined to be 11.50, 12.19, 15.25, 15.75, 16.61 and 20.90 eV, respectively. These peak positions agree well with the He I data of Potts *et al.*,²³ Dixon *et al.*,²⁴ Werner *et al.*,¹⁹ and Pradeep and Shirley.²² Interestingly, the TPES of CH_2Cl_2 and CH_2Br_2 appear to be similar in appearance with the absence of the peak at 12.52 eV in CH_2Cl_2 . This peak may be present but only very weakly, but from this data alone, it is unclear. This peak was not seen in the He I data of Potts *et al.*,²³ Dixon *et al.*,²⁴ Werner *et al.*,¹⁹ and Pradeep and Shirley.²²

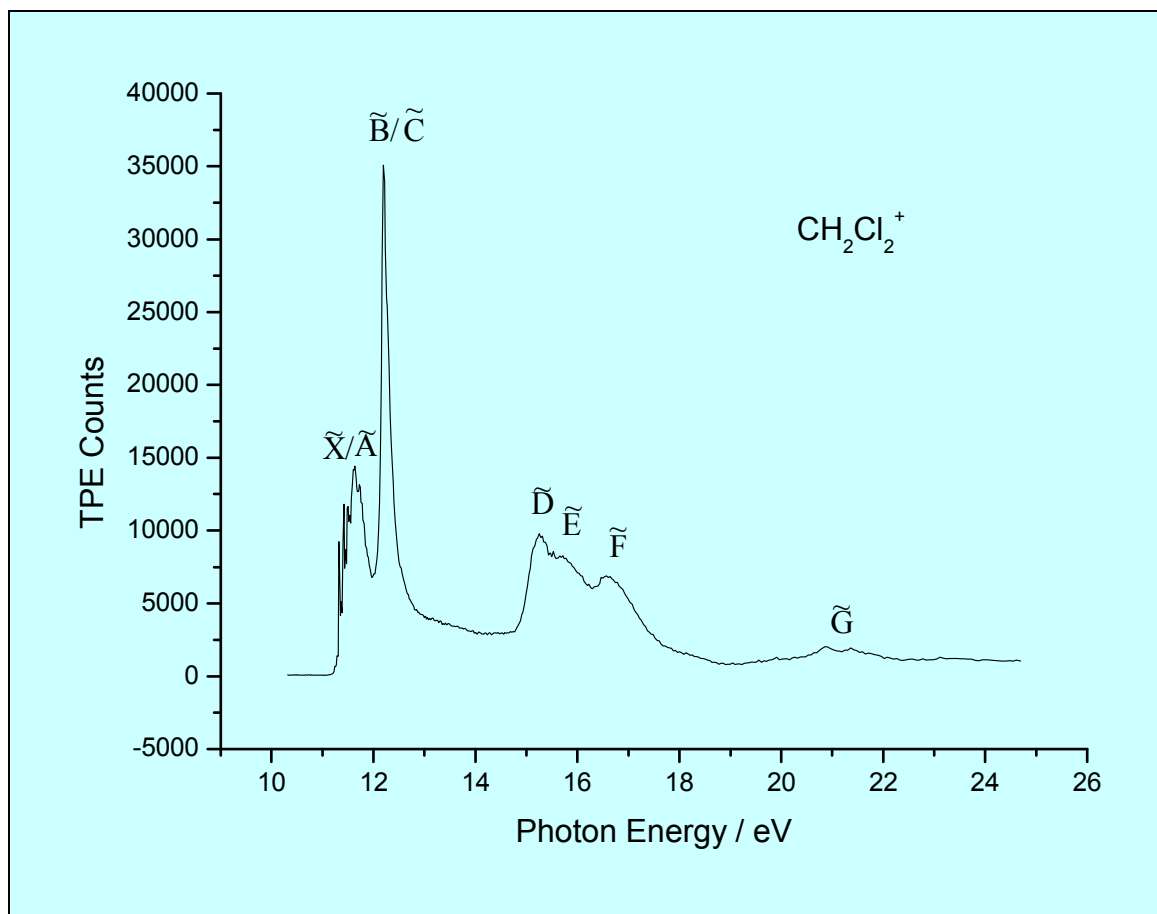


Figure 4.5 The TPES of CH_2Cl_2 with an optical resolution of 3\AA .

Clearly vibrational structure is resolved in the \tilde{X}/\tilde{A} state of the parent ion. A higher resolution scan was recorded (1 \AA resolution) from $11.25 - 11.79\text{ eV}$ and is shown in Fig. 4.6. Several vibronic peaks are observed, and are tabulated in Table 4.4. The main progression of 3 members has a constant separation of $645 \pm 100\text{ cm}^{-1}$. These peak positions are in excellent agreement with Potts *et al.*²³ The higher resolution of our spectrum means that we are also able to resolve a second, weaker progression, with each component of the main series having a peak 320 cm^{-1} to higher energy. Vibrational structure was observed in the analogous photoelectron band of CH_2F_2 by Seccombe *et al.*⁷ where one vibrational series of spacing 1030 cm^{-1} was observed. Seccombe *et al.* were not able to assign this progression definitively, but suggested it was due to either ν_2 or ν_3 . Since there is a significant reduction in the spacing of the main progression for CH_2Cl_2 , this vibration is assigned to motion involving the halogen atom(s). Therefore this progression is assigned to the ν_3 vibration (CCl_2 stretch) which has a_1 symmetry. Being a vibration belonging to the totally symmetric irreducible representation of the C_{2v} point group, it is allowed in the photoelectron spectrum. The weaker progression is more difficult to assign. It may be due to the ν_2 (CH_2 scissors) a_1 vibration, although the magnitude of the vibrational energy seems large.

Table 4.4 Peak positions and assignments associated with the \tilde{X} state of CH_2Cl_2^+ .

Peak	Position / eV	Assignment
I	11.322	$\nu_2 = \nu_3 = 0$
II	11.364	ν_2
III	11.408	ν_3
IV	11.453	$\nu_3 + \nu_2$
V	11.487	$2\nu_3$
VI	11.526	$2\nu_3 + \nu_2$

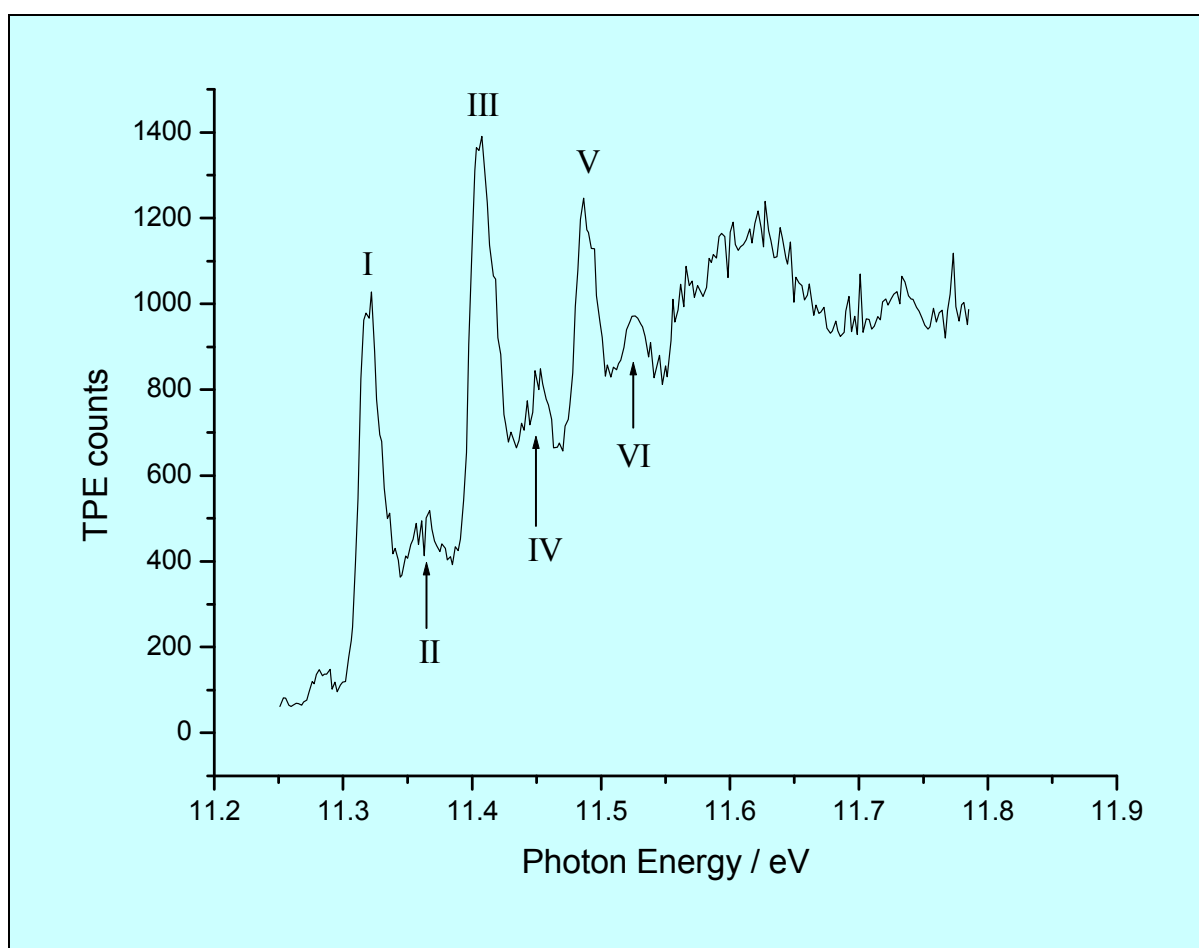


Figure 4.6 The high resolution TPEPICO spectrum of CH_2Cl_2 with an optical resolution of 1 Å.

4.4.2.2 Scanning TPEPICO experiments.

The scanning TPEPICO spectrum of CH_2Cl_2 was measured between 10.3-24.8 eV at a spectral resolution of 3 Å and an ion time-of-flight resolution of 64 ns. Ion yield plots are shown in Fig. 4.7. Parent ion as

well as the fragment ions CHCl_2^+ , CH_2Cl^+ , CHCl^+ and CH_2^+ were detected. CHCl_2^+ is not included in the ion yields as this ion cannot be separated from the parent ion at a time of flight resolution of 64 ns. Fixed energy time of flight spectra with 8 ns time of flight resolution have been used to identify this fragment ion, but an accurate appearance potential could not be extracted. Fig. 4.8. shows several fixed energy measurements at different photon energies. The top three spectra (CHCl_2^+) were recorded from the \tilde{D} , \tilde{E} and \tilde{F} states at energies of 15.25, 15.75 and 16.61 eV whilst the other spectrum (parent ion) was taken from the \tilde{B}/\tilde{C} state (12.9 eV). It can be clearly seen that a shift occurs, this shift corresponding to the loss of a hydrogen atom. Therefore the appearance potential of CHCl_2^+ lies somewhere between 12.9 and 15.2 eV.

It should also be noted that the ion yield curve for CHCl^+ does not represent its true relative intensity. Due to the fact that the identities of fragment ions are determined by their masses, and the masses of CH_2Cl^+ and CHCl^+ are very similar, the true ion yield plot was impossible to extract. The ion time of flights overlap due to broadening of peaks due to translational energy. Therefore the cross sections taken from our maps did not include all CHCl^+ ions in the CHCl^+ ion yield curve.

A comparison of appearance potentials for each fragment ion with previous work is shown in Table 4.5. All previous values with the exception of Werner *et al.*¹⁹ were obtained using the electron impact mass spectrometric methods. Werner *et al.*¹⁹ are the only group to have used photons as an excitation source. With the exception of Reed and Snedden,⁸ the appearance potential of CH_2Cl^+ agrees well with all previous measurements. Reed and Snedden's value is 0.9 eV higher, this could be due to the use of electrons as the excitation source.³¹ Cl^+ was detected by Haney and Franklin and Decorpo *et al* but not in this study. It could be possible that Cl^+ forms from an ion pair formation mechanism, hence not detected by the TPEPICO technique as only ions with associated electrons can be observed. However Decorpo *et al* found no evidence of the process:



in their negative ion spectra. CH_2^+ was detected with an appearance potential of 18.8 ± 0.3 eV, 1.8 eV higher than Haney and Franklins' value. Overall the literature shows little agreement on how CH_2Cl_2^+ fragments under VUV conditions.

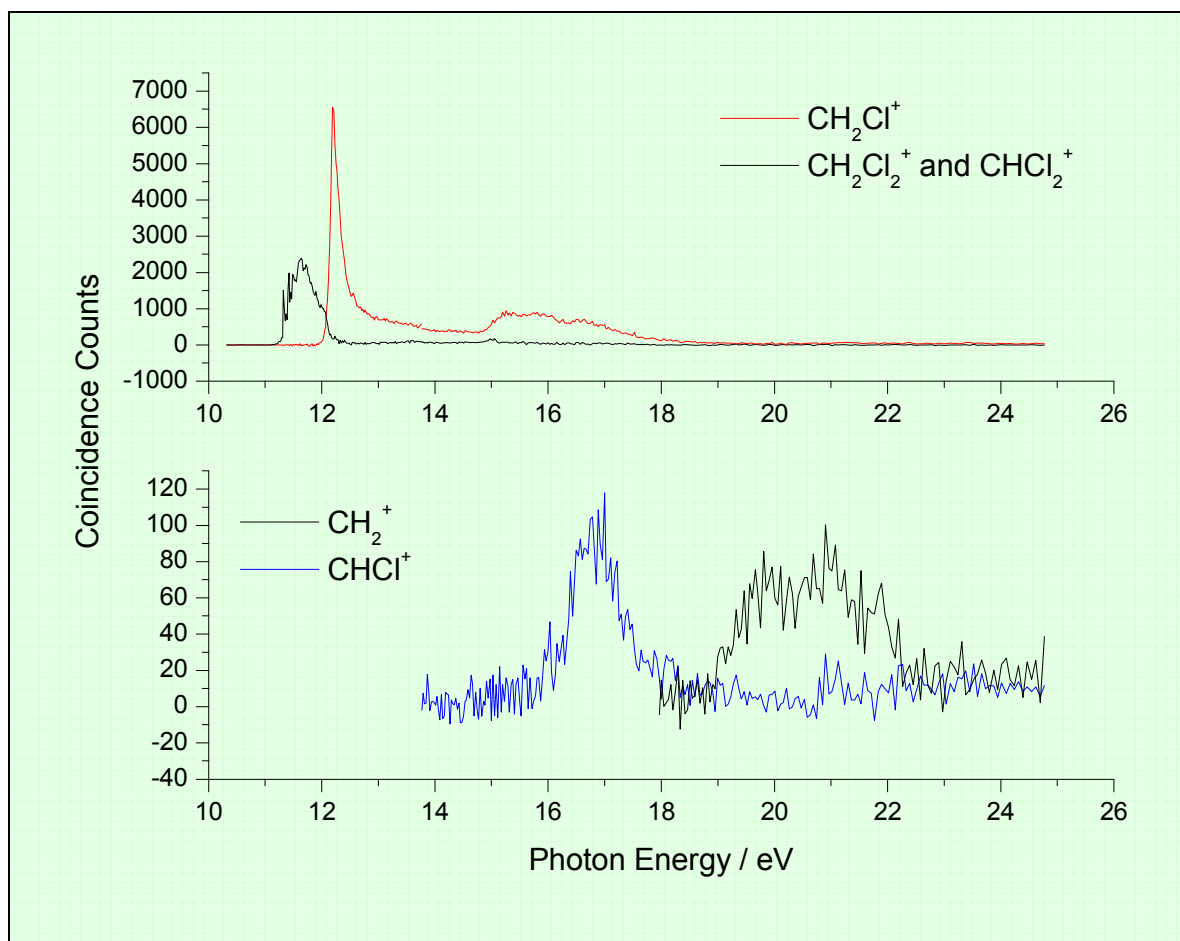


Figure 4.7 Ion yield plots of CH_2Cl_2^+ , CH_2Cl^+ (where $x = 1$ or 2), CHCl^+ and CH_2^+ measured with an optical resolution of 3\AA and a TOF resolution of 64 ns . Due to mass resolution, CH_2Cl^+ signal has some CHCl^+ in it. This is not important since the former is much stronger. The CHCl^+ ion yield may not be the true intensity since care was taken to exclude all the overlapping CH_2Cl^+ signal.

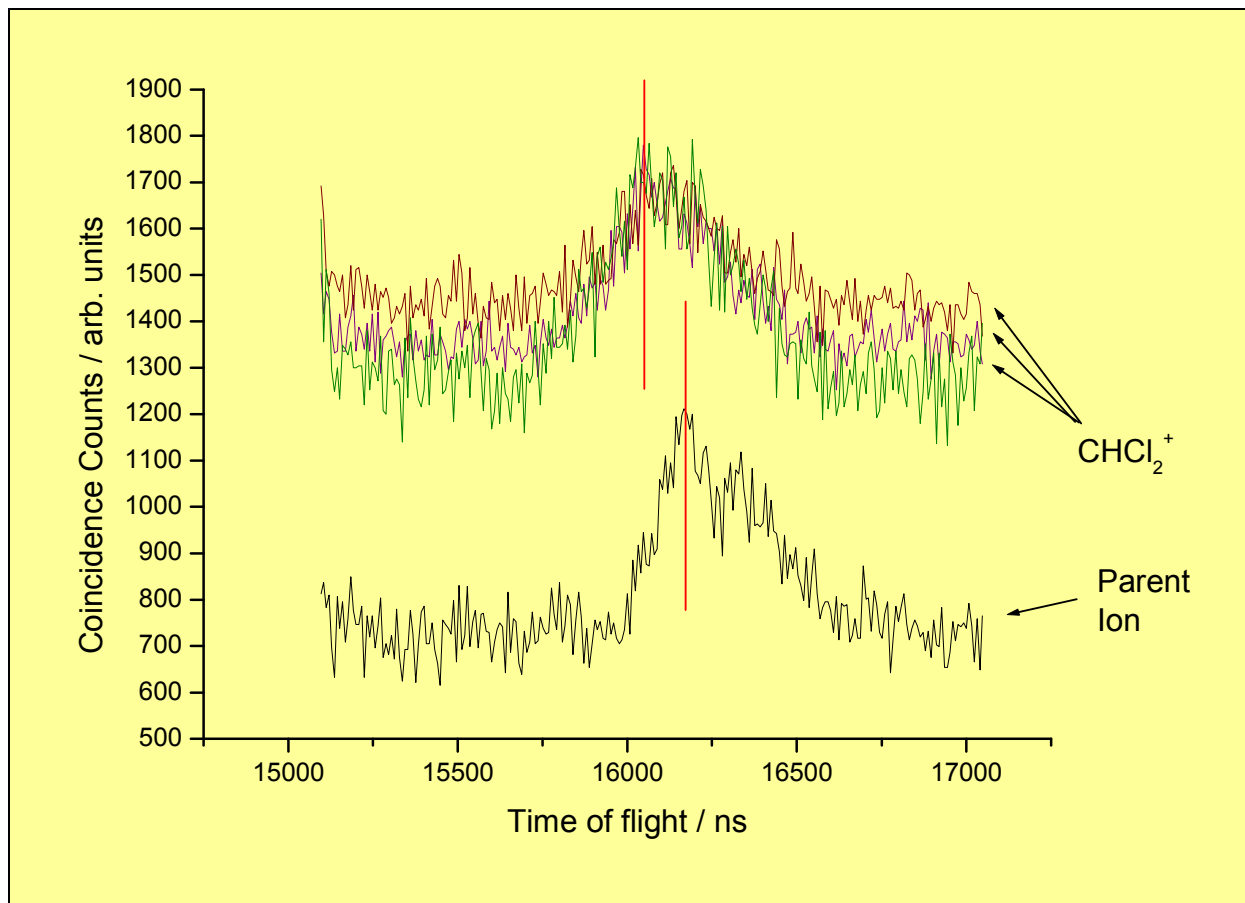


Figure 4.8 TPEPICO-TOF spectra at various excitation wavelengths in the CH_xCl_2^+ region (where $x = 0, 1$ or 2). Measured with a TOF resolution of 8 ns. The vertical red lines mark the peaks of the TOF spectra.

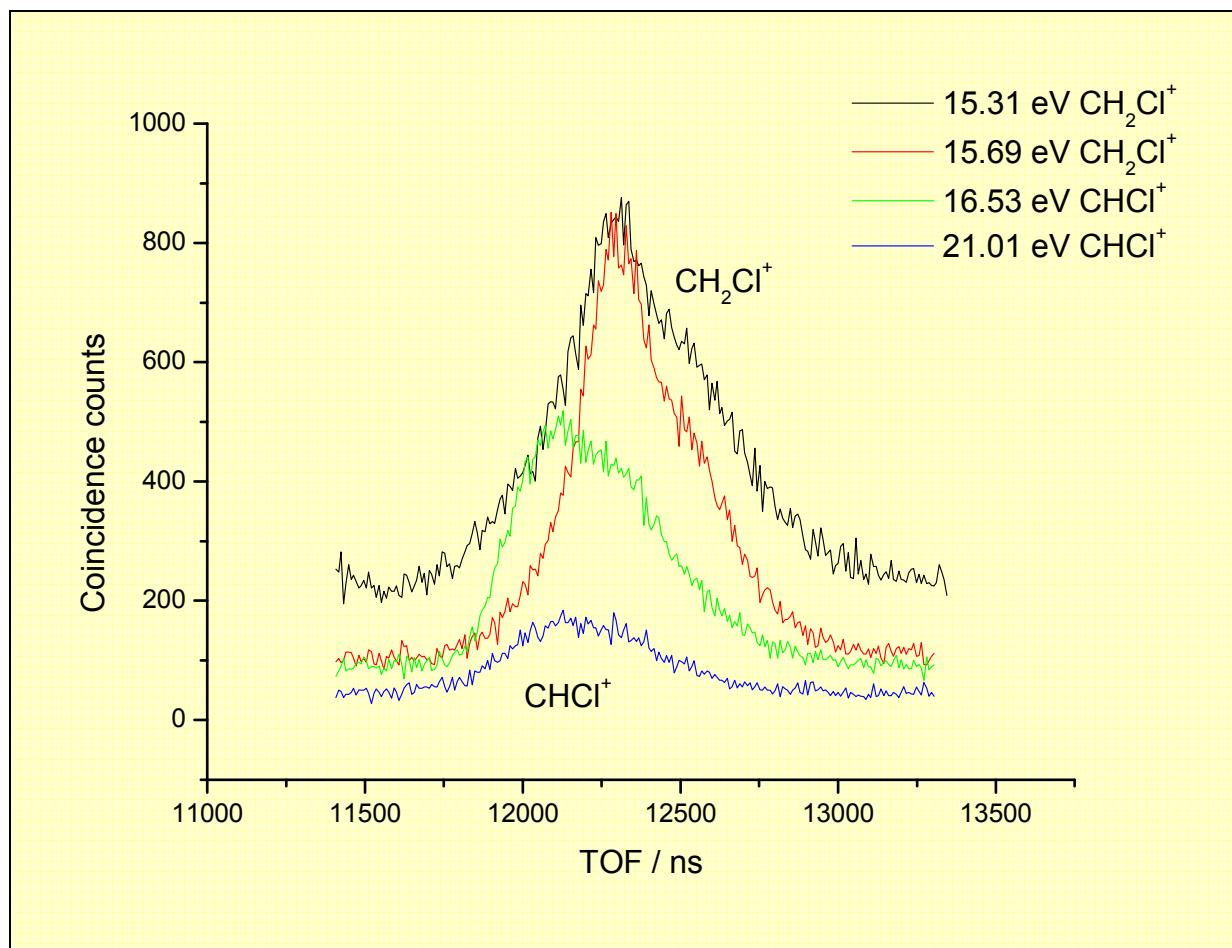


Figure 4.9 TPEPICO-TOF spectra at various excitation wavelengths in the CH_xCl^+ region (where $x = 0, 1$ or 2). Measured with a TOF resolution of 8 ns.

Table 4.5 Appearance potentials / eV of the fragment ions formed following photoexcitation of CH_2Cl_2 .

Daughter Ion	Reed and Snedden ⁸	Harrison and Shannon ¹⁵	Martin <i>et al.</i> ¹⁶	Haney and Franklin ⁹	Haney and Franklin ¹⁷	DeCorpo <i>et al.</i> ¹⁰	Lossing ¹⁸	Werner <i>et al.</i> ¹⁹	Holmes <i>et al.</i> ¹³	This Study
CH_2Cl^+	12.89±0.03	12.1±0.1	12.12±0.05				12.15	12.14±0.02	12.1	12.0±0.1
CHCl_2^+										12.9-15.2
CHCl^+	13.00±0.10									15.8±0.5
CH_2^+				17.0						18.8±0.3
CH^+	21.72±0.04									
Cl^+					17.4	17.4±0.1				
C^+	25.5±0.1									

4.4.2.3 Fixed Energy TPEPICO Experiments.

Several TPEPICO-TOF spectra of the parent ion were recorded at 11.27, 10.88 and 10.69 eV with a TOF resolution of 8 ns. The observed spectra represent the superposition of the three isotopomers of CH_2Cl_2 . Three gaussians, each representing an isotopomer of CH_2Cl_2 have been compared to the spectral feature. The heights are determined by the relative abundance, the time of flight by mass and the full width at half

maximums calculated from the Franklin equation. The sum of these fits give a total fit that should simulate the raw TPEPICO-TOF spectra. It can be seen from figure 4.10 that the total fit is reasonably good.

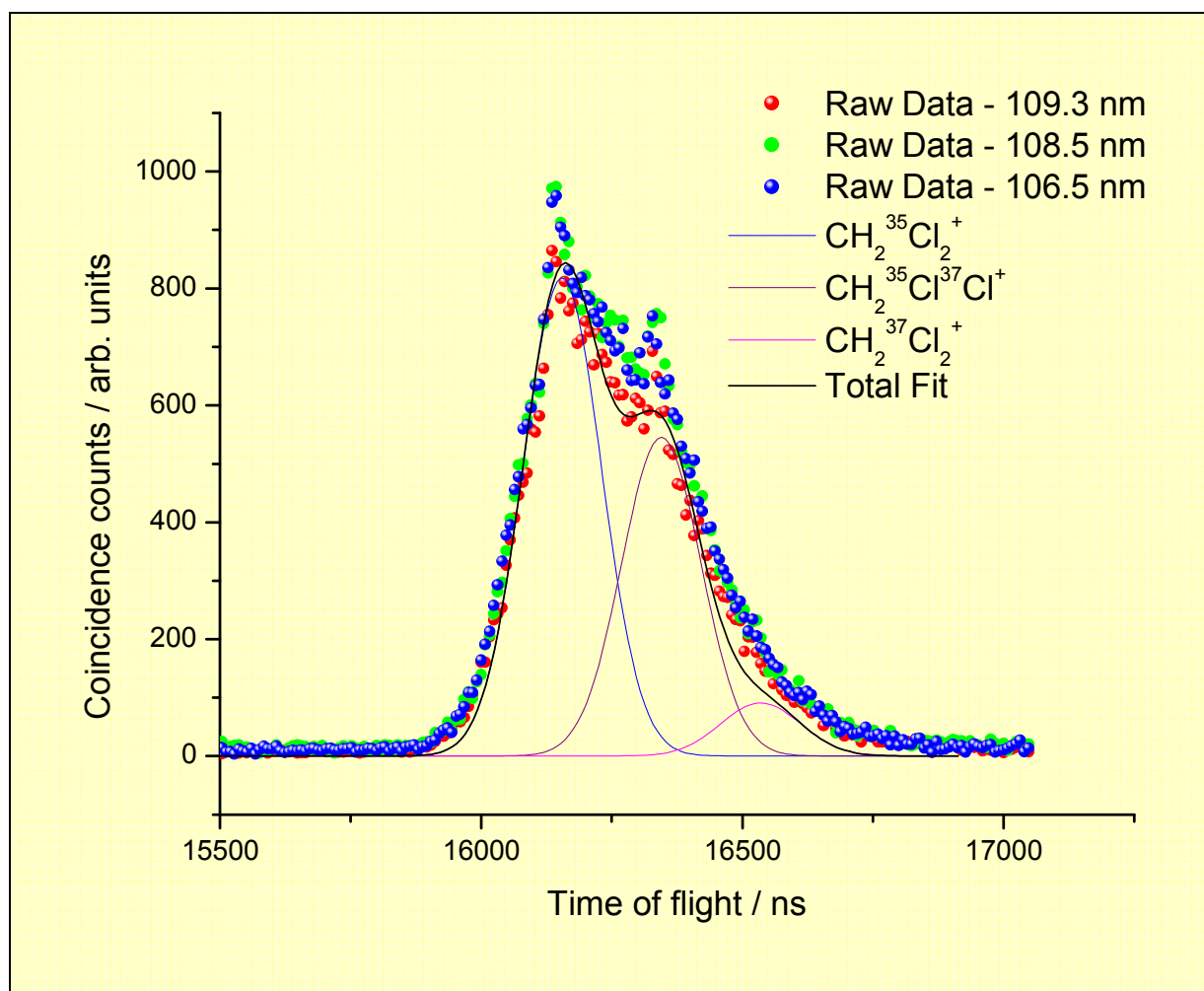


Figure 4.10 Comparison of the sum of three gaussian fits of the three isotopomers of CH_2Cl_2^+ to TPEPICO-TOF spectra of CH_2Cl_2^+ .

Table 4.6 Mean translational KE releases ($\langle \text{KE} \rangle_t$) of the two-body fragmentation processes of the valence states of CH_2Cl_2^+ .

	Fragment	Photon energy / eV	E _{avail} ^a / eV	<KE> _t / eV	Fractional Ratio ^b		
					Experimental	Statistical	Impulsive
CH ₂ Cl ₂ ⁺ \tilde{B}/\tilde{C}	CH ₂ Cl ⁺	12.28	0.24	0.13±0.04	0.54	0.10	0.43
CH ₂ Cl ₂ ⁺ \tilde{B}/\tilde{C}	CH ₂ Cl ⁺	12.40	0.36	0.16±0.04	0.45	0.10	0.43
CH ₂ Cl ₂ ⁺ \tilde{D}	CH ₂ Cl ⁺	15.27	3.23	1.30±0.06	0.40	0.10	0.43
CH ₂ Cl ₂ ⁺ \tilde{E}	CH ₂ Cl ⁺	15.69	3.65	0.79±0.05	0.22	0.10	0.43

^a E_{avail} = Photon Energy – thermochemical threshold for forming the daughter ion + thermal energy of parent molecule at 298 K

^b Fractional ratio = <KE>_t / E_{avail}

TPEPICO-TOF spectra were measured with a TOF resolution of 8 ns for CH₂Cl₂⁺ → CH₂Cl⁺ + Cl at photon energies of 12.28, 12.40, 15.27 and 15.69 eV. The excitation energies correspond to the initial formation of various parts of the \tilde{B}/\tilde{C} state and the \tilde{D} and \tilde{E} states of the parent ion. Experimental values of <KE>_t and the fractional ratios as well as the theoretical statistical and impulsive limits are given in Table 4.6. In fitting the peak shape of the daughter ions which include one or more Cl atoms allowance has been made for the two isotopes of chlorine (75% Cl³⁵, 25% Cl³⁷). It can be seen that the values of <KE>_t and the fractional ratios corresponding to the \tilde{B}/\tilde{C} and \tilde{D} state do not conform accurately to either of the mechanism limits in Table 4.6. This is probably due to fact that these measurements were made close to the threshold of formation. The spectrum recorded from the \tilde{D} state appears to fit well to the impulsive model. The <KE>_t determined for dissociation at the \tilde{E} state appears to have both statistical and impulsive character. It can be tentatively said that overall, there is a transition from statistical to impulsive behaviour as the photon energy increases. This mimics the behaviour described earlier for CH₂Br₂.

TPEPICO-TOF spectra were also recorded for the process CH₂Cl₂ → CHCl₂⁺ + H. Unfortunately values of <KE>_t could not be determined due to unfavourable kinematics.

4.4.3 CBr₂Cl₂

4.4.3.1 Threshold photoelectron spectrum

The TPES of CBr₂Cl₂ was recorded from 9.9-24.8 eV at a spectral resolution of 3Å. The onset of ionisation is observed at 10.31 eV and peaks are observed at 10.81, 10.95, 11.21, 11.37, 11.66, 11.90, 12.18, 12.84, 15.86, 17.83 and 19.85 corresponding to the \tilde{X} , \tilde{A} , \tilde{B} , \tilde{C} , \tilde{D} , \tilde{E} , \tilde{F} , \tilde{G} , \tilde{H} and \tilde{I} states respectively. The values measured are in good agreement with the He I data of Bunzli *et al.*²⁸

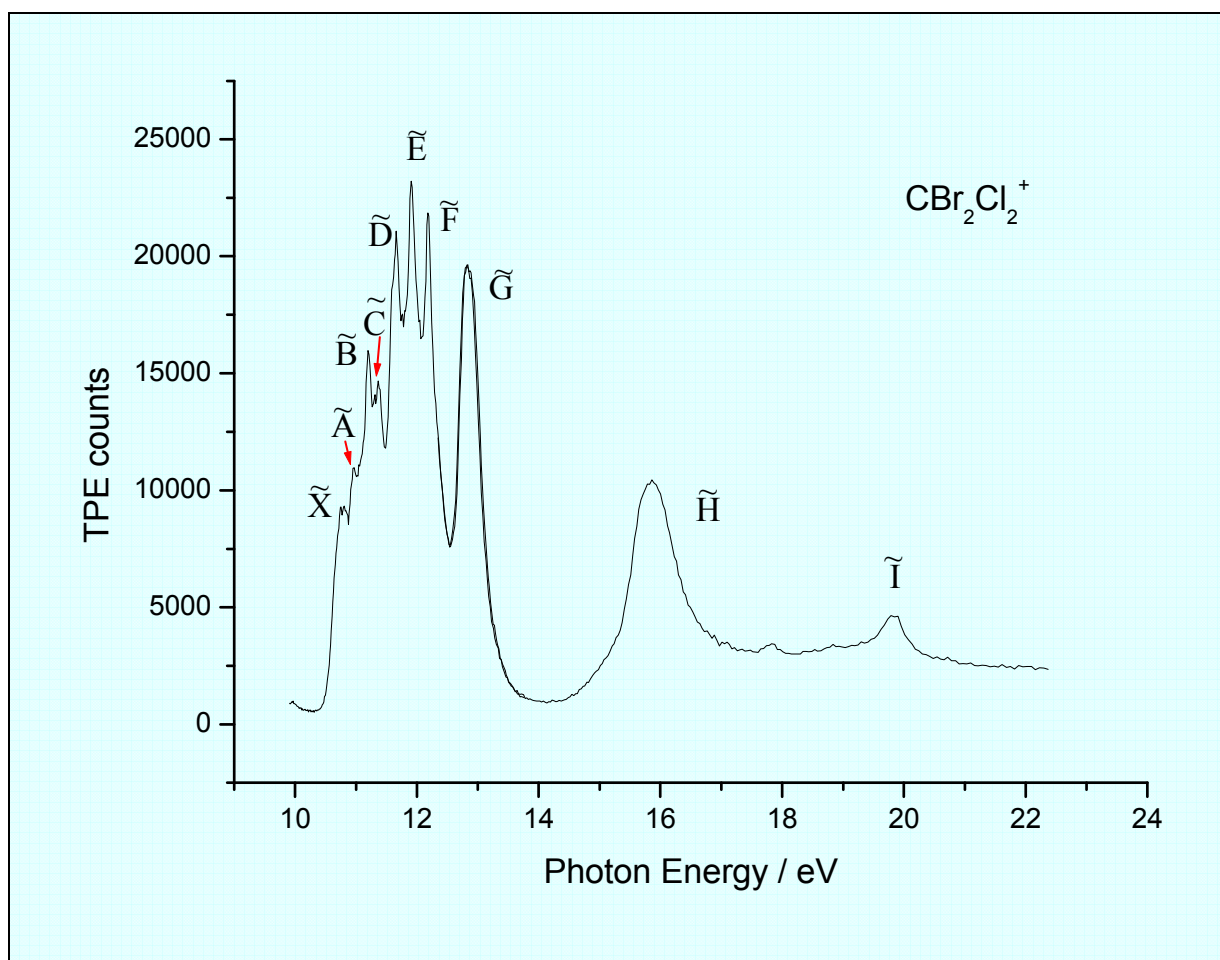


Figure 4.11 TPES of CBr_2Cl_2 with an optical resolution of 3\AA .

4.4.3.2 Scanning TPEPICO experiments.

The scanning TPEPICO spectrum of CBr_2Cl_2 was measured between 10.3–24.8 eV at a spectral resolution of 3\AA and an ion time-of-flight resolution of 128 ns. Ion yield plots are shown in Fig 4.12. Whilst the fragment ions CBrCl_2^+ , CBr_2Cl^+ , CBrCl^+ , CCl_2^+ , CCl^+ and CBr^+ are detected, neither the parent ion nor the fragment CBr_2^+ are observed at any photon energy. Appearance potentials extracted from the ion yield plots are given in Table 4.7. This is the first observation of appearance potentials of fragment ions from CBr_2Cl_2 . The large errors quoted for the values for CBr_2Cl^+ , CBrCl^+ , CCl_2^+ and CCl^+ result from the shallow onsets of these ions. No previous fragmentation studies have been performed hence there are no comparisons with other measurements.

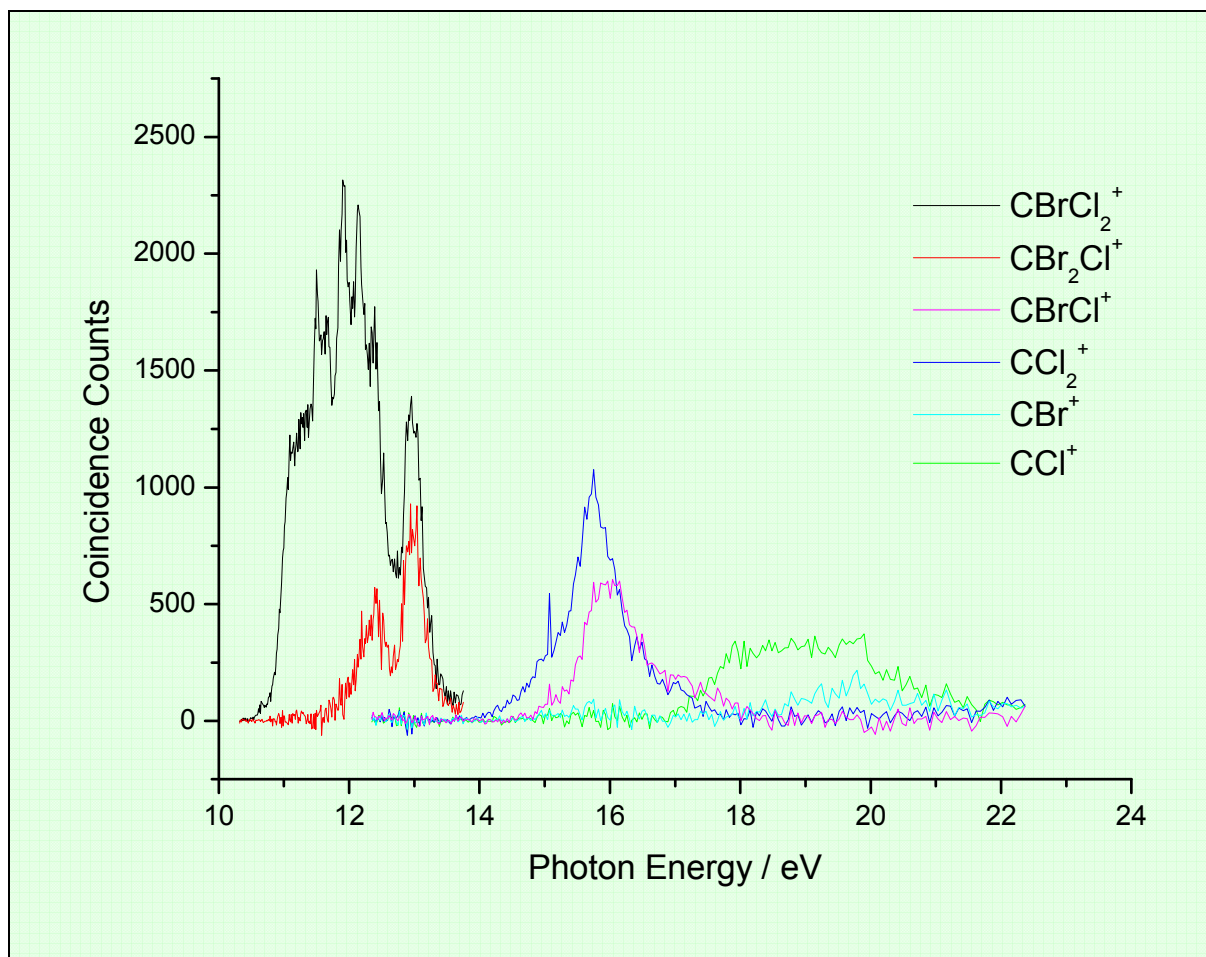


Figure 4.12 Ion yield plots of CBrCl_2^+ , CBr_2Cl^+ , CBrCl^+ , CCl_2^+ , CBr^+ and CCl^+ measured with an optical resolution of 3\AA and a TOF resolution of 128 ns.

Table 4.7 and Fig. 4.12 are a good illustration of the relative strengths of the C-Br and C-Cl bonds. For example, CBrCl_2^+ has a lower appearance potential than CBr_2Cl^+ and CBrCl^+ has a lower appearance potential than CCl_2^+ . This is consistent with the C-Br bond being weaker than the C-Cl bond. The low lying \tilde{X} , \tilde{A} and \tilde{B} states dissociate solely to form CBrCl_2^+ . The absence of parent ion suggests that all these three states of $\text{CBr}_2\text{Cl}_2^+$ are dissociative in the Franck-Condon region. The \tilde{C} , \tilde{D} , \tilde{E} and \tilde{F} states dissociate to both CBrCl_2^+ and CBr_2Cl^+ . CBrCl^+ , CCl_2^+ , CBr^+ and CCl^+ are formed from the higher excited ionic states of CBr_2Cl_2 .

Table 4.7 Appearance energies of the fragment ions formed following photoexcitation of CBr_2Cl_2 .

Fragment Ion	Appearance Potential / eV
CBrCl_2^+	10.45 ± 0.2
CBr_2Cl^+	11.59 ± 0.5
CBrCl^+	14.88 ± 0.5
CCl_2^+	13.88 ± 0.5
CCl^+	17.01 ± 0.5
CBr^+	18.2 ± 1.0

4.4.3.3 Fixed Energy TPEPICO Experiments.

TPEPICO-TOF spectra were measured with a TOF resolution of 8 ns for the process $\text{CBr}_2\text{Cl}_2^+ \rightarrow \text{CBrCl}_2^+ + \text{Br}$ at photon energies that correspond to the initial formation of the \tilde{X} , \tilde{A} , \tilde{B} , \tilde{C} , \tilde{D} , \tilde{E} , \tilde{F} and \tilde{G} states of parent ion. Similar spectra were also recorded for the process $\text{CBr}_2\text{Cl}_2^+ \rightarrow \text{CBr}_2\text{Cl}^+ + \text{Cl}$ at photon energies of 11.92, 12.20 and 12.85 eV corresponding to the \tilde{E} , \tilde{F} and \tilde{G} states of parent ion. In the case of both these daughter ions, the isotope effect becomes quite complicated here resulting in 6 isotopomers. Allowance has been made for both isotopes of chlorine and bromine. Difficulties arose in the calculation of E_{avail} and hence the experimental fractional ratio due to unknown values in the thermochemistry. By equating the appearance potential of CBrCl_2^+ (10.45 eV) to the enthalpy of the unimolecular reaction $\text{CBr}_2\text{Cl}_2 \rightarrow \text{CBrCl}_2^+ + \text{Br}$, new thermodynamic information can be yielded. It is noted that this estimate only provides an upper limit to $\Delta_r H^0$ and therefore to $\Delta H_f(\text{CBrCl}_2^+)$. The enthalpies of formation for CBr_2Cl_2 and Br are well known (9 and 112 kJ mol⁻¹ respectively at 298K). This yields a value of 905 ± 20 kJ mol⁻¹ for $\Delta H_f(\text{CBrCl}_2^+)$. By approximating the heat of reaction to the appearance potential, the available energy can be calculated by simple subtracting 10.45 eV from the photon energy. The internal energy addition is now not required as the appearance potential is a room temperature measurement. Experimental values of $\langle \text{KE} \rangle_t$ and the fractional ratios as well as the theoretical statistical and impulsive limits are given in Table 4.8.

Table 4.8 Mean translational KE releases ($\langle \text{KE} \rangle_t$) of the two-body fragmentation processes of the valence states of $\text{CBr}_2\text{Cl}_2^+$.

	Fragment	Photon energy / eV	$E_{\text{avail}} / \text{eV}$	$\langle \text{KE} \rangle_t / \text{eV}$	Fractional Ratio		
					Experimental	Statistical	Impulsive
$\text{CBr}_2\text{Cl}_2^+$	CBrCl_2^+	10.78	0.33	0.28±0.03	0.85	0.10	0.19
\tilde{X}							
$\text{CBr}_2\text{Cl}_2^+$	CBrCl_2^+	10.97	0.52	0.41±0.05	0.78	0.10	0.19
\tilde{A}							
$\text{CBr}_2\text{Cl}_2^+$	CBrCl_2^+	11.21	0.76	0.57±0.06	0.75	0.10	0.19
\tilde{B}							
$\text{CBr}_2\text{Cl}_2^+$	CBrCl_2^+	11.37	0.92	0.57±0.07	0.75	0.10	0.19
\tilde{C}							
$\text{CBr}_2\text{Cl}_2^+$	CBrCl_2^+	11.67	1.22	0.65±0.07	0.53	0.10	0.19
\tilde{D}							
$\text{CBr}_2\text{Cl}_2^+$	CBrCl_2^+	11.92	1.47	0.50±0.04	0.34	0.10	0.19
\tilde{E}							
$\text{CBr}_2\text{Cl}_2^+$	CBrCl_2^+	12.20	1.75	0.65±0.05	0.37	0.10	0.19
\tilde{F}							
$\text{CBr}_2\text{Cl}_2^+$	CBrCl_2^+	12.85	2.40	0.50±0.20	0.21	0.10	0.19
\tilde{G}							

\tilde{G}							
$\text{CBr}_2\text{Cl}_2^+$	CBr_2Cl^+	11.92	0.33	0.69 ± 0.04	2.07	0.10	0.30
\tilde{E}							
$\text{CBr}_2\text{Cl}_2^+$	CBr_2Cl^+	12.20	0.61	0.67 ± 0.04	1.09	0.10	0.30
\tilde{F}							
$\text{CBr}_2\text{Cl}_2^+$	CBr_2Cl^+	12.85	1.25	0.68 ± 0.03	0.54	0.10	0.30
\tilde{G}							

^a $E_{\text{avail}} = \text{Photon Energy} - \text{thermochemical threshold for forming the daughter ion} + \text{thermal energy of parent molecule at 298 K}$

^b $\text{Fractional ratio} = \langle \text{KE} \rangle_t / E_{\text{avail}}$

Comparison of the experimental fractional ratios with the statistical and impulsive limits highlights possible problems with either the calculation of excess energy or the difficulty in fitting $\langle \text{KE} \rangle_t$ for complicated isotopomer distributions. The experimental fractional ratios are much higher than those of the calculated limits. As stated earlier, the calculation of $\Delta H_{\text{reaction}}$ provides an upper limit. Therefore the excess energy may be significantly higher, hence providing a lower percentage of energy being partitioned into translation. However, as with both CH_2Br_2 and CH_2Cl_2 , the common trend of decreasing $\langle f \rangle_t$ (experimental) as the photon energy increases is observed.

4.5 Discussion

4.5.1 Elucidation of dominant fragmentation channels.

It is necessary to categorise the various pathways of fragmentation into two types to enable the rationalisation of the trends observed in this chapter. Firstly, the absence of a significant barrier along the reaction coordinate and secondly, the presence of a substantial barrier along the reaction coordinate. The former possesses a loose transition state and is present for processes involving bond fission only. The latter type of dissociation channel is categorised by the transition state which may be expressed as constrained. Constrained transition states occur for processes that involve simultaneous bond cleaving and forming. The height of the barrier critically depends on the amount of steric constraint within the molecule of interest e.g. for the process $\text{CBr}_2\text{X}_2 \rightarrow \text{CBr}_2^+ + \text{X}_2$, the size of the barrier increases with steric constraint and hence the size X. Fragments formed by more than one bond fission will have more than one possible dissociation channel. Comparison of appearance energies with thermochemical thresholds may yield important information regarding the nature of the fragmentation channel. Each channel will have a unique thermochemical threshold, hence the identity of the dominating dissociation channel can be determined.

Fragmentation studies of CCl_3X^+ and CF_2X_2^+ revealed that CCl_3Br^+ , CCl_3F^+ , CF_2Br_2^+ and CF_2Cl_2^+ behave differently to CCl_3H^+ and CF_2H_2^+ . It was found that the former dissociate via the higher energy pathways and vice versa for the latter. The difference in behaviour was rationalised by the small size of the hydrogen atom. In this chapter, analysis is extended to the CX_2Y_2 series (where X, Y = H, Cl or Br). This leads to the question of whether CX_2Y_2^+ dissociates in a similar way to CCl_3X^+ and CF_2X_2^+ . The dissociation of CX_2Y_2^+ is slightly blurred due to the lack of thermochemical data (ΔH_f s of many of the fragment ions) and poor time of flight resolution. This is highlighted if we first consider CH_2Br_2^+ . Fragment ions CH_2Br^+ , CHBr^+ , CBr^+ and CH_2^+ have been observed. It is noted that CHBr_2^+ is not observed although the process $\text{CH}_2\text{Cl}_2 \rightarrow \text{CH}_2\text{Cl}_2^+ + \text{H}$ is observed here and $\text{CH}_2\text{F}_2 \rightarrow \text{CHF}_2^+ + \text{H}$ was detected in a previous study.⁷ There is only one possible dissociation channel for CH_2Br^+ as there is only one bond fission ($\text{CH}_2\text{Br}_2 \rightarrow \text{CH}_2\text{Br}^+ + \text{Br}$). Although CBr^+ has been observed, poor time of flight resolution has rendered the extraction of an appearance potential impossible. In the case of CHBr^+ , as well as the poor time of flight resolution problem there also exists a lack of a value of $\Delta H_f(\text{CHBr}^+)$ in the literature. Therefore it is impossible to calculate a dissociation energy. None of this is the case for formation of CH_2^+ however. Since the value of the appearance potential is lower than the ΔH_{rxn} associated with the highest energy process which produces atomic products, the lower energy process which produces molecular bromine must be involved. This process is likely to have a barrier along the exit channel of the potential energy surface. Whilst considering CH_2Cl_2^+ , no such problems occur with thermochemistry but the problem of time of flight resolution still remains due to the presence of the two hydrogens. CH_2Cl^+ , CHCl_2^+ , CHCl^+ and CH_2^+ have been detected although it is not possible to extract an ion yield plot for CHCl_2^+ due to overlapping fragments resulting from poor time of flight resolution. The relevant channels in this case are CHCl^+ and CH_2^+ . That is, only these two fragments have more than one bond fission and have an associated appearance potential. The appearance potential of CHCl^+ is below the threshold for the high energy pathway and therefore must proceed via the low energy channel forming with HCl as opposed to its atomic counterpart. CH_2^+ forms above the ΔH_{rxn} associated with the highest energy process which produces atomic products. This suggests that the highest energy pathway dominates. The fragmentation of $\text{CBr}_2\text{Cl}_2^+$ is difficult to rationalise due to many unknown heats of formation. CBrCl_2^+ , CBr_2Cl^+ , CBrCl^+ , CCl_2^+ , CCl^+ and CBr^+ have been observed. The heats of formation of CBrCl_2^+ , CBr_2Cl^+ and CBrCl^+ are unknown and hence it is not possible to calculate the ΔH_{rxn} of the possible channels involving these fragments. Therefore the dissociation pathways involving these fragments cannot be determined. Time of flight resolution is not a problem in this case. The appearance potential of CCl_2^+ has been determined to be 13.88 eV, 1.5 eV higher than the lower energy pathway but below the higher channel involving atomic products. It is therefore probable that CCl_2^+ is produced via the higher energy process. The appearance potential of CCl^+ is above the highest energy threshold ($\text{CBr}_2\text{Cl}_2^+ \rightarrow \text{CCl}^+ + 2\text{Br} + \text{Cl}$). This ΔH_{rxn} is over 2 eV higher than the next highest threshold producing $\text{CCl}^+ + \text{BrCl} + \text{Br}$. It is therefore most probable that CCl^+ is produced with atomic products. Formation of

CBr^+ has an appearance potential of 18.2 eV. This value is below the highest energy process, but above the two lower energy channels. It is noted that these lower energy pathways have similar dissociation energies and hence it is not possible to associate the fragmentation unambiguously to one of these channels.

If the CX_2Y_2 series were to behave similarly to the CCl_3X^+ and CF_2X_2^+ series, then CH_2Br_2^+ and CH_2Cl_2^+ would fragment similarly to CCl_3H^+ and CF_2H_2^+ . The latter two molecules fragmented *via* the lowest energy processes, hence constrained transition states were involved with the processes likely to have large barriers along the exit channel. In addition $\text{CBr}_2\text{Cl}_2^+$ would fragment similarly to CCl_3Br^+ , CCl_3F^+ , CF_2Br_2^+ and CF_2Cl_2^+ . The latter molecules fragmented *via* the highest energy processes and hence loose transition states. It has been found that the CX_2Y_2^+ series does not behave similarly and that rationale of steric constraint does not apply here. It is a conclusion of this chapter that the fragmentation pathways cannot be predicted on steric factors alone and that the situation is more complex than first thought. It is also noted that all the molecules presented in this chapter have a similar amount of steric constraint to molecules in the CCl_3X^+ and CF_2X_2^+ series.

4.5.2 Determination of the dissociation dynamics.

The values of $\langle \text{KE} \rangle_t$ and $\langle f \rangle_t$ for the dissociation of CH_2Br_2^+ to CH_2Br^+ indicate that the \tilde{E} state of the parent ion, photoionised at 14.25 eV, dissociates by a mostly impulsive mechanism. The \tilde{F} state of the parent ion photoionised at 14.85 eV dissociates by a statistical mechanism. Unfortunately it was not possible to fit the \tilde{B}/\tilde{C} state, probably due to the small available energy. This trend of decreasing proportion of available energy channelled into translation as the photon energy is increased is probably a reflection of an increase in the density of states as the energy of excitation increases. It is noted that CHBr_2^+ does not appear at any energy even though its formation is thermochemically allowed. Selectivity of dissociation in the \tilde{B}/\tilde{C} state is explained by the fragmentation by an impulsive mechanism. Removal of an electron of predominantly bromine lone pair character, creates a hole localised at the bromine atom, which is subsequently dispersed by rapid charge delocalisation. For fast dissociations, selectivity towards CH_2Br^+ can therefore be observed. Thus, as with CF_2Cl_2^+ , the selectivity can only be achieved for a rapid process.

The values of $\langle \text{KE} \rangle_t$ and $\langle f \rangle_t$ for the dissociation of CH_2Cl_2^+ to CH_2Cl^+ indicate that there is a trend of decreasing proportion of available energy channelled into translation as the photon energy is increased. As with the formation of CH_2Br^+ , this probably reflects the increase in the density of states as the energy of excitation increases. Initial excitation of the \tilde{B}/\tilde{C} state of parent ion actually exceeds the fraction of energy partitioned into translation that the impulsive model predicts. This model assumes that the recoiling fragments are not rigid and that some of this energy is partitioned into vibration. It therefore

seems likely that the amount of energy partitioned into vibration in the \tilde{B}/\tilde{C} state is less than predicted by the pure impulsive model. This can be rationalised if the repulsion between the two atoms of the breaking bond is not sufficient to cause energy transfer to the vibrational modes of the daughter fragments which recoil as rigid bodies.

The \tilde{D} state appears to dissociate by an impulsive mechanism and the \tilde{E} state by a hybrid of both impulsive and statistical mechanisms. Although the appearance energy of CHCl_2^+ could not be determined accurately it is unlikely to form close to its thermochemical threshold for similar reasons to CHBr_2^+ not forming.

The values of $\langle \text{KE} \rangle_t$ and $\langle f \rangle_t$ for the dissociation of $\text{CBr}_2\text{Cl}_2^+$ to CBr_2Cl^+ and CBrCl_2^+ indicate that there are possible problems with either the calculation of the excess energy or difficulty in fitting $\langle \text{KE} \rangle_t$ for complicated isomer distributions. If the former is true then this provides good evidence that the actual thermochemical threshold for the formation of CBr_2Cl^+ and CBrCl_2^+ is much lower than the appearance potential of these ions. This is similar to the formation of CF_3^+ from CF_4 .² Comparison of the experimental fractional ratios with statistical and impulsive limits yield little information about the dynamics of this system. There is however a trend for the experimental fractional ratio to decrease as the photon energy increases.

4.6 CONCLUSIONS

A comprehensive study of the fragmentation behaviour of the valence states of CX_2Y_2^+ (X, Y = H, Cl or Br) over the photon energy range $\sim 10 - 25$ eV has been performed. Threshold photoelectron spectra and ion yield plots have been obtained with the experiment operating in scanning energy mode. In general, the threshold electron spectra are in excellent agreement with those measured using He I and He II radiation. Full characterisation of the data for CH_2Cl_2 and CH_2Br_2 is hampered due to poor time of flight resolution. In addition, interpretation of the ion yield plots of CH_2Br_2 and CBr_2Cl_2 is hampered by a lack of thermochemical data. In cases where ions can be produced in a variety of dissociation channels, comparison of the appearance potential with $\Delta_f H^\circ$ indicates that the CX_2Y_2 series does not exhibit similar behaviour to the CCl_3X or CF_2X_2 series.^{6,7} That is, the behaviour observed for the CCl_3X and CF_2X_2 series, which can be rationalised by loose- or tightly-constrained transition states, is not observed for CX_2Y_2 .

High resolution (8 ns) TPEPICO-TOF spectra have been measured for the dissociations which involve the fission of a single C-X(Y) bond, with the experiment operating in the fixed energy mode. Values of $\langle \text{KE} \rangle_t$ and $\langle f \rangle_t$ have been determined, and those predicted for statistical and pure impulsive models have been calculated. In general, there is a trend from impulsive to statistical behaviour as the photon energy

increases. The results show clearly that the molecules do not reach the large molecule limit until highly excited valence states have been populated.

4.7 References :

1. J. C. Creasey, H. M. Jones, D. M. Smith, R. P. Tuckett, P. A. Hatherly, K. Codling and I. Powis, *Chem. Phys.*, 1993, **174**, 441.
2. J. C. Creasey, D. M. Smith, R. P. Tuckett, K. R. Yoxall, K. Codling and P. A. Hatherly., *J Phys Chem.*, 1996, **100**, 4350.
3. D. M. Smith, R. P. Tuckett, K. R. Yoxall, K. Codling and P. A. Hatherly, *Chem. Phys. Lett.*, 1993, **216**, 493.
4. D. M. Smith, R. P. Tuckett, K. R. Yoxall, K. Codling, P. A. Hatherly, J. F. M. Aarts and M. Stankiewicz, *J. Chem. Phys.*, 1994, **101**, 10559.
5. K.J. Boyle, G.K. Jarvis and R.P. Tuckett, *J. Chem. Soc. Farad. Trans.*, 1998, **94**, 1045.
6. D. P. Seccombe, R. Y. L. Chim, G. K. Jarvis and R. P. Tuckett, *Phys. Chem. Chem. Phys.*, 2000, **2**, 769.
7. D. P. Seccombe, R. P. Tuckett and B. O. Fisher, *J. Chem. Phys.*, 2001, **114**, 4074.
8. R. I. Reed, W. [Snedden](#)., *J. Chem. Soc. Faraday Trans.*, 1956, **55**, 876.
9. M.A.Haney, J.L. Franklin, *J.Chem. Phys.*, 1968, **48**, 4093.
10. J.J. DeCorpo, D.A. Bafus, J.L. Franklin, *J. Chem. Thermodyn.*, 1971, **3**, 125.
11. B.P. Tsai, T. Baer, A.S. Werner, *J. Phys. Chem.*, 1975, **79**, 570.
12. O. Kaposi, M. Riedel, K. Vass-Balthazar, G.R. Sanchez, L. Lelik, *Acta Chim. Acad. Sci. Hung.*, 1976, **89**, 221.
13. J.L. Holmes, F.P. Lossing, R.A. McFarlane, *Int. J. Mass Spectrom. Ion Phys.*, 1988, **86**, 209.
14. Z.-X. Ma, C.-L. Liao, C.Y. Ng, N.G. Ma, W.-K. Li, *J. Chem. Phys.*, 1993, **99**, 6470.
15. A.G. Harrison, T.W. Shannon, *Can. J. Chem.*, 1962, **40**, 1730.
16. R.H. Martin, F.W. Lampe, R.W. Taft, *J. Am. Chem. Soc.*, 1966, **88**, 1353.
17. J.L. Franklin, M.A. Haney, *Energy distribution in ionic decomposition processes, Recent Developments in Mass Spectroscopy*, ed. K. Ogata and T. Hayakawa Baltimore Univ. Park Press, Baltimore, MD, 1970, 909.
18. F.P. Lossing, *Bull. Soc. Chim. Belg.*, 1972, **81**, 125.
19. A.S. Werner, B.P. Tsai, T. Baer, *J. Chem. Phys.*, 1974, **60**, 3650.
20. W. Von Niessen, L. Asbrink, G. Bieri, *J. Electron Spectrosc. Relat. Phenom.*, 1982, **26**, 173.
21. K. Wittel, H. Bock, *Chem. Ber.*, 1974, **107**, 317.
22. T. Pradeep and D. A. Shirley, *J. Electron Spectrosc. Relat. Phenom.*, 1993, **66**, 125.

23. A. W. Potts, H. J. Lempka, D. G. Streets and W. C. Price, *Phil. Trans. Roy. Soc. Lond. A.*, 1970, **268**, 59.
24. R. N. Dixon, J. N. Murrell and B. Narayan, *Mol. Phys.*, 1971, **20**, 611.
25. K. Kimura, S. Katsumata, Y. Achiba, T. Yamazaki, S. Iwata, *Handbook of HeI Photoelectron Spectra of Fundamental Organic Compounds*, Japan Scientific Soc. Press, Tokyo, 1981.
26. M.J.S. Dewar, S.D. Worley, *J. Chem. Phys.*, 1969, **50**, 654.
27. V. Cermak, *Collection Czech. Chem. Commun.*, 1968, **33**, 2739.
28. J.C. Bunzli, D.C. Frost, F.G. Herring, C.A. McDowell, *J. Electron Spectrosc. Relat. Phenom.*, 1976, **9**, 289.
29. M. W. Chase, *J. Phys. Chem. Ref. Data*, 1998, Monograph No. 9.
30. S. G. Lias, J. E. Bartmess, J. F. Liebman, J. L. Holmes, R. D. Levin and W. G. Mallard, *J. Phys. Chem. Ref. Data*, 1988, **17**, supplement 1.
31. T. Shimanouchi, *Tables of Molecular Vibrational Frequencies consolidated volume I National Bureau of Standards*, 1972, 1.
32. G. H. Wannier, *Phys. Rev.*, 1953, **90**, 817.
33. J. L. Franklin, P. M. Hierl and D. A. Whan, *J. Chem. Phys.*, 1967, **47**, 3184.

CHAPTER 5 : FRAGMENTATION OF ENERGY-SELECTED SF₅CF₃⁺ PROBED BY THRESHOLD PHOTOELECTRON PHOTOION COINCIDENCE (TPEPICO) SPECTROSCOPY : THE BOND DISSOCIATION ENERGY OF SF₅-CF₃, AND ITS ATMOSPHERIC IMPLICATIONS

5.1 Introduction

The greenhouse effect is usually associated with small polyatomic molecules such as CO₂, H₂O, CH₄, N₂O and O₃. The ‘natural’ greenhouse gases, mainly CO₂ and H₂O, have been responsible for hundreds of years for maintaining the temperature of the earth at *ca.* 290 K, suitable for habitation. The ‘enhanced’ greenhouse gases, mainly CH₄, N₂O and O₃, have concentrations in the atmosphere which have increased dramatically in the last 50-100 years, have infrared (IR) absorptions where CO₂ and H₂O do not absorb, and are believed to be the main culprits for global warming. It is now clear, however, that there are larger polyatomic gases of low concentrations in the atmosphere which can contribute significantly to global warming because of their exceptionally strong IR absorption in the parts of the 5-25 μm region where other greenhouse gases do not absorb. A notable example is SF₆, which has a global warming potential (GWP) of 22,200 relative to CO₂ over a time horizon of 100 years. In a recent paper,¹ Sturges *et al.* have detected SF₅CF₃ in the atmosphere. Previously unreported, it is believed to be anthropogenic in nature, and to be a breakdown product of SF₆ in high voltage equipment. IR absorption measurements have shown that it has the highest radiative forcing per molecule of any gas found in the atmosphere to date (0.57 W m⁻² ppb⁻¹). Antarctic firm measurements suggest that it has grown from a concentration of near zero in the late 1960s to about 0.12 parts per trillion in 1999, and stratospheric profiles suggest that the lifetime of this species in the atmosphere is between several hundred and a few thousand years. It is estimated that the GWP of SF₅CF₃ is 18,000 relative to CO₂, with only SF₆ having a higher value. The authors conclude that, whilst still a relatively minor problem, nevertheless it is important to control the source(s) of SF₅CF₃ into the atmosphere in order to guard against an undesirable accumulation of this strong greenhouse gas.

From an applied, atmospheric viewpoint, one of the main questions to answer is whether SF₅-CF₃ can be broken down by UV photodissociation in the stratosphere, or whether the loss of this species from the atmosphere is governed by bimolecular ionic reactions (*i.e.* electron attachment and ion-molecule reactions) and vacuum-UV photodissociation processes in the mesosphere. The latter processes are considered in the next chapter, but the strength of the SF₅-CF₃ bond is needed to answer this fundamental question. Photodissociation generally occurs through excitation of a molecule to a repulsive state. Close to the energy threshold, the cross-section for photodissociation is negligibly small. Thus,

CF₄ has a dissociation energy (to CF₃ + F) of 5.61 eV,² but VUV photons with energies in excess of 12 eV are required to photodissociate CF₄.³ Likewise, the bond dissociation energy of SF₆ (to SF₅ + F) is 3.82 eV,⁴ but photodissociation is not observed until the photon energy exceeds *ca.* 10 eV.⁵ In the lower stratosphere, the highest-energy photons have an energy of *ca.* 4.0 eV. It seems unlikely, therefore, that SF₅CF₃ will be destroyed in this region through photolytic breaking of either a C–F or a S–F bond. If the S–C bond in SF₅CF₃ is relatively weak (< 2.5 eV or 250 kJ mol⁻¹), SF₅CF₃ could, in principle, be broken down by UV photolysis. However, although an absorption spectrum has not been recorded, there is no evidence from a preliminary electron energy loss spectrum for dissociative excited states of SF₅CF₃ lying *ca.* 3–8 eV above its ground state.⁶ If the bond strength is rather greater, then the removal of SF₅CF₃ from the atmosphere will, like CF₄ and SF₆, be governed by ionic or vacuum-UV processes occurring in the mesosphere.⁷

This chapter reports a comprehensive study of the fragmentation of the parent cation of SF₅CF₃ excited by photons in the range 12–26 eV by threshold photoelectron – photoion coincidence (TPEPICO) spectroscopy. It follows on from previous studies of CF₄⁺ and SF₆⁺.^{8,9} A technique, developed for recent work on SeF₆ and TeF₆ and described in Chapter 8,¹⁰ has been used here to determine the dissociative ionisation energy of CF₄ (to CF₃⁺ + F + e⁻), SF₆ (to SF₅⁺ + F + e⁻) and SF₅CF₃ (to CF₃⁺ + SF₅ + e⁻) at 0 K. In this chapter, these thresholds are called the *first* dissociative ionisation energies of these molecules, although it is noted that the dissociation channel SF₅CF₃ → SF₄⁺ + CF₄ + e⁻ lies lower in energy than CF₃⁺ + SF₅ + e⁻ (Section 5.6). It is then possible to determine the SF₅–CF₃ bond dissociation energy and the enthalpy of formation of SF₅CF₃ at 0 K. Also, the threshold photoelectron spectrum of SF₅CF₃ is reported in the range 12–26 eV, the coincidence ion yields over this energy range, and the mean translational kinetic energy (KE) release into the fragment ions. Some indication of the dynamics of photodissociation of excited electronic states of SF₅CF₃⁺ can be inferred.

5.2 The first dissociative ionisation energy (DIE) of CF₄, SF₆ and SF₅CF₃

The parent cations of CF₄, SF₆ and SF₅CF₃ have the common property that the parent ion is not observed in a conventional 70 eV electron-impact mass spectrum.¹¹ In other words, the ground electronic state of these cations is dissociative in the Franck-Condon region, dissociating on a timescale that is very much faster than the transit time of the ion through a magnetic or quadrupole mass spectrometer. For CF₄⁺ and SF₆⁺, it is obvious that dissociation must occur by cleavage of a single C–F or S–F bond to form CF₃⁺ or SF₅⁺ + F. With SF₅CF₃⁺, it is assumed that cleavage of the S–C bond will occur. Since the CF₃⁺ + SF₅ + e⁻ threshold lies *ca.* 0.8 eV below that of SF₅⁺ + CF₃ + e⁻ (Section 5.2), the former products are expected to be produced from photoionisation of SF₅CF₃ through the repulsive ground state of the parent cation.

The first DIE of CF_4 , SF_6 and SF_5CF_3 is defined as the 0 K energy of $\text{CF}_3^+ + \text{F} + \text{e}^-$, $\text{SF}_5^+ + \text{F} + \text{e}^-$, and $\text{CF}_3^+ + \text{SF}_5 + \text{e}^-$ relative to the ground vibronic state of CF_4 , SF_6 and SF_5CF_3 , respectively.

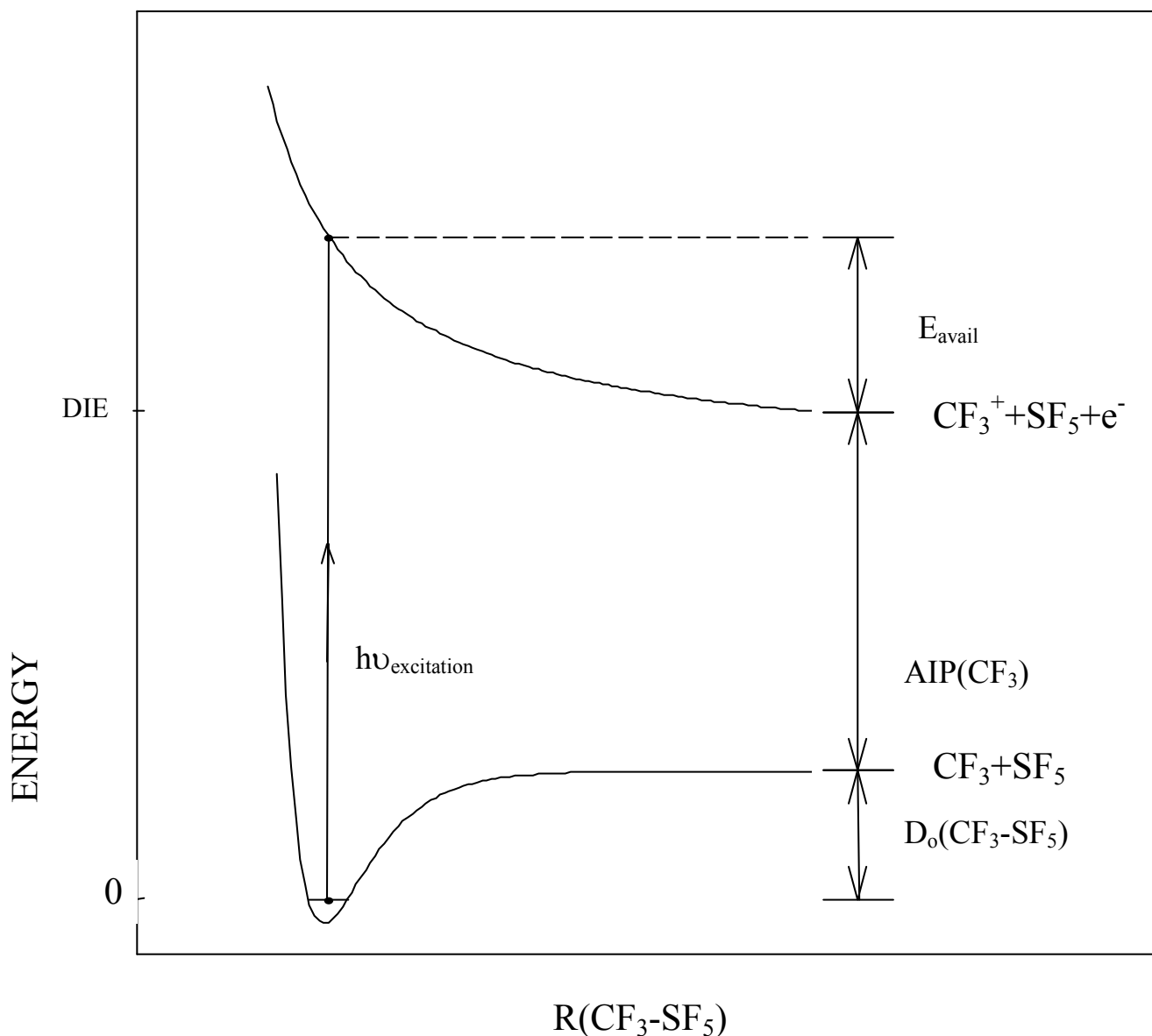


Figure 5.1 The energetics of dissociation of the ground state of SF_5CF_3 and SF_5CF_3^+ (see equations 5.1 and 5.2).

The determination of the DIE of species whose ground electronic state of the parent ion is repulsive in the Franck-Condon region is a notoriously difficult problem, because its value is likely to be significantly less than the energy corresponding to the onset of ionisation of the neutral precursor (Fig. 5.1). Thus the photoelectron spectrum of the precursor molecule can only give an upper bound to its first DIE. This problem is well known for both CF_4 and SF_6 , and the DIE of these species has been the subject of much controversy. From Fig. 5.1, it is clear that :

$$\text{DIE (AB)} = D_0(\text{A-B}) + \text{AIP (A)} \quad (5.1)$$

where A–B refers to CF₃–F, SF₅–F or CF₃–SF₅, D₀(A–B) is the dissociation energy of the A–B bond, and AIE (A) is the adiabatic ionisation potential of the A free radical. The principal unknown in the estimation of the DIE of CF₄ and SF₆ is the AIP of the CF₃ and SF₅ radicals. Whilst the CF₃–F and SF₅–F bond dissociation energies are known to an accuracy of *ca.* 10 kJ mol⁻¹ or 0.1 eV,^{2,4} the experimental values for the AIP of the CF₃ and SF₅ radicals are still uncertain at the level of *ca.* ±0.3 and ±1.0 eV, respectively. The problem with CF₃ arises essentially due to the change from pyramidal to planar geometry upon ionisation. A consensus has emerged that the AIP of CF₃ lies between 8.8 and 9.1 eV,^{12,13} with the most complete *ab initio* calculation giving 9.05 eV.¹⁴ Experimental values for the AIP of SF₅ lie in the larger range 9.6–11.5 eV, a review being given in ref. 4. The consensus now is that the high values are in error, and the value of 9.60 ± 0.05 eV⁴ obtained from a guided ion beam study of the charge transfer reaction of SF₅⁺ with Xe is probably correct; the most complete *ab initio* study to date gives 9.71 eV.¹⁵ For SF₅CF₃, the estimation of its first DIE needs a knowledge of both the SF₅–CF₃ bond dissociation energy and the AIP of the CF₃ radical. Neither is well characterised.

One method to determine the DIE of CF₄, SF₆ and SF₅CF₃ directly is to use the fact that, in the Franck-Condon region, the ground state of the parent cation lies above the DIE, and perform a photoelectron – photoion coincidence experiment to measure the translational KE released into the A⁺ + B fragments. From an analysis of the width and shape of the fragment ion (A⁺) time-of-flight distribution in the (T)PEPICO spectrum measured at a photon energy *hν*, it is possible to determine the kinetic energy released in fragmentation at that one energy. This will correspond to some fraction of the available energy, where

$$E_{\text{avail}} = h\nu + (\text{thermal energy of AB}) - \text{DIE(AB)} \quad (5.2)$$

The size of the fraction is governed by the dynamics of the decay mechanism,¹⁶ and cannot be determined directly from a measurement at one single photon energy. However, by measuring the KE release continuously as a function of photon energy and assuming that the fractional KE release is independent of energy, an extrapolation to a KE release of zero gives an intercept corresponding to the DIE of AB. This method was used to determine the DIE of SeF₆ and TeF₆,¹⁰ and obtained values for the 0 K enthalpy of formation of SeF₅⁺ and TeF₅⁺ (see Chapter 8). However, there were no other data with which to compare the results, so the method could not be validated. Here, it is used to determine the DIE for CF₄ and SF₆. From the former result, the 0 K enthalpy of formation of CF₃⁺ and, *via* Δ_fH⁰₀(CF₃),² the AIP of CF₃ is determined. The value of the AIP, 8.84 ± 0.20 eV, is in good agreement with recent experimental

determinations^{12,13,17} and theory.^{14,18} The SF₆ result determines $\Delta_f H^0_0$ (SF₅⁺). Using the recommended value for $\Delta_f H^0_0$ (SF₅) from the ion beam study of Fisher *et al.*,⁴ a value for the AIP of SF₅ of 9.8 ± 0.2 eV is obtained. This value is at the lower end of the wide range of values in the literature and, within error limits, is in agreement with the guided ion beam result.⁴ Following these ‘test’ experiments, the first DIE of SF₅CF₃ has been measured. Using the AIP (CF₃) result above, in an indirect manner, the dissociation energy of the SF₅–CF₃ bond has been determined.

5.3 Experimental

The photoionisation experiments required the use of the electron analyser and the time of flight drift tube described earlier in Chapter 2. Synchrotron radiation dispersed with the 1m Seya-Namioka monochromator on beamline 3.1 at SRS (Daresbury, UK) was used as the photon source. The two gratings used were calibrated using argon. Spectra were flux normalised *via* the visible fluorescence of a NaSal window. SF₅CF₃ was manufactured by Flura Corporation, USA (99.99 %) and used without further purification. The gas bottle was immersed in a jacketed ice-cooled water bath to stabilise the temperature and hence the pressure.

5.4 Determination of the total mean translational kinetic energy release, $\langle KE \rangle_t$

The kinetic energy release distribution and hence the total, mean translational kinetic energy release, $\langle KE \rangle_t$, were determined from the fragment ion peak shape obtained in the fixed photon energy experiment by the method described in detail elsewhere.²¹ Each spectrum is fitted to a basis set of KE releases, the kinetic energy release distribution (KERD), given by $\epsilon_i(n) = (2n-1)^2 \Delta E$, with $n=1,2,3 \dots$. ΔE , the minimum energy release in the basis set, depends primarily on the statistical quality of the data ; in theory, the higher the signal-to-noise ratio of the spectrum, the lower ΔE and the higher n can be set to obtain the best fit.²¹ Each computed peak in the KERD spans the range of energies $4(n-1)^2 \Delta E$ to $4n^2 \Delta E$. The reduced probability of each discrete energy, $P[\epsilon_i(n)]$, is varied to minimise the least-squared errors between the simulated and experimental TOF spectra. From the derived $P[\epsilon_i(n)]$ vs. $\epsilon_i(n)$ distribution, it is simple to calculate the total mean translational KE release, $\langle KE \rangle_t$. The analysis assumes a two-body process, corresponding to the cleavage of one bond only, and conservation of linear momentum. This method is clearly applicable for fragmentation of CF₄⁺, SF₆⁺ and SF₅CF₃⁺ to CF₃⁺ + F, SF₅⁺ + F, and CF₃⁺ + SF₅, respectively, but not for processes such as dissociation of SF₅CF₃⁺ to SF₃⁺ + CF₄ + F. The analysis does not allow for anisotropy in the dissociation. The values of $\langle KE \rangle_t$ can be compared with E_{avail} (defined in equation (5.2)) to determine the fraction of the available energy being channelled into translational energy of the fragments. In the experiments to determine the DIEs of CF₄, SF₆ and SF₅CF₃, this procedure is simplified by constraining n to be 1, and only varying ΔE (section 5.1). The single peak

in the KERD, convoluted with the thermal energy of the parent molecule prior to ionisation, then spans the range of energies from 0 to $4\Delta E$, with a mean value of $2\Delta E$. The probability is constant within this range, and zero outside. This mean value is likely to be very similar to the value of $\langle KE \rangle_t$ obtained from the full KERD.

For a pure impulsive dissociation, applicable to the ground states of CF_4^+ , SF_6^+ and $SF_5CF_3^+$, the release of energy occurs after the fragment ion has relaxed to its final geometry.^{23,24} The repulsion of the atoms as the bond breaks is then so great that intramolecular collisions result between the recoiling atoms and the remainder of their recoiling fragments, and transfer of energy occurs to vibrational modes of the fragments. If the dissociation applies a torque to the fragments, rotation may also be excited. Under these circumstances, $\langle KE \rangle_t$ and E_{avail} are related by simple kinematics :²³

$$\frac{\langle KE \rangle_t}{E_{avail}} = \frac{\mu_b}{\mu_f} \quad (5.3)$$

where μ_b is the reduced mass of the two atoms whose connecting bond is broken, and μ_f is the reduced mass of the two products of the dissociation. This model was developed for dissociation of polyatomic ions to a fragment molecular ion and neutral atom,²³ but it is simple to show that it is valid also for a *molecular* neutral fragment. The maximum fraction of the available energy that can be channelled into translational energy of the products is predicted by this model ; for cleavage of the C–F bond in CF_4^+ , S–F bond in SF_6^+ , and S–C bond in $SF_5CF_3^+$, this fraction is 0.49, 0.72 and 0.20, respectively. The model predicts a linear dependence of $\langle KE \rangle_t$ with E_{avail} . The DIE can be found by extrapolating the plot of $\langle KE \rangle_t$ vs. $h\nu$ to $\langle KE \rangle_t=0$. Being a classical model, the extrapolation should be linear even for very low values of $\langle KE \rangle_t$.

By comparison, the minimum fraction of the available energy is channelled into translation for a statistical dissociation. Klotz²⁵ has then shown that, for dissociation of a parent ion to a daughter ion plus neutral atom, $\langle KE \rangle_t$ and E_{avail} are related by :

$$E_{avail} = \frac{r-1}{2} \langle KE \rangle_t + \langle KE \rangle_t + \sum_i \frac{h\nu_i}{\exp(h\nu_i / \langle KE \rangle_t) - 1} \quad (5.4)$$

where r and ν_i are the number of rotational degrees of freedom and the vibrational frequency of the i th vibrational mode of the daughter ion. Such dissociations assume that the ground electronic state of the parent ion is bound, at least in some regions of its multi-dimensional potential energy surface, and

knowledge of the vibrational frequencies of the daughter ion is required. If these values are not known, it is possible to estimate a lower limit to the fractional release by :

$$\frac{\langle \text{KE} \rangle_t}{E_{\text{avail}}} = \frac{1}{x + 1} \quad (5.5)$$

where x is the number of vibrational degrees of freedom in the transition state.²⁶ For SF_5CF_3^+ , $x=24$, leading to a fractional release > 0.04 . From eqn (4), $\langle \text{KE} \rangle_t$ is approximately proportional to E_{avail} . The extrapolation to zero $\langle \text{KE} \rangle_t$, however, is not completely linear, with a higher slope when approaching threshold as quantum effects become important. A linear extrapolation can therefore give a value for the DIE which is too low, and an underestimation of the AIE of the A radical.

5.5 Results

5.5.1 Measurement of the first dissociative ionisation energy of CF_4 and SF_6

To validate the method for determining the first DIE of SF_5CF_3 , the TPEPICO spectrum of CF_4 and SF_6 in the scanning photon energy mode from the onset of ionisation (*ca.* 15.5 and 15.3 eV, respectively) over the range of energies of the ground and low-lying excited states of the parent ion was recorded. For CF_4 , the spectrum was recorded from 66 to 88 nm (15.5 to 18.8 eV) in 64 equally-spaced wavelength channels. The integrated accumulation time per wavelength channel ranged from *ca.* 20-40 minutes. This energy range encompasses the onset of ionisation of CF_4 through the $\tilde{\text{X}}^2\text{T}_1$, $\tilde{\text{A}}^2\text{T}_2$ and $\tilde{\text{B}}^2\text{E}$ states of CF_4^+ . These three ionic states all dissociate to CF_3^+ . The dissociation mechanism of the $\tilde{\text{A}}^2\text{T}_2$ and $\tilde{\text{B}}^2\text{E}$ states is uncertain.²⁴ However, it seems likely that the low-energy parts of the $\tilde{\text{X}}^2\text{T}_1$ state dissociate directly in an impulsive manner from its repulsive potential energy surface to $\text{CF}_3^+ + \text{F}$.

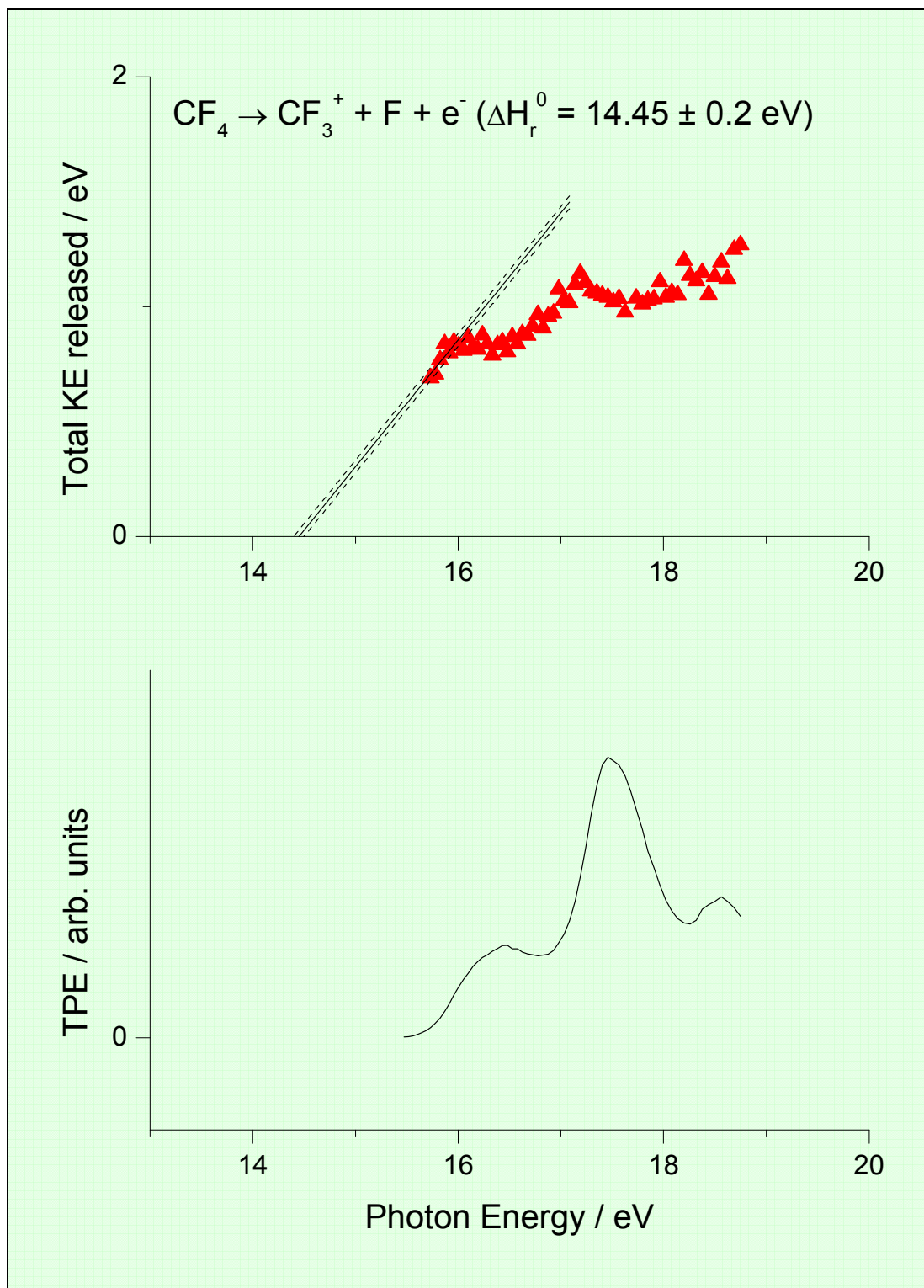


Figure 5.2 (a) Mean total kinetic energy released in the reaction $\text{CF}_4 + h\nu \rightarrow \text{CF}_3^+ + \text{F} + \text{e}^-$ for photon energies in the range 15.5 to 18.8 eV. A linear extrapolation to zero kinetic energy gives the dissociative ionisation energy of CF_4 , 14.45 ± 0.20 eV. The error in each value of the kinetic energy release is *ca.* 20%. (b) Threshold photoelectron spectrum (TPES) of CF_4 over the same range of energies.

Fig 5.2(a) reveals the mean translational KE released for fragmentation to $\text{CF}_3^+ + \text{F}$, whilst Fig 5.2(b) shows the threshold photoelectron spectrum (TPES) of CF_4 over the energy range 15.5 to 18.8 eV. The KE data were extracted from the multiple TOF spectra by the simplified way described in Section 5.4. As

an example, Fig. 5.3(a) shows the TOF spectrum for CF_3^+ from CF_4 recorded at a photon energy of 16.05 eV, for which a mean KE release of 0.81 ± 0.11 eV was obtained. A few TOF spectra were checked more rigorously by determining the full KE release distribution (Section 4), but the $\langle \text{KE} \rangle_t$ values showed little deviation from the values shown in Figures 5.2(a). Values of the mean KE release range from 0.7 to 1.3 eV, with a general trend of an increasing KE release as the photon energy increases. However, the increase is not linear, suggesting that the dissociation mechanism varies for different parts of the $\tilde{\text{X}}^-$, $\tilde{\text{A}}^-$ and $\tilde{\text{B}}^-$ -state potentials of CF_4^+ . There appears to be a trend for a linear increase in the KE release when $h\nu$ corresponds to energies below the Franck-Condon maximum of each of these three states of CF_4^+ . As the photon energy passes through each Franck-Condon maximum, the KE release then appears to decrease. This phenomenon is also observed in the $\tilde{\text{X}}$, $\tilde{\text{A}}$, $\tilde{\text{B}}$ and $\tilde{\text{C}}$ states of SF_6^+ (see below). One explanation for this effect is that, as the photon energy is increased across a photoelectron band, symmetric vibrations are excited. If these modes do not couple efficiently to the reaction coordinate, the additional energy supplied by the photon will not all appear as an increase in the translational energy of the products. It should also be noted that these effects are only observed due to the high signal-to-noise ratio of the TPEPICO spectra. In particular, the spectra are superior to those of SeF_6^+ and TeF_6^+ ,¹⁰ where no such effects were observed. Only a linear increase in the KE release with increasing photon energy over the range of the ground and first three excited electronic states was observed for SeF_6^+ and TeF_6^+ ,¹⁰ with any small deviations being obscured by the limited signal-to-noise ratio of these spectra.

To determine the DIE of CF_4 , the KE releases from only the eight lowest photon energies of Fig. 5.2(a) have been extrapolated, since impulsive dissociation is most likely to pertain for these points. These data points lie on a straight line with a positive slope of 0.55. This value for the fractional energy release is consistent with the prediction of the pure-impulsive dissociation model, 0.49. Assuming that the decay mechanism of the $\tilde{\text{X}}^2\text{T}_1$ state of CF_4^+ does not change if it were possible to access the potential energy curve at energies below 15.5 eV, the extrapolation of this linear region to zero KE gives the first DIE of CF_4 to be 14.45 ± 0.20 eV. Using enthalpies of formation at 0 K for CF_4 (-927 kJ mol^{-1}) and F ($+77 \text{ kJ mol}^{-1}$),²⁷ a $\Delta_f H^\circ(\text{CF}_3^+)$ at 0 K of $390 \pm 19 \text{ kJ mol}^{-1}$ is determined. Constraining $\Delta_f H^\circ_0(\text{CF}_3)$ to be $-463 \pm 4 \text{ kJ mol}^{-1}$,² the adiabatic ionisation potential (AIP) of the CF_3 radical is determined to be $853 \pm 19 \text{ kJ mol}^{-1}$ or 8.84 ± 0.20 eV. It is noted that the linear region of the graph (Fig. 5.2(a)) leading to the Franck-Condon maximum of the $\tilde{\text{A}}$ state of CF_4^+ also appears to extrapolate to an intercept of 14.45 eV, but with a reduced slope.

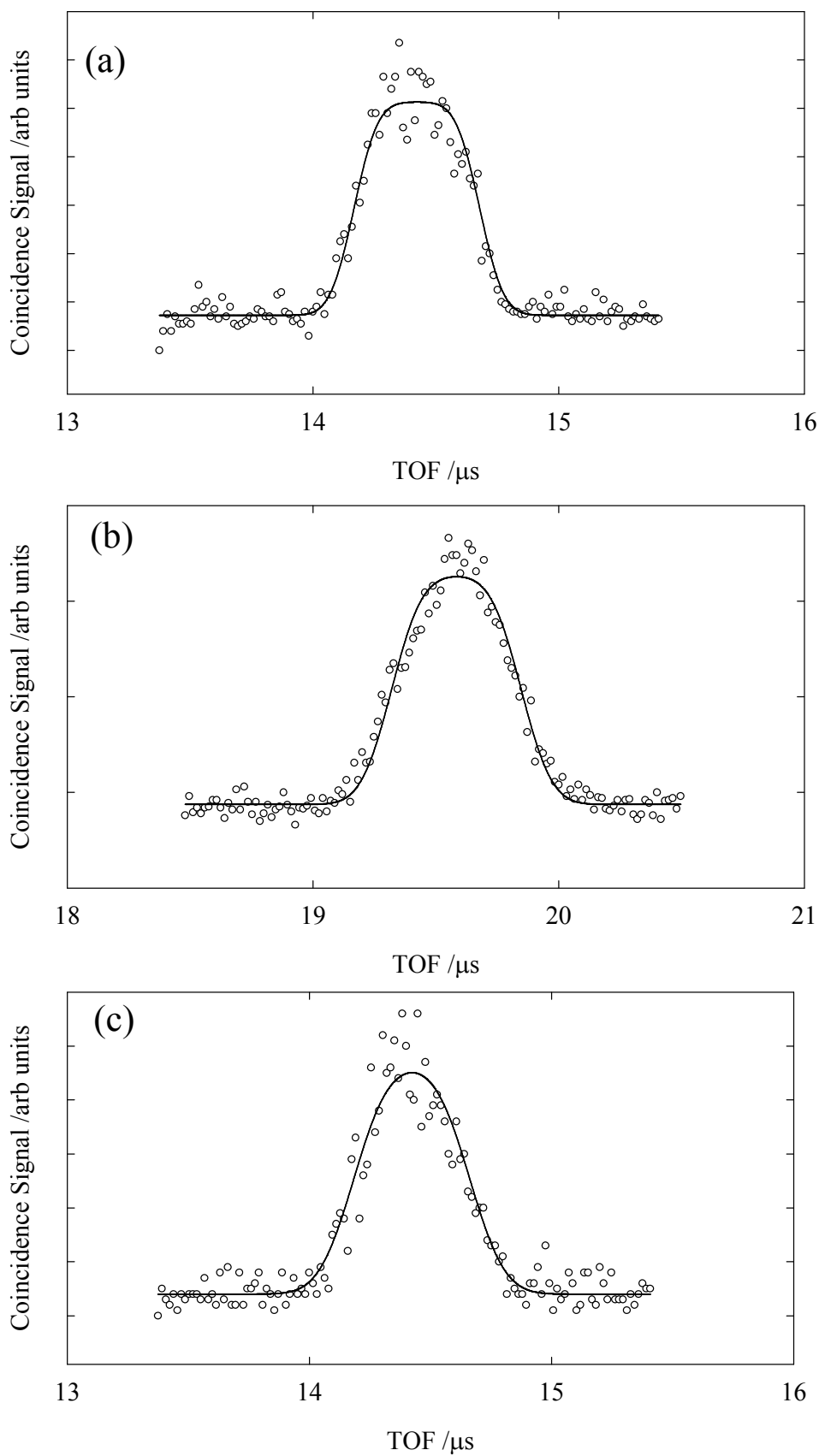


Figure 5.3 TPEPICO-TOF spectra (open circles) for (a) $\text{CF}_3^+ / \text{CF}_4$, (b) $\text{SF}_5^+ / \text{SF}_6$ and (c) $\text{CF}_3^+ / \text{SF}_5\text{CF}_3$ recorded at photon energies of 16.05, 15.72 and 14.09 eV, respectively. Shown as solid lines, the data fit to mean kinetic energy releases of 0.81, 0.83 and 0.24 eV, respectively (see text).

A similar experiment was performed for SF₆ over the range 65 to 82 nm (15.1 to 19.1 eV). This energy range encompasses the \tilde{X}^2T_{1g} , \tilde{A}^2T_{1u} , \tilde{B}^2T_{2u} and \tilde{C}^2E states of SF₆⁺, all of which dissociate solely to SF₅⁺.⁸ The method of analysis was that used for CF₃⁺/CF₄. Fig 5.4(a) shows the mean KE measured for fragmentation to SF₅⁺ + F as a function of photon energy, whilst Fig 5.4(b) shows the TPES of SF₆. Only one isotopomer of the daughter ion (³²S¹⁹F₅⁺) was used to determine the mean KE releases. As an example, Fig. 5.3(b) shows the TOF spectrum of SF₅⁺/SF₆ recorded at 15.72 eV, from which a mean KE release of 0.83 ± 0.07 eV was determined. The general trend of an increasing KE release with increasing photon energy is observed but, as in CF₄, the increase is not linear. Data from the eleven lowest photon energies fit to a straight line with a slope of 0.39, whereas the pure-impulsive model predicts a fractional energy release of 0.72. This discrepancy may relate to the non-planarity of the fragment SF₅⁺ cation. Indeed, there is even uncertainty in the geometry of this ion, with two isomers (one square pyramidal C_{4v}, one trigonal bipyramid D_{3h}) predicted to have comparable energies,²⁸ although this prediction has been disputed.¹⁵ Extrapolation to a KE release of zero yields the DIE of SF₆ to SF₅⁺ + F + e⁻ to be 13.6 ± 0.1 eV. Using the 0 K enthalpy of formation for SF₆ (-1206 kJ mol⁻¹), the value of Δ_fH⁰ (SF₅⁺) is directly determined to be 29 ± 10 kJ mol⁻¹. Constraining Δ_fH⁰ (SF₅) to the value of -915 ± 18 kJ mol⁻¹ recommended by Fisher *et al.*,⁴ the AIP of the SF₅ radical is determined to be 944 ± 21 kJ mol⁻¹ or 9.8 ± 0.2 eV. Again, it is noted that the linear region of Fig. 5.4(a) under the Franck-Condon maximum of the \tilde{A} state of SF₆⁺ at 17.0 eV appears to extrapolate back to the same intercept of 13.6 eV.

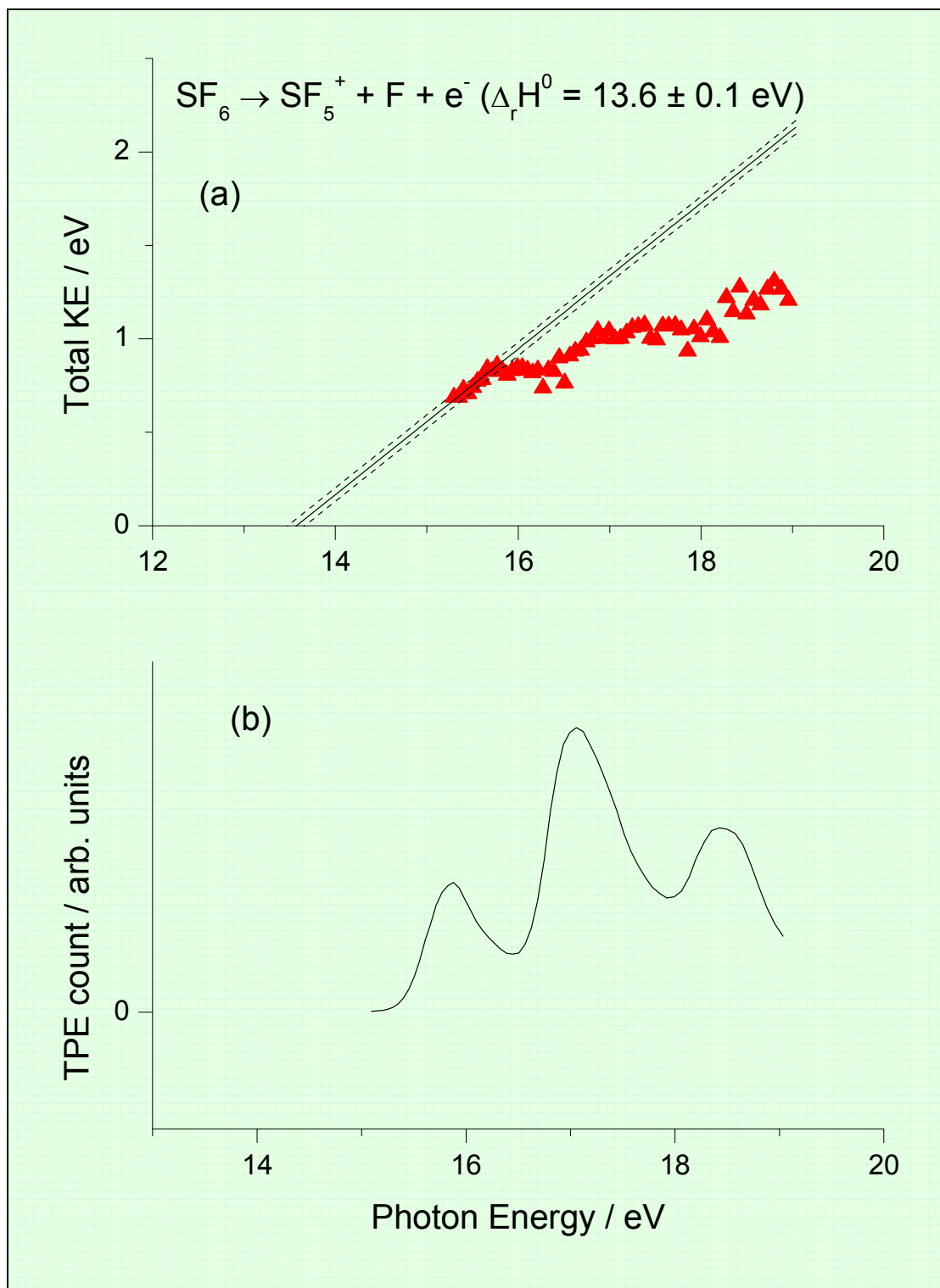


Figure 5.4 (a) Mean total kinetic energy released in the reaction $SF_6 + h\nu \rightarrow SF_5^+ + F + e^-$ for photon energies in the range 15.1 to 19.1 eV. A linear extrapolation to zero kinetic energy gives the dissociative ionisation energy of SF_6 , 13.6 ± 0.1 eV. The error in each value of the kinetic energy release is *ca.* 20 %. (b) Threshold photoelectron spectrum of SF_6 over the same range of energies.

At this stage, a comment on the assumptions and limitations of this extrapolation method. The quoted errors for CF_4 and SF_6 arise from random statistical errors in the data. There are three factors which might produce systematic errors which have been ignored in the analysis. First, if the extrapolation to

zero $\langle KE \rangle_t$ is not linear, an error will result in the DIE. This seems unlikely for CF_4^+ and SF_6^+ , for reasons explained earlier. Second, the single-value KE release determined at each photon energy from the multiple CF_3^+ or SF_5^+ TOF spectra represents a mean value; each $P[\varepsilon_t(n)]$ vs. $\varepsilon_t(n)$ distribution is constrained to $n=1$. Given the broad distribution of $P[\varepsilon_t(n)]$ vs. $\varepsilon_t(n)$ when each TOF spectrum is fitted to the full KE release distribution, $\langle KE \rangle_t$ may be different from the mean KE release. Third, anisotropic effects have been observed for F-atom loss from the \tilde{X}^2T_{1g} state of SF_6^+ with β parameters ranging from 0.9 to 1.3.²⁹ Likewise, fragment ion anisotropy has been demonstrated both in the F 1s core ionisation³⁰ and the valence ionisation³¹ of CF_4 . In the experiments, the polarisation of the VUV photon beam is perpendicular to the TOF axis. The energy releases are determined from the flight times of the fragment ions, or a projection of the recoil velocity on to the TOF axis. It is therefore possible that anisotropy in the fragmentation may lead to a consistent under- or over-estimation of $\langle KE \rangle_t$, which could cause a small systematic error in the intercept when extrapolating the $\langle KE \rangle_t$ values to zero. However, this effect is difficult to quantify, and it is not even obvious whether it under- or over-estimates the DIE. The justification for ignoring all three factors is that the enthalpies of formation at 0 K of CF_3^+ and SF_5^+ which is determined directly from the DIE data, 390 ± 19 and 29 ± 10 kJ mol⁻¹, agree within experimental error with the previous best estimates, namely 410 ± 4 and 11 ± 18 kJ mol⁻¹, respectively.^{2,4}

5.5.2 Measurement of the first dissociative ionisation energy of SF_5CF_3

The onset of ionisation of SF_5CF_3 , *ca.* 12.9 eV, lies significantly lower in energy than that in either CF_4 or SF_6 . This arises because its highest-occupied molecular orbital (HOMO) has a very different character to that of CF_4 or SF_6 . With SF_5CF_3 , it is essentially a S–C σ -bonding orbital,³² whereas the HOMO of both CF_4 and SF_6 is a F 2p π non-bonding orbital with an ionisation energy similar to that of an isolated fluorine atom.^{8,33} Over the range 80 to 97 nm (12.8 to 15.5 eV), which encompasses all the ground state and the lower-lying part of the first excited state of the parent cation (Figure 5.5(b)), SF_5CF_3 dissociates exclusively to CF_3^+ . Therefore the scanning-energy TPEPICO spectrum of SF_5CF_3 from 80 to 97 nm in 64 channels was recorded. The mean KE releases are much smaller than in CF_4 and SF_6 , ranging from 0.05 to 0.4 eV (Fig. 5(a)). Fig. 3(c) show the TOF spectrum of CF_3^+/SF_5CF_3 recorded at 14.09 eV from which a mean KE release of 0.24 ± 0.05 eV was determined. Within experimental error, the 35 lowest-energy data points fit to a straight line with a slope of 0.19, in excellent agreement with the prediction of the pure-impulsive model of 0.20.²³ Extrapolation to a KE release of zero yields the first DIE of SF_5CF_3 to $CF_3^+ + SF_5 + e^-$ to be 12.9 ± 0.4 eV. The relatively large error in the DIE reflects the small slope of the KE release vs. photon energy graph, and the shallow nature of the extrapolation. It should be noted that the DIE, unlike that of CF_4 and SF_6 , is coincidentally isoenergetic with the ionisation onset of the first photoelectron band of SF_5CF_3 .

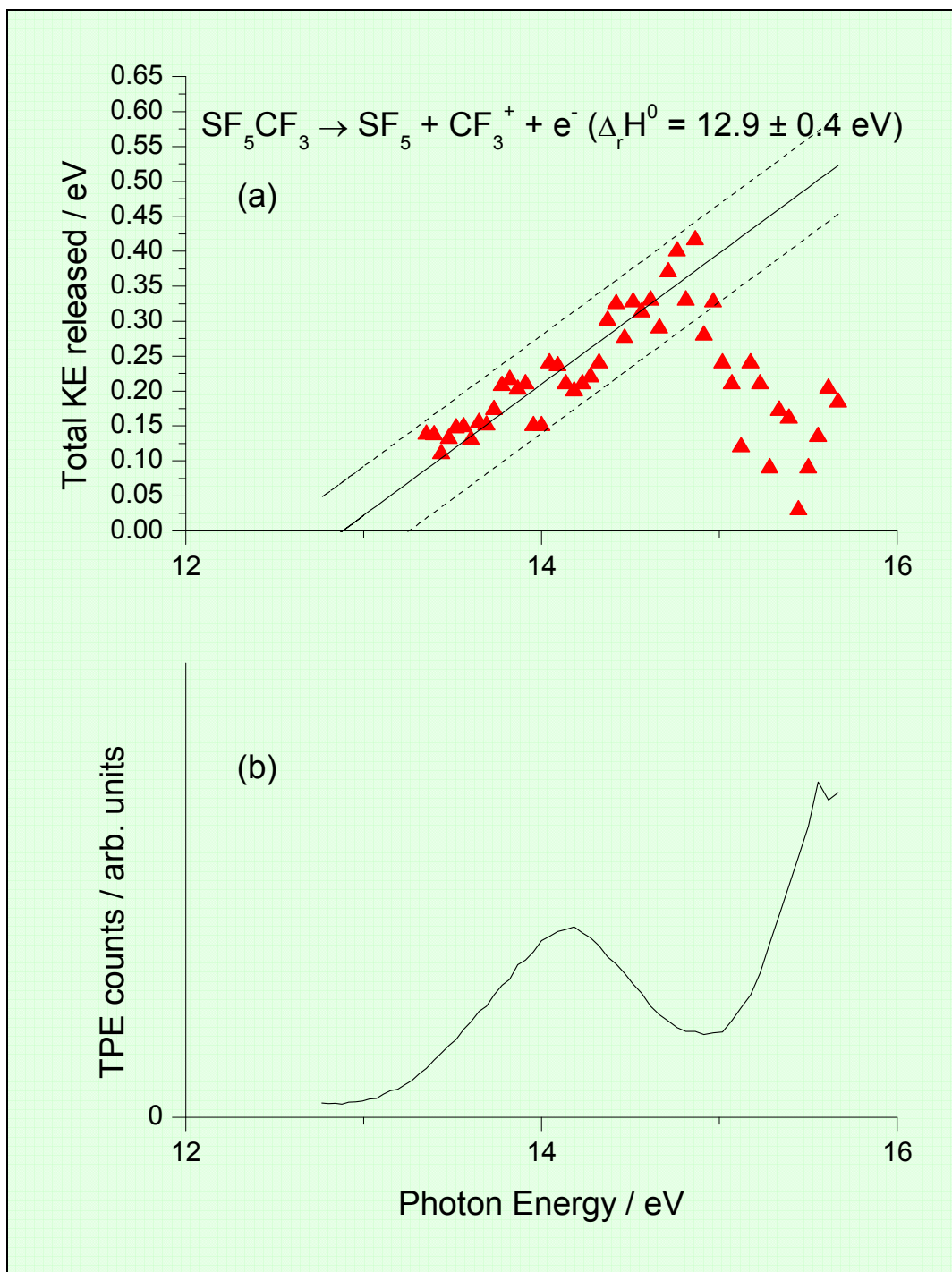


Figure 5.5 (a) Mean total kinetic energy released in the reaction $\text{SF}_5\text{CF}_3 + h\nu \rightarrow \text{CF}_3^+ + \text{SF}_5 + \text{e}^-$ for photon energies in the range 13.3 to 15.5 eV. A linear extrapolation to zero kinetic energy gives the first dissociative ionisation energy of SF_5CF_3 , $12.9 \pm 0.4 \text{ eV}$. The error in each value of the kinetic energy release is *ca.* 20%. (b) Threshold photoelectron spectrum of SF_5CF_3 over the same range of energies.

Two important thermochemical data can now be determined. First, using values for the 0 K enthalpies of formation of CF_3^+ ($390 \pm 19 \text{ kJ mol}^{-1}$) (Section 5.1) and SF_5 ($-915 \pm 18 \text{ kJ mol}^{-1}$),⁴ the $\Delta_f H^0$ (SF_5CF_3) is determined to be $-1770 \pm 47 \text{ kJ mol}^{-1}$. This value is significantly lower than that quoted in the JANAF tables,²⁷ $-1700 \pm 63 \text{ kJ mol}^{-1}$ from a review over twenty years old but is in agreement within experimental

error. Second, using the value for AIP (CF₃) determined in Section 5.1, 8.84 ± 0.20 eV, the dissociation energy of the SF₅–CF₃ bond at 0 K is determined to be 4.06 ± 0.45 eV or 392 ± 43 kJ mol⁻¹. Using the value for the AIP (SF₅) from Fisher *et al.*,⁴ 9.60 ± 0.05 eV, the *second* DIE of SF₅CF₃ (defined here to be SF₅⁺ + CF₃ + e⁻) is calculated to be 13.66 ± 0.45 eV. This energy is *ca.* 0.8 eV higher than the first DIE to SF₅ + CF₃⁺ + e⁻, and explains why only the CF₃⁺ fragment ion is observed for dissociation of the low-energy regions of the ground-state potential of SF₅CF₃⁺.

5.5.3 Threshold photoelectron spectrum of SF₅CF₃

The threshold photoelectron spectrum (TPES) of SF₅CF₃ was measured from 12.7 to 26.4 eV with a constant wavelength resolution of 0.3 nm (Fig. 5.6(a)). No vibrational structure is observed. The onset of ionisation, defined as the energy at which signal is first observed above the level of background noise, is 12.92 ± 0.18 eV. It is noted that this onset will depend on the sensitivity of the apparatus, especially if there is a large change in geometry upon ionisation. That is, a more sensitive apparatus should detect signal closer to the true onset than a less sensitive one. However, it is assumed that this error is small compared to the quoted error. Simple *ab initio* calculations on the structure of SF₅CF₃ at the Hartree-Fock level predict bond angles close to either 90.0° (*e.g.* FSF) or 109.4° (*e.g.* FCS), a S–F bond length of 1.58 Å, a S–C length of 1.87 Å, and a C–F length of 1.30 Å,³² in good agreement with the experimental structure from gas-phase electron diffraction.³⁴ No other structures of molecules with stoichiometry C₁S₁F₈ are stable. The HOMO of SF₅CF₃ has a large S–C σ-bonding character, whereas the next three orbitals lie *ca.* 0.1 au or 2.7 eV lower in energy and are F 2pπ non-bonding in character. Furthermore, no minimum-energy geometry of the ground electronic state of SF₅CF₃⁺ can be obtained at either the Hartree-Fock or the MP2(full)/6-31g(d) level, indicating that this state is unbound.

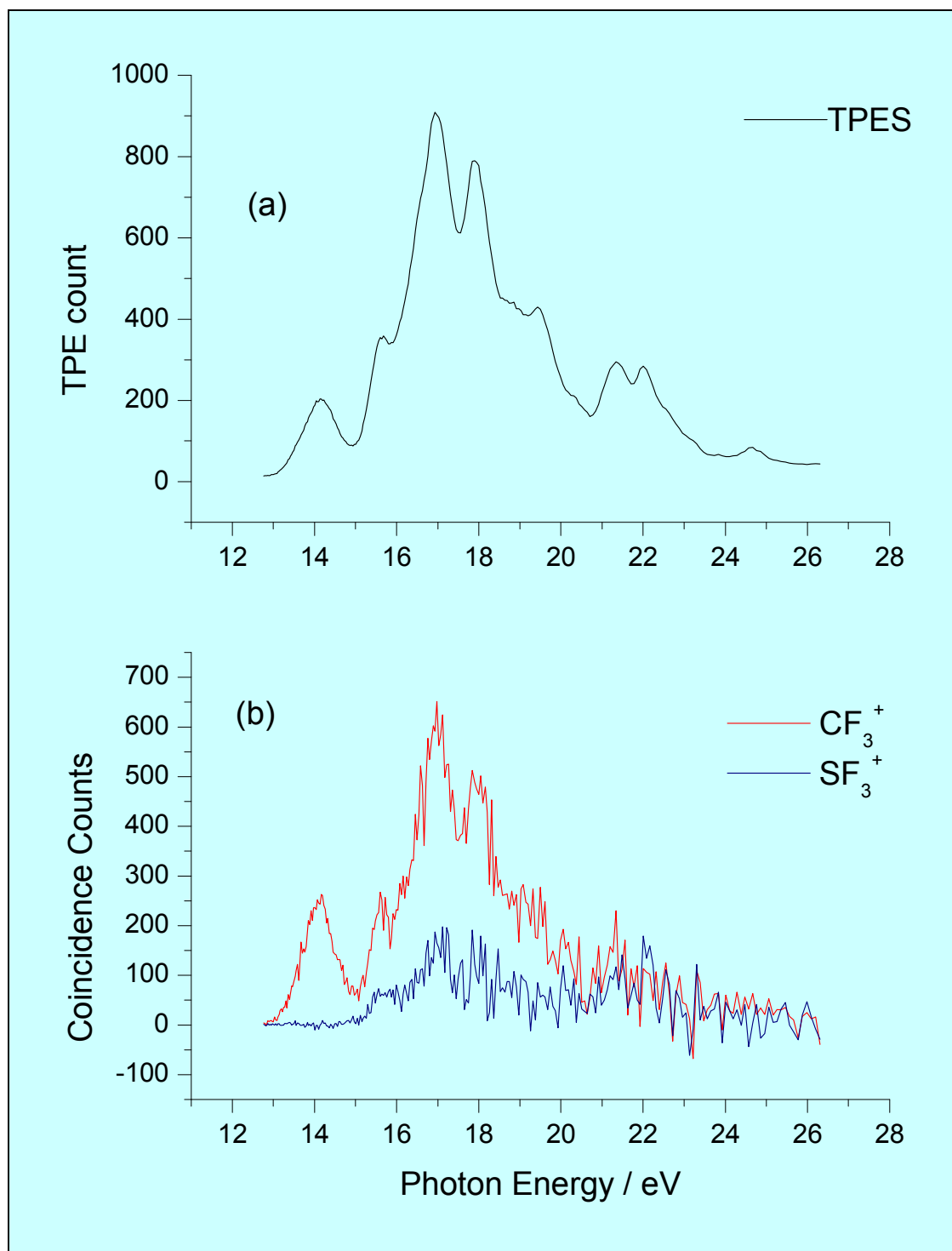


Figure 5.6 (a) Threshold photoelectron spectrum of SF_5CF_3 at a resolution of 0.3 nm. The electronic states of the parent cation are labelled $\tilde{\text{X}}$ through $\tilde{\text{G}}$ (Table 5.2). (b) Coincidence ion yields of CF_3^+ and SF_3^+ , the two most intense fragment ions.

Peaks in the TPES are observed at 14.13, 15.68, 16.94, 17.86, 19.44, 21.34, 22.01 and 24.67 eV. The peak at 14.13 eV is associated with electron removal from the S–C σ -bonding HOMO, and it is noted the large difference (greater than 1 eV) between the onset of ionisation and the vertical IP. This suggests a significant change in geometry, probably in the S–C bond length, between neutral and cation, and would

be compatible with the ground state of the cation being repulsive along a cut through the potential energy surface along the S–C coordinate. The low value of this vertical IP, *ca.* 2 eV lower than that in both CF₄ and SF₆ where the HOMO has F 2p π non-bonding character, has already been noted. The broad peak at 16.94 eV, *ca.* 2.7 eV above the ground state, probably corresponds to several bands produced by removal of a F 2p π non-bonding electron. No attempt has been made to assign the other peaks in the TPES.

5.5.4 Scanning-energy TPEPICO spectrum of SF₅CF₃

The TPEPICO spectrum of SF₅CF₃ was measured from 12.7 to 26.4 eV with an optical resolution of 0.3 nm. Fig. 5.7 shows the ions produced from the TPEPICO spectrum, summed over this range of energies. The parent ion is not observed. The five fragment ions observed are, in order of increasing mass, CF₂⁺, CF₃⁺, SF₃⁺, SF₄⁺ and SF₅⁺. CF₃⁺ and SF₃⁺ are the dominant ions, with CF₂⁺ and SF₄⁺ very weak. The relative intensities of the most intense ions (CF₃⁺, SF₃⁺ and SF₅⁺) are *ca.* 38:13:1, and it is noted that these three ions are also the most intense and formed in approximately this ratio in the 70 eV electron-impact mass spectrum of SF₅CF₃.¹¹ The coincident ion yields of CF₃⁺ and SF₃⁺ are shown in Fig. 5.6(b). The appearance potential (AP) at 298 K of these two ions are determined to be 12.92 ± 0.18 eV (for CF₃⁺) and 14.94 ± 0.13 eV (for SF₃⁺). The average internal energy of SF₅CF₃ at 298 K is calculated to be 0.17 eV,²⁷ so this corresponds to APs at 0 K of 13.09 ± 0.18 eV (CF₃⁺) and 15.11 ± 0.13 eV (SF₃⁺). The weakness of the signals for the other three fragment ions is reflected in large uncertainties in their APs. The APs at 298 K are determined to be 13.9 ± 1.2, 13.5 ± 1.5 and 16.0 ± 2.0 eV for SF₅⁺, SF₄⁺ and CF₂⁺, respectively.

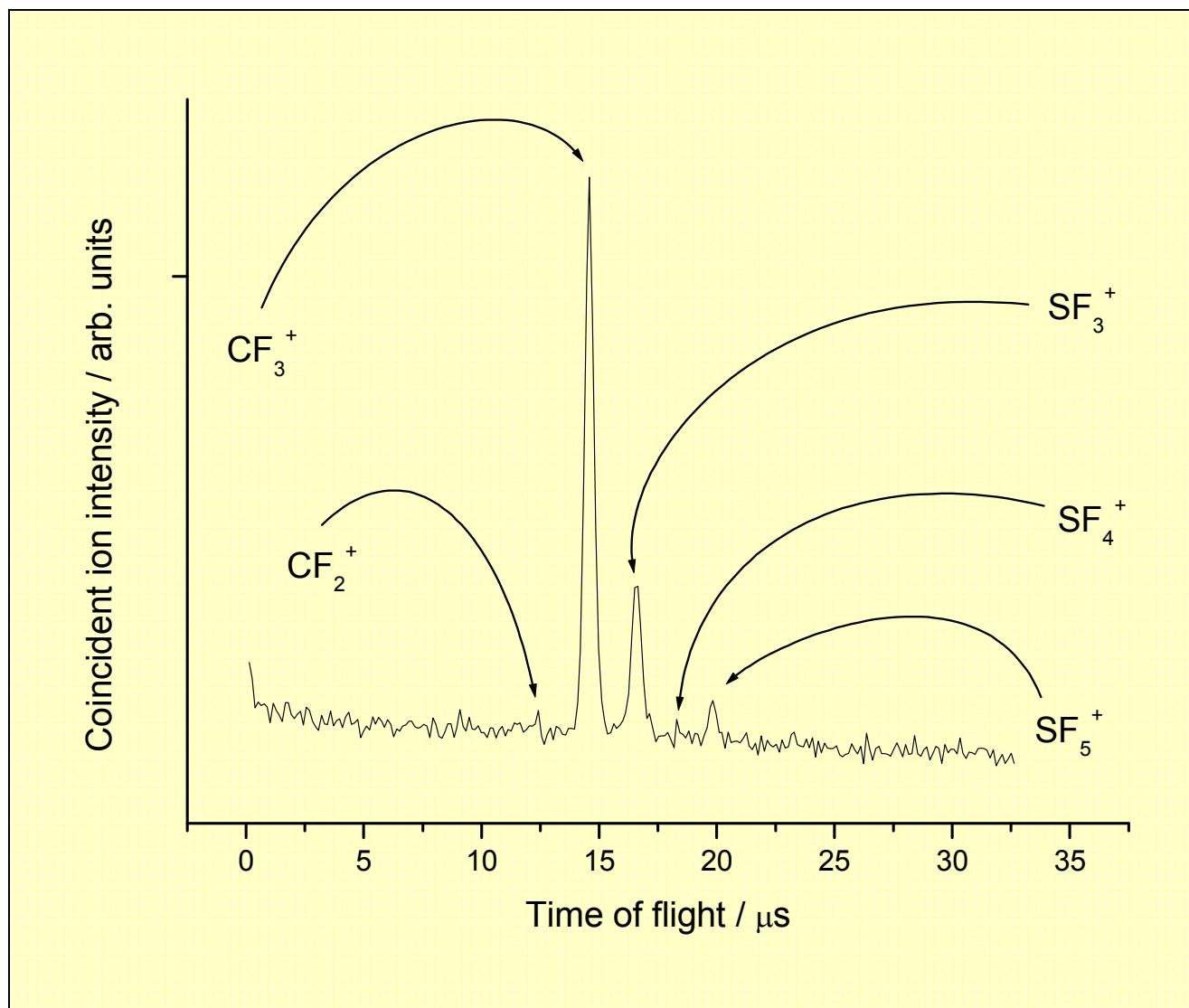


Figure 5.7 Time-of-flight spectrum of the fragment ions from SF_5CF_3 , summed over the range of photoexcitation energies 12.7 to 26.4 eV.

The shape of the CF_3^+ ion yield follows that of the TPES of SF_5CF_3 from the onset of ionisation to *ca.* 20 eV, and clearly the states of the parent ion with vertical energies below 20 eV dissociate predominantly to CF_3^+ . The AP at 298 K of CF_3^+ corresponds to the onset of ionisation of SF_5CF_3 , which is close to its first DIE to $\text{CF}_3^+ + \text{SF}_5 + \text{e}^-$. The AP of SF_5^+ , 13.9 eV with relatively large errors, also corresponds closely to the calculated second DIE of SF_5CF_3 to $\text{SF}_5^+ + \text{CF}_3 + \text{e}^-$, 13.66 ± 0.45 eV. The SF_5^+ signal is so weak that it is not possible to say whether there is any correlation between its ion yield and the electronic states of SF_5CF_3^+ as revealed in the TPES. The thermochemical threshold for dissociative ionisation of SF_5CF_3 to $\text{SF}_3^+ (+ \text{CF}_4 + \text{F})$ is 13.01 eV (Section 5.5.6), considerably below the observed AP at 298 K of SF_3^+ , 14.94 ± 0.13 eV. In fact, this AP appears to correspond to the onset of ionisation to the $\tilde{\text{A}}$ state of SF_5CF_3^+ , indicating electronic state specificity in the fragmentation of SF_5CF_3^+ to form SF_3^+ . Furthermore, peaks in the SF_3^+ ion yield also correlate weakly with peaks in the TPES of SF_5CF_3 at

16.94, 17.86, 19.44, 21.34 and 22.01 eV. Thermochemistry shows that, at energies between threshold and 17.02 eV, SF_3^+ can only form in association with the neutral products $\text{CF}_4 + \text{F}$ (see Section 5.5.6). The ion yields of CF_2^+ and SF_4^+ are extremely weak. As with SF_5^+ , it is not possible to say whether there is any correlation between their ion yields and peaks in the TPES of SF_5CF_3 . Thermochemistry, however, shows that, certainly at low energies above threshold, CF_2^+ can only form in conjunction with SF_6 , and SF_4^+ with CF_4 (Section 5.5.6). Thus, for the three fragment ions formed involving more than one bond cleavage (CF_2^+ , SF_3^+ and SF_4^+), a fluorine migration must occur across the S–C bond to produce the necessary neutral partner(s). Such intramolecular rearrangements, involving migration of a fluorine atom *via* a tightly-constrained transition state, have been observed in the fragmentation of perfluorocarbon cations, C_xF_y^+ .^{33,36}

5.5.5 Fixed-energy TPEPICO spectra of SF_5CF_3

TPEPICO-TOF spectra of SF_5CF_3 were recorded at a resolution of 16 ns for the CF_3^+ fragment at photon energies of 14.25, 15.69, 16.98, 17.97 and 19.07 eV, corresponding to the first five peaks in the TPES of SF_5CF_3 . Accumulation times per spectrum ranged between 2 and 8 hours. Fig. 5.8 shows the TPEPICO-TOF spectrum of $\text{CF}_3^+/\text{SF}_5\text{CF}_3$ at an excitation energy of 14.25 eV, corresponding to the vertical ionisation potential to the ground state of the parent ion. The spectrum is fitted with $\Delta E = 0.03$ eV, $n = 3$, and $\langle \text{KE} \rangle_t$ is determined to be 0.32 ± 0.05 eV (Table 5.1). This value of $\langle \text{KE} \rangle_t$ corresponds to 21% of the available energy, in excellent agreement with the prediction of the pure-impulsive model.²³ This is to be expected, because the ground state of SF_5CF_3^+ at the Franck-Condon maximum lies over 1 eV higher in energy than the dissociative limit to $\text{CF}_3^+ + \text{SF}_5 + \text{e}^-$. Dissociation from this repulsive potential energy surface is therefore expected to occur rapidly, probably on a sub-picosecond timescale, with a relatively large amount of the available energy released into translation of the two fragments. The $\langle \text{KE} \rangle_t$ values determined for the other $\text{CF}_3^+/\text{SF}_5\text{CF}_3$ spectra are shown in Table 5.1. As the photon energy increases from 14.25 to 19.07 eV, the values of $\langle \text{KE} \rangle_t$ only increase by *ca.* 0.1 eV, so the fractional release into translational energy of the $\text{CF}_3^+ + \text{SF}_5$ products decreases. It appears, therefore, that the dissociation mechanism becomes progressively more statistical in nature as higher-lying electronic states of SF_5CF_3^+ are populated. This may be attributed to an increase in the density of vibronic states with increasing photon energy. Thus, higher states of the parent ion are more likely to find non-radiative decay pathways (*e.g. via* internal conversion) into lower states, and possibly into regions of the \tilde{X} -state potential of SF_5CF_3^+ from which statistical dissociation can occur. This phenomenon, that the value of $\langle \text{KE} \rangle_t$ does not increase as rapidly with photon energy as a pure-impulsive model would predict, has also been observed in $\text{CF}_3^+/\text{CF}_4$ and $\text{SF}_5^+/\text{SF}_6$,⁸ and for single bond cleavages in the CCl_3X^+ and CF_2X_2^+ series of molecules.^{37,38} In all these cases, the ground state of the parent cation in the Franck-Condon region lies above the first dissociative ionisation energy.

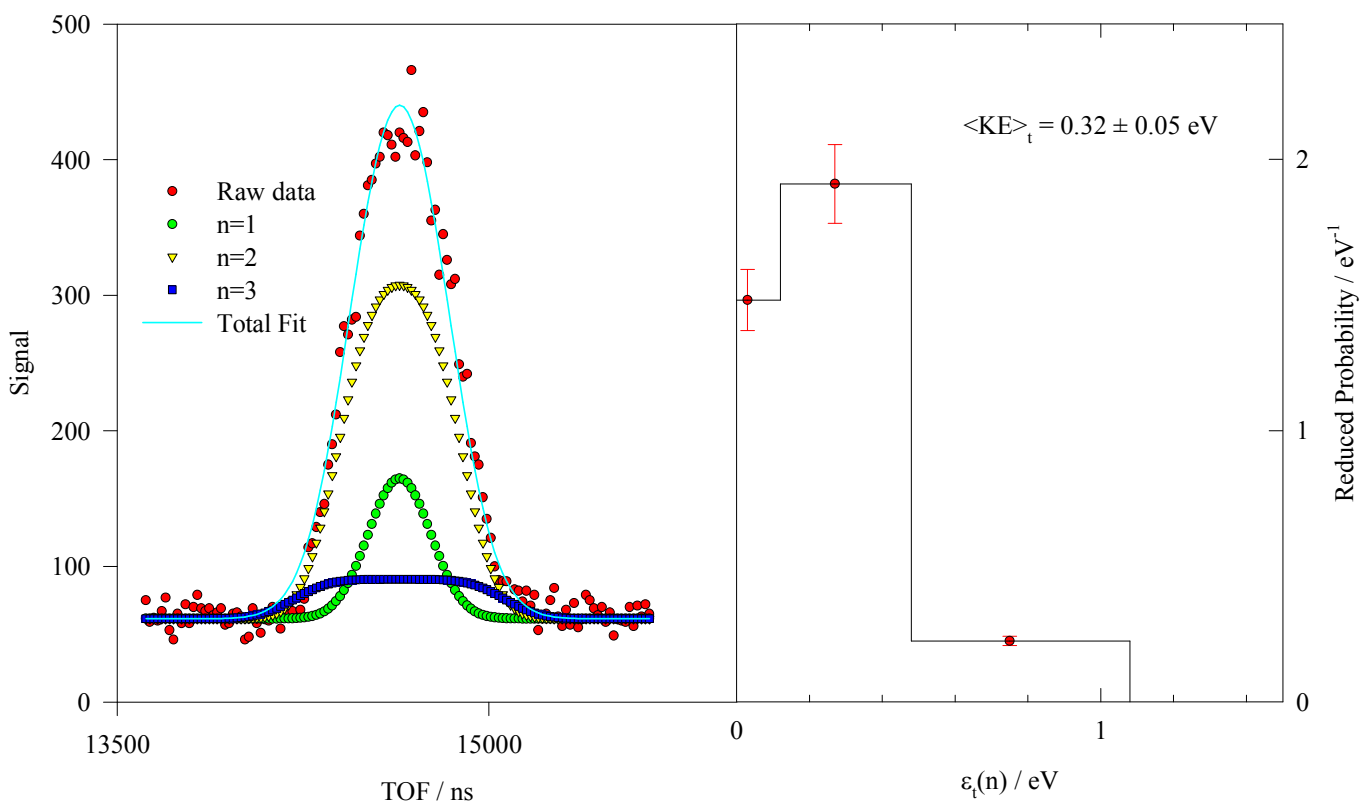


Figure 5.8 (a) Coincidence TOF spectrum (dots) of CF_3^+ from SF_5CF_3 photoionised at 14.25 eV into the ground, \tilde{X} state of the parent cation. The solid line gives the best fit to the data, comprised of three contributions ($n=1-3$) in the basis set for $\epsilon_t(n)$. The reduced probability of each contribution is shown in (b). The fit yields a total mean translational kinetic energy into $\text{CF}_3^+ + \text{SF}_5$ of $0.32 \pm 0.05 \text{ eV}$ which constitutes 21 % of the available energy.

Table 5.1 Total mean translational kinetic energy release, $\langle \text{KE} \rangle_t$, of the two-body fragmentation of the valence states of SF_5CF_3^+

Parent ion	Daughter ion	E / eV	$E_{\text{avail}} / \text{eV}^a$	$\langle \text{KE} \rangle_t / \text{eV}$	$\langle f \rangle_{t, \text{exp}}^b$	$\langle f \rangle_{t, \text{stat}}$	$\langle f \rangle_{t, \text{imp}}$
SF_5CF_3^+	CF_3^+	19.07	6.34	0.37 ± 0.01	0.06	0.04	0.20
	CF_3^+	17.97	5.24	0.40 ± 0.01	0.08	0.04	0.20
	CF_3^+	16.98	4.25	0.38 ± 0.01	0.09	0.04	0.20
	CF_3^+	15.69	2.96	0.29 ± 0.02	0.10	0.04	0.20
	CF_3^+	14.25	1.52	0.32 ± 0.05	0.21	0.04	0.20

^a $E_{\text{avail}} = \text{Photon Energy} - \text{thermochemical threshold for forming the daughter ion} + \text{thermal energy of parent molecule at 298 K}$

^b Fractional ratio = $\langle \text{KE} \rangle_t / E_{\text{avail}}$

One TPEPICO-TOF spectrum was measured for SF_3^+ with a resolution of 16 ns at a photon energy of 16.98 eV. The peak shape of the daughter ion fits to a KE release of 0.17 ± 0.01 eV into SF_3^+ . A value of $\langle \text{KE} \rangle_t$ cannot be determined since dissociation involves more than one bond cleavage. No other fragment ions were measured as signal levels were too weak.

5.5.6 Thermochemistry

The 0 K energies of various dissociation channels of SF_5CF_3^+ can now be determined (Table 5.2). Values for the first DIE of SF_5CF_3 (12.9 eV), adiabatic IPs for CF_3 (8.84 eV) and SF_5 (9.60 eV) have been determined by this work and by Fisher *et al.*⁴ respectively, and the bond dissociation energies for $\text{SF}_x^+ - \text{F}$ from the guided ion beam study.⁴ The $\text{CF}_3 - \text{F}$ bond dissociation energy (5.61 eV) is taken from Asher and Ruscic,² whilst that of $\text{CF}_2^+ - \text{F}$ (6.32 eV) is calculated assuming an IP for CF_2 of 11.44 eV.³⁹ The largest uncertainty in these energies occurs in channels involving SF_3^+ and SF_4^+ , at the level of *ca.* 0.3-0.5 eV. The interpretation of the mechanism of reactions which form these ions, however, does not depend on the precise values of the bond dissociation energies.

Table 5.2 Energetics of important dissociation channels and ionisation potentials of SF₅CF₃.

Neutral / parent ion	Dissociation channel	Dissociation energy / eV ^a	Vertical ionisation potential / eV
SF ₅ CF ₃ ⁺ \tilde{G}			24.67
SF ₅ CF ₃ ⁺ \tilde{F}			22.01
SF ₅ CF ₃ ⁺ \tilde{E}			21.34
SF ₅ CF ₃ ⁺ \tilde{D}			19.44
	CF ₃ ⁺ + SF ₃ + 2F + e ⁻	19.28	
	CF ₂ ⁺ + SF ₅ + F + e ⁻	19.22	
	SF ₃ ⁺ + CF ₃ + 2F + e ⁻	18.62	
	SF ₄ ⁺ + CF ₃ + F + e ⁻	18.26	
SF ₅ CF ₃ ⁺ \tilde{C}			17.86
	SF ₅ ⁺ + CF ₂ + F + e ⁻	17.37	
	SF ₃ ⁺ + CF ₃ + F ₂ + e ⁻	17.02	
SF ₅ CF ₃ ⁺ \tilde{B}			16.94
SF ₅ CF ₃ ⁺ \tilde{A}			15.68
	CF ₃ ⁺ + SF ₄ + F + e ⁻	15.41	
	CF ₂ ⁺ + SF ₆ + e ⁻	15.40	
SF ₅ CF ₃ ⁺ \tilde{X}			14.13
	SF ₅ ⁺ + CF ₃ + e ⁻	13.66	
	SF ₃ ⁺ + CF ₄ + F + e ⁻	13.01	
	CF ₃ ⁺ + SF ₅ + e ⁻	12.90	
	SF ₄ ⁺ + CF ₄ + e ⁻	12.65	
	SF ₅ + CF ₃	4.06	
SF ₅ CF ₃ \tilde{X}			0

^a Dissociation energies of channels involving CF₃⁺ and SF_x⁺ (x=3-5) are calculated from the experimental DIE of SF₅CF₃ to CF₃⁺ + SF₅ + e⁻ (12.9 eV), bond dissociation energies at 0 K of SF_x⁺ from Fisher *et al.*,⁴ adiabatic IPs for CF₃ and SF₅ of 8.84 and 9.60 eV (see text), and a bond dissociation energy for CF₃-F of 5.61 eV.² Channels involving CF₂⁺ are calculated using an enthalpy of formation for this ion of 922 kJ mol⁻¹.³⁹

Products formed by cleavage of the S-C bond are easy to understand. As shown earlier, the onset of ionisation of SF₅CF₃ at 298 K is 12.92 ± 0.18 eV, corresponding to 13.1 ± 0.2 eV at 0 K, lies slightly higher in energy than the experimentally-deduced value for the first DIE of 12.9 ± 0.4 eV. In this respect, SF₅CF₃ behaves similarly to CCl₄, whose first DIE to CCl₃⁺ + Cl + e⁻ lies close to the onset of ionisation

to the \tilde{X} state of CCl_4^+ .⁴⁰ The KE releases from $\text{SF}_5\text{CF}_3^+ \tilde{X} \rightarrow \text{CF}_3^+ + \text{SF}_5$ are therefore relatively small, making an accurate extrapolation to zero KE difficult to achieve. The calculated dissociation threshold of SF_5CF_3 to $\text{SF}_5^+ + \text{CF}_3 + \text{e}^-$, 13.66 eV, lies within error at the same energy as the experimentally-determined threshold of 13.9 ± 1.2 eV. In other words, SF_5^+ turns on, albeit very weakly, at its thermochemical threshold. For photon energies above this threshold, dissociation to $\text{CF}_3^+ + \text{SF}_5 + \text{e}^-$ dominates that to $\text{CF}_3 + \text{SF}_5^+ + \text{e}^-$. This effect has also been observed for reactions of cations with recombination energies in excess of 13.66 eV with SF_5CF_3 , where the CF_3^+ product dominates SF_5^+ .⁴¹

Channels involving more complicated photodissociation processes are perhaps more interesting. The threshold for production of SF_3^+ at 298 K is measured to be 14.94 ± 0.13 eV. This threshold corresponds to the onset of ionisation to the second band in the TPES of SF_5CF_3 , and suggests a non-statistical electronic state-selective fragmentation of the \tilde{A} state of SF_5CF_3^+ is occurring. Even allowing for a significant uncertainty in the enthalpy of formation of SF_3^+ , it is clear from Table 2 that this channel is energetically only open if SF_3^+ forms in conjunction with $\text{CF}_4 + \text{F} + \text{e}^-$ (dissociation energy 13.01 eV). SF_3^+ cannot form with CF_3 and either F_2 or 2F , since these channels lie *ca.* 2.1 or 3.7 eV above the experimentally-determined AP of SF_3^+ . Likewise, SF_4^+ and CF_2^+ form very weakly with APs of 13.5 and 16.0 eV. Table 2 shows that SF_4^+ can only form with CF_4 , and CF_2^+ with SF_6 at energies close to their respective thresholds. Thus, all these three fragmentation channels must involve a fluorine atom migration across the S–C bond to form the requisite neutral partner.

5.6 Discussion

The TPEPICO data in both the scanning photon and the fixed photon energy modes have been discussed in Sections 5.4 and 5.5. Here, only the results to determine the dissociative ionisation energy of CF_4 , SF_6 and SF_5CF_3 are discussed. The value of the AIP of the CF_3 radical, and hence the DIE of CF_4 , has been controversial for many years. As described in Section 5.2, the difficulty in measuring accurately the AIP of CF_3 arises because of the change in geometry between the neutral (pyramidal, C_{3v}) and ionised (planar, D_{3h}) forms of the radical, resulting in a negligibly-small Franck-Condon overlap factor at threshold.¹⁸ The experimental data up to 1998 were reviewed,¹² and an upper limit of 8.8 ± 0.2 eV for the AIP of CF_3 was recommended. Since then, a new *ab initio* calculation¹⁴ and further photoionisation experiments on $\text{CF}_3\text{Br} \rightarrow \text{CF}_3^+ + \text{Br} + \text{e}^-$ ¹⁷ both suggest that the AIP (CF_3) is somewhat higher, between 9.0 and 9.1 eV. In addition, Irikura¹³ has suggested that some of the low values of the AIP (<8.6 eV) from ion-molecule chemical reactions may be in doubt, because entropy effects have been ignored in determining whether such reactions may proceed at a reasonable rate. The new result does not add significantly to this controversy. However, it is gratifying that the extrapolation method (Fig. 5.2(a)) gives a value for the DIE of CF_4 , 14.45 ± 0.20 eV, which leads to a value for the AIP of the CF_3 radical, 8.84 ± 0.20 eV, which is consistent with the recommendations of two recent reviews.^{12,13} It seems unlikely that this method will

ever be able to give an accuracy in the DIE better than *ca.* ± 0.1 eV, when an extrapolation of over 1 eV, as here, is involved.

The range of values in the recent literature for the AIP of the SF₅ radical is even greater, with values spanning *ca.* 9.6 to 11.5 eV.⁴ The lowest value of 9.60 ± 0.05 eV, and probably the most reliable because it is a *direct* measurement, comes from a guided ion beam mass spectrometric study.⁴ Both the new value for the first DIE of SF₆, 13.6 ± 0.1 eV, and that derived for the AIP of SF₅, 9.8 ± 0.2 eV, are in excellent agreement with the results of Fisher *et al.*⁴ The AIP result is also in good agreement with two independent Gaussian-2 *ab initio* calculations.^{15,42} All three values are slightly higher than that calculated, 9.52 eV, at the CCSD(T) level of theory.⁴³

The purpose of these CF₄ and SF₆ experiments was *not* to measure new values for the ionisation potentials of the CF₃ and SF₅ radicals, but rather to validate the extrapolation method described in Section 5.2. The results show that this has been achieved. Within the limitations of this method described in Section 5.1, therefore, confidence can be given to the KE extrapolation data for SF₅CF₃ (Fig. 5.5(a)), and the determination of its first DIE to CF₃⁺ + SF₅ + e⁻. From this value, the 0 K enthalpy of formation of SF₅CF₃ and D₀(SF₅-CF₃) has been determined. The strength of the SF₅-CF₃ bond, 4.06 ± 0.45 eV, is slightly greater than that of the SF₅-F bond in SF₆, 3.82 eV.⁴ The atmospheric implication of this measurement is that SF₅CF₃, like SF₆ and CF₄, is very unlikely to be broken down by UV radiation in the stratosphere. Also like CF₄ and SF₆,⁷ the reactions of O (¹D) and the OH radical with SF₅CF₃ are likely to be very slow. Taken together, these data are consistent with the observed atmospheric profile of SF₅CF₃ in the stratosphere, which has been interpreted to indicate a lifetime of the order of one thousand years.¹ Its removal from the atmosphere is likely to be determined by ionic processes (*i.e.* electron attachment and ion-molecule reactions) and possibly VUV photodissociation with Lyman- α radiation occurring in the mesosphere. The rate constant for electron attachment to SF₅CF₃ at room temperature in a Swarm apparatus has recently been measured.⁴⁴ Its value suggests a lifetime of SF₅CF₃ in the atmosphere of less than 1000 years.

5.7 Conclusions

Using tunable VUV radiation from a synchrotron source and threshold photoion-photoelectron coincidence spectroscopy, the fragmentation of the valence states of SF₅CF₃⁺ over the energy range 12 to 26 eV has been studied. Threshold electron spectra and coincidence ion yields have been recorded with the experiment operating in the scanning photon energy mode. CF₃⁺ is the most intense fragment ion over this range of energies, and its ion yield follows that of the TPES of SF₅CF₃ from *ca.* 12-20 eV. SF₃⁺ is the second most intense fragment ion. Its ion yield shows some evidence for state-selective fragmentation; its appearance potential lies *ca.* 1.9 eV above the lowest dissociation threshold to SF₃⁺ +

$\text{CF}_4 + \text{F} + \text{e}^-$, and correlates with the onset of the first-excited electronic state of SF_5CF_3^+ . The ion yields of SF_5^+ , SF_4^+ and CF_2^+ are weak. SF_5^+ turns on at the thermochemical dissociation energy of $\text{SF}_5^+ + \text{CF}_3 + \text{e}^-$. Like SF_3^+ , SF_4^+ and CF_2^+ turn on at energies which are only compatible with the lowest-energy dissociation channel involving that ion. Thus SF_3^+ can only form in conjunction with $\text{CF}_4 + \text{F} + \text{e}^-$, SF_4^+ with $\text{CF}_4 + \text{e}^-$, and CF_2^+ with $\text{SF}_6 + \text{e}^-$. In all cases, a fluorine atom must migrate across the S–C bond.

In the fixed photon energy mode, the translational kinetic energy released into $\text{CF}_3^+ + \text{SF}_5$ has been measured at five different excitation energies over the range 14 to 19 eV. The values of $\langle \text{KE} \rangle_t$ range from 0.29 to 0.40 eV. Whereas dissociation of the ground state of SF_5CF_3^+ appears to follow a pure-impulsive model with a fractional release into translational energy of 0.19, that from excited states shows a lower fractional release. It appears that the dissociation mechanism becomes more statistical as higher states of SF_5CF_3^+ are populated. This phenomenon has been observed in other molecules (*e.g.* CF_4 and SF_6), where the ground state of the parent ion in the Franck-Condon region lies above the first DIE.⁵

The scanning photon energy TPEPICO experiment has also been used to measure the first DIE of CF_4 (to $\text{CF}_3^+ + \text{F} + \text{e}^-$), SF_6 (to $\text{SF}_5^+ + \text{F} + \text{e}^-$), and SF_5CF_3 (to $\text{CF}_3^+ + \text{SF}_5 + \text{e}^-$), obtaining values of 14.45 ± 0.20 , 13.6 ± 0.1 , and 12.9 ± 0.4 eV, respectively. From the first two results, we determine values for the adiabatic IP of the CF_3 and SF_5 free radicals to be 8.84 ± 0.20 and 9.8 ± 0.2 eV, respectively. These results are in good agreement with what is believed to be the most reliable values in the recent literature. The fractional kinetic energy release from $\text{SF}_6^+ \rightarrow \text{SF}_5^+ + \text{F}$ is significantly less than that predicted by the pure-impulsive model,²³ whereas that from CF_4^+ or $\text{SF}_5\text{CF}_3^+ \rightarrow \text{CF}_3^+ + \text{F}$ or SF_5 is in good agreement with this model. This result may relate to uncertainty in the geometry of SF_5^+ .²⁸ From the first DIE of SF_5CF_3 , the enthalpy of formation at 0 K of SF_5CF_3 (-1770 ± 47 kJ mol⁻¹) and the dissociation energy of the SF_5 – CF_3 bond at 0 K (4.06 ± 0.45 eV) are determined. These errors are determined by the formal method of propagation of errors, but they are dominated by the uncertainty in the first DIE of SF_5CF_3 . The new value for the enthalpy of formation of SF_5CF_3 is 70 kJ mol⁻¹ lower than that given in the JANAF tables.²⁷ Its value has already been used to determine possible product channels for reactions of small atmospheric cations (*e.g.* N^+ , N_2^+ , O_2^+) with SF_5CF_3 .⁴¹ This type of reaction is just one of several bimolecular processes which could remove this molecule from the atmosphere. Indeed, the electron attachment data strongly suggest that dissociative electron attachment is the dominant removal process.⁴⁴

The high value of the SF_5 – CF_3 bond dissociation energy suggests that it is unlikely to be broken down by UV photodissociation in the stratosphere. Furthermore, from a preliminary electron energy loss spectrum,⁶ there is no evidence for excited states of SF_5CF_3 which dissociate to $\text{SF}_5 + \text{CF}_3$ lying *ca.* 3–8 eV above its ground state with appreciable absorption cross-sections. If photon-induced processes dominate the removal of SF_5CF_3 from the earth's atmosphere, vacuum-UV photodissociation with

Lyman- α radiation in the mesosphere seems more likely. The measurement of the absorption cross-section of SF₅CF₃ at 121.6 nm, similar to that made for CF₄ and SF₆,⁷ would be useful additional data in determining more accurately the lifetime of SF₅CF₃ in the atmosphere. The data is considered in Chapter 6. The results in this chapter have recently been published.⁴⁵

5.8 References

1. W. T. Sturges, T. J. Wallington, M. D. Hurley, K. P. Shine, K. Sihra, A. Engel, D. E. Oram, S. A. Penkett, R. Mulvaney and C. A. M. Brenninkmeijer. *Science*, 2000, **289**, 611.
2. R. L. Asher, B. Ruscic. *J. Chem. Phys.*, 1997, **106**, 210.
3. L. C. Lee, X. Wang and M. Suto. *J. Chem. Phys.*, 1986, **85**, 6294.
4. E. R. Fisher, B. L. Kickel and P. B. Armentrout, *J. Chem. Phys.*, 1992, **97**, 4859.
5. D. Blechschmidt, R. Haensel, E. E. Koch, U. Nielsen and T. Sagawa, *Chem. Phys. Lett.*, 1972, **14**, 33.
6. P. A. Kendal and N. J. Mason, *J. Electron Spec. Rel. Phenom.*, 2001, **120**, 27.
7. A. R. Ravishankara, S. Solomon, A. A. Turnipseed and R. F. Warren, *Science*, 1993, **259**, 194.
8. J. C. Creasey, H. M. Jones, D. M. Smith, R. P. Tuckett, P. A. Hatherly, K. Codling and I. Powis, *Chem. Phys.*, 1993, **174**, 441.
9. D. M. Smith, R. P. Tuckett, K. R. Yoxall, K. Codling, P. A. Hatherly, J. F. M. Aarts and M. Stankiewicz, *J. Chem. Phys.*, 1994, **101**, 10559.
10. G. K. Jarvis, C. A. Mayhew, R. Y. L. Chim, R. A. Kennedy and R. P. Tuckett, *Chem. Phys. Lett.*, 2000, **320**, 104.
11. W. G. Mallard and P. J. Linstrom, 2000, *NIST Chemistry Webbook, NIST Standard Reference Database Number 69* (<http://webbook.nist.gov>).
12. G. K. Jarvis and R. P. Tuckett, *Chem. Phys. Lett.*, 1998, **295**, 145.
13. K. K. Irikura, *J. Amer. Chem. Soc.*, 1999, **121**, 7689.
14. P. Botschwina, M. Horn and R. Oswald, S. Schmatz, *J. Elec. Spec. Rel. Phen.*, 2000, **108**, 109.
15. K. K. Irikura, *J. Chem. Phys.*, 1995, **102**, 5357.
16. P. A. Hatherly, D. M. Smith and R. P. Tuckett, *Zeit. Phys. Chem.*, 1996, **195**, 97.
17. G. A. Garcia, P. M. Guyon and I. Powis, *J. Phys. Chem. A.*, 2001, **105**, 8296.
18. M. Horn, M. Oswald, R. Oswald and P. Botschwina, *Ber. Buns. Phys. Chem.*, 1995, **99**, 323.

19. P. A. Hatherly, M. Stankiewicz, K. Codling, J. C. Creasey, H. M. Jones and R. P. Tuckett, *Meas. Science and Tech.*, 1992, **3**, 891.
20. W. C. Wiley and I. H. Maclaren, *Rev. Sci. Instrum.*, 1955, **26**, 1150.
21. G. K. Jarvis, D. P. Seccombe and R. P. Tuckett, *Chem. Phys. Lett.*, 1999, **315**, 287.
22. C.E. Moore, 1971, *Atomic energy levels NSRDS-NBS volume 35*.
23. G. E. Busch and K. R. Wilson, *J. Chem. Phys.*, 1972, **56**, 3626.
24. I. Powis, *Mol. Phys.*, 1980, **39**, 311.
25. C. E. Klots, *J. Chem. Phys.*, 1973, **58**, 5364.
26. E. Illenberger and J. Momigny, *Gaseous Molecular Ions*, 1992, Springer, New York.
27. M. W. Chase, *J. Phys. Chem. Ref. Data*, 1998, *monograph number 9*.
28. H. Becker, J. Hrusak, H. Schwarz and D. K. Bohme, *J. Chem. Phys.*, 1994, **100**, 1759.
29. D. S. Peterka, M. Ahmed, C. Y. Ng and A. G. Suits, *Chem. Phys. Lett.*, 1999, **312**, 108.
30. Y. Muramatsu, K. Ueda, Y. Shimizu, H. Chiba, K. Amano, Y. Sato and H. Nakamatsu, *J. Phys. B.*, 1999, **32**, L213.
31. I. Powis, 2001, *unpublished data*.
32. P. J. Knowles, 2000, *private communication*.
33. R. N. Dixon and R. P. Tuckett, *Chem. Phys. Lett.*, 1987, **140**, 553.
34. C. J. Marsden, D. Christen, H. Oberhammer, *J. Mol. Struct.*, 1985, **131**, 299.
35. G. K. Jarvis, K. J. Boyle, C. A. Mayhew and R. P. Tuckett, *J. Phys. Chem. A.*, 1998, **102**, 3219.
36. G. K. Jarvis, K. J. Boyle, C. A. Mayhew and R. P. Tuckett, *J. Phys. Chem. A.*, 1998, **102**, 3230.
37. D. P. Seccombe, R. Y. L. Chim, G. K. Jarvis and R. P. Tuckett, *Phys. Chem. Chem. Phys.*, 2000, **2**, 769.
38. D. P. Seccombe, R. P. Tuckett and B. O. Fisher, *J. Chem. Phys.*, 2001, **114**, 4074.
39. T. J. Buckley, R. D. Johnson, R. E. Huie, Z. Zhang, S. C. Kuo and R. B. Klemm, *J. Phys. Chem.*, 1995, **99**, 4879.
40. D. M. Smith, R. P. Tuckett, K. R. Yoxall, K. Codling and P. A. Hatherly, *Chem. Phys. Lett.*, 1993, **216**, 493.
41. C. Atterbury, R. A. Kennedy, C. A. Mayhew and R. P. Tuckett, *Phys. Chem. Chem. Phys.*, 2001, **3**, 1949.
42. Y. S. Cheung, Y. J. Chen, C. Y. Ng, S. W. Chiu and W. K. Li, *J. Am. Chem. Soc.*, 1995, **117**, 9725.

43. C. W. Bauschlicher and A. Ricca, *J. Phys. Chem. A.*, 1998, **102**, 4722.
44. R. A. Kennedy and C. A. Mayhew, *Int. J. Mass Spectrom.*, 2001, **206**, i.
45. R. Y. L. Chim, R. A. Kennedy, R. P. Tuckett, W. Zhou, G. K. Jarvis, D. J. Collins and P. A. Hatherly, *J. Phys. Chem.*, 2001, **105**, 8403.

CHAPTER 6 : THE VACUUM-UV ABSORPTION SPECTRUM OF SF₅CF₃, AND IMPLICATIONS FOR ITS LIFETIME IN THE EARTH'S ATMOSPHERE

6.1 Introduction

Two years ago, a compound previously undetected in the earth's atmosphere, trifluoromethyl sulfur pentafluoride (SF₅CF₃), was reported by Sturges *et al.*¹ The processes that remove a pollutant from the earth's atmosphere include reaction with the OH· radical in the troposphere ; UV photolysis (200-300 nm) and reactions with O (¹D) in the stratosphere ; and reactions with small cations, free electrons and vacuum-UV (VUV) photons (especially at the Lyman-α wavelength of 121.6 nm) in the upper stratosphere and mesosphere. Although not yet measured, it is believed that the reactions of both OH· and O (¹D) with SF₅CF₃, like those with CF₄ and SF₆,² will be very slow ($< 10^{-16}$ cm³ molecule⁻¹ s⁻¹). UV photolysis in the lower stratosphere seems very unlikely because the S–C bond strength has been measured indirectly by photoelectron – photoion coincidence spectroscopy to be as high as 4.06 ± 0.45 eV,³ similar to that of the S–F bond in SF₆.⁴ Short wavelength light ($\lambda = 200\text{-}300$ nm) which reaches the stratosphere has enough energy to photodissociate SF₅CF₃. The cross section at these wavelengths close to threshold, however, is expected to be very small, as the electronic transition is from a bound to a repulsive state. Indeed, no absorption has been observed for $\lambda > 190$ nm, and electron energy loss spectroscopy (EELS) has shown that, for vertical excitation, the lowest-lying excited electronic state of SF₅CF₃ lies more than 8 eV ($\lambda < 155$ nm) above the ground state.⁵

Interest has therefore centred on the reactions that could remove SF₅CF₃ in the upper stratosphere and mesosphere above *ca.* 60 km. The total rate of removal of SF₅CF₃, in units of molecules per unit volume per unit time, by its reactions with cations, electrons and photons is given by :

$$\text{Rate} = [\text{SF}_5\text{CF}_3] \cdot \left(\sum_{ions} k_{ion}[\text{ion}] + k_e[e^-] + \sigma_{121.6} J_{121.6} \right) \quad (6.1)$$

where k_{ion} and k_e are the bimolecular rate constants for reactions of a cation or electron with SF₅CF₃, $\sigma_{121.6}$ and $J_{121.6}$ are the absorption cross-section of SF₅CF₃ and the mesospheric solar flux at 121.6 nm, and the square brackets signify the concentration of a species. The value of $J_{121.6}$ is well established.⁶ It is noted that equation (6.1) assumes that an ion-molecule reaction, electron attachment and VUV absorption leads to the removal of every SF₅CF₃ molecule by the formation of dissociation products. This assumption is true for ion-molecule reactions, but is not necessarily so for the other two processes.

The rate constants for reactions of SF₅CF₃ with a large number of small cations have been measured in a selected ion flow tube apparatus at 298 K.^{7,8} Most reactions proceed with rate constants close to the capture limit. However, those of the most abundant ions in the mesosphere (O₂⁺ and NO⁺)⁹ have rate constants which are very much slower, due to the low recombination energies of these ions. Thus, ion-molecule reactions are unlikely to contribute significantly to the total removal rate of SF₅CF₃ from the atmosphere. Electron attachment experiments have been performed in *ca.* 1 bar of N₂ and Ar buffer gases at 298 K under non-thermal swarm conditions.¹⁰ The rate constant was measured as a function of mean electron energy in the range 0.04 – 1.90 eV, with k_e increasing as the mean electron energy decreases. The electron attachment rate constant with thermal electrons at 298 K, $\bar{\epsilon} = 0.038$ eV, was estimated to be $7.7 \pm 0.6 \times 10^{-8}$ cm³ molecule⁻¹ s⁻¹, and significantly the only observed product was SF₅⁻ from dissociative attachment. These results have been confirmed by others.^{11,12} This process therefore does remove SF₅CF₃ from the earth's atmosphere, and Kennedy and Mayhew, like others before for both SF₅CF₃ and SF₆,^{2,11-13} assumed that it was dominant. The first observation of the absorption cross section of SF₅CF₃ in the VUV, and especially at the Lyman- α wavelength of 121.6 nm where the solar mesospheric flux is the greatest is reported. As mentioned earlier, a pseudo-absorption spectrum has been measured by EELS at a resolution of *ca.* 0.5 eV.⁵ The data could not be put on to an absolute scale of photon absorption cross section as a function of energy. It was noted, however, that SF₅CF₃, certainly unlike CF₄,² did absorb significantly at 121.6 nm. The third term of the right hand side of equation (6.1) may therefore contribute significantly to the total removal rate of SF₅CF₃ from the earth's mesosphere, leading to a decrease in the lifetime of SF₅CF₃ in the atmosphere.

6.2 Experimental

The VUV absorption apparatus has been described elsewhere.¹⁴ Radiation from a synchrotron passes through the exit slit of a VUV monochromator, through a 2-stage differential pumping section, and through a 1 mm thick stainless steel microchannel plate into an absorption cell of length, L , 300 mm. A pressure differential of 1000:1 across the microchannel plate is possible. The gas pressure in the absorption cell, in the range 5-60 μ bar, is measured by a Balzers capacitance manometer, and is maintained constant *via* a slow controlled flow of gas. The VUV radiation at the end of the cell is detected through a sodium-salicylate-coated window and a visible photomultiplier tube operating in the photon counting mode. Since the pressure of gas and optical path length are known, measurement of the ratio of transmitted intensity observed for background (no gas) and sample spectra (with gas) can yield, *via* the Beer Lambert law, absolute absorption cross sections. In the calculation of I_o/I at every value of the VUV energy, allowance is made for the natural decay of the VUV flux over the time of an experiment. No allowance is made for the small pressure gradient within the absorption cell due to gas leakage through the microchannel plate, and the small effects of second-order radiation from the VUV monochromator are ignored. It is estimated that cross sections are accurate to *ca.* 15-20 %.

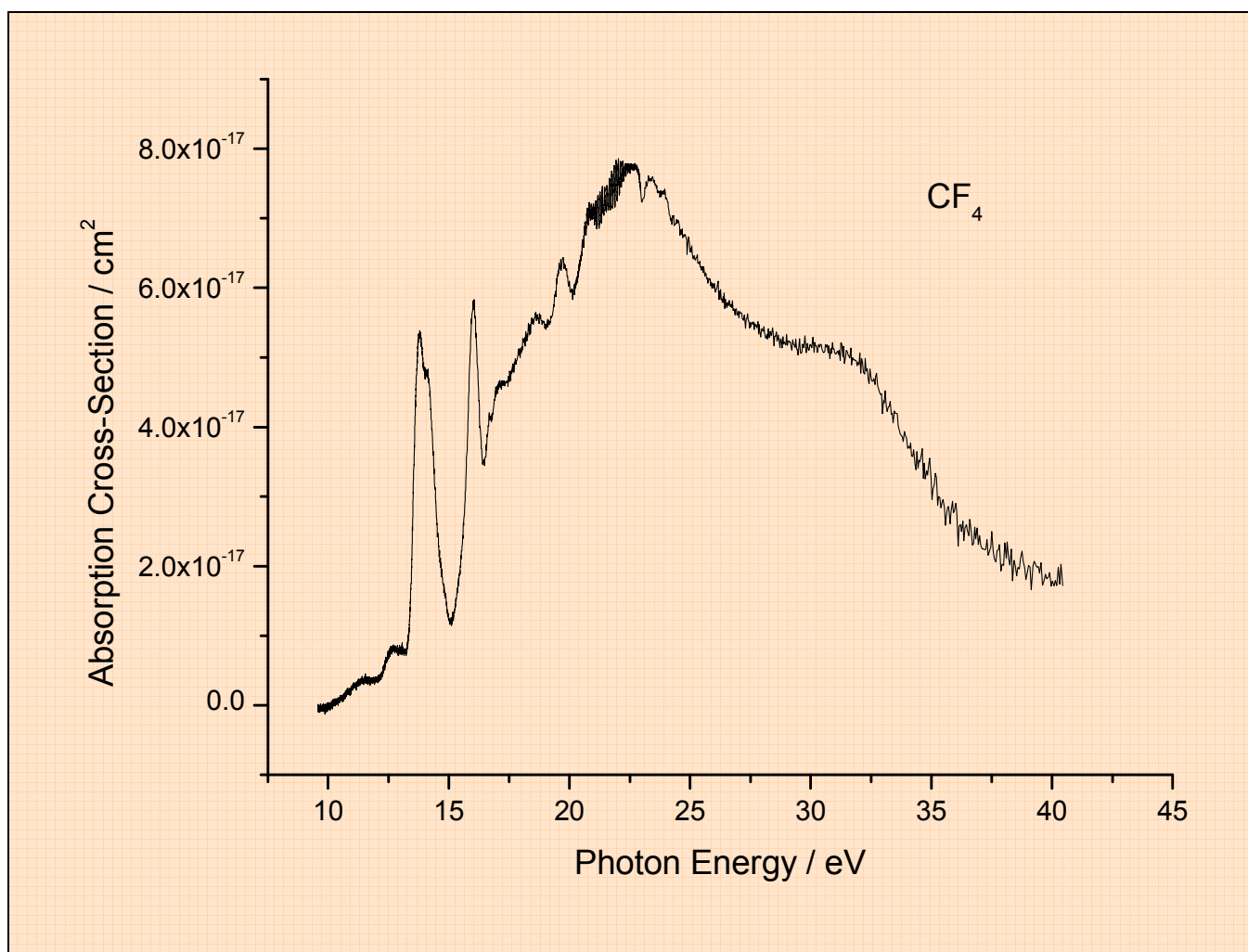


Figure 6.1 Vacuum-UV absorption spectrum of CF_4 recorded at a resolution of 0.08 nm.

Preliminary experiments were performed at the Bessy I source in Berlin using the 1.5 m NIM-2 beamline with a lamellar 1200 l/mm gold-coated Zeiss grating. Using 100 μm entrance and exit slits giving a photon resolution of *ca.* 0.08 nm, the absorption spectrum of CF_4 in the range 10–40 eV is shown in Fig. 6.1. The cross-section at 10.2 eV, Lyman- α radiation, is too small to measure accurately, but has been measured by Ravishankara *et al.*² to be less than $8 \times 10^{-22} \text{ cm}^2 \text{ molecule}^{-1}$. The spectrum is in good agreement with that recorded by Lee *et al.*¹⁵ at an inferior resolution of 0.2 nm. In particular, the $(1t_1)^- 13p$, $(4t_2)^- 13s$ and $(1e)^- 13p/(4t_2)^- 13d$ Rydberg states at 13.6, 13.9 and 15.9 eV are clearly observed.¹⁶ The cross sections at the maxima of the well-resolved first and third peaks are 5.5×10^{-17} and $5.8 \times 10^{-17} \text{ cm}^2 \text{ molecule}^{-1}$, in excellent agreement with the values obtained by Lee *et al.*¹⁵ The absorption spectrum of SF_3CF_3 was obtained using beamline SA63 of the Super-Aco synchrotron source in Paris, with a 1 m normal incidence monochromator equipped with a 1200 l/mm grating. Using a photon resolution of 0.12 nm, the absorption spectrum in the range 6–26 eV is shown in Fig. 6.2. The widths of the peaks are

determined by molecular properties and not by the resolution of the incident VUV beam, since the spectrum is invariant to the slitwidth of the monochromator. The spectrum up to 12.4 eV (100 nm) is in good agreement with that obtained by EELS, which approximates to absorption spectroscopy for high incident electron energies, although absolute values of σ were not determined.⁵ It is determined that the cross section of SF₅CF₃ at 10.2 eV, Lyman- α radiation, is $1.5 \pm 0.3 \times 10^{-17} \text{ cm}^2 \text{ molecule}^{-1}$, where the Beer-Lambert law is expressed as $\ln(I_0/I) = \sigma L[\text{SF}_5\text{CF}_3]$. No attempt has been made to assign the peaks in the spectrum, although peaks below 14.1 eV, the vertical ionisation potential to the ground state of SF₅CF₃⁺,³ must correspond to Rydberg states of SF₅CF₃ converging on either the ground or excited states of SF₅CF₃⁺.

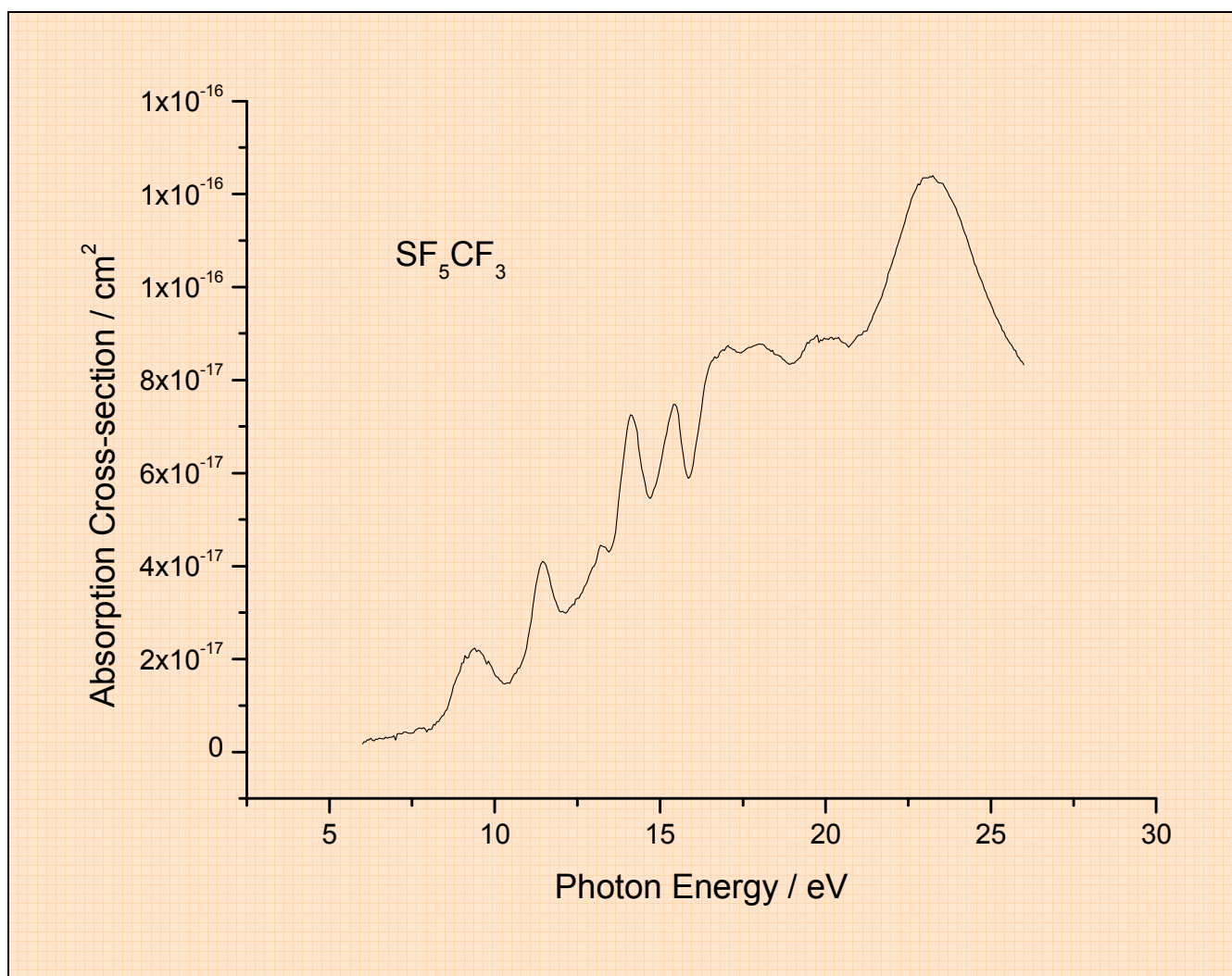


Figure 6.2 Vacuum-UV absorption spectrum of SF₅CF₃ recorded at a resolution of 0.12 nm

6.3. The lifetime of SF₅CF₃ in the earth's atmosphere

At this point I would like to thank Dr. R. P. Tuckett for the many ideas he contributed to this section. The values for the electron attachment rate constant, the absorption cross-section at 121.6 nm, and atmospheric lifetimes of CF₄, SF₆ and SF₅CF₃ are given in Table 6.1. The almost infinite value for the

lifetime of CF₄, greater than 50000 years,^{2,18} arises because this molecule shows no absorption at 121.6 nm, attaches electrons at a negligibly slow rate, and does not react with O₂⁺ or NO⁺. By comparison, SF₆ and SF₅CF₃ both attach electrons at a fast rate (greater than 10⁻⁸ cm³ molecule⁻¹ s⁻¹) and show significant absorption with Lyman-α radiation. Furthermore, the height profiles of SF₆ and SF₅CF₃ are similar in the atmosphere.¹ It is therefore sensible to make quantitative comparisons between these two molecules.

Table 6.1 Thermal electron attachment rate constants, absorption cross-sections at 121.6 nm, and atmospheric lifetimes for CF₄, SF₆ and SF₅CF₃.

Perfluoro compound	k_e (298 K) / cm ³ s ⁻¹	$\sigma_{121.6}$ / cm ²	lifetime / years
CF ₄	< 10 ⁻¹⁶ ^a	< 8 x 10 ⁻²² ^b	> 50000 ^{b,c}
SF ₆	2.3 x 10 ⁻⁷ ^{d,e}	1.76 x 10 ⁻¹⁸ ^b	> 800 ^d
SF ₅ CF ₃	7.7 x 10 ⁻⁸ ^f	1.5 x 10 ⁻¹⁷ ^g	ca. 1000 ^{f,h}

^a Biehl *et al.*⁶ ^b Ravishankara *et al.*² ^c Schumacher *et al.*¹⁷ ^d Miller *et al.*¹² ^e Cicerone *et al.*¹⁸
^f Adams *et al.*⁹ ^g this work ^h Sailer *et al.*¹¹

It is noted that k_e for SF₅CF₃ at 298 K is three times smaller than for SF₆, whereas the absorption cross-section is 8.5 times larger. Therefore, the pseudo-first-order rate constant for removal of SF₅CF₃ by electrons divided by that due to photons at the same altitude of the mesosphere, $k_e[e^-] / \sigma_{121.6}J_{121.6}$, is 25.5 times smaller than this ratio for SF₆. (This assumes that electron attachment leads to total destruction of SF₆, to SF₅⁻.) Assuming an incorrect value for k_e of 1 x 10⁻⁹ cm³ molecule⁻¹ s⁻¹, Ravishankara *et al.*² determined that this ratio of pseudo-first-order rate constants for SF₆ was 3.2, and obtained an atmospheric lifetime of 3200 years. Using the much larger and correct value for k_e (SF₆) of 2.3 x 10⁻⁷ cm³ molecule⁻¹ s⁻¹, Morris *et al.*¹³ showed that this ratio of pseudo-first-order rate constants was 1998, and determined a lower limit to the atmospheric lifetime of 800 years. The lower limit arises because they assumed that every electron attachment event led to the permanent removal of SF₆ from the atmosphere. Reddmann *et al.*²⁰ considered a number of scenarios for the destruction of SF₆⁻. They found that if less than 100 % was destroyed, the lifetime was increased ; they calculated values spanning 400 to 10000 years, depending on the loss mechanism and the value for the electron density in the upper stratosphere / mesosphere.

Assuming that the analysis of Morris *et al.*¹³ for SF₆ is correct, then the predominant removal process for SF₅CF₃ remains electron attachment and not VUV photolysis, since the ratio of the pseudo-first-order rate

constants for SF₅CF₃ is 1998 / 25.5 or 78.3, *i.e.* still much greater than unity. It is more difficult, however, to convert these first-order rate constants into an atmospheric lifetime for SF₅CF₃. The chemical lifetime, τ_{chemical} , can be written as $1 / (k_e[e^-] + \sigma_{121.6}J_{121.6})$, but the value obtained is a function of position, particularly altitude, in the atmosphere. In the troposphere, τ_{chemical} will be infinite because both the concentration of electrons and $J_{121.6}$ are effectively zero at low altitude, but in the mesosphere it will be much less. Put another way, multiplication of k_e for either SF₆ or SF₅CF₃ by a typical electron density in the mesosphere, 10^1 – 10^3 cm⁻³,⁹ yields a chemical lifetime for either species which is much shorter than the average atmospheric lifetime, simply because most of the SF₆ or SF₅CF₃ does not reside in the mesosphere.

Global atmospheric lifetimes, such as those reported for SF₆,^{2,13} are obtained from globally-averaged loss frequencies. In forming the average, the pseudo-first-order destruction rate constant for each region of the atmosphere is weighted according to the number of molecules of compound in that region,

$$\langle k \rangle_{\text{global}} = \frac{\sum_i k_i V_i n_i}{\sum_i V_i n_i} \quad (6.2)$$

where i is a region, k_i is a pseudo-first-order rate constant for region i , V_i is the volume of region i , and n_i is the number density of the compound under study in region i . The averaging process thus needs input from a 2-D or 3-D model of the atmosphere in order to supply the values of n_i . Differences in the kinetic model (k_i) and the atmospheric distributions (n_i) from different climate / transport models account for the variety of atmospheric lifetimes that have been reported.^{2,13,20} For molecules such as SF₆ which are only destroyed in the mesosphere above 60 km, the importance of both these factors has been explored by Hall and Waugh.²¹ Their results show that because the fraction of the total number of SF₆ molecules in the mesosphere is very small, the global atmospheric lifetime is very much longer than the mesospheric, chemical lifetime. Thus, they quote that if the mesospheric loss frequency is 9×10^{-8} s⁻¹, corresponding to a local lifetime of 129 days, then the global lifetime ranges between 1424 and 1975 years, according to which climate / transport model is used.

SF₆ attaches electrons with a temperature-independent rate constant close to the theoretical limit for s-wave capture of *ca.* 2×10^{-7} cm³ molecule⁻¹ s⁻¹.¹⁹ Morris *et al.*¹³ assume complete destruction of the transient SF₆⁻ anion and determine a lower limit to the atmospheric lifetime of 800 years. They conclude that the inclusion of electron attachment reactions can never reduce the lifetime of any long-lived greenhouse molecule, such as SF₅CF₃, below this limit of 800 years. Very recently, Miller *et al.*¹² have measured the electron attachment rate constant to SF₅CF₃ as a function of temperature in the range 296-

563 K. Their value at room temperature is in excellent agreement with the estimate of Kennedy and Mayhew,¹⁰ they determine that k_e decreases very slightly with decreasing T, and deduce an activation barrier of 2.4 kJ mol⁻¹. By extrapolating their data to 250 K, an average temperature in the mesosphere, they estimate that k_e (SF₅CF₃) at this temperature is 4 times smaller than that of SF₆, but approximately 4 times larger than that of c-C₄F₈. Since the lower-limit lifetime of the former is 800 years and that of the latter 1400 years,¹³ Miller *et al.*¹² deduce that the lifetime of SF₅CF₃ is probably of the order of 1000 years.

Table 6.2 Energetics of reactions of SF₅CF₃ at 0 K with zero-energy electrons and photons.

Reaction	$\Delta_r H^0 / \text{kJ mol}^{-1}$ (eV)	
	Scheme A ^a	Scheme B ^b
SF ₅ CF ₃ + e ⁻ (0 eV) → SF ₅ ⁻ (-1282) + CF ₃ (-463) ^c (-1621 or -1770)	-124 (-1.29)	+25 (+0.26)
→ CF ₃ ⁻ (-639) + SF ₅ (-915) ^d	+67 (+0.69)	+216 (+2.24)
SF ₅ CF ₃ + hν (10.2 eV) → SF ₅ (-915) + CF ₃ (-463) (-1621 or -1770)	-741 (-7.68)	-592 (-6.14)
→ CF ₃ ⁺ (+409) + SF ₅ ⁻ (-1282)	-236 (-2.45)	-87 (-0.90)
→ SF ₅ ⁺ (+29) + CF ₃ ⁻ (-639)	+27 (+0.28)	+176 (+1.82)

^a Scheme A assumes $\Delta_f H^0$ (SF₅CF₃) = -1621 kJ mol⁻¹.²²

^b Scheme B assumes $\Delta_f H^0$ (SF₅CF₃) = -1770 kJ mol⁻¹.³

^c Reference 24, and assuming the ionisation energy of CF₃ is 9.04 eV²⁵ and the electron affinity is 1.82 eV.²⁶ The values in brackets of column 1 are 0 K enthalpies of formation, in units of kJ mol⁻¹.

^d Reference 4, and assuming the ionisation energy of SF₅ is 9.8 eV³ and the electron affinity is 3.8 eV.^{27,28} The values in brackets of column 1 are 0 K enthalpies of formation, in units of kJ mol⁻¹.

To improve the kinetic part of the atmospheric destruction model for SF₅CF₃ from which the lifetime is obtained, knowledge is needed of the fate of transient SF₅CF₃⁻ anions formed by the attachment of thermal-energy electrons, and of excited SF₅CF₃* produced by photoexcitation at 121.6 nm. Some

destruction pathways are listed in Table 6.2. The feasibility of these pathways can be assessed by combining literature 0 K thermochemical data for CF_3 , CF_3^+ , CF_3^- , SF_5 , SF_5^+ and SF_5^- with the 0 K enthalpy of formation of SF_5CF_3 . The values adopted for CF_3 , CF_3^+ , CF_3^- , SF_5 , SF_5^+ and SF_5^- are given in brackets in Column 1 of Table 6.2, in units of kJ mol^{-1} . There are two recent theoretical values for $\Delta_f H^0_0$ (SF_5CF_3), $-1621 \text{ kJ mol}^{-1}$ (G2)²² and $-1623 \text{ kJ mol}^{-1}$ (MP2)¹². The JANAF tables quote $\Delta_f H^0_0$ (SF_5CF_3) = $-1700 \pm 63 \text{ kJ mol}^{-1}$.²³ A recent determination of the dissociative ionisation energy of SF_5CF_3 (*i.e.* $\Delta_f H^0_0$ for the reaction $\text{SF}_5\text{CF}_3 \rightarrow \text{CF}_3^+ + \text{SF}_5 + e^-$) yielded $\Delta_f H^0_0$ (SF_5CF_3) = $-1770 \pm 47 \text{ kJ mol}^{-1}$.³ Using the G2 value for $\Delta_f H^0_0$ (SF_5CF_3) from Ball²² (Scheme A in Table 6.2), dissociative attachment of a zero-energy electron to SF_5CF_3 to form $\text{SF}_5^- + \text{CF}_3$ is energetically feasible, but the products cannot be $\text{CF}_3^- + \text{SF}_5$. This is consistent with the results of the electron attachment experiments performed in N_2 and Ar buffer gases,¹⁰ where the only observed product ion was SF_5^- . With Lyman- α photoexcitation (10.2 eV), the limit $\text{SF}_5 + \text{CF}_3$ is easily accessible. It is also possible to reach the ion-pair limit $\text{CF}_3^+ + \text{SF}_5^-$, but not $\text{SF}_5^+ + \text{CF}_3^-$. Using the more negative experimental value for $\Delta_f H^0_0$ (SF_5CF_3) from Chim *et al.*³ (Scheme B in Table 2), the same conclusions hold except electron attachment to form $\text{SF}_5^- + \text{CF}_3$ becomes marginally endothermic by 25 kJ mol^{-1} . The main conclusion from the data of Table 6.2 is that energetically-accessible exit channels in which the S–C bond is broken exist for both zero-energy electron attachment to SF_5CF_3 and Lyman- α photoexcitation of SF_5CF_3 . Both processes, therefore, are likely to destroy SF_5CF_3 with unit efficiency.

6.4 Conclusions

The vacuum-UV absorption cross-section of SF_5CF_3 in the range 50-150 nm have been measured. The cross-section at 121.6 nm is $1.5 \pm 0.3 \times 10^{-17} \text{ cm}^2$. By comparison with data for SF_6 , it is deduced that electron attachment in the mesosphere is the dominant removal process of SF_5CF_3 from the earth's atmosphere, with VUV photodissociation only contributing *ca.* 1 % to the pseudo-first-order rate constant. The atmospheric lifetime, however, is determined primarily by the rate of transport of SF_5CF_3 from the earth's surface to the mesosphere. This chapter agrees with the conclusions of others^{1,5,10,12} that its atmospheric lifetime is *ca.* 1000 years. The results of this chapter have very recently been published,²⁹ and our data is in good agreement with another VUV absorption study published as this chapter was being written.³⁰

6.5 References

1. W. T. Sturges, T. J. Wallington, M. D. Hurley, K. P. Shine, K. Sihra, A. Engel, D. E. Oram, S. A. Penkett, R. Mulvaney, C. A. M. Brenninkmeijer, *Science*, 2000, **289**, 611.
2. A. R. Ravishankara, S. Solomon, A. A. Turnipseed, R. F. Warren, *Science*, 1993, **259**, 194.
3. R. Y. L. Chim, R. A. Kennedy, R. P. Tuckett, W. Zhou, G. K. Jarvis, D. J. Collins, P. A. Hatherly, *J. Phys. Chem. A.*, 2001, **105**, 8403.
4. E. R. Fisher, B. L. Kickel, P. B. Armentrout, *J. Chem. Phys.*, 1992, **97**, 4859.
5. P. A. Kendall, N. J. Mason, *J. Elec. Spec. Rel. Phen.*, 2001, **120**, 27.
6. T. N. Woods, W. K. Tobiska, G. J. Rottman, J. R. Worden, *J. Geophys. Res. A.*, 2000, **105**, 27195.
7. C. Atterbury, R. A. Kennedy, C. A. Mayhew, R. P. Tuckett, *Phys. Chem. Chem. Phys.*, 2001, **3**, 1949.
8. C. Atterbury, A. D. J. Critchley, R. A. Kennedy, C. A. Mayhew, R. P. Tuckett, *Phys. Chem. Chem. Phys.*, 2002, **4**, 2206.
9. N. G. Adams, D. Smith, *Contemp. Phys.*, 1988, **29**, 559.
10. R. A. Kennedy, C. A. Mayhew, *Int. J. Mass Spectrom.*, 2001, **206**, i.
11. W. Sailer, H. Drexel, A. Pelc, V. Grill, N. J. Mason, E. Illenberger, J. D. Skalny, T. Mikoviny, P. Scheier, T. D. Mark, *Chem. Phys. Letts.*, 2002, **351**, 71.
12. T. M. Miller, S. T. Arnold, A. A. Viggiano, W. B. Knighton, *J. Chem. Phys.*, 2002, **116**, 6021.
13. R. A. Morris, T. M. Miller, A. A. Viggiano, J. F. Paulson, S. Solomon, G. Reid, *J. Geophys. Res. D.*, 1995, **100**, 1287.
14. A. Hoxha, R. Loch, B. Leyh, D. Dehareng, K. Hottmann, H. W. Jochims, H. Baumgartel, *Chem. Phys.*, 2000, **260**, 237.
15. L. C. Lee, X. Wang, M. Suto, *J. Chem. Phys.*, 1986, **85**, 6294.
16. H. Biehl, K. J. Boyle, R. P. Tuckett, H. Baumgartel, H. W. Jochims, *Chem. Phys.*, 1997, **214**, 367.
17. R. Schumacher, H. R. Sprunken, A. A. Christodoulides, R. N. Schindler, *J. Phys. Chem.*, 1978, **82**, 2248.
18. R. F. Cicerone, *Science*, 1979, **206**, 59.
19. T. M. Miller, A. E. S. Miller, J. F. Paulson, X. Liu, *J. Chem. Phys.*, 1994, **100**, 8841.
20. T. Reddmann, R. Ruhnke, W. Kouker, *J. Geophys. Res. D.*, 2001, **106**, 14525.
21. T. M. Hall, D. W. Waugh, *J. Geophys. Res. D.*, 1998, **103**, 13327.
22. D. W. Ball, *J. Mol. Struct. – TheoChem.*, 2002, **578**, 29.
23. M. W. Chase, *J. Phys. Chem. Ref. Data*, 1998, Monograph No. 9.
24. B. Ruscic, J. V. Michael, P. C. Redfern, L. A. Curtiss, K. Raghavachari, *J. Phys. Chem. A.*, 1998, **102**, 10889.
25. G. A. Garcia, P. M. Guyon, I. Powis, *J. Phys. Chem. A.*, 2001, **105**, 8296.

26. H. J. Deyerl, L. S. Alconcel, R. E. Continetti, *J. Phys. Chem. A.*, 2001, **105**, 552.
27. M. F. Fenzlaff, R. Gerhard, E. Illenberger, *J. Chem. Phys.*, 1988, **88**, 149.
28. E. C. M. Chen, L-R. Shuie, E. D. D'sa, C. F. Batten, W. E. Wentworth, *J. Chem. Phys.*, 1988, **88**, 4711.
29. R. Y. L. Chim, R. A. Kennedy, R. P. Tuckett, *Chem. Phys. Letts.*, 2003, **367**, 697.
30. K. Takahashi, T. Nakayama, Y. Matsumi, S. Solomon, T. Gejo, E. Shigemasa and T. J. Wallington, *Geophys. Res. Letters*, 2002, **29(15)**, article 1712.

CHAPTER 7 : FRAGMENTATION OF THE VALENCE ELECTRONIC STATES OF SF₅Cl⁺ PROBED BY THRESHOLD PHOTOELECTRON- PHOTOION COINCIDENCE SPECTROSCOPY

7.1 Introduction

Very few fragmentation studies of SF₅Cl are reported in the literature. Only one of these use a continuum excitation source. Much of the interest in SF₆ derivatives comes from their use or their possible use in reactive plasmas. Dekock *et al.*¹ have recorded the valence photoelectron spectrum (He I and He II) of SF₅Cl from which the ionisation potentials of the various electronic states of the parent ion can be determined. Harland and Thynne² have studied SF₅Cl via mass spectrometric methods using electrons as the excitation source. The experimental data are limited largely due to the ionisation thresholds being smeared out as a result of the high energy tail of the electron energy distribution. Harland and Thynne in this study were interested in the negative ion formation in this system. Baumgartel *et al.* have also performed a mass spectrometric study of SF₅Cl. In these experiments photons were used instead of electrons as the excitation source in the energy range 12-20 eV. Using a selected ion flow tube (SIFT) apparatus, Atterbury *et al.*³ have investigated the positive ion chemistry of SF₅Cl. Rate coefficients and ion production branching ratios were determined for reactions with several different cations.

This chapter reports a comprehensive study of the fragmentation of the parent cation of SF₅Cl excited by photons in the range 12-21 eV by threshold photoelectron photoion spectroscopy. Three types of experiments have been performed, scanning energy TPEPICO, fixed energy TPEPICO and continuing a technique developed for recent work on SeF₆ and TeF₆,⁵ an experiment that yields the first dissociative ionisation energy of SF₅Cl (to SF₅⁺ + Cl + e⁻). In addition, the threshold photoelectron spectrum of SF₅Cl is reported in this chapter for the first time allowing elucidation of any autoionisation effects.

7.2 Experimental

The photoionisation experiments required the use of the electron analyser and the time of flight drift tube described earlier in Chapter 2. Synchrotron radiation dispersed with the 1m Seya-Namioka monochromator on beamline 3.1 at SRS (Daresbury, UK) was used as the photon source. The medium energy grating was used and was calibrated using argon. Spectra were flux normalised via the visible fluorescence of a NaSal window.

7.3 Energetics of the key dissociation channels

The energetics of the key dissociation channels and ionisation potentials (vertical and adiabatic) of the valence states of SF₅Cl⁺ are given in Table 7.1. The dissociation energy ($\Delta_f H^0$) was calculated by taking the difference in the heats of formation ($\Delta_f H^0$) of products and reactants (see Chapter 4). The effects of

internal energy are avoided if 0 K values of $\Delta_f H^0$ are used. All neutral enthalpies of formation (0 K) were taken from the JANAF tables.⁶ The values of the enthalpies of formation for SF_x^+ ($x=3-5$) correspond to those used in Chapter 5; namely, $\Delta_f H^0(SF_3^+) = 322 \text{ kJ mol}^{-1}$,⁷ $\Delta_f H^0(SF_4^+) = 365 \text{ kJ mol}^{-1}$,⁷ and $\Delta_f H^0(SF_5^+) = 29 \text{ kJ mol}^{-1}$.⁸ The enthalpy of formation of SF_4Cl^+ was calculated by equating the appearance potential of SF_4Cl^+ (14.8 eV, see section 7.4.2) to the enthalpy of the unimolecular reaction $SF_5Cl \rightarrow SF_4Cl^+ + F + e^-$. It is noted that this estimate only provides an upper limit to $\Delta_f H^0$ and therefore to $\Delta_f H^0(SF_4Cl^+)$. The enthalpies of formation of SF_5Cl , F and Cl are well known (-1026, 77 and 120 kJ mol⁻¹ respectively).⁶ This yields a value of 325 kJ mol⁻¹ for $\Delta_f H^0(SF_4Cl^+)$. The vertical and adiabatic ionisation potentials included in Table 7.1 are taken from Dekock *et al.*¹

Table 7.1 Energetics of the key dissociation channels of SF_5Cl .

Neutral/Parent Ion	Dissociation Channel	Adiabatic (vertical) Ionisation potential / eV	Dissociation Energy / eV
$SF_5Cl^+ \tilde{I}$		(25.1)	
$SF_5Cl^+ \tilde{H}$		(21.9)	
$SF_5Cl^+ \tilde{G}$		(21.0)	
$SF_5Cl^+ \tilde{F}$		(18.88)	
$SF_5Cl^+ \tilde{E}$		(18.07)	
	$SF_3^+ + Cl + 2F$		16.81
$SF_5Cl^+ \tilde{D}$		16.29(16.72)	
	$SF_4^+ + Cl + F$		16.46
$SF_5Cl^+ \tilde{C}$		(15.90)	
$SF_5Cl^+ \tilde{B}$		(15.35)	
	$SF_3^+ + Cl + F_2$		15.21
	$SF_4Cl^+ + F$		14.80
$SF_5Cl^+ \tilde{A}$		14.19(14.79)	
	$SF_3^+ + FCl + F$		14.25
	$SF_4^+ + FCl$		13.90
$SF_5Cl^+ \tilde{X}$		12.33(12.87)	
	$SF_5^+ + Cl$		12.18

7.4 Results

7.4.1 Threshold photoelectron spectrum of SF_5Cl

The threshold photoelectron spectrum of SF_5Cl was measured from 12.0 - 20.6 eV with a constant wavelength resolution of 0.3 nm (Figure 7.1). No vibrational structure is observed. The onset of ionisation, defined as the energy at which signal is first observed above the level of background noise, is 12.24 eV. Peaks are observed at 13.02, 15.66, 16.69, 18.04 and 19.17 eV. The first 5 peaks correspond to

the \tilde{X} , $(\tilde{A}/\tilde{B}/\tilde{C})$, \tilde{D} , \tilde{E} and \tilde{F} states of the parent ion and the agreement of these energies with the He I and He II data by Dekock *et al.*¹ is reasonable. It can be informative to compare the relative intensities of the peaks in the threshold photoelectron and He I photoelectron spectra. Since the latter is recorded with a fixed-energy photon source, only electrons arising from direct ionisation are likely to be detected. By contrast, the threshold photoelectron spectrum is measured by scanning the energy of a continuum radiation source. Hence, in addition to direct ionisation, electrons arising from autoionisation processes will be detected provided their energy is close to threshold. It is noted that the relative intensities of the bands are different between the two conditions. In the threshold photoelectron spectrum, the relative intensity of the \tilde{X} state is anomalously low, whilst that of the unresolved $\tilde{A}/\tilde{B}/\tilde{C}$ states is high.

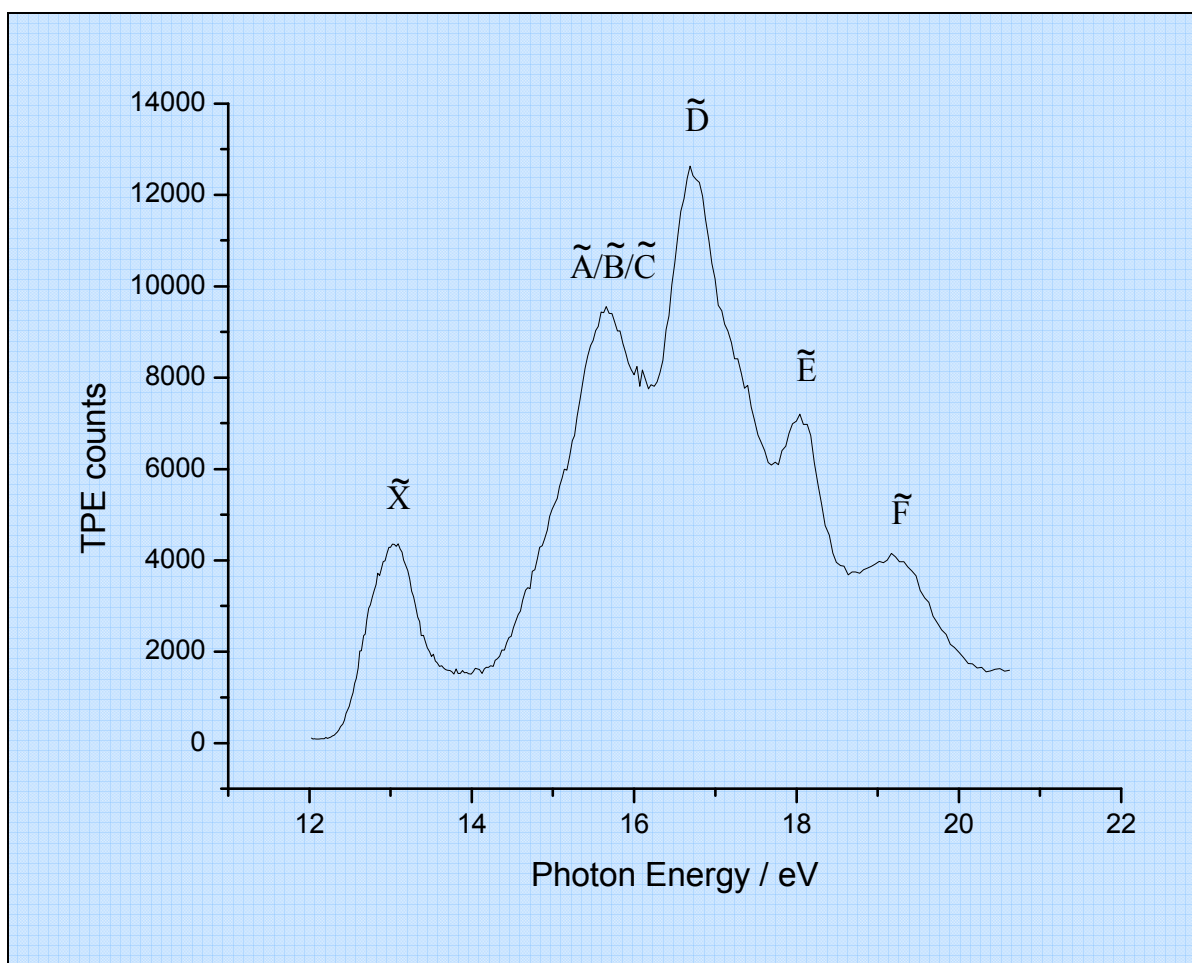


Figure 7.1 Threshold photoelectron spectrum of SF₅Cl at a resolution of 0.3 nm.

7.4.2 Scanning-energy TPEPICO spectrum of SF₅Cl

The scanning-TPEPICO spectrum of SF₅Cl was measured from 12.0 - 20.6 eV with an optical resolution of 0.3 nm and an ion time-of-flight resolution of 64 ns. The four fragments that are observed are SF₅⁺, SF₄Cl⁺, SF₄⁺ and SF₃⁺. The parent ion is not observed. The coincident ion yields are shown in Figure 7.2 and appearance potentials extracted from the ion yield plots are given in Table 7.2. The \tilde{X} state forms solely SF₅⁺ whose signal appears to fall off during the $(\tilde{A}/\tilde{B}/\tilde{C})$ states. SF₄Cl⁺ seems to mirror the

threshold photoelectron spectrum in the ($\tilde{A}/\tilde{B}/\tilde{C}$) and \tilde{D} states. In addition, the SF_4^+ and SF_3^+ signal correspond to the \tilde{D} and \tilde{E} , and \tilde{E} and \tilde{F} states, respectively. It is noted that parent ion is not formed at any photon energy and therefore the ground and excited states of parent ion are dissociative in the Franck-Condon region. This is to be expected as the thermochemical threshold of $\text{SF}_5^+ + \text{Cl}$, 12.18 eV, lies below the onset of ionisation.

Table 7.2 Appearance potentials of the fragment ions following photoexcitation of SF_5Cl .

Daughter Ion	Baumgartel <i>et al.</i> ³	Harland and Thynne ²	This Study
SF_5^+	12.32	13.2	12.3 ± 0.2
SF_4Cl^+	14.76	15.9	14.8 ± 0.2
SF_4^+	15.87		16.2 ± 0.2
SF_3^+	16.2		16.8 ± 0.4

In addition, SF_4^+ and SF_3^+ have very weak, minor thresholds at 14.8 ± 0.2 and 15.0 ± 0.4 eV, respectively, *i.e.* at energies significantly below the major appearance potential. The major thresholds of the fragment ions compare well with the photoionisation mass spectrometric measurements of Baumgartel *et al.*³ The appearance potentials obtained by Harland and Thynne² compare less favourably, but this can be explained by their use of electrons as an excitation source. Baumgartel *et al.*³ also report the observation of SCl^+ , but this has since been attributed to an impurity.⁹

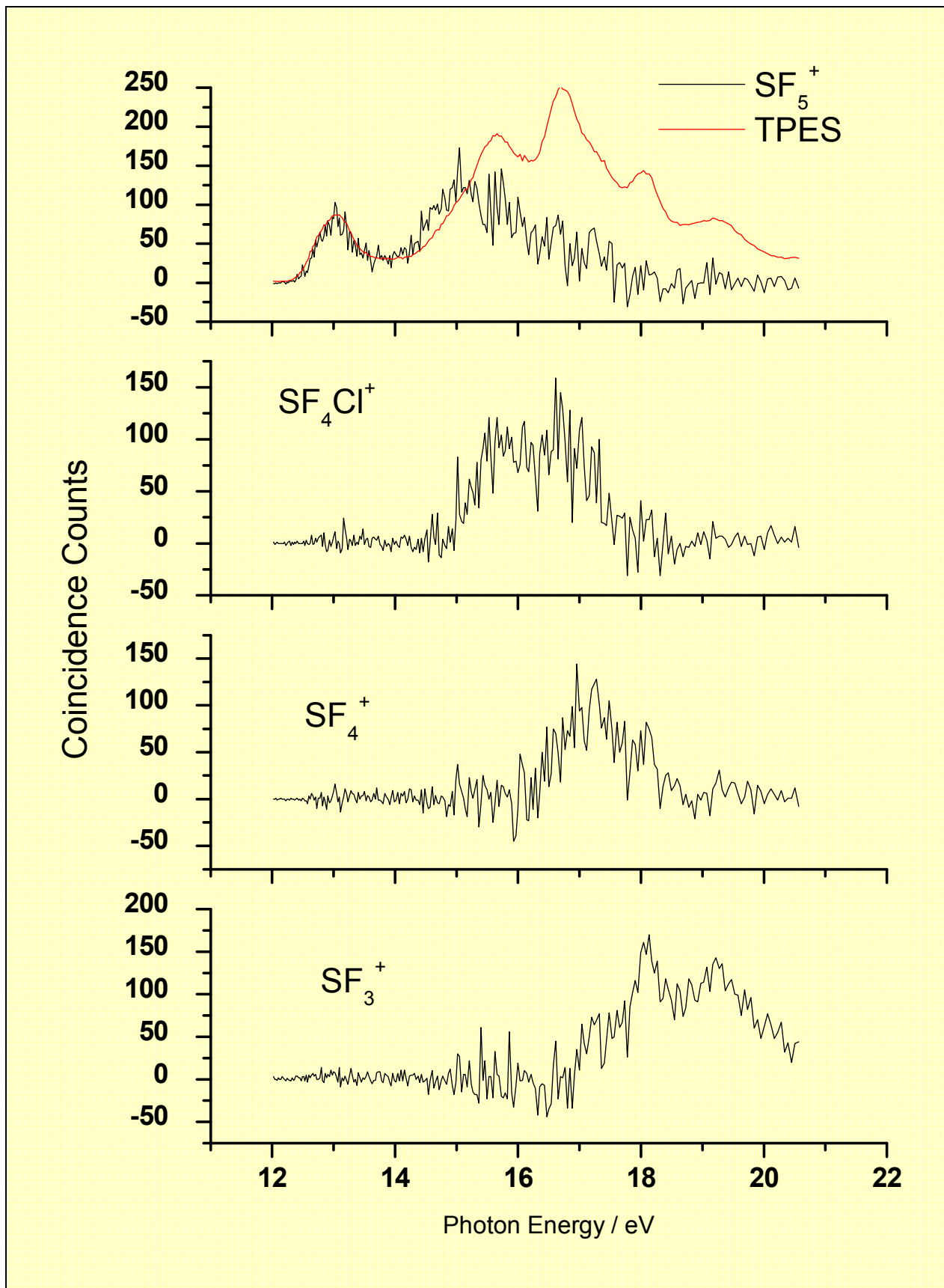


Figure 7.2 Ion yield plots of SF_5^+ , SF_4Cl^+ , SF_4^+ and SF_3^+ measured with an optical resolution of 0.3 nm and a TOF resolution of 64 ns.

7.4.3 Fixed-energy TPEPICO experiments

TPEPICO-TOF spectra of SF₅Cl were recorded at a resolution of 16 ns for the SF₅⁺ fragment at photon energies of 13.05, 15.12, 15.90 and 16.87 eV and for the SF₄Cl⁺ fragment at photon energies of 15.90 and 16.87 eV. Experimental values of <KE>_t and the fractional ratios as well as the theoretical statistical and impulsive limits are given in Table 7.3. A detailed description of the calculation of the statistical and impulsive decay limits is given in Chapter 2. The two isotopes of chlorine (75% ³⁵Cl, 25% ³⁷Cl) have been allowed for in the experimental values quoted for SF₄Cl⁺/SF₅Cl in Table 7.3. The thermal internal energy of SF₅Cl is calculated to be 0.13 eV (vibrational frequencies taken from Shimanouchi).¹⁰

Table 7.3 Mean translational KE releases (<KE>_t) of the two-body fragmentation processes of the valence states of SF₅Cl⁺.

Fragment	Photon Energy / eV	E _{avail} ^a / eV	<KE> _t / eV	Fractional Ratio ^b		
				Experimental	Statistical	Impulsive
SF ₅ ⁺	13.05	1.00	0.26	0.26	0.06	0.61
SF ₅ ⁺	15.12	3.07	1.23	0.40	0.06	0.61
SF ₅ ⁺	15.90	3.85	0.64	0.17	0.06	0.61
SF ₅ ⁺	16.87	4.82	1.37	0.28	0.06	0.61
SF ₄ Cl ⁺	15.90	1.23	1.14	0.93	0.06	0.71
SF ₄ Cl ⁺	16.87	2.20	1.35	0.61	0.06	0.71

^aE_{avail} = Photon Energy – thermochemical threshold for forming daughter ion + thermal energy of parent molecule at 298 K.

^b Fractional ratio = <KE>_t / E_{avail}.

The experimental fractional ratios, fitted for SF₅⁺ all seem to point to hybrid statistical and impulsive decay mechanisms. There appears to be no pattern as the photon energy increases. In measurements on other molecules reported in this thesis, the decay mechanism becomes progressively more statistical in nature as higher-lying electronic states are populated. This behaviour was attributed to an increase in the density of vibronic states with increasing energy. The results here do not reflect this behaviour. Figure 7.3 shows the TPEPICO-TOF spectra of SF₅⁺, whose <KE>_t values are included in Table 7.3. It can be seen that with respect to the full width at half maximum, that the time of flight spectrum at 16.87 eV > that at 15.12 eV > that at 15.90 eV > that at 13.05 eV. This trend is also observed in the <KE>_t values in Table 7.3. For SF₄Cl⁺, comparison of the experimental fractional ratios with the statistical and impulsive limits highlights possible problems with the calculation of the available energy. The experimental fractional ratios appear to be a little high, since the value for SF₄Cl⁺ photoexcited at 15.90 eV gives an experimental value outside both experimental limits. As stated in section 7.3, the calculation Δ_rH⁰ and hence Δ_rH⁰(SF₄Cl⁺) provides an upper limit. Therefore the excess energy may be significantly higher, hence providing a lower percentage of energy being partitioned into translation.

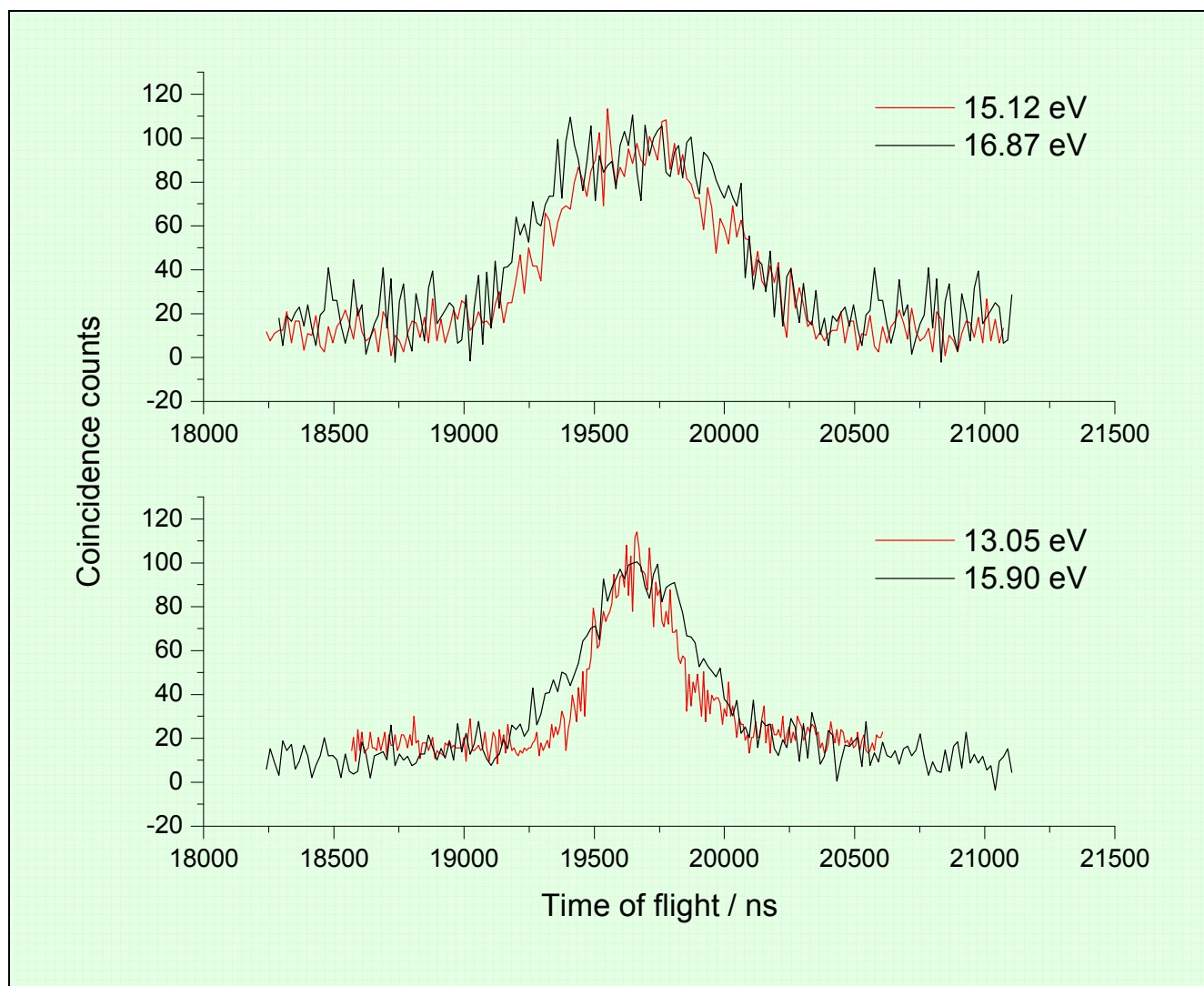


Figure 7.3 Time of flight spectra of SF_5^+ from SF_5Cl at various energies.

7.4.4 Measurement of the first dissociative ionisation energy of SF_5Cl

Over the range 87–103 nm (12.0–14.3 eV), which encompasses all the ground state and the lower-lying part of the first excited state of parent ion, SF_5Cl dissociates exclusively to $\text{SF}_5^+ + \text{Cl} + \text{e}^-$. Therefore the scanning-energy TPEPICO spectrum of SF_5Cl from 87–103 nm in 64 channels was recorded with a high time of flight resolution of the SF_5^+ fragment (16 ns). The theory underlying this experiment was described earlier in Chapter 5. Figure 7.4(a) shows the mean kinetic energy measured for fragmentation to $\text{SF}_5^+ + \text{Cl} + \text{e}^-$ as a function of energy, whilst Figure 7.4(b) shows the threshold photoelectron spectrum of SF_5Cl . Within experimental error, the lowest 23 data points fit to a straight line with a gradient of 0.16. It is noted that this value is significantly less than the prediction of 0.61 for an impulsive decay mechanism. The wrong gradient, also too low, is also observed for $\text{SF}_6 \rightarrow \text{SF}_5^+ + \text{F} + \text{e}^-$.⁸ Extrapolation to zero kinetic

energy release yields the first dissociative ionisation energy of $\text{SF}_5\text{Cl} \rightarrow \text{SF}_5^+ + \text{Cl} + \text{e}^-$ to be 12.3 ± 0.2 eV. Using the 0 K enthalpy of formation for SF_5Cl ($-1026 \text{ kJ mol}^{-1}$) and Cl (120 kJ mol^{-1}), the enthalpy of formation of SF_5^+ is directly determined to be $42 \pm 20 \text{ kJ mol}^{-1}$. This is in good agreement with the value obtained in Chapter 5 for the process $\text{SF}_6 \rightarrow \text{SF}_5^+ + \text{F} + \text{e}^-$, $29 \pm 10 \text{ kJ mol}^{-1}$ and the value recommended by Fisher *et. al.*⁷ from their guided ion beam experiment of $11 \pm 18 \text{ kJ mol}^{-1}$.

This experiment has now been performed on the ground electronic state of CF_3 -containing and XF_5 -containing molecular ions ($X = \text{S}, \text{Se}$ or Te). Details of the SeF_6 and TeF_6 study are given in Chapter 8. We comment that the gradient seems to give the correct value for $\text{CF}_3^+ + \text{X}$ ($X = \text{F}$ or SF_5) dissociations, but values which are too low for $\text{XF}_5^+ + \text{Y}$ ($X = \text{S}, \text{Se}$ or Te ; $\text{Y} = \text{F}$ or Cl) dissociations. The mathematical model, giving

$$\text{slope} = \frac{\mu_b}{\mu_f} \quad (8.1)$$

where μ_b is the reduced mass of the two atoms whose connecting bond is broken and μ_f is the reduced mass of the two products of the dissociation, does **not** depend on the geometry of either the fragment ion or the neutral.¹¹ This phenomenon therefore cannot be explained by invoking any geometry change in formation of either CF_3^+ or SF_5^+ from the respective neutral. The only difference between these two groups of ions seems to be that the SF_5^+ -containing ions dissociate further to SF_4^+ and SF_3^+ with relatively low amounts of extra photon energy, whereas this is not observed for the CF_3^+ -containing ions.

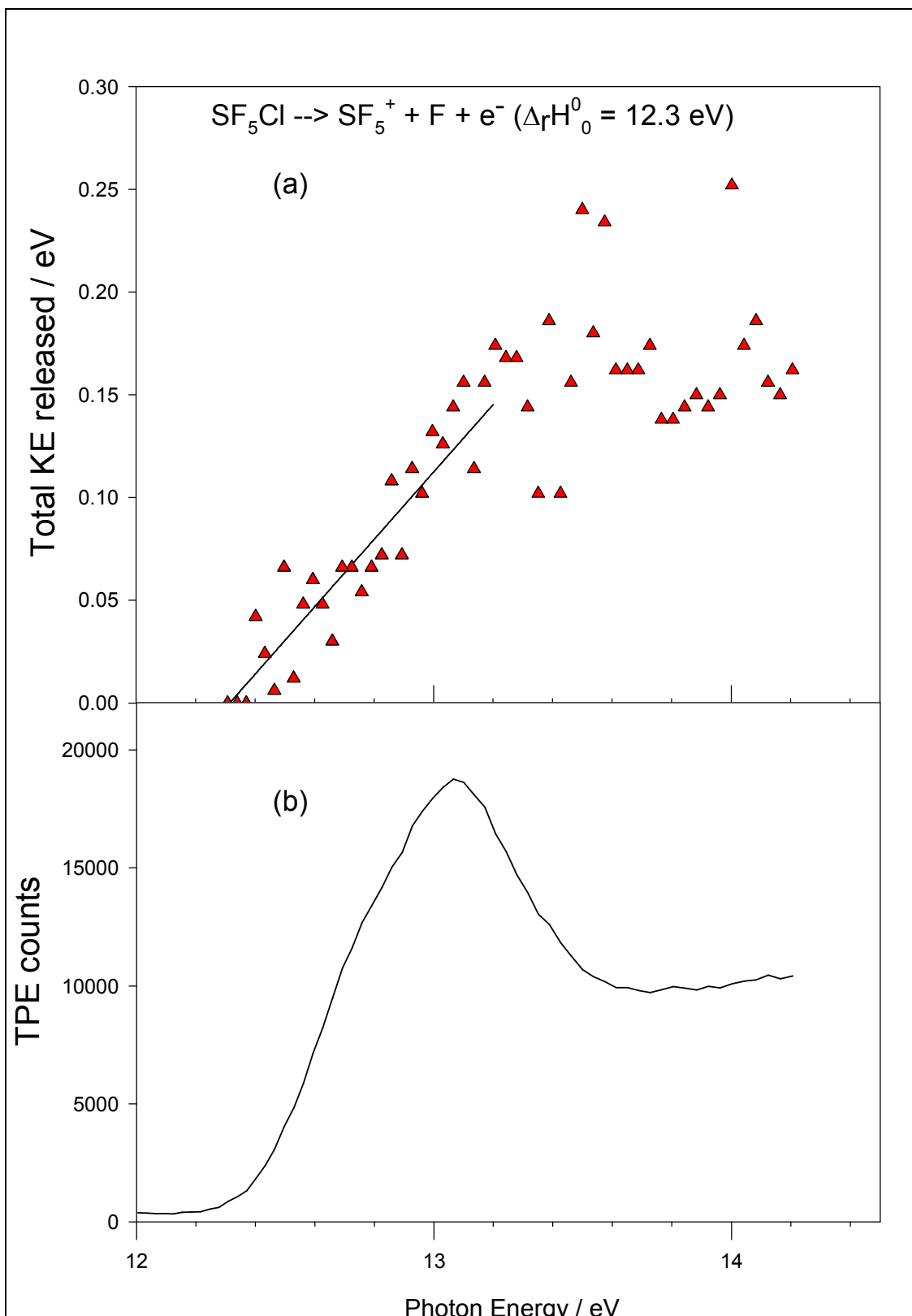


Figure 7.4 (a) Mean total kinetic energy released in the reaction $\text{SF}_5\text{Cl} + h\nu \rightarrow \text{SF}_5^+ + \text{F} + \text{e}^-$ for photon energies in the range 12.0-14.3 eV. A linear extrapolation to zero kinetic energy gives the dissociative ionisation energy SF_5Cl , 12.3 eV. (b) Threshold photoelectron of SF_5Cl over the same energy range.

7.5 Discussion

7.5.1 Elucidation of dominant fragmentation channels

In the range 12.0 - 20.6 eV, it has been shown that SF_5Cl^+ dissociates to SF_5^+ , SF_4Cl^+ , SF_4^+ and SF_3^+ . SF_5^+ is observed with a threshold of 12.3 eV. Since only one bond is broken to form SF_5^+ , there is only one possible dissociation channel, $\text{SF}_5\text{Cl} \rightarrow \text{SF}_5^+ + \text{Cl} + \text{e}^-$. This appearance potential is very close to the dissociation energy calculated in Table 7.1 (12.18 eV). The same point is valid for SF_4Cl^+ . Since only one bond is broken to form SF_4Cl^+ , there is only one possible dissociation channel, $\text{SF}_5\text{Cl} \rightarrow \text{SF}_4\text{Cl}^+ + \text{F} + \text{e}^-$.

The main threshold for SF_4^+ occurs at 16.2 ± 0.2 eV. This is still not high enough to access the higher energy process $\text{SF}_5\text{Cl} \rightarrow \text{SF}_4^+ + \text{F} + \text{Cl} + \text{e}^-$ which has a dissociation energy of 16.46 eV. This means that, at the lowest energies, SF_4^+ must form *via* the lower-energy pathway with a molecular product, FCl. At higher energies, formation with two atoms, F + Cl, seems more likely. Similar points can be made for SF_3^+ . The main threshold for SF_3^+ occurs at 16.8 eV. There are now three possible dissociation channels open. Since the appearance potential lies close to the thermochemical threshold associated with the highest-energy channel, it is likely that dissociation to SF_3^+ occurs with 2 fluorine atoms and one chlorine atom. This selectivity may be caused by the fact that a sterically hindered, tightly constrained transition state is required to form the fluorine molecule. The minor threshold (if the signal is real) at 15.0 ± 0.4 eV is tentatively assigned to the pathway that produces FCl and F neutrals.

7.5.2 Determination of the dissociation dynamics.

The values of $\langle \text{KE} \rangle_t$ and $\langle f \rangle_t$ for the dissociation of SF_5Cl^+ to SF_5^+ show a different behaviour to what has usually been observed in this thesis. Here, there is no gradual change in decay mechanism from impulsive to statistical decay as the photon energy and hence the available energy is increased. In Chapter 4, this behaviour was elucidated by the increase in density of electronic states as the photon energy was increased. This is not observed here. The \tilde{X} state of the parent ion, photoionised at 13.05 eV, dissociates to SF_5^+ with both statistical and impulsive character ($\langle f \rangle_t = 0.26$). At 15.12 eV, the $\tilde{A}/\tilde{B}/\tilde{C}$ state of parent ion increases in impulsive character with $\langle f \rangle_t = 0.40$. The \tilde{D} state of the parent ion, photoionised at 15.90 eV, only 0.78 eV higher than the $\tilde{A}/\tilde{B}/\tilde{C}$ state shows mostly statistical character. The experimental fractional ratio then increases again to 0.28 in the \tilde{E} state of the parent ion indicating both statistical and impulsive nature. The \tilde{E} state of the parent ion is only 0.93 eV higher lying than the \tilde{D} state. The reliability of these results is increased by the observation of the full width at half maximums of the TPEPICO-TOF spectra in Figure 7.3. This behaviour is noteworthy since the change in dissociation dynamics changes dramatically in a very small energy range and is therefore highly state specific. The

only other molecular ion which shows comparable behaviour is NF_3^+ ,^{12,13} where the low-lying electronic states which dissociate to NF_2^+ show oscillating values for $\langle f \rangle_t$. In particular, the $\tilde{A} \ ^2\text{E}$ state of NF_3^+ , formed from ionisation of a F lone-pair electron, shows a large value of both $\langle \text{KE} \rangle_t$ and $\langle f \rangle_t$, whereas higher-lying states show smaller values of both quantities.

The values of $\langle \text{KE} \rangle_t$ and $\langle f \rangle_t$ for the dissociation of SF_5Cl^+ to SF_4Cl^+ indicate that there are possible problems with the calculation of the excess energy. This provides good evidence that the actual thermochemical threshold for the formation of SF_4Cl^+ is much lower than the appearance potential of this ion. This is similar to the formation of CF_3^+ from CF_4 .¹⁴ Comparison of the experimental fractional ratios with statistical and impulsive limits yield little information about the dynamics of this system. There is however a trend for the experimental fractional ratio to decrease as the photon energy increases.

7.6 Conclusions

A comprehensive study of the fragmentation behaviour of the valence states of SF_5Cl^+ over the photon energy range $\sim 12 - 21$ eV has been performed. Threshold photoelectron spectra and ion yield plots have been obtained with the experiment operating in scanning energy mode. In general, the threshold photoelectron spectra are in excellent agreement with those measured using He I and He II radiation.¹ In cases where ions can be produced in a variety of dissociation channels, comparison of the appearance potential with $\Delta_r H^\circ$ has allowed the pathways to be determined.

High resolution (16 ns) TPEPICO-TOF spectra have been measured for the dissociations which involve the fission of a single bond, with the experiment operating in the fixed energy mode. Values of $\langle \text{KE} \rangle_t$ and $\langle f \rangle_t$ have been determined, and those predicted for statistical and pure impulsive models have been calculated. Fragmentation to SF_5^+ exhibits highly state-specific behaviour. In the case of SF_5Cl^+ to SF_4Cl^+ , problems in the calculation of the available energy result in poor correlation when comparing experimental $\langle f \rangle_t$ to statistical and impulsive $\langle f \rangle_t$ s. However a trend for the experimental fractional ratio to decrease as the photon energy increases is observed.

7.7 References

1. R.L. DeKock, B.R. Higginson, D.R. Lloyd, *Faraday Discuss. Chem. Soc.*, 1972, **84**, 54.
2. P. Harland and Thynne, *J. Phys. Chem.*, 1969, **73**, 4031.
3. H. Baumgartel, H. -W. Jochims, E. Ruhl, *Z. Naturforsch. B.*, 1989, **44**, 21.
4. C. Atterbury, A. D. J. Critchley, R. A. Kennedy, C. A. Mayhew and R. P. Tuckett, *Phys. Chem. Chem. Phys.*, 2002, **4**, 2206.

5. G. K. Jarvis, C. A. Mayhew, R. Y. L. Chim, R. A. Kennedy, R. P. Tuckett, *Chem. Phys. Lett.*, 2000, **320**, 104.
6. M. W. Chase, *J. Phys. Chem. Ref. Data*, 1998, Monograph No. 9.
7. E. R. Fisher, B. L. Kickel and P. B. Armentrout, *J. Chem. Phys.*, 1992, **97**, 4859.
8. R. Y. L. Chim, R. A. Kennedy, R. P. Tuckett, W. Zhou, G. K. Jarvis, D. J. Collins and P. A. Hatherly, *J. Phys. Chem.*, 2001, **105**, 8403.
9. H. –W. Jochims. 2000, *private communication*.
10. T. Shimanouchi, *Tables of Molecular Vibrational Frequencies consolidated volume I National Bureau of Standards*, 1972, 1.
11. R. A. Kennedy, 2002, *private communication*.
12. P. I. Mansell, C. J. Danby and I. Powis, *J Chem Soc Faraday Trans 2*, 1981, **77**, 1449.
13. D. P. Secombe, G. K. Jarvis, B. O. Fisher and R. P. Tuckett, *Chem Phys.*, 1999, **250**, 335.
14. D. M. Smith, R. P. Tuckett, K. R. Yoxall, K. Codling, P. A. Hatherly, J. F. M. Aarts and M. Stankiewicz, *J Chem Phys.*, 1994, **101**, 10559.

CHAPTER 8 : FRAGMENTATION OF THE VALENCE ELECTRONIC STATES OF SeF_6^+ AND TeF_6^+ PROBED BY THRESHOLD PHOTOELECTRON-PHOTOION COINCIDENCE SPECTROSCOPY

8.1 Introduction

Very little is known about the positive ion thermodynamics of SeF_6 and TeF_6 . Potts *et al.*¹ and Addison *et al.*² have recorded valence photoelectron spectra (PES) from which the ionisation potentials of the various electronic states of the parent ion can be determined. However, nothing is known about how these states decay or the enthalpies of formation of any of the fragment ions that might form. In this chapter synchrotron radiation has been used to perform a threshold photoelectron-photoion coincidence (TPEPICO) study of these two compounds to determine some of these properties. Such determinations are also of fundamental interest, as useful insight can be gained by comparison of similar species, such as SF_6^+ , as to what influences the decay dynamics of such molecular ions.

TPEPICO data on these molecules are also useful for the analysis of positive ion charge transfer data, not only in terms of thermodynamic information, but also for comparison of branching ratios at energies consistent with the recombination energy of the reactant ion. This complementary ion-molecule kinetics study of reactions of SF_6 , SeF_6 and TeF_6 with small cations has been reported elsewhere.³

8.2 Experimental

The experimental procedure for the acquisition of the TPEPICO data has been presented in detail previously^{4,5}. The photoionisation experiments required the use of the electron analyser and the time of flight drift tube described earlier in Chapter 2. Synchrotron radiation dispersed with the 1m Seya-Namioka monochromator on beamline 3.1 at SRS (Daresbury, UK) was used as the photon source. The two gratings used were calibrated using argon. Spectra were flux normalised *via* the visible fluorescence of a NaSal window.

As well as energy-selected fragmentation patterns, the kinetic energy released for a specific mode of fragmentation can also be determined from an analysis of the observed time-of-flight (TOF) peak shape of the daughter ion⁶. This experiment is performed with an improved TOF resolution than for the energy-scanning experiments from which the fragmentation patterns are determined. This experiment was only performed here for the XF_5^+ ion ($X = \text{Se}$ or Te). In these experiments an improved TOF resolution of 16 ns was used.

The SeF₆ and TeF₆ gases (purity *ca.* 99%) were obtained from Fluorochem Ltd. and used directly without further purification.

8.3 Results

8.3.1 Threshold photoelectron spectra

Figs. 8.1 and 8.2 show the threshold photoelectron spectra (TPES) for SeF₆ and TeF₆, respectively. The first onset of signal observed in the TPES occurs at 15.3 ± 0.2 eV and 15.4 ± 0.2 eV for SeF₆ and TeF₆ respectively. These values are in approximate agreement with those obtained by Potts *et al.*¹ (SeF₆: 15.4 ± 0.2 ; TeF₆: 15.6 ± 0.2). The adiabatic ionisation potential (IP) of a molecule is defined as the difference in energy between the lowest lying level of the neutral ($J''=0, v''=0$) and the lowest lying level of the ion ($J^+ = 0, v^+ = 0$). Therefore, to calculate the adiabatic IP, the thermal energy of the neutral molecule prior to ionisation must be taken into account. Using vibrational frequencies taken from Claassen *et al.*⁷ for SeF₆ and TeF₆, the average internal energy is calculated to be 0.14 eV and 0.17 eV at 298K, respectively. This consequently gives the ionisation potential for SeF₆ and TeF₆ as 15.44 ± 0.20 and 15.57 ± 0.20 eV. It should also be noted that the first onset is prone to error caused by the sensitivity of the instrument, especially if there is a large change in geometry upon ionisation; that is, a more sensitive instrument should detect a signal closer to the true onset than a less sensitive one. However, it is assumed that this error is small compared to the errors quoted. By comparison with the known ionisation potential of SF₆ (15.33 ± 0.03 eV)⁸ these data show that there is an increase in the ionisation potential as one moves down the group 6B hexafluorides (i.e. SF₆ < SeF₆ < TeF₆). This observation is in agreement with the spectra of Potts *et al.*¹

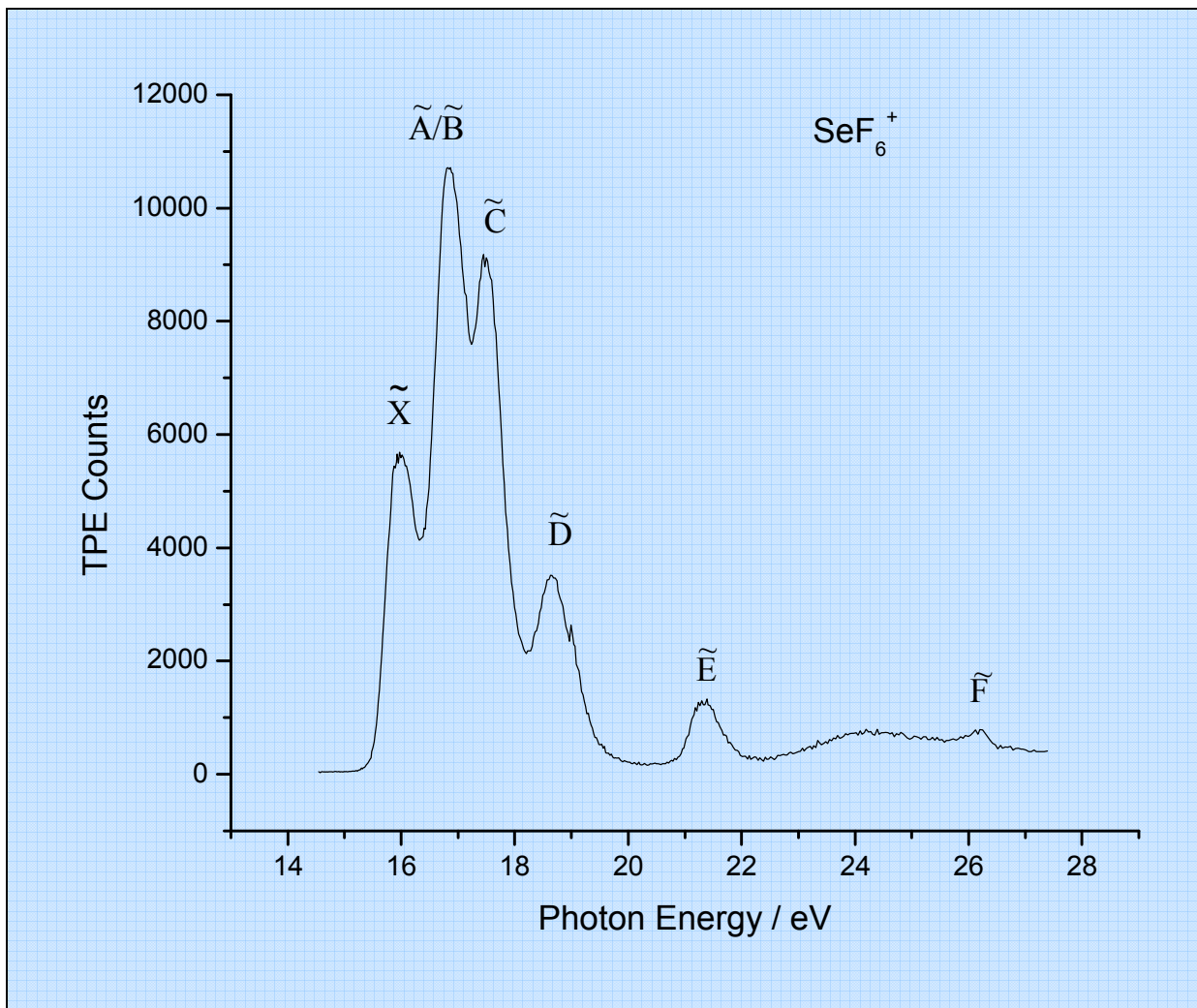


Figure 8.1 Threshold photoelectron spectrum of SeF_6 at a resolution of 0.3 nm

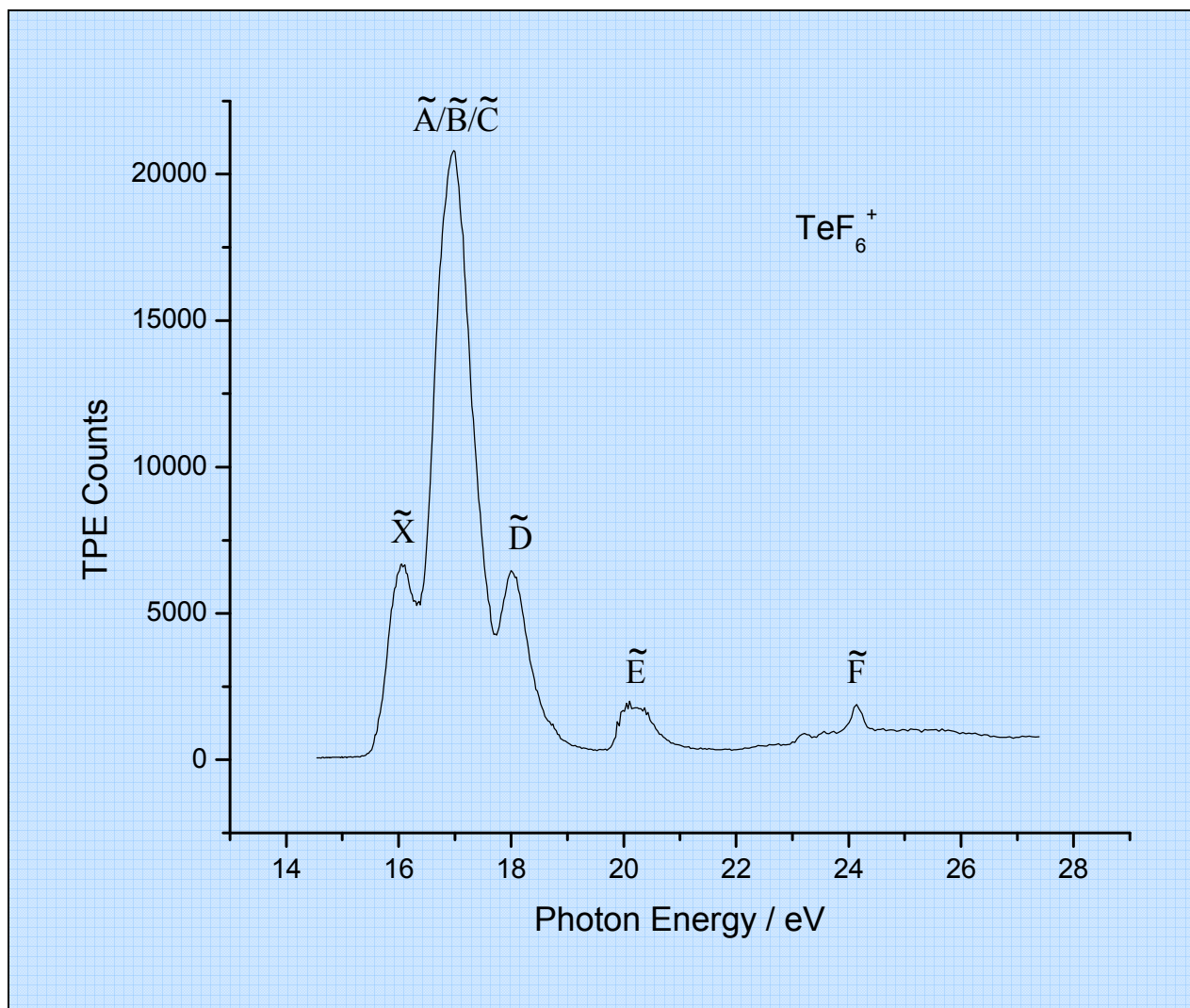


Figure 8.2 Threshold photoelectron spectrum of TeF_6 at a resolution of 0.3 nm

By comparison with the observed TPES of SF_6 recorded at a comparable resolution⁹, assignments of the photoelectron bands of SeF_6 and TeF_6 have been made and the states are labelled accordingly in Figs. 8.1 and 8.2. In both cases, the symmetries of the \tilde{X} , \tilde{A} , \tilde{B} , \tilde{C} , \tilde{D} , \tilde{E} and \tilde{F} states are assumed to be as for SF_6 ; that is, ${}^2T_{1g}$, ${}^2T_{1u}$, ${}^2T_{2u}$, 2E_g , ${}^2T_{2g}$, ${}^2T_{1u}$ and ${}^2A_{1g}$, respectively. For SeF_6 the relative intensities and energies of the photoelectron bands are similar to those observed for SF_6 , giving extra confidence to these assignments. It should be noted that the \tilde{A} and \tilde{B} bands are not resolved at this resolution in either molecule.⁹ The main difference appears to be a general reduction in the energy separation of the

electronic states. For TeF₆, if the assignment is correct, this reduction is even more pronounced with the \tilde{A} , \tilde{B} and \tilde{C} states all merging into one photoelectron band. Support for this effect comes from a comparison of the X-F bond-length of the three molecules (SF₆: $1.557 \pm 0.001 \text{ \AA}^{10}$; SeF₆: $1.678 \pm 0.001 \text{ \AA}^{11}$; TeF₆: $1.824 \pm 0.004 \text{ \AA}^{12}$). The implication of this increase in bond-length along the series S, Se, Te is that interactions between the fluorine atoms, which one might expect to cause a spreading of the energies of the observed ionic electronic states, will decrease as one moves down the group, consequently reducing the energy differences between the states.

8.3.1 Scanning TPEPICO experiments.

Figures 8.3 and 8.4 show the ion yield spectra for SeF₆ and TeF₆, respectively. The ion yield diagrams for SeF₆, TeF₆ (and also SF₆)⁹ are qualitatively very similar. In all three, the parent molecular ion is absent and XF₅⁺ appears at the onset of ionisation. The ground electronic states of all three ions must therefore be repulsive in the Franck-Condon region. As the photon energy is increased, XF₄⁺ is formed, closely followed within about 1 eV by XF₃⁺, with XF₂⁺ being formed at higher energies still. SeF₆ appears to behave almost exactly like SF₆, with the higher-energy part of the \tilde{C} state of the parent ion dissociating into SeF₄⁺, the \tilde{D} state dissociating into SeF₄⁺ and SeF₃⁺, and the \tilde{E} state dissociating into SeF₃⁺. TeF₆, by contrast, does not produce TeF₄⁺ or TeF₃⁺ until the \tilde{E} state.

The experimental appearance potentials of the fragment ions XF₅⁺, XF₄⁺, XF₃⁺ and XF₂⁺ for SeF₆ and TeF₆ are shown in Table 8.1. Also shown are experimental data for SF₆ taken from Creasey *et al.*⁹ The lowest possible observable appearance potential for a particular fragment ion can be estimated from:

$$\text{AP (lowest)} \cong \Delta_f\text{H}[\text{products}]_{0\text{K}} - \Delta_f\text{H}[\text{XF}_6]_{298\text{K}} \quad (8.1)$$

This corresponds to reactant molecules with the mean internal energy at 298K forming products in their lowest rovibronic energy levels and with no relative translation. This neglects the possible lowering of the appearance energy due to the presence of XF_6 molecules containing more than the average amount of internal energy at 298K. Estimates of this lowering indicate that it is unlikely to exceed 20 kJ mol^{-1} . The observed appearance potential will be an upper bound to $\text{AP}(\text{lowest})$, as it may not be possible to access the products in their lowest rovibronic state. Therefore, by taking the enthalpies of formation of the neutrals at 298K ($-1117 \pm 21 \text{ kJ mol}^{-1}$ for SeF_6 , $-1318 \pm 21 \text{ kJ mol}^{-1}$ for TeF_6)⁸ and the enthalpies of formation of F and F_2 (77.3 ± 0.3 and 0 kJ mol^{-1} , respectively)⁸, an upper limit for the 0K enthalpies of formation of the fragment ions can be calculated. Calculations for the smaller fragments obviously depend on whether F_2 is formed as the parent molecular ion dissociates. In Table 1, the limits for these enthalpies of formation, calculated assuming both that F_2 forms and that only $n\text{F}$ forms ($n = 1$ to 4) are listed. For the XF_2^+ calculation, it has been assumed that 2F_2 molecules are the neutrals in the ‘ F_2 formed’ calculation. For comparison, these calculations were also performed for the experimental data of Creasey *et al.*⁹ on SF_6 . Finally, included in Table 1 are the known enthalpies of formation (at 298K) of the fragment ions of SF_6 . Data for SF_4^+ , SF_3^+ and SF_2^+ were taken from Lias *et al.*⁸ The value for SF_5^+ was taken from a study of the kinetics of the $\text{HCl}^+ + \text{SF}_6 \rightarrow \text{SF}_5^+ + \text{HF} + \text{Cl}$ ion-molecule reaction.¹³ This value is 45 kJ mol^{-1} lower than that obtained by Lias *et al.*⁸ It is noted that the Lias *et al.*⁸ value was obtained from a study of the kinetics of the $\text{CF}_3^+ + \text{SF}_6 \rightarrow \text{SF}_5^+ + \text{CF}_4$ ion-molecule reaction, where the enthalpy of formation of CF_3^+ is of critical importance. This value for CF_3^+ has been the subject of recent controversy,^{14,15} and for this reason the value for SF_5^+ of Tichy *et al.*¹³ is preferred.

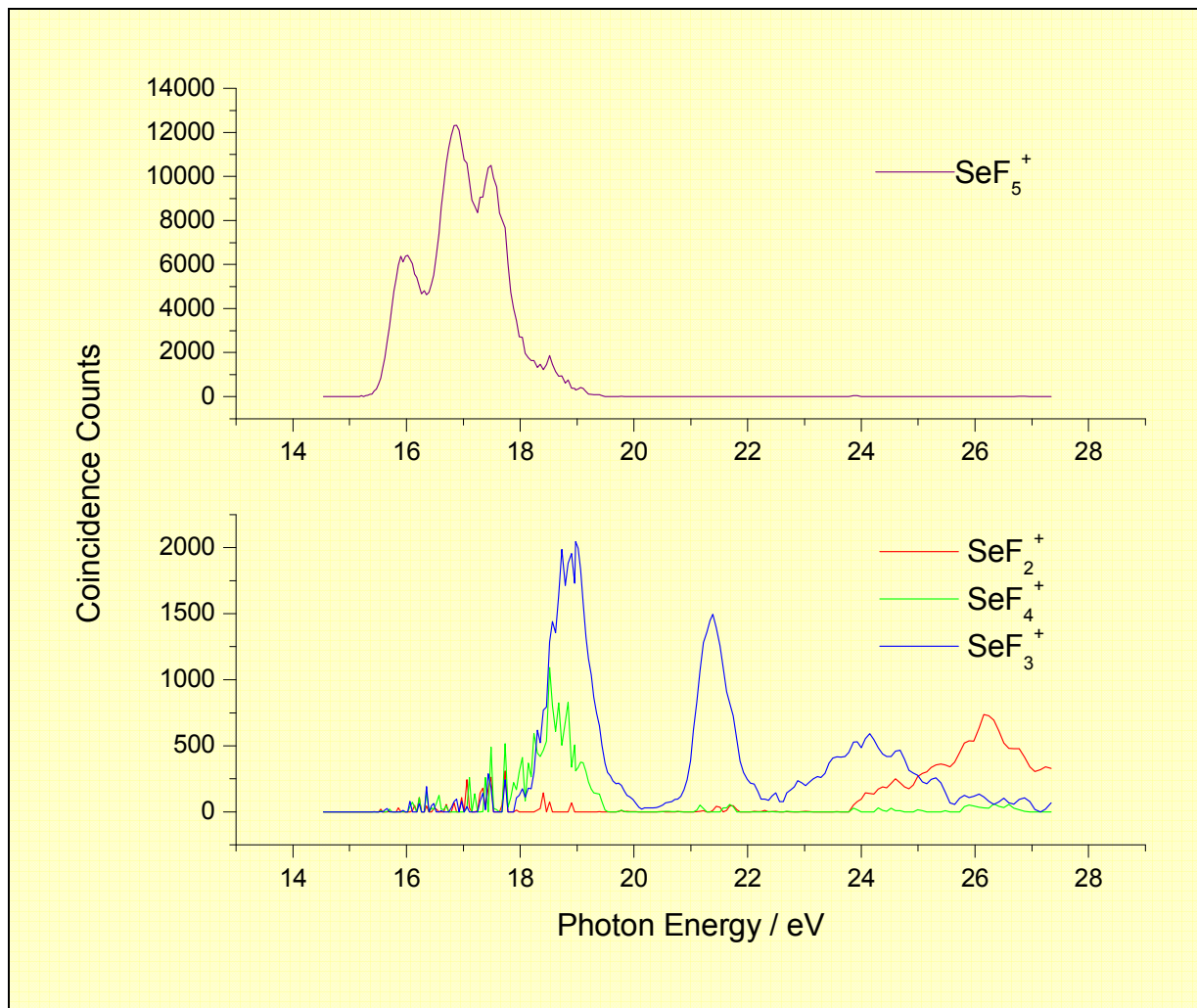


Figure 8.3 TPEPICO coincidence ion yields of SeF_5^+ , SeF_4^+ , SeF_3^+ and SeF_2^+ .

Table 8.1 Thermochemistry of fragment ions produced from photoionisation of SF₆, SeF₆ and TeF₆

Parent	Fragment	AE (eV) ^a	$\Delta_f H^\circ$ ^{a,b} (kJ mol ⁻¹) (F ₂ formed)	$\Delta_f H^\circ$ ^{a,b} (kJ mol ⁻¹) (nF formed)	$\Delta_f H^\circ$ ^{c,d,e} (kJ mol ⁻¹)
SF₆	SF ₅ ⁺	15.5 ± 0.2	-	197 ± 20	52
	SF ₄ ⁺	18.4 ± 0.3	554 ± 29	399 ± 29	403
	SF ₃ ⁺	19.2 ± 0.3	554 ± 29	399 ± 29	376
	SF ₂ ⁺	27.0 ± 0.5	1384 ± 48	1074 ± 48	678
SeF₆	SeF ₅ ⁺	15.3 ± 0.2	-	281 ± 28	166 ± 52
	SeF ₄ ⁺	17.6 ± 0.2	581 ± 36	426 ± 36	426 ± 36
	SeF ₃ ⁺	17.8 ± 0.2	523 ± 28	368 ± 28	368 ± 28
	SeF ₂ ⁺	23.6 ± 0.2	1160 ± 28	850 ± 28	<850 ± 28
TeF₆	TeF ₅ ⁺	15.4 ± 0.2	-	90 ± 28	4 ± 62
	TeF ₄ ⁺	19.7 ± 0.3	583 ± 36	428 ± 36	428 ± 36
	TeF ₃ ⁺	20.0 ± 0.2	535 ± 28	380 ± 28	380 ± 28
	TeF ₂ ⁺	23.0 ± 0.2	901 ± 28	591 ± 28	<591 ± 28

^a Values for SF₆ from Creasey *et al.*⁹

^b Upper limits for the enthalpies of formation of the fragment ions calculated from the appearance potentials as observed in the TPEPICO experiment. The first column indicates the limit if F₂ is allowed as one (or both in the case of XF₂⁺) of the neutrals, the second if only nF is allowed.

^c Literature values for the enthalpies of formation of the fragment ions from SF₆ extracted from refs 8 and 13 – see text.

^d Values given in this column for SeF₆ and TeF₆ represent the best estimates of the enthalpies of formation of the fragment ions as discussed in the text. For XF₅⁺, the values given are calculated from the analysis of the kinetic energy released in fragmentation.

^e Note that literature values are at 298K whereas those calculated from the TPEPICO work will be more consistent with 0 K enthalpies of formation. However, differences are likely to be < 20 kJ mol⁻¹.

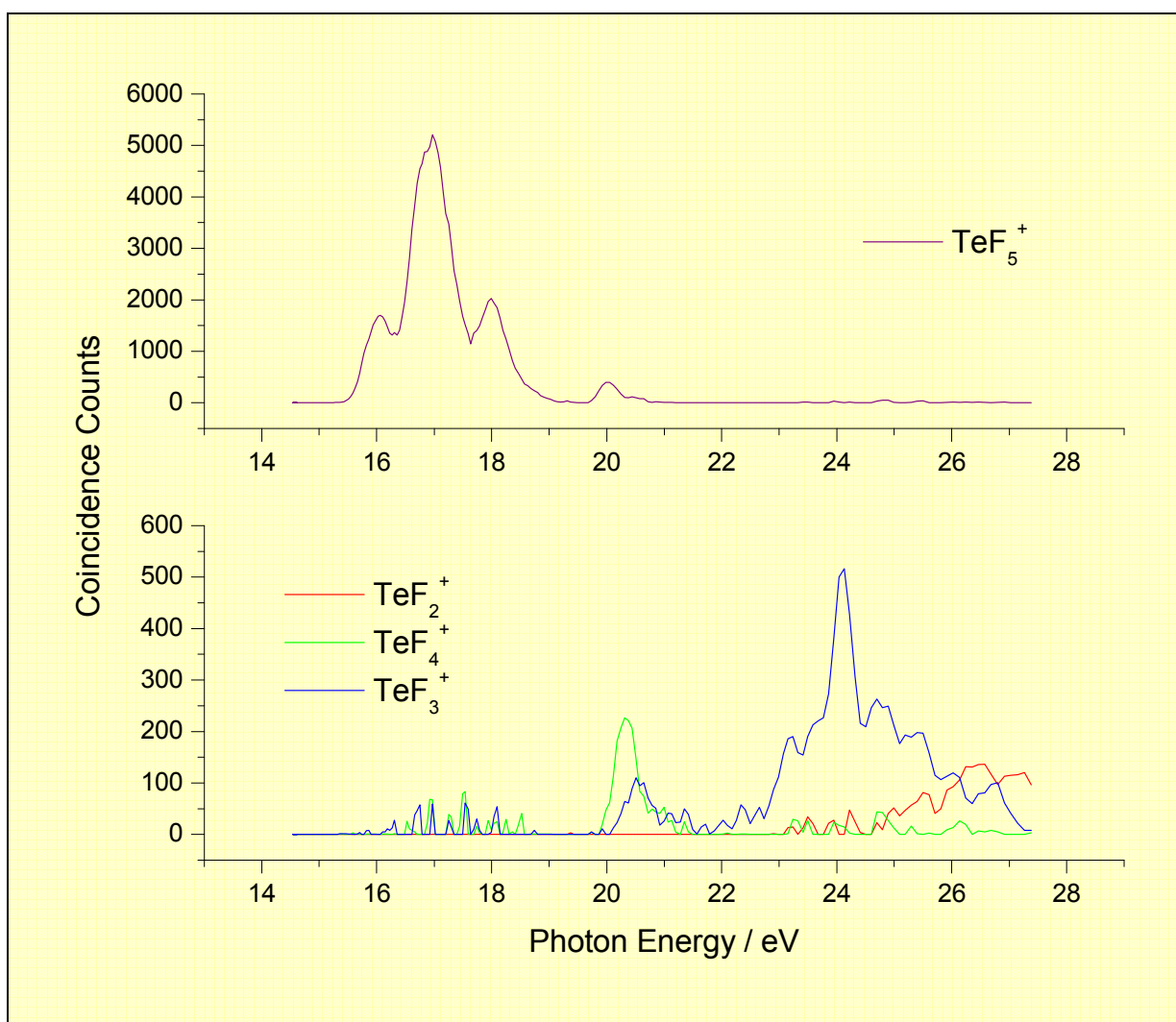


Figure 8.4 TPEPICO coincidence ion yields of TeF_5^+ , TeF_4^+ , TeF_3^+ and TeF_2^+ .

As stated above, all three species behave similarly in regards to their fragmentation. Therefore it seems reasonable to draw some conclusions about the calculated thermochemical onsets from a comparison with the SF_6 data. For SF_6 it can be seen that the onsets for SF_4^+ and SF_3^+ lie very close to the thermochemical threshold, if the neutral products are 2F and 3F respectively. Therefore it seems plausible that SeF_6 and TeF_6 behave in a similar way. In other words, the enthalpies of formation of SeF_4^+ , SeF_3^+ , TeF_4^+ and TeF_3^+ are likely to be close to 426 ± 36 , 368 ± 28 , 428 ± 36 and $380 \pm 28 \text{ kJ mol}^{-1}$, respectively. Since SF_5^+ and SF_2^+ have their first appearance potentials well in excess of the thermochemical threshold for $\text{SF}_{6-n}^+ + n\text{F}$ production, then it is not possible to narrow down any further the choice of limits for the Se and Te containing ions from these data alone. The reason why SF_5^+ does not form at its thermochemical threshold is simply because the IP of SF_6 lies well above the $\text{SF}_5^+ + \text{F}$ dissociative ionisation limit. The reason why SF_2^+ does not form at its thermochemical threshold is not clear from these data alone.

8.3.2 Kinetic energy release measurements

As neither SeF_6^+ or TeF_6^+ are observed in the scanning-energy TPEPICO experiment, the ground electronic states of both molecular ions are anticipated to be dissociative in the Franck-Condon region. This then implies that the thermochemical limit to form XF_5^+ will lie below the observed onset of ionisation. Throughout this chapter, the phrase ‘dissociative ionisation energy’ (as described in Chapter 5) is used to describe the energy of $\text{XF}_5^+ + \text{F} + \text{e}^-$ relative to the ground state of XF_6 . In the case of SF_6 , although the IP occurs at $15.33 \pm 0.03 \text{ eV}$,⁸ the dissociative ionisation energy to form SF_5^+ is $14.0 \pm 0.1 \text{ eV}$.¹³ Therefore, to obtain a more accurate value for the enthalpy of formation of SeF_5^+ and TeF_5^+ , the measurement of the kinetic energy released in fragmentation close to threshold has been attempted. If a molecular ion decays statistically, the onset of the first fragment ion should also correspond to the dissociative ionisation energy. Consequently, there is essentially zero energy released into fragmentation

at this excitation energy. In the case of SeF₆, TeF₆ (and SF₆), however, the first onset is likely to be above the dissociative ionisation energy for the reasons stated above, so the kinetic energy released in fragmentation will be non-zero. Therefore, the kinetic energy released in fragmentation will give a lower limit of how much 'extra' energy is available to the dissociation process. However, as the percentage of the available energy that is released into translation is not known due to a lack of knowledge of the decay dynamics, a single kinetic energy release measurement will not provide an absolute value for the dissociative ionisation energy. For example, in a statistical dissociation, the excess energy is randomised into all the molecular vibrations and a comparatively low kinetic energy release would be observed.¹⁶ Conversely, if the parent ion decays impulsively, as is likely to be the case here, there is not enough time for randomisation of the energy to occur and substantially more energy will be partitioned into translation.¹⁷ Furthermore, the amount of kinetic energy observed in an impulsive decay will depend on how rigid the fragment ion remains as it dissociates.¹⁸ Therefore the measurement of the kinetic energy released in fragmentation over a range of energies from *ca.* 15.7 to 17.7 eV has been attempted to see if any patterns in the decay mechanism can be discerned. If the pattern is clear it should then be possible to predict at what photon energy the kinetic energy released in fragmentation is zero. This energy should correspond to the dissociative ionisation energy.

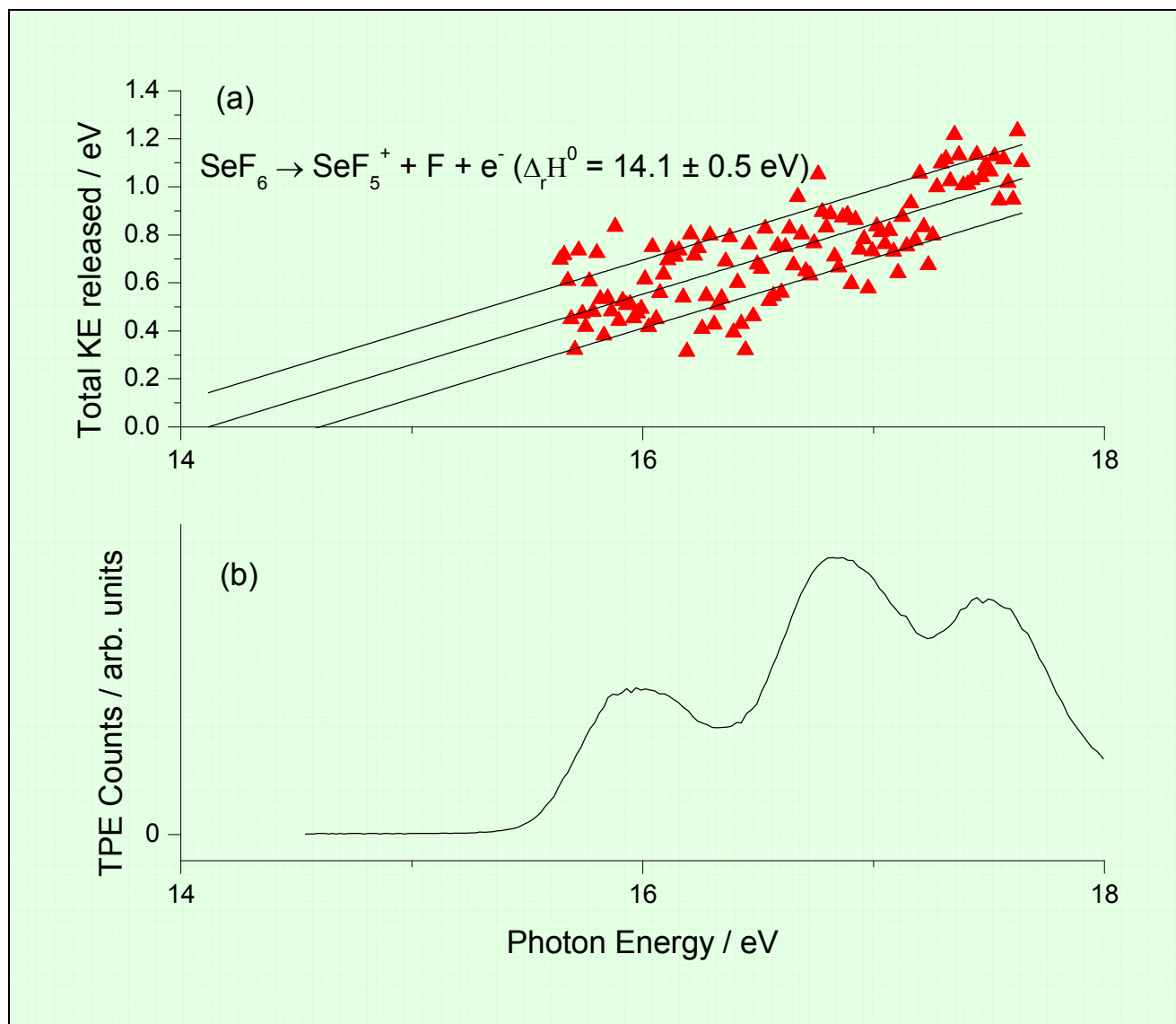


Figure 8.5 (a) Measured total kinetic energy released in the process $\text{SeF}_6 + h\nu \rightarrow \text{SeF}_5^+ + \text{F} + \text{e}^-$ for photon energies in the range 15.7 to 17.7 eV. A linear extrapolation to zero kinetic energy gives the dissociative ionisation energy of the reaction. The error in each value of the total kinetic energy is *ca.* 20%.

(b) Threshold photoelectron spectrum of SeF_6 .

Figs. 8.5 and 8.6 show the results obtained for SeF_6 and TeF_6 , respectively. Panel (a) reveals the measured kinetic energy released into fragmentation and panel (b) shows the TPES for comparison over the appropriate energy region. The kinetic energy was extracted from the TOF spectra in a more simplified way to that usually used.⁶ Each TOF spectrum was assumed to represent a single kinetic energy release (rather than a distribution of releases) convoluted with the thermal energy of the molecules

prior to ionisation. All isotopes of Se and Te were considered (their masses and natural abundance taken from reference 19), and the size of the kinetic energy release was varied until a minimum in the sum of the squares of the errors was obtained. As examples, Fig. 8.7 shows two typical TOF spectra for SeF₆ (upper panel) and TeF₆ (lower panel) recorded at photon energies of 16.8 and 16.9 eV, from which kinetic energy releases of 0.83 and 0.69 eV, respectively, were obtained. The simplification of assuming only a single release was introduced to reduce the fitting time and parameters involved. A few TOF spectra were checked more rigorously using a range of kinetic energy releases,⁶ but results showed little deviation from those seen in Figs. 8.5 and 8.6.

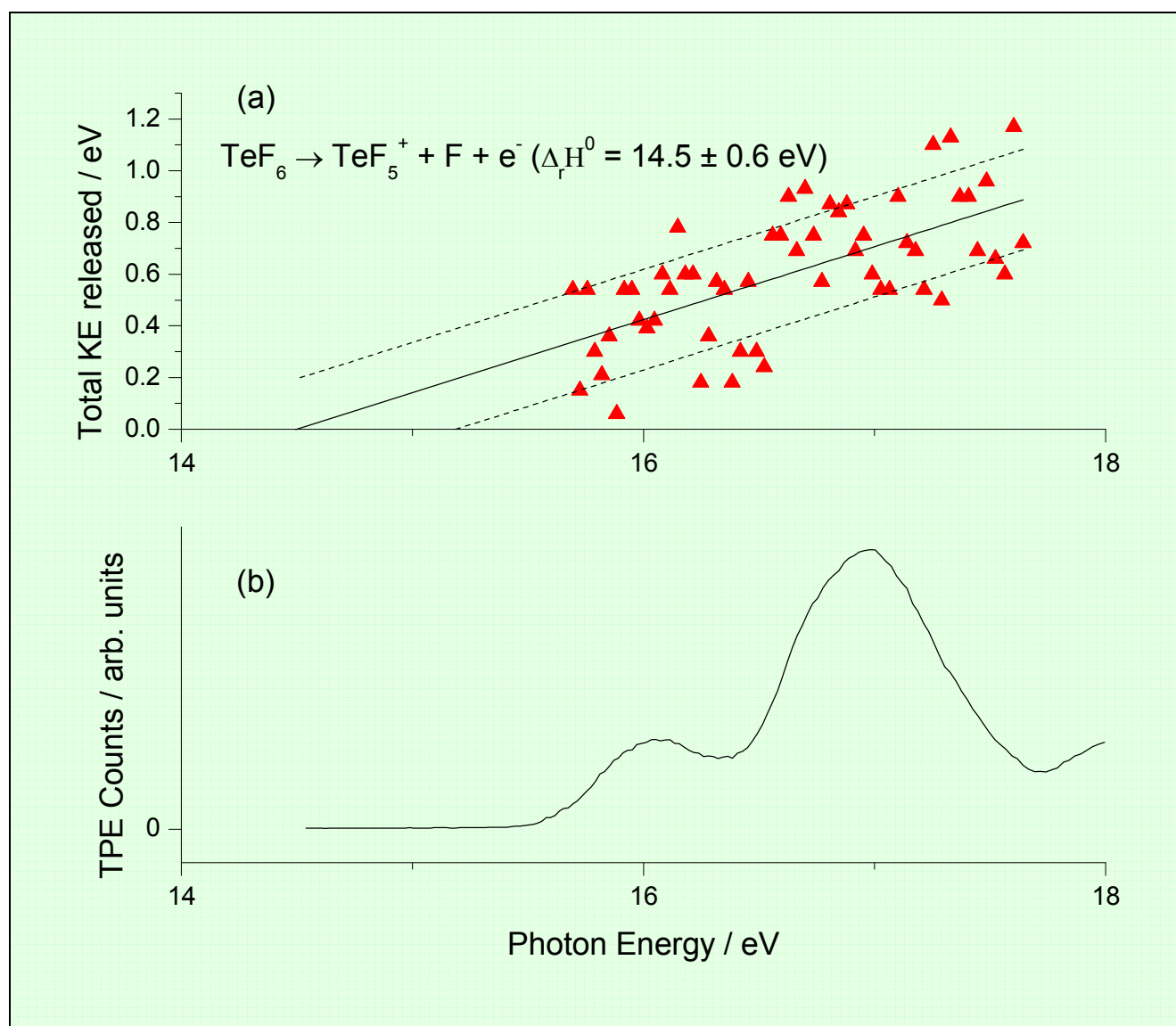


Figure 8.6 (a) Measured total kinetic energy released in the process $\text{TeF}_6 + h\nu \rightarrow \text{TeF}_5^+ + \text{F} + \text{e}^-$ for photon energies in the range 15.7 to 17.7 eV. A linear extrapolation to zero kinetic energy gives the dissociative ionisation energy of the reaction. The error in each value of the total kinetic energy is *ca.* 20%. (b) Threshold photoelectron spectrum of TeF_6 .

Although there is considerable scatter in the data for both SeF_5^+ and TeF_5^+ , there is a clear general trend of a linear increase in the observed kinetic energy release with photon energy for both ions. This is to be expected as most kinetic energy release models for impulsive decay predict a linear relationship between the available energy and the kinetic energy released.^{17,18} The solid lines in Figs. 8.5 and 8.6 are the linear least-squares fits to the data which were used to perform the extrapolation to zero kinetic energy. A further conclusion from the data is that the decay mechanism does not change in a dramatic way across the energy range studied. If it did, then a clear deviation from the straight line relationship for the kinetic energy released might be observed. Providing the mechanism of decay for the molecular ion does not change if it were accessed at energies below 15.7 eV, then the extrapolation of the linear fit to zero kinetic energy will give the dissociative ionisation energy to form $\text{XF}_5^+ + \text{F} + \text{e}^-$. This was determined to be 14.1 ± 0.5 eV and 14.5 ± 0.5 eV for SeF_6 and TeF_6 , respectively. From these dissociation energies it is possible to calculate the enthalpies of formation of the fragment ions SeF_5^+ and TeF_5^+ to be 166 ± 52 and 4 ± 62 kJ mol⁻¹, respectively.

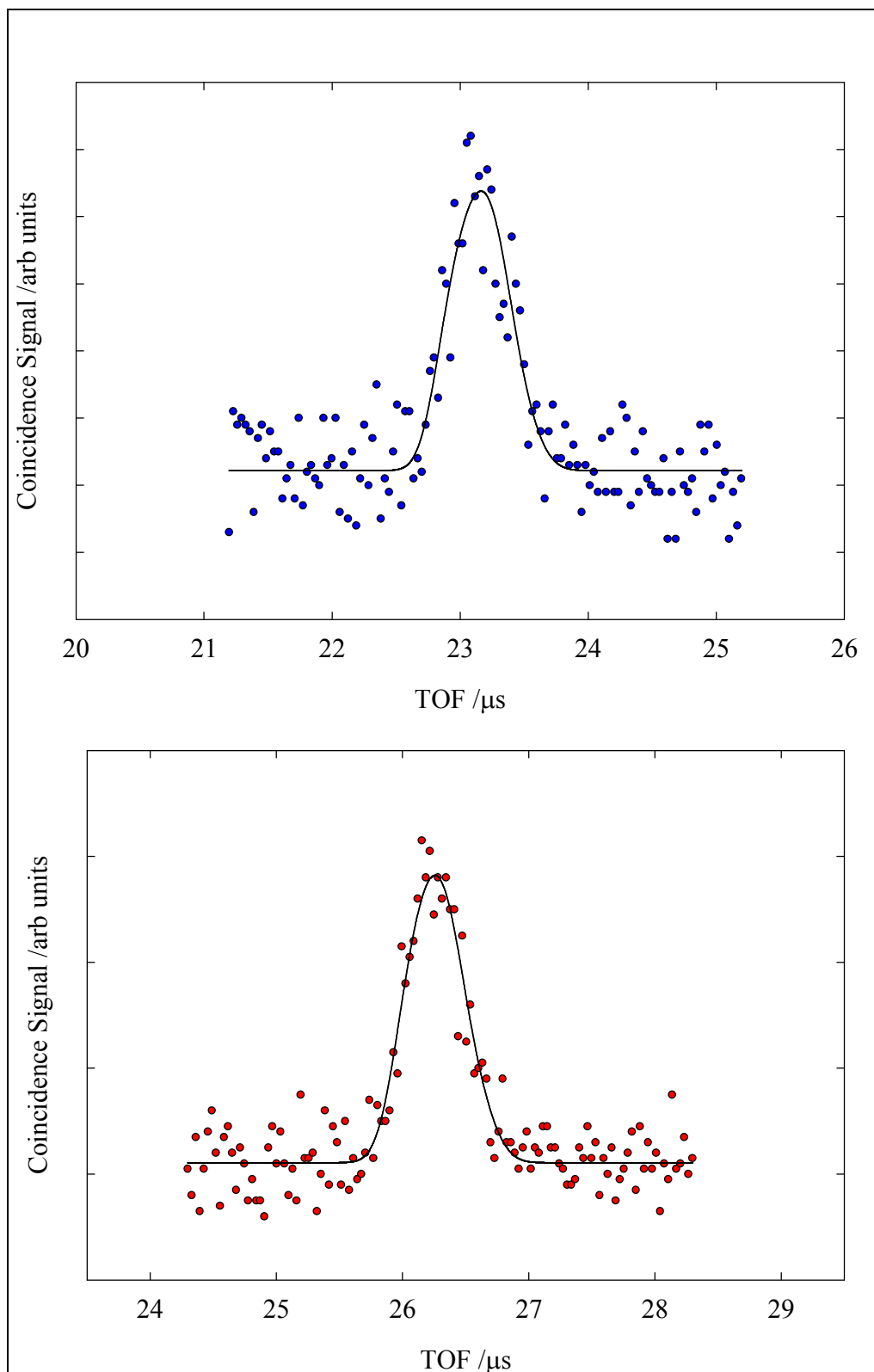


Figure 8.7 TPEPICO-TOF spectra (symbols) for (a) $\text{SeF}_5^+/\text{SeF}_6$ and (b) $\text{TeF}_5^+/\text{TeF}_6$ recorded at a photon energy of 16.8 eV and 16.9 eV respectively. Shown as lines, the data fit to single kinetic energy releases of 0.83 and 0.69 eV, respectively (see text).

Interestingly, the slope of the straight line fit of the kinetic energy release as a function of the photon energy is similar for both SeF_6 and TeF_6 , showing that $\sim 30\%$ of the available energy is released into translation. This indicates that a similar decay mechanism is taking place for both molecules. This fractional release is substantially less than that predicted by a pure impulsive model;¹⁷ the predicted releases for SeF_5^+ and TeF_5^+ are 89% and 94%, respectively. Clearly this model does not accurately describe the decay process. To calculate the energy released by a statistical model, knowledge of the vibrational frequencies of the daughter ion is required. These are not available, though it is possible to estimate a lower limit to the release by²⁰:

$$\text{Kinetic energy released} \geq \text{Available Energy} / (x+1), \quad (8.2)$$

where x is the number of vibrational degrees of freedom in the transition state. For both molecules, with $x = 15$ this leads to a fractional release of $\sim 6\%$. The observed releases therefore lie between the statistical and pure impulsive models. This may indicate that the excited XF_6^+ ions (XF_6^{+*}) survive long enough for some randomisation of the available energy to take place before dissociation occurs. One might expect that such a mechanism would produce a non-linear relationship of the kinetic energy release with the photon energy if the process depends critically on the lifetime of XF_6^{+*} . However, since the data appears to give a linear relationship within experimental error and the dissociative ionisation energies are similar to those obtained for SF_6 ,¹³ confidence can be given to the estimates of these first dissociative ionisation energies of SeF_6 and TeF_6 . The sizeable errors are likely to account for any non-linearity in the decay pattern that may be present below the IP of each molecule.

8.4 Conclusions

By performing TPEPICO spectroscopy on SeF_6 and TeF_6 , upper limits on the enthalpies of formation of their fragment ions have been determined from their experimental onsets. By using the kinetic energy released in fragmentation over a range of photon energies, the first dissociative ionisation limit to $\text{XF}_5^+ + \text{F} + \text{e}^-$ has been determined using an extrapolation procedure. Although errors in such a measurement are large due to considerable scatter in the data, this experiment proves that such a determination can be

informative. With improved statistics from longer acquisition times, it might be possible to reduce these errors considerably. Due to beam-time constraints, however, such measurements are impractical at present and the efficiency of the experiment specifically for the measurement of TOF spectra would need improvement. For example, the use of a cooled molecular beam sample would help by reducing the thermal population observed in the TOF spectra. With decreased errors, the appearance of fine structure in the kinetic energy release as a function of the available energy may provide more details on the mechanisms of decay. The work described in this chapter has recently been published.²¹

8.5 References

1. A. W. Potts, H. J. Lempka, D. G. Streets and W. C. Price, *Phil. Trans. Roy. Soc. (London)*, 1970, **A268**, 59.
2. B. M. Addison, K.H. Tan, G.M. Bancroft, F. Cerrina, *Chem. Phys. Lett.*, 1986, **129**, 468.
3. G. K. Jarvis, R.A. Kennedy, C. A. Mayhew, and R. P. Tuckett, *J. Phys. Chem. A*, 2000, **104**, 10766.
4. D. M. Smith, R. P. Tuckett, K. Yoxall, K. Codling, P. A. Hatherly, J. F. M. Aarts, and M. Stankiewicz, *J. Chem. Phys.*, 1994, **101**, 10559.
5. P. A. Hatherly, D. M. Smith, and R. P. Tuckett, *Z. Phys. Chem. (Munich)*, 1996, **195**, 97.
6. G. K. Jarvis, D. P. Seccombe, R. P. Tuckett, *Chem Phys Lett.*, 1999, **315**, 287.
7. H. H. Claassen, G. L. Gordon, J. H. Holloway, H. Selig, *J. Chem. Phys.*, 1970, **53**, 341.
8. S. G Lias, J. E. Bartmess, J. F. Liebman, J. L. Holmes, R. D. Levin, W. G. Mallard, *J. Phys. Chem. Ref Data*. 1988, **17**, supplement 1.
9. J. C. Creasey, H. M. Jones, D. M. Smith, R. P. Tuckett, P. A. Hatherly, K. Codling and I. Powis, *Chem. Phys.*, 1993, **174**, 441.
10. A. A. Ischenko, J. D. Ewbank and L. Schafer, *J. Chem. Phys.*, 1994, **98**, 4287.
11. P. Maggard, V. A. Lobastov, L. Schafer, J. D. Ewbank and A. A. Ischenko, *J. Phys. Chem.* 1995, **99**, 13115.
12. H. M. Seip and R. Stolevik, *Acta Chemica Scandinavica*, 1966, **20**, 1535.
13. M. Tichy, G. Javahery, N. D. Twiddy and E. E. Fergusson, *Int. J. Mass Spec. Ion Phys.*, 1987, **79**, 231
14. G. K. Jarvis and R. P. Tuckett, *Chem. Phys. Lett.*, 1998, **295**, 145.
15. R. L. Asher, and B. Ruscic, *J. Chem. Phys.*, 1997, **106**, 210.
16. C. E. Klots, *J. Chem. Phys.*, 1973, **58**, 5364.

17. K. E. Holdy, L. C. Klotz and K. R. Wilson, *J. Chem. Phys.*, 1970, **52**, 4588.
18. G. E. Busch and K. R. Wilson, *J. Chem. Phys.*, 1972, **56**, 3626.
19. D. R. Lide, *CRC Handbook of Chemistry and Physics*, 76th ed., 1996, CRC Press.
20. E. Illenberger and J. Momigny, *Gaseous Molecular Ions*, 1992, Springer-Verlag New York.
21. G. K. Jarvis, C. A. Mayhew, R. Y. L. Chim, R. A. Kennedy, R. P. Tuckett, *Chem. Phys. Lett.*, 2000, **320**, 104.